

STUDY OF THE THERMOSPHERE-IONOSPHERE COUPLING
UNDER VARYING GEOPHYSICAL CONDITIONS.

Thesis submitted to
Gujarat University.

For the Degree of
Doctor of Philosophy

In

Physics

By
Tarun Kumar Pant

March-1998

Physical Research Laboratory
Navarangpura
Ahmedabad 380 009
Gujarat (India)

**Dedicated
To
Parents**

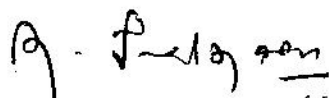
CERTIFICATE

I hereby declare that the work presented in this thesis is original and has not formed the basis for the award of any degree or diploma by any University or Institution.



Tarun Kumar Pant
(Author)

Certified by :



Prof. R. Sridharan,
(Thesis Supervisor)
Physical Research Laboratory,
Ahmedabad 380 009,
India.

Contents

Acknowledgements	viii
Abstracts	xi
1 Introduction	1
1.1 Ionosphere	5
1.2 Sources and Sinks of Energy for the Thermosphere	6
1.3 Thermosphere - Ionosphere coupling	11
1.4 Chemical Coupling	13
1.5 Dynamical Coupling	16
1.5.1 Diffusion	17
1.6 Low Latitude F-region Electrodynamics	20
1.7 F-region Dynamo	21
1.8 Wind Induced Movement	28
1.9 Ion-drag	31
1.10 Equatorial Spread-F (ESF)	35
1.11 Midnight Temperature Maximum (MTM)	39
1.12 Thermospheric Models	43
2 Instrumentation	47

2.1	Upper Atmosphere Airglow	47
2.2	Emission Lines of Atomic Oxygen	48
2.3	Present Study	56
2.4	Theory of Fabry-Perot Spectrometer	58
2.5	Parameter Selection and Technical Details	62
2.5.1	Fabry-Perot Etalon	62
2.5.2	Static Aperture Size, Field of View and Resulting Luminosity	63
2.5.3	LRP Criterion	64
2.5.4	Interference Filter	65
2.5.5	Photomultiplier Tube	68
2.5.6	Data Acquisition System	68
2.6	Working of the High Resolution Central Aperture Scanning Fabry-Perot Spectrometer	69
2.7	Retrieval of Doppler Parameters from Observed Interference Fringes	74
2.8	Spectral Line Shape	77
2.8.1	Determination of P_j 's	78
2.8.2	The Noise Reduction and Estimation of Background	81
2.8.3	Estimation of Errors in the Evaluation of Doppler Parameters	83
2.9	Limitations in the Retrieval of Doppler Parameters	85
2.9.1	Aperture Tilt	86
2.9.2	Airglow Intensity Changes	86
2.9.3	Velocity Gradients and Gross Motions	87
2.9.4	Contamination from Nearby Emissions	87
3	Low Latitude TIS During Quiet Times	89
3.1	Introduction	89

3.2	The Servo Mechanism	92
3.3	The F-layer Movement and the Continuity Equation	94
3.4	Wind Induced Drifts	95
3.5	Electromagnetic Drifts	95
3.6	Diffusion	97
3.6.1	Solar Heating Effects	99
3.7	The Servo Model	101
3.8	The Night Stationary Level	104
3.9	The F-peak Position Vs. the Temperature, Winds and Electric Fields	105
3.10	Variations of Thermospheric Parameters over Mt.Abu	111
3.11	The Low Latitude Thermosphere Ionosphere System	123
3.12	Conclusions	134
4	Low Latitude TIS During Storm Times	136
4.1	Geomagnetic Storms	136
4.2	Sun as a Source of Energetic Plasma	136
4.3	Interaction of Earth's Magnetosphere with the Solar Wind	139
4.4	Magnetic Reconnection and Flux Transfer Events	142
4.5	Current Issues of Magnetosphere - Ionosphere Coupling	145
4.6	Evolution of a Geomagnetic Storm	147
4.7	Geomagnetic Storm and the Use of Indices	150
4.8	The Atmospheric Energetics and Dynamics during Geomagnetic Storms	153
4.9	Geomagnetic Storms-The Low Latitude TIS during Geomagnetic Storms	156
4.10	Temporal Evolution of Storm Effects over Low Latitude Regions	159
4.11	Data Presentation	164
4.12	Temperature variations over Mt.Abu	169

4.13	The Low Latitude Thermosphere-Ionosphere Coupling During Geomagnetic storms	176
4.14	Airglow Intensity Variations during Storms	189
4.15	Conclusions	193
5	Variabilities in the Thermospheric Temperatures and their Representation by the Model	195
5.1	Introduction	195
5.2	Development of MSIS model - A Perspective	196
5.3	Low Latitude Thermospheric Temperature During Storms and 'MSIS' Model .	205
5.4	Deviation of Thermospheric Temperatures from the MSIS Model	206
5.5	Time Response of Low Latitude Thermosphere to Geomagnetic Forcings	209
5.6	Parameterisation of D_{st} and Augmentation of the MSIS Model	214
5.7	Thermospheric Temperatures During Geomagnetically Quiet Conditions and the Model (MSIS) Predictions	216
5.8	Neutral Dynamical Effects	219
5.9	Electrodynamical Effects	222
5.10	Augmentation of the MSIS Model for Quiet Conditions	225
5.11	Limitations of Ground Based (Optical) Spectroscopic Techniques in Estimating the Thermospheric Temperatures	237
5.12	Station Processor	240
6	Parameterisation of Local and Nonlocal Processes and their Incorporation into the MSIS Model	247
6.1	Introduction	247
6.2	Manifestations of Equatorial Ionisation Anomaly over Equatorial and Low Latitudes	248

6.3	The Equatorial Temperature and Wind Anomaly	254
6.4	Plausible Causative Mechanisms of ETWA	257
6.5	Temperature Anomaly in ETWA: Ion-drag and/or Chemical Heating	262
6.6	Dynamics Explorer Satellite (DE-2) Data: An Overview	268
6.6.1	Choice of the DE-2 Data for the Present Study	269
6.7	Local Time Variation of ETWA	271
6.8	Quantification of ETWA	274
6.8.1	Contribution Due to Chemical Heating	274
6.8.2	Contribution of Ion-drag	281
6.9	Seasonal Dependence of the Thermospheric Response to the External Forcings	285
6.10	Results on Thermospheric Temperatures and I-MSIS Prediction	290
6.11	Conclusions	311
7	Summary	312
7.1	Scope of Future Work	317

Acknowledgments

In the preparation of this thesis, I have gathered a considerable amount of indebtedness which is a pleasure to record.

First of all, I express my sincere thanks and a deep sense of gratitude to my thesis supervisor Prof. R. Sridharan, for his invaluable guidance. I have been immensely benefited by his vast knowledge of the various aspects of upper atmospheric physics. His expertise as a true experimentalist, his deep insight into the scientific problems, clarity of thoughts and the lucid explanations provided me a clear perspective to understand the earth's environment and different instrumental techniques. I owe him my gratitude for giving my scientific career a solid foundation and a direction to work on.

I owe my heartfelt thanks to Prof. R. Raghavarao for his constant encouragement and deep concern in the progress of my work. His thought provoking arguments and valuable suggestions have helped me a great deal in understanding the subject I have dealt with. I also thank him for giving me the opportunity to make use of the Dynamics Explorer (DE-2) satellite data which formed a substantial part of my thesis. The DE-2 data on magnetic tapes (in binary form) was made available to Prof. Raghavarao by his colleagues at NASA, namely Drs. W. R. Hoegy and L. E. Wharton. My thanks are due to them also. I acknowledge with pleasure the help rendered by Mr. Ramani of ISAC, Bangalore (now at SAC, Ahmedabad) to read the DE-2 data and make it compatible with our IBM RS 6000 computer system.

It is my pleasure to thank Dr. (Mrs.) R. Suhasini who familiarised me with the science of data analysis. It has been a joy working with Dr. R. Sekar. His to the point comments and a clear understanding of the basics have helped me a great deal in improving my understanding of the subject. I thank Prof. B. H. Subbaraya for taking a keen interest in my progress and encouraging me. I am also grateful to Prof. B. G. Anandarao, Harish Chandra and H. S. S. Sinha for making critical and useful

comments during my assessment reviews.

The kind of affection, inspiration, support and also the practical training I got from my group members, is really an experience to cherish. I thank Mr. R. Narayanan for his concern and help in making me understand the basic physics involved in functioning of the optical instruments fabricated in house. Mr. N. K. Modi has always been there to provide the necessary support in electronics. My thanks to him. It was a pleasure working with Mr. Narayanan and Modi in the out station field campaigns. I very fondly recall my Tirupati and Mt.Abu campaigns with Mr. C. L. Piplapure. I am thankful to him for always helping me in need. It's also a pleasure to thank Mrs. Vijaya Mutagi for her help, care and affection extended to me during my tenure as a research scholar. I thank Miss Ranna Patel and Mrs. Manisha Pandya for helping me in the data analysis. My special thanks to Dr. S. Gurubaran, Dr. D. Pallam Raju, Alok and Dipu, with whom I had many useful discussions.

The timely help rendered by various departments and facilities in PRL makes it a pleasure to work in this institute. In this context I thank Mrs. R. Bharucha and the library staff for their prompt and efficient services. My sincere thanks to Mr. C. L. Gajjar of PRL workshop for his help in various stages of the instrument fabrication. I also thank Mr. D. R. Ranpura of the Photography and Documentation section for his help. I must thank Mr. P. S. Shah and his colleagues at the computer center for providing a congenial environment to work day and night. Thanks are also due to Mr. N. R. K. Pillai for typing this thesis and helping me in preparing various scientific documents from time to time. I also acknowledge Messrs. Philip Samuel and N. P. M. Nair for their assistance.

I cherish every single moment spent with my friends in the laboratory and hostel. I thank all of them and in particular Abhijit, Bhushan, Ban, Biju, Jyoti, Manish, Prabir, Prashant, Prahlad, Prasenjit, Rama, Ramani, Ratan, Sam, Sandeep, Santhanam, Shikha, Siva and Watson. Their company had made my stay in PRL a joy forever.

I am at a loss of words in expressing my thanks to Varun and Joona, who have always been there to help me, to boost my morale whenever I felt low in spirits. I have found lifelong friends in them. Last but not least, I am deeply indebted to my mom, dad, chachu and chachi for their continuous support. The love and care they showered on me is beyond words. Their constant encouragement always kept me in high spirits. The affectionate letters from my sisters Ninu and Sonu always filled me with joy and vigour. Som (my brother-in-law) has been very affectionate and helpful. I owe my heartfelt thanks to all of them.

Abstract

The present study deals with the nature of the coupling of low latitude thermosphere ionosphere system (TIS) under varying geophysical conditions. The thermospheric parameters studied were temperature and meridional winds obtained by using nighttime high resolution central aperture scanning Fabry-Perot spectrometers for the Optical Aeronomy Laboratory at Mt.Abu (24.6° N, 72.7° E). Ionospheric parameters such as F-layer equilibrium height and electron density at 250 km were obtained by means of ground based ionosonde at Ahmedabad (23° N, 72.1° E). Data from the satellite Dynamics Explorer - 2 (DE-2) was also made use of in order to overcome the limitations imposed by the ground based spectroscopic measurements, in the present investigation. The work carried out towards the completion of this thesis is presented as follows.

- A brief introduction of the earth's upper atmosphere is provided in chapter 1. Different, basic energetic and dynamic, aspects of the low latitude thermosphere and the ionosphere in terms of their coupling are described. The less understood prominent low latitude, large scale processes like equatorial spread F and Midnight Temperature Maximum (MTM) are discussed.
- Chapter 2 describes the selection of various suitable instrument parameters of our instrument i.e. high resolution central aperture scanning Fabry-Perot spectrometer. The data analysis techniques adopted is also described in appropriate details.
- Chapter 3 provides the results of the study of low latitude TIS coupling during low solar activity epoch and geomagnetically quiet periods. Rishbeth's servo model was used to study the nature and the extent of the coupling in low latitude TIS. The observed temperatures and winds were

used as an input to the model. This study brought out the dominant role played by the thermospheric parameters over ionosphere during geomagnetically quiet and low solar activity phases. This study also confirmed the existence of enhanced observed temperatures with its prominent day to day and short temporal variabilities.

- In chapter 4, we discuss the behaviour of the low latitude TIS during geomagnetically perturbed periods. We studied the changes in low latitude TIS in terms of its energetics and dynamics during disturbed periods. These changes are a result of the high latitude-low latitude coupling. We concluded that the temperatures at low latitudes undergo severe modulations under the influence of storm time meridional circulation, ring current, and traveling atmospheric disturbances. In this chapter we also show that the servo model is equally applicable for the magnetically disturbed periods as well.
- Chapter 5 comprises of the discussions and results on the detailed investigation done in order to account for the differences observed between the measured and MSIS model predicted thermospheric temperatures. This was done for both geomagnetically quiet and disturbed periods. These results show that geomagnetic index D_{st} in the form of $\frac{d}{dt}D_{st}$ is a better index than A_p to represent low latitude TIS. This index has also been successfully used to improve the MSIS model. The limitations involved in the use of spectroscopically observed temperatures for the augmentation of the model has also been discussed in this chapter.
- In chapter 6 we give the details of the estimation of contributions from local processes like ETWA. To estimate the extent of heating due to ETWA, DE-2 data on composition and temperature were used. Contribution from both the processes i.e. chemical heating and ion-drag which are supposed

to be responsible for the generation of ETWA, was estimated. Finally, the results dealing with all the three namely, ring current, ion-drag and chemical heating, are presented in this chapter.

The results presented and discussed in this thesis bring out the importance of the various local and non local processes which contribute significantly to the low latitude energetics. However it was realised that more quantitative information on these processes is needed to improve the existing thermospheric models to make them represent the low latitude temperatures more realistically.

Chapter 1

Introduction

The Earth's atmosphere which corotates with it, is categorized into five regions namely *troposphere* (0-15 km), *stratosphere* (15-50 km), *mesosphere* (50-90 km), *thermosphere* (90-400 km) and *exosphere* higher above and are separated by not so well defined boundaries namely *tropopause* (170K), *stratopause*(260K), and *mesopause* (150K) respectively [Figure(1.1)]. These regions are defined broadly on the basis of variation in the atmospheric temperature. About 99.9% of the mass of the atmosphere is concentrated below 90 km, while only one part in 10^5 is distributed above it. The upper boundary of the Earth's atmosphere is not sharply defined, but gradually extends into the thin interplanetary medium. Owing to these facts, the mean free path (which is inversely proportional to density) of the major atmospheric constituents in the dense lower atmosphere is very small and therefore, the turbulent mixing of constituents dominates over individual molecular diffusion processes. Hence, the main constituents of lower atmosphere are homogeneously mixed, and this region is termed as *homosphere*. The homosphere is characterized by a mean atmospheric density of ~ 24 amu. There exists a rather sharply defined upper limit for the homosphere, which is known as the *turbopause* (~ 110 km). At this altitude the mixing due to turbulence almost ceases, and processes concerning molecular diffusion become dominant. This leads to gradual diffusive separation of each

individual atmospheric species existing at and above the turbopause. As a result, the vertical distribution of the atmospheric species is governed by their molecular masses and consequently the composition varies with altitude resulting in the so called *heterosphere*. The density of the individual specie decreases with

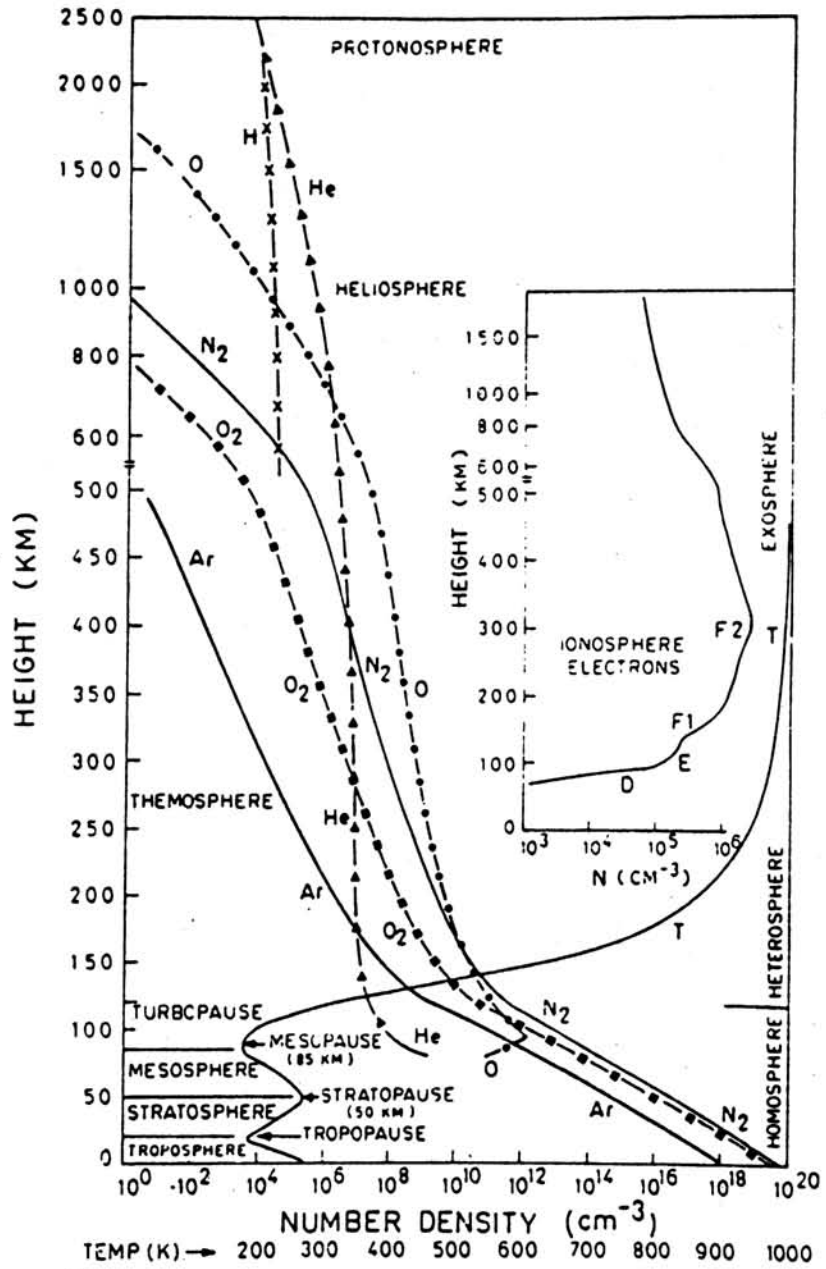


Figure 1.1: Altitude variation of the thermal and composition structure of the atmosphere

altitude and eventually leads to a situation where the atomic and molecular motions, which are constantly under the influence of gravity, become almost collision free. Under such conditions, the molecules and atoms with larger kinetic energy can escape from the earth's atmosphere once and for all. The region where such an escape from the atmosphere becomes significant is called the *exosphere* and is usually at $\sim 400\text{km}$. However, this altitude is not very precisely defined and is highly dependent on the solar activity.

The upper atmospheric part of the earth's environment where the present study is focussed upon, is the *thermosphere*. The thermosphere extends from the coldest ($\sim 150\text{K}$) to the hottest ($\sim 1600\text{K}$) part of the the earth's atmosphere with atomic and molecular oxygen (O, O_2) and molecular nitrogen (N_2) as the main constituents of this medium. As has been mentioned already, the thermosphere is the region where the atmospheric species are in diffusive equilibrium. The $\frac{O}{O_2}$ concentration ratio increases rapidly upwards from about 100 km indicating the existence of diffusive separation at that altitude [Schaefer and Brown, 1964]. This also indicates that in the thermosphere molecular oxygen gets photodissociated to form atomic oxygen by interacting with solar EUV radiation. Since, the scale height of the thermospheric constituents vary over a wide range, the relative composition of the thermosphere changes markedly with height, the lighter gases becoming progressively more abundant. Significant amount of ionisation is also produced due to interaction of solar EUV radiation with the thermospheric species. In fact, most of the ionisation present in the atmosphere is produced in the thermosphere. Very little amount of Ar, He, N, NO etc. are known to be present. The thermal structure of this region is maintained primarily by the energy received from the sun. A brief discussion on the ionosphere is provided in the next section, followed by details of the energetics of the thermosphere.

1.1 Ionosphere

Like in the case of neutral atmosphere, the ionosphere is also divided into regions namely D, E and F. It has also been found that within F layer also, distinct ledges of ionisation get formed during daytime which are named as F_1 and F_2 . Though, the boundaries of these layers gradually merge into each other, the boundary between D and E region is assumed at ~ 90 km altitude and that between the E and F regions at 150 km. The lower extent of the ionosphere is often taken to be at ~ 50 km. As has already been explained, the ionisation is produced in the earth's atmosphere by a wide spectrum of solar radiation. During solar maximum, the solar X-radiation of roughly $1-8 \text{ \AA}$ provide the major source of ionisation for the D-layer. $H \text{ Ly } \alpha$ 1216 \AA absorbed by NO is the important ionising radiation for D-layer during solar minimum. Apart from this, there is a cosmic ray contribution too in the D-region ionisation. The $796-1027 \text{ \AA}$ band in UV radiation provides most of the E-region ionisation. Another contribution to E-region ionisation comes from solar X-radiation in the range $8-140 \text{ \AA}$. The F-region ionisation is also provided by solar UV radiation whose upper limit is approximately around 796 \AA roughly in the range $140-796 \text{ \AA}$.

The E-region and lower F-region are almost devoid of negative ions. For instance NO^+ , O_2^+ are the important ions below ~ 150 km. While above 150 km the plasma is dominated by O^+ ions. In lower altitude regions, where molecular ions dominate, the plasma density is drastically reduced at night due to faster dissociative recombination reactions. The plasma higher above (H^+ , O^+ ions) remains throughout the night. The processes of photo-ionisation, dissociative recombination and radiative recombination are replete in these regions. It has been found that in the ionosphere, the electrons at two different altitude regions follow different loss mechanisms. Below 150 km, the molecular dissociative recombinations determine the electron loss rate, while at greater heights

ion-molecule interchange reactions determine the loss rate of electrons. The transition between these two regions occurs in the F-region at about 160-200 km. When this transition region coincides with the level at which the F-region ionisation production is maximum, the former splits into F₁ and F₂ layers [Ratcliffe 1956].

Apart from this, the ionosphere is the region where ‘*atmospheric dynamos*’ are active and electric fields are produced. These electric fields induce currents and motions in the ionospheric plasma. At times, various kinds of plasma instabilities also get initiated in this region. The plasma tends to diffuse because of its own pressure gradients and also under the action of gravity and the earth’s magnetic field. Appropriate details of the transport processes driving the plasma in upper atmosphere and also of the various interactions between the neutral and ionised species are provided later in this chapter.

1.2 Sources and Sinks of Energy for the Thermosphere

Solar EUV and UV radiation are the primary sources of energy for the thermosphere. Their distribution is accomplished through various processes with different efficiencies of transfer of energy into thermosphere in the form of heating [figure(1.2)]. The lower thermosphere has a large optical depth to solar EUV, UV radiation and therefore absorption of these radiations peaks in this region. Schumann- Runge continuum ($\sim 1300 - 1750\text{\AA}$) is the dominant heat source between 90-150km in the lower thermosphere through molecular dissociation of O_2 , and through collisional quenching of the reaction product, i.e. $O(^1D)$ which leads to local heating of the thermosphere in this region. The heating efficiency of this process is $\sim 33\%$ [Stolarski *et al.* 1975, 1976]. So, nearly one third of the Schumann-Runge continuum photon energy goes into heating. In the middle and upper thermosphere, the absorption of solar EUV photon

($\leq 1027\text{\AA}$), through photo-ionisation contributes towards thermospheric heating. In fact, it is the subsequent collisions of the primary photoelectrons with surrounding ions and neutrals which lead to heating of the local thermospheric gas with an efficiency of $\sim 5\%$ [Stolarski *et al.* 1975, 1976, Torr *et al.* 1980]. Significant amount of photoelectron energy is lost to space in the form of airglow emissions from the excited atomic and molecular states. A very comprehensive set of observations on photoelectron flux was provided by instruments onboard Atmospheric Explorer satellite (AE-E) [Lee *et al.* 1980].

The ions produced by the photoionisation process eventually get thermalised by various ion-molecule exothermic reactions. Most of the energy carried by the ions goes directly into the heating of the local thermosphere [Torr *et al.* 1980]. Torr *et al.* [1980] presented improved thermospheric heating efficiency rates for various

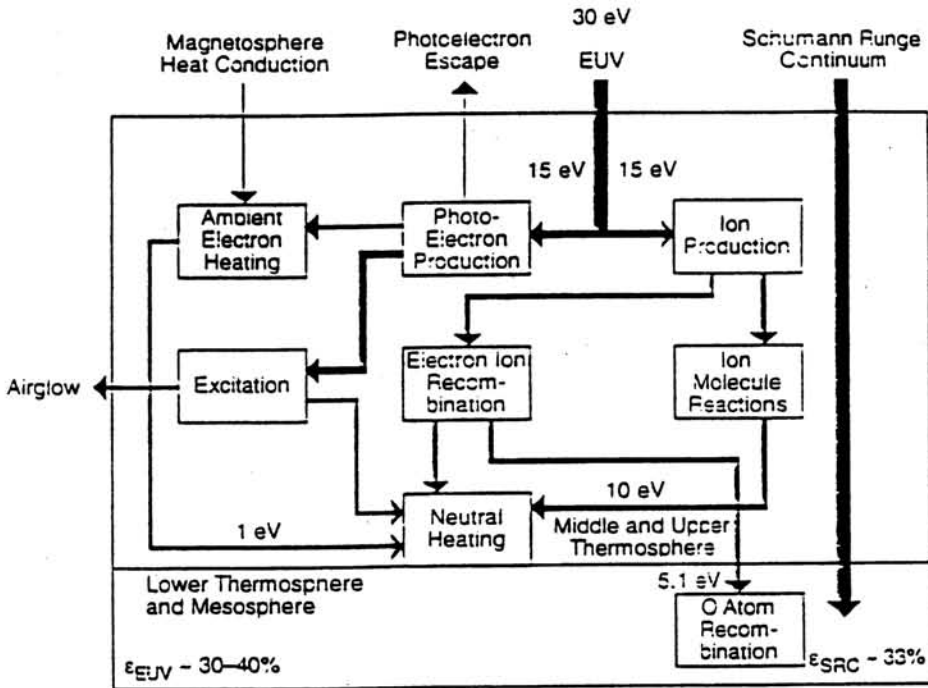


Figure 1.2: Distribution of solar EUV and UV radiation in the thermosphere. (Roble, *Geophys. monogh.* 1987)

processes for different seasonal and solar cycle effects and show their altitudinal and a temporal dependence due to the diurnal variation of the density of minor constituents and the reaction rates.

Hedin [1983] showed that for solar maximum condition, the global mean temperatures estimated on the basis of EUV and UV flux were significantly higher when compared with the MSIS model predictions. This difference was later explained on the basis of radiative cooling by the $5.3\mu\text{m}$ band of NO . And thus, the importance of the radiative cooling in the lower thermosphere ($\sim 100\text{km}$) due to the CO_2 and other trace gases was realised, in order to explain the overall thermospheric energy budget. Energy is also transferred into the thermosphere from the lower atmospheric regions in the form of tides, gravity and planetary waves. Tides are the sub-harmonic oscillations of a solar day and are excited by the variation in the diurnal absorption of solar insolation. Absorption of IR radiation by water vapour

are excited by the variation in the diurnal absorption of solar insolation. Absorption of IR radiation by water vapour at $\sim 15\text{km}$ and absorption of UV radiation ($2000-3000\text{\AA}$) by Ozone near 30-60km, are the main sources of the diurnal and semidiurnal tides in thermosphere. The topography, frontal system, convection and wind shears in lower atmosphere i.e. around tropopause also have been regarded as the sources of the Gravity waves [*Hines 1960, Lindzen 1981, Manson et al. 1991*]. The amplitude of these gravity and tidal wave modes grows while propagating upwards in order to conserve the energy, as the atmospheric density decreases with altitude. Most of these modes get saturated in the lower thermospheric regions ($\sim 90\text{km}$) and break into smaller eddies, thereby, depositing energy and momentum to the mean background flow [*Garcia and Solomon 1985*].

Groves and Forbes [1984] presented the mean heating rates as a function of altitude and latitude. They found that the tidal heating maximises at $\sim 90\text{km}$. The global integral tidal heating from 150-400km was estimated to be $\sim 6 \times 10^9$ watts i.e. $\sim 7\%$ of the EUV deposition rate. And in the altitude range of 90-150km, the heating rate was $\sim 7.6 \times 10^{10}$ watts i.e. 7% of UV heating in the same region. However, the correct estimation of their contribution to thermospheric energy budget is rather complex because of their very high day to day variabilities. Therefore, the quantification of these tidal, gravity and planetary wave modes had been the theme of important future scientific programs like TIMED (Thermosphere Ionosphere Mesosphere Energetics and Dynamics) satellite mission and the international PSMOS (Planetary Scale Mesopause Observing System) programme of co-ordinated ground based observations.

Apart from the solar EUV and UV radiation, tides and gravity waves; high latitude sources of heating are necessary to maintain the global thermospheric

energy budget. These sources include the Joule heating, direct energetic particle precipitation over high latitudes and from the magnetospheric ring current. The modeling of these sources is extremely difficult because of very high temporal and spatial variabilities associated with them. However, the global joule heating rate in thermosphere has been found to be $\sim 0.3 - 1.5 \times 10^{11}$ Watts depending on the geomagnetic activity level. Based on satellite observations on precipitating particle fluxes, the particle heating is found to be around $0.05 - 0.6 \times 10^{11}$ watts depending on the solar activity [Killeen and Roble 1986, Fuller-Rowell and Evans 1987]. It is clear from the above discussion that it requires a comprehensive understanding of various energy sources, which influence the mean thermal budget of thermosphere, originating from the mesosphere and the stratosphere lower below, and from the magnetosphere higher above.

Most of the thermal energy deposited in thermosphere (upper) is redistributed through vertical heat conduction (molecular and eddy) into the lower atmosphere where the processes of radiative cooling (~ 90 km) becomes important. As a result, large temperature gradients characterize this region. In recent times, a number of studies using ground based sounding techniques such as optical spectroscopy, radar, ionosonde etc., along with *insitu* satellite observations have provided valuable information on the dynamical properties of the upper atmosphere and the F-region of ionosphere. Further, the so called 'space weather' related issues necessitates our complete understanding of thermospheric variabilities in terms of both the energy and the dynamics, as a part of the ongoing changes in solar terrestrial environment.

1.3 Thermosphere - Ionosphere coupling

One of the most remarkable properties of the thermosphere is its symbiotic relationship with the ionosphere and this distinguishes it from the other regions of earth's atmosphere. Almost all the dynamical features of the upper atmosphere are controlled by the processes which are a result of the prevailing thermosphere - ionosphere coupling. The redistribution of energy received by the upper atmosphere through different sources [figure(1.3)] is, facilitated by the neutral dynamical, chemical, electrodynamical and fluid dynamical processes. There are two aspects in the study of such a coupled system i.e., thermosphere-ionosphere system (TIS). One from the point of view of the average behaviour (climatology) and the other dealing with its instantaneous, hour-to-hour, day-to-day, and even longer temporal variabilities (i.e., the weather). These variations are manifestations of couplings, time delays and feedback mechanisms that are inherent to the system.

Sources (\Rightarrow)
Sinks (\Leftarrow)

Atmospheric Phenomena & Dynamical Interactions

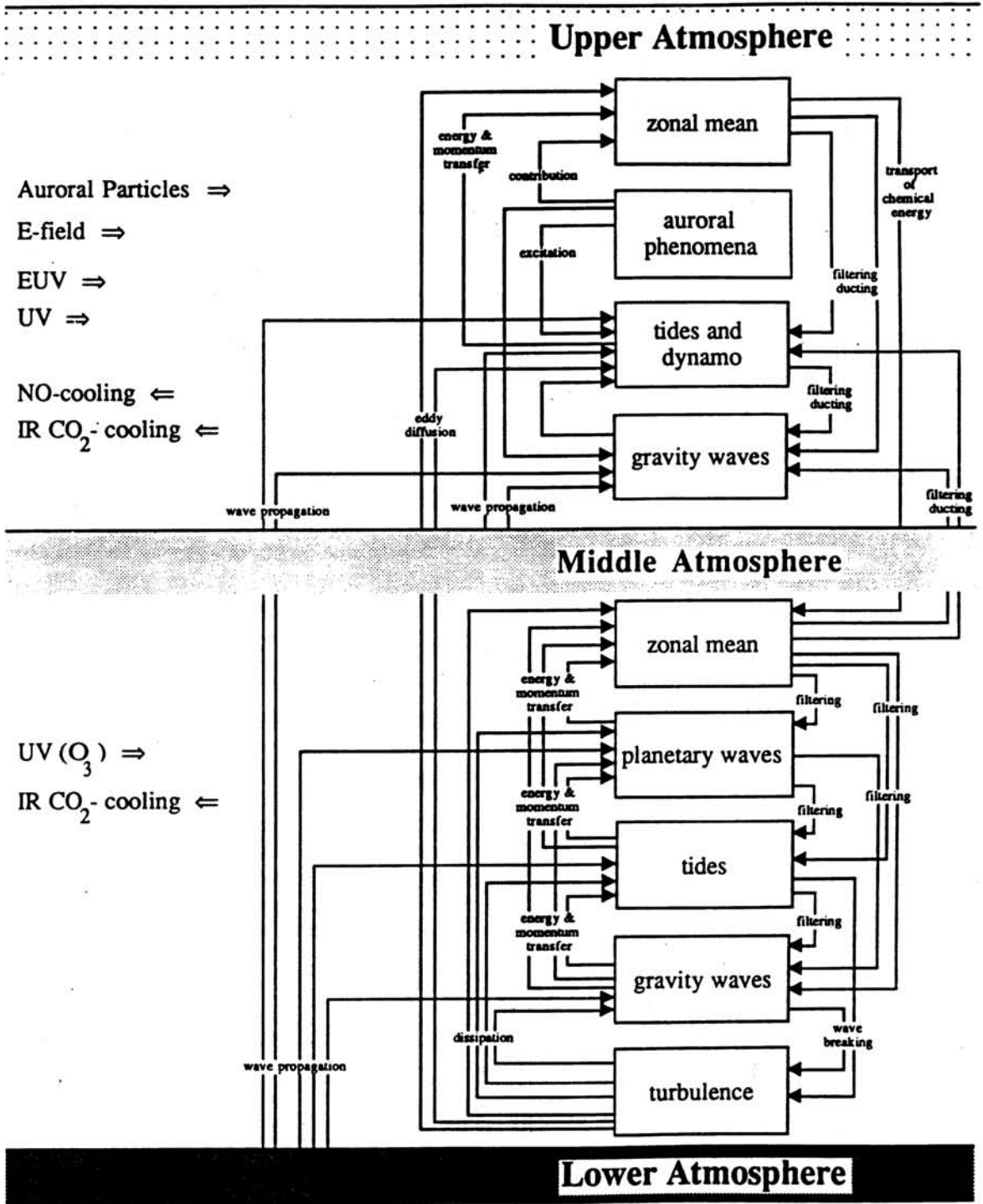


Figure 1.3: The different sources of energy for the thermosphere. (Chan et al., Geophys. monogh. 1987)

Characteristic variabilities of the various forcing factors like solar, interplanetary, magnetospheric and mesospheric processes can also contribute to the TIS variabilities. Perhaps, one of the most important aspects of the thermosphere - ionosphere coupling is the chemistry involved between them. Apart from the direct photoionisation, the absorbed solar energy results in the metastable excited states of various thermospheric atoms and molecules as an end product through chemical reactions. The ionic pairs and the atmospheric species in metastable excited states provide a reservoir for solar energy deposited in the thermosphere. In their life time, the species mentioned above redistribute the energy mainly through collision processes, but a significant part of the energy gets partitioned in further production of ions, formation of other metastable species, and to the ambient through momentum transfer and nonlocal deposition of energy. By the nature of their basic properties, both the neutral and ionised species make chemical interactions an important coupling mechanism between the neutral atmosphere i.e. the thermosphere and the F-region of the ionosphere.

1.4 Chemical Coupling

As mentioned earlier, in the F-region of the ionosphere (i.e. 200 km - 500 km) and the upper thermosphere the most abundant constituents are O and O^+ . Though, the movement of the ions in the F-region of the ionosphere is highly constrained by the earth's magnetic field, these ions take active part in the upper atmospheric chemistry and play a very important role. For instance, photoionisation of the dominant neutral constituents viz. the atomic oxygen leads to the formation of O^+ in different energy states such as $O^+(^4S)$, $O^+(^2D)$ and $O^+(^2P)$ in approximately 43%, 29%, 28% proportion [Torr and Torr, 1982]. Each of these ions take part in different chemical schemes, giving rise to different reaction products. The basic nature of chemistry at any particular altitude is

dictated by the rate at which the production and loss of the ionisation and the involved transport processes are operating. The life time of these ions at any altitude depends to a great extent on the chemistry prevailing at those heights. The life time of important thermospheric O^+ ion is only a few seconds in lower thermosphere (~ 100 km) which increases to order of days in upper thermosphere. As is known, while photoionisation is the main production process for majority of ions, the important loss mechanisms are (i) atomic ion and electron recombination (radiative recombination) and (ii) molecular ions and electron (dissociative) recombination.

At any given instant of time, the distribution of ionisation, electrons for instance, is described by the following continuity equation:

$$\frac{1}{q} = \frac{1}{\beta N_e} + \frac{1}{\alpha N_e^2} \quad (1.1)$$

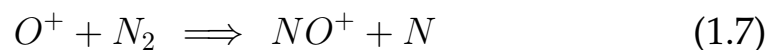
where ' q ' is the production rate of ionization, ' α ' is the dissociative recombination coefficient while ' β ' is the effective loss coefficient, which is a function of molecular density. Eq. (1.1) leads to following two limiting cases, namely:

$$q = \alpha N_e^2 \quad \text{if } \beta \gg \alpha N; \text{ so that } N_{M^+} \gg N_{A^+} \quad (1.2)$$

$$q = \beta N_e \quad \text{if } \beta \ll \alpha N; \text{ so that } N_{M^+} \ll N_{A^+} \quad (1.3)$$

N_{M^+} , N_{A^+} are the molecular ion and atomic ion density respectively. Here, the sum of N_{M^+} and N_{A^+} equals to the net electron density N_e to maintain the charge neutrality condition which prevails in the upper atmosphere at all the times. From equation (1.1) it could be seen that (i) if the ions are mainly molecular as in the E and lower F-region then the rate of electron loss is determined by the dissociative recombination as is given by αN_e^2 ; (ii) when the majority are atomic ions, as one encounters in the upper F-layer, the loss rate is determined by the two step effective recombination which is given by βN_e . In summary,

the important processes in the F-region could be written as:



Therefore the upper F-region ionisation (≥ 200 km) is governed by the linear loss rate i.e. βN_e , while the square loss rate prevails for lower F-region i.e., below ~ 150 km.

The excited metastable species give out characteristic emissions known as 'airglow' from different altitudes within the thermosphere and the F-region of the ionosphere. The emission relevant to the present investigation is OI6300Å which originates at an altitude region centered around 250km. These emissions provide valuable information about the state of the thermosphere and the ionosphere at any given time in terms of the kinetic temperature and large scale motions i.e. winds. By thermodynamic considerations, the estimated kinetic temperature is a good measure of the local temperature at the height of the emission layer. Therefore, the study of airglow emissions has found an important place in the investigation of the thermosphere - ionosphere system [Roble *et al.* 1968; Hernandez *et al.* 1975]. The metastable specie $O(^1D)$ which emits the radiation described above, has a lifetime of ~ 110 seconds. This time is long enough for $O(^1D)$ to attain thermal equilibrium before undergoing de-excitation. Daytime F-region chemistry is much more complex, in the context

of the metastable $O(^1D)$ state, as there are three processes simultaneously operative and contribute towards net $O(^1D)$ production. These processes are photodissociation, photoelectron impact and dissociative recombination. From the above, it could be seen that the atmospheric chemistry, apart from being an important coupling mechanism for thermosphere and ionosphere, also yields important information about the dynamic state of the system at any given instant of time.

1.5 Dynamical Coupling

Another significant aspect of the thermosphere - ionosphere coupling is the transport processes active within the system. Significant nonlocal effects can be initiated by the physical transport of species like, for instance, the neutrals, ions and metastable species away from the region in which they are either formed or expected to remain otherwise, before actually distributing their energy to the ambient species. As a result, several large scale dynamical processes get initiated in upper atmosphere. These processes include both the neutral as well as the ionised species. The dynamics of the charged species is further affected by the presence of magnetic and electric fields and also on the surrounding neutral density. Consequently, at different altitudes in thermosphere depending upon the competing processes, different transport effects take control of the overall dynamics. In the F-region, transport processes namely diffusion and plasma drifts are dominating and compete with the chemistry to take control of the overall behaviour of the system. These two processes are described briefly in following sections.

1.5.1 Diffusion

In the presence of vertical gravitational field and its own partial pressure gradients, the F-region plasma has a tendency to diffuse through the ambient neutral atmosphere. Under equilibrium conditions, the density gradient is always downward for any orientation of magnetic field [Kelley 1989]. These density gradients force the plasma to diffuse. The electrons, because of their lighter mass, diffuse faster than the ions. A stage is soon reached where the electrons and ions are well separated from each other during their motion. This charge separation gives rise to a polarisation electric field which in turn constrains the electron's faster motion and simultaneously enhances the ion diffusion. Dynamically both the ions and the electrons, held together by the above mentioned electric field diffuse together. This diffusion is rightly called the '*ambipolar diffusion*'.

However, in the F-region, the movement of ions and electrons is constrained only along the magnetic field lines as their gyrofrequencies are much higher than corresponding collision frequencies at these altitudes. Apart from diffusion, it depends also on the orientation of magnetic field lines i.e, the magnetic dip angle. The diffusion becomes insignificant at a place where the dip angle is zero. At the dip-equator, the field lines are horizontal, hence the diffusion effects would be negligible there. However, over low latitudes, the diffusion processes are quite significant and play an important role in coupling the neutrals and ions. During night times, in the absence of production, the energetics of the thermosphere and the ionosphere is essentially decided by the relative time scales of diffusion and the loss processes. The loss coefficient ' β ' being altitude dependent, decreases exponentially with altitude i.e, the plasma life time increases with increasing altitude in F-region. Under these circumstances, above a certain height, the plasma diffusion becomes fast enough to

redistribute the plasma before it can interact chemically with other species. As a result, the concentration of ions or electrons do not increase indefinitely with altitude, as the ambient diffusion takes over above a certain height and a dynamic equilibrium is maintained. The F-region peak altitude represents the transition zone between the region in chemical equilibrium and the one in diffusive equilibrium and at the F2 peak, they balance out each other. This interplay of chemistry and diffusion process characterizes the dynamic nature of the F-region, which is coupled with the thermosphere and renders a typical distribution pattern for ionisation in nighttime thermosphere. It is important to mention here that the chemistry and the transport due to diffusion are inherent to the system (TIS) dynamics, but there are other forcings which can induce additional drifts to the already moving plasma. These forcings would not only affect the distribution of plasma, but influence the thermosphere - ionosphere energetics and dynamics as a whole.

Apart from the diffusion effects, the plasma experiences a drift. As explained earlier, the diffusion depends on the plasma density gradients; while the plasma drifts are initiated by the electric fields prevailing in the upper atmosphere. They are affected by the motion of neutral species primarily through the collisions between the neutral and charged species. It is very well understood now that it is the zonal flow of neutral species in thermosphere which gives rise to electric fields due to the global scale dynamo action, leading to the plasma drift.

In the early stages of measurements on plasma drifts, a number of observations remained unexplained for lack of proper understanding on the exact nature of coupling between the neutral and the ionised species in the upper atmosphere. For instance, the apparent correlation between the components of plasma drift velocity parallel to and perpendicular to the geomagnetic field

[Behnke and Harper, 1973; Taylor et al. 1974] could not be attributed purely to either ionospheric movement or to thermospheric dynamics alone. Therefore, other dynamical features of ion-neutral interactions had to be invoked. And, due to the lack of sufficient information on these interactions, a need for an empirical model concerning the F-region of ionosphere and thermosphere, was realised.

Though, the work on these empirical models began much earlier [Jones and Gallet, 1962] more upto-date efforts on this actually commenced with Rishbeth et al. [1978]. Rishbeth et al. [1978] proposed a model called the *servo model* which provided very useful insight into the various physical mechanisms operating in midlatitude F-region and addressed various questions regarding plasma drifts (as mentioned already). This model was based on more realistic assumptions, where the thermosphere and the ionosphere was considered to be a coupled two component system. Perhaps, this attempt was the first such attempt where both the ionosphere and the thermosphere were thought to be dynamically coupled and were addressed to simultaneously. Though, the details of this model would be presented in chapter 3, it is important to mention here that, as a fundamental assumption in servo-model, the F-layer was taken as a unit subject to forces in the prevailing thermospheric background. Hence, all the forcings, originated because of the neutral flow or any agency outside the F-region, were treated as external perturbations like for instance the electric field induced plasma drifts.

Many observational studies, too, did confirm that the thermosphere and the ionosphere truly behaved as a coupled system and the movement of the F-region during different geophysical conditions, with external perturbations indicated towards the extent of coupling between the two. Since then, a number of ground based studies have enabled determination of the average seasonal,

solar cycle, and magnetic effects on the equatorial and low latitude plasma drifts and thermospheric neutral winds, and their control over the F-region plasma density distribution. *Rishbeth's* servo model, in a sense, gave a new impetus to the study of the low and equatorial F-region electrodynamics, neutral dynamical aspects of low and equatorial thermosphere and their mutual interactions, which could be considered to have been pivotal for the present understanding of low latitude thermosphere-ionosphere system.

In this context, various aspects of F-region electrodynamics are discussed in the following text.

1.6 Low Latitude F-region Electrodynamics

The general morphological features of E and F-region plasma drifts and current systems have been studied with incoherent and coherent scatter radars, ionosondes, magnetometers and spaced receiver scintillation techniques. The E and F region electrodynamic drifts are driven primarily by the dynamo electric field. During the quiet geomagnetic periods, the daytime electric fields are produced by the insitu diurnal tide, generated in upper atmosphere and by the upward propagating (2,4) semidiurnal tide [*Richmond et al.* 1976]. The semidiurnal tide becomes increasingly important in the latitude range of 20° to 30° and higher. The large scale diurnal wind generated by the insitu tides flows in the zonal direction and sweeps the ionospheric plasma across the magnetic field lines. This motion of the plasma across the magnetic field line gives rise to electromagnetic force which in turn separates the charges, creating an electric field, which is eastward during the day. During daytime the magnitude of these electric fields are essentially determined by the winds in the E-region

and the ionospheric conductivity. The electric field and the ionospheric currents remain active predominantly in the E-region (~ 100 - 125 km). Nevertheless, these fields and currents do exist in F-region also, which are generated mainly by the F-region dynamo action. The two dynamo regions are threaded by the magnetic field lines which are highly conducting during daytime. As a result, F-region electric fields are largely short circuited during the day by the highly conducting E-region. Therefore, the overall dynamics is driven by the E-region tidal wind generated fields. But, during nighttime, F-region dynamo gains control over E-region dynamo, and governs the overall plasma motion. To highlight the importance of F-region dynamo in this context, a brief account of the dynamo action is provided in the following section.

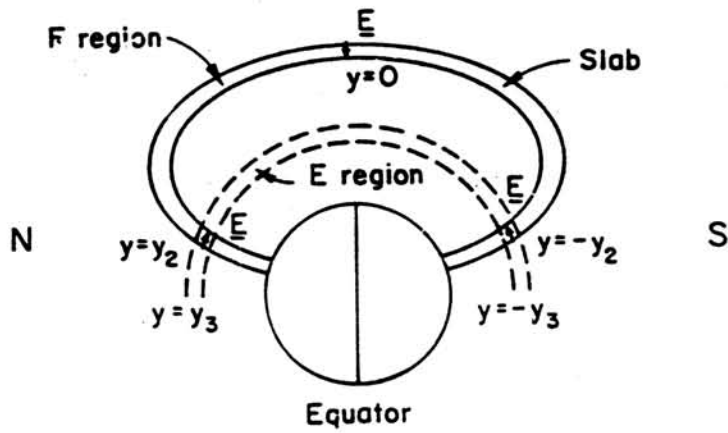
1.7 F-region Dynamo

The thermospheric wind system produced by the pressure inequalities due to the solar EUV heating is the main driving force for the F-region dynamo. During nighttime, when the E-region ionisation almost vanishes, the F-region plasma forms a layer with a well defined lower boundary. The F-region can therefore be approximated to a slab configuration, as depicted in figure(1.4). The F-region plasma has a constant, finite Pedersen conductivity inside the slab and zero outside, a constant zonal wind U is also assumed to be prevalent in this slab. Because of the eastward zonal wind U forcing the plasma across the magnetic field \vec{B} , a polarisation electric field \vec{E} gets generated, as seen clearly in the figure. The electric field \vec{E} thus induced, gives rise to a zonal drift motion V_D in the F-region plasma. It is important to note that, during nighttime, the induced zonal motion in plasma is in the same direction i.e. eastward as that of the neutral wind U . For the vertical electric field, the charge separation would occur in such a way that the overall current J_z becomes zero.

$J_z = \sigma_p E_z + \sigma_p U_z B_z = 0$ which implies $E_z = -U_z B_z$. For a perfect F-region dynamo, the above equation can be generalised and written as $\vec{E} + \vec{U} \times \vec{B} = 0$.

The physical meaning of this equation is that the electromagnetic force \vec{E} on the plasma vanishes and the thermospheric wind blows freely without ion-drag irrespective of the density and the altitude of the plasma inside F-region. The proof of this, comes in the form of nighttime observations pointing towards the near equality of the zonal plasma drift and neutral wind velocities. This also points towards a drastic reduction in nighttime ion drag. Since during the day, the integrated E-region Pedersen conductivity is comparable or more than the magnetic field line integrated F-region conductivity, the F-region field cannot build up and, hence, the F-region ion drag remains high. An interesting aspect of E and F-region dynamos is that both have different electrical characteristics to justify treating them as two separate (though coupled) systems. The E-region dynamo acts essentially as a voltage generator: the dynamo delivers a relatively constant electric field of order $\vec{U} \times \vec{B}$ but drives a current that varies markedly according to the conductivity, especially between the day and the night. While, the F-region dynamo has a higher internal impedance and is essentially a current generator, which delivers a current given by the following equation [Rishbeth 1981].

$$\vec{J} = \frac{\vec{B} \times \nabla \vec{P}}{(B^2 \sin I)} \quad (1.10)$$



ACTUAL GEOMETRY
a

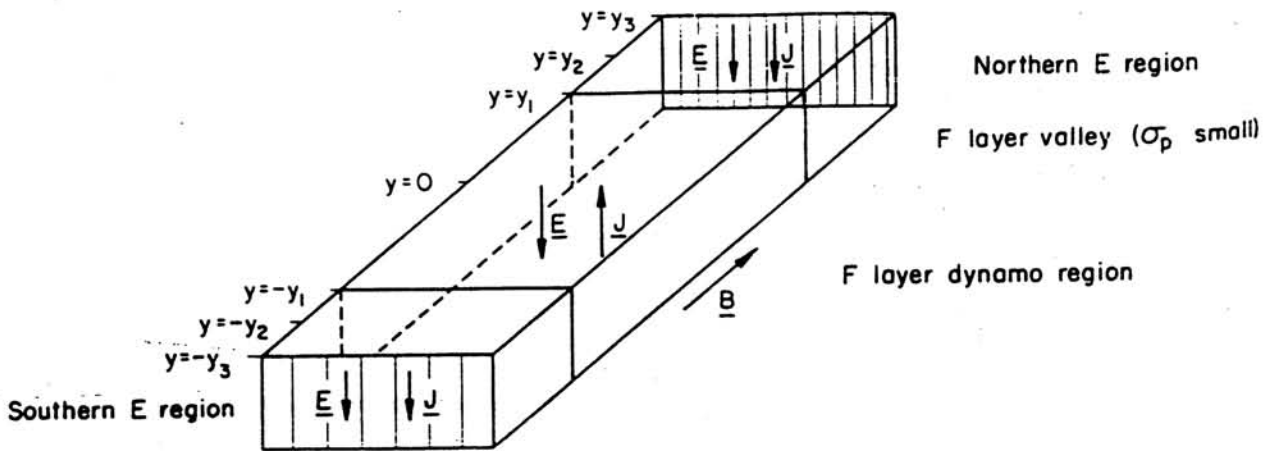


Figure 1.4: The schematic showing the action of F-region dynamo.
(Kelley 1989)

In the relation above, \vec{J} is the current density, I the magnetic dip angle. Only the horizontal components of pressure difference ∇P are effective in the above equation. The vertical component is balanced by the gravity since the neutral air is in hydrostatic equilibrium to a good approximation. The magnitude of the current does not vary markedly with location and time, except near the minima and maxima of pressure [Rishbeth 1981]. If the current is prevented from flowing freely by some boundary conditions (e.g. during nighttime when the E-region conductivity is negligible) the polarisation electric field gets developed [Rishbeth 1971, Heelis et al. 1974]. As has already been described earlier in this section, this electric field in turn would give rise to drifts in the F-region plasma.

In the equatorial ionosphere an electric field of 1mV/m corresponds to an F-region $\vec{E} \times \vec{B}$ plasma drift of about 30-40m/s. At latitudes close to the dip equator the vertical plasma motions result primarily from the zonal electric fields. Measurements on F-region vertical drift have been made from India and Peru [Fejer et al. 1991]. Figure(1.5) depicts the typical vertical and zonal plasma drifts for equinox solar maximum conditions, the observations from Jicamarca are compared with the numerical simulation results. The agreement between the two indicates towards the extent of our current understanding of the low and equatorial electrodynamics. However, globally new studies of low latitude plasma drifts, fields etc. have been carried out using an ion-drift meter (IDM) and vector field measurements on board Dynamics Explorer (DE-2) satellite, Atmospheric Explorer (AE-E) and San Marco satellites. The plasma field measurements along with electric fields and currents often show scatter and fluctuations with quasi periodicities varying from few minutes to few tens of minutes.

Large day to day variabilities, too, are a common occurrence [Balachandran

et al. 1992, *Sastri* 1995, *Fejer* 1997 and references therein]. These fluctuations have been explained by the variability of low latitude tidal winds, irregular winds in dynamo regions, and conjugate hemisphere dynamo effect. Atmospheric gravity waves with 1-10 hr periodicity and planetary waves with periods longer than 2 days are also thought to be important sources of quiet time electric fields and plasma drift variabilities [*Chen* 1992, *Earle and Kelley* 1987, *Forbes and Leveroni* 1992].

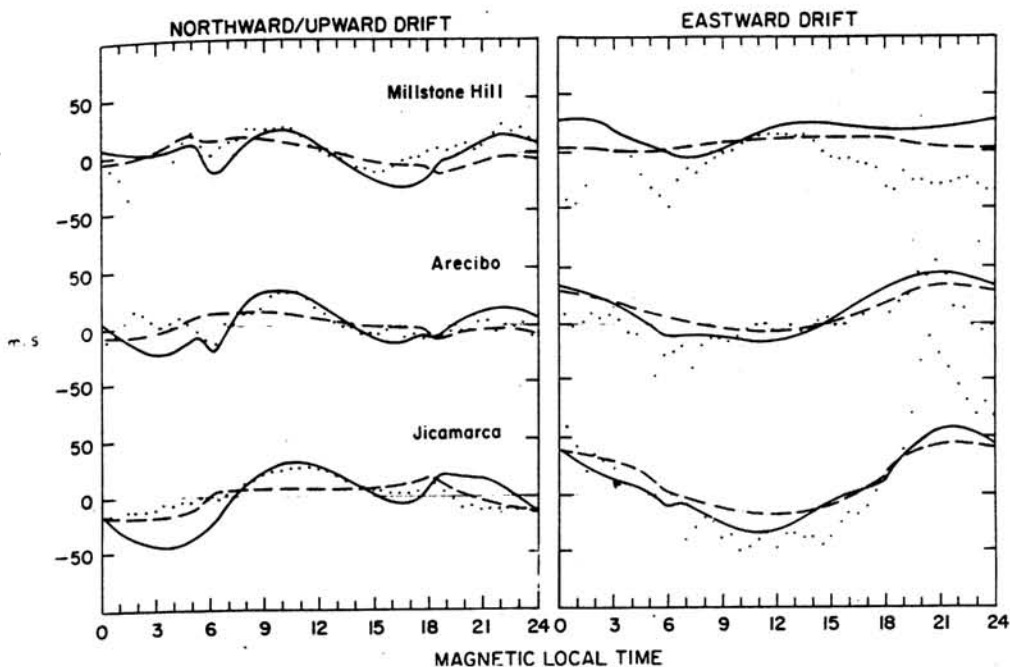


Figure 1.5: Average equinoctial northward/upward and eastward plasma drifts measured at Jicamarca (points) and also Millstone Hill with drifts estimated by two simulations: without tidal forcing (dashed line) and with tidal forcing (solid line). (Fejer 1991)

Fejer [1997] reviewed the characteristics of the low latitude F-region zonal plasma drifts, while discussing their variations over Arecibo with solar cycle, season and magnetic activity. It has been shown that the F-region Pedersen conductivity increases by a factor of about 10 from solar minimum to solar maximum epoch. At the same time, the E-region conductivity was found to be unchanged with solar activity. This leads to larger polarisation electric fields and closer coupling between the neutral wind and plasma drifts during solar maximum for all the seasons. In recent studies it has been suggested that the F-region dynamo effects are important even during daytime [Crain *et al.* 1993]. On certain occasions eastward plasma drift velocities larger than the neutral wind velocities at altitudes 300-400km in

been reported; the cause is yet to be explained [Coley *et al.* 1994]. Modeling of these various electrodynamical effects is a challenging task because of the complex coupled thermosphere-ionosphere system. It becomes still more difficult during the geomagnetically disturbed times because of the additional magnetospheric and ionospheric dynamos being active then [Senior and Blanc 1984, Fejer 1990, 1997]. Mendillo *et al.* [1992] have shown that the effects of storm time electric fields and thermospheric winds over F-region depends on the orientation of the magnetic field which results from the deviation of geomagnetic equator from the geographic equator or in other words the magnetic declination effects.

As it has been described above, the low and equatorial electric fields play an important role in the ionospheric dynamics by imparting drift to the ionospheric plasma, in various geophysical conditions. In this context, the F-region ($\vec{E} \times \vec{B}$) vertical drift imposed on the plasma is very significant over latitudes close to the magnetic equator, whereas at latitudes away from the magnetic equator, the meridional component of the neutral wind contributes significantly to plasma drifts, apart from diffusion. The additional drift induced on the ionisation can push the plasma into region where the diffusion and loss coefficients are different. This would not only cause a change in the plasma distribution but would in turn modify the thermospheric dynamics too which has created the electric fields in the first place. The perturbations in electric fields are important in the context of certain F-region plasma instability process also. The following section summarises the important observations and results on thermospheric wind induced plasma movement in F-region of ionosphere.

1.8 Wind Induced Movement

Thermospheric wind motions apart from redistributing the energy, induce significant changes on the ionosphere. Since the F-region plasma is restrained to move only along the magnetic field lines, the neutral meridional wind imparts momentum to the plasma moving it in the same plane. As a result they can move up/down along the field lines depending upon whether the winds are equatorward or poleward. It is important to note that the zonal wind component induces a drift on the plasma through generation of electric field (dynamo mechanism) while meridional wind imparts direct momentum by setting the plasma into motion. This interaction of thermospheric wind on ionospheric plasma provides a dynamical linkage between the two constituents, i.e. the ionosphere and the thermosphere.

At the same time, the zonal wind component gives rise to electric fields which in turn leads to the generation of many important processes in the ionosphere. Changes in ionospheric parameters in turn affect the thermospheric parameters. Figure(1.6) illustrates both the aspects of thermospheric wind effect over the ionosphere. This figure emphasises the role of meridional wind on the ionosphere by pushing it to regions where the loss coefficient is different, and the importance of zonal winds in creating the electric fields which form a part of the closed circuit between the E and F-region during daytime. Most of the existing information on thermospheric winds are obtained by using optical measurement techniques, in particular from the Doppler line profile analysis of $\text{OI}6300\text{\AA}$ emission from the ionosphere. Horizontal and vertical wind measurements from Natal, Brazil (5.9°S , 32.5°W geographic) made as a part of the

BIME (Brazilian Ionosphere Modification Experiment) are important to mention in this context [*Biondi and Sipler 1985*]. In an even, earlier result wind measurements from Marshall inlands (9.4°N , 35.2°W , geographic) revealed interesting unexplained features like converging horizontal meridional wind flow associated with simultaneous downward vertical velocity and an increase in temperature overhead [*Sipler 1983*]. *Meriwether et al.* [1986] provided valuable information on the seasonal variation of these winds from Arequipa Peru (16.2°S , 71.4°W , geographic).

Studies from India, Mt.Abu (23.4°N , 72.7°E , 20° diplat.) brought forth the day-to-day variations in neutral meridional thermospheric wind [*Gurubaran et al. 1993*]. Both zonal and meridional component of the thermospheric wind, provide information about the dynamical state of thermosphere at any given time. Simultaneous temperature measurements complete the story. For instance, the mid latitude observations of strong surges in meridional wind field associated

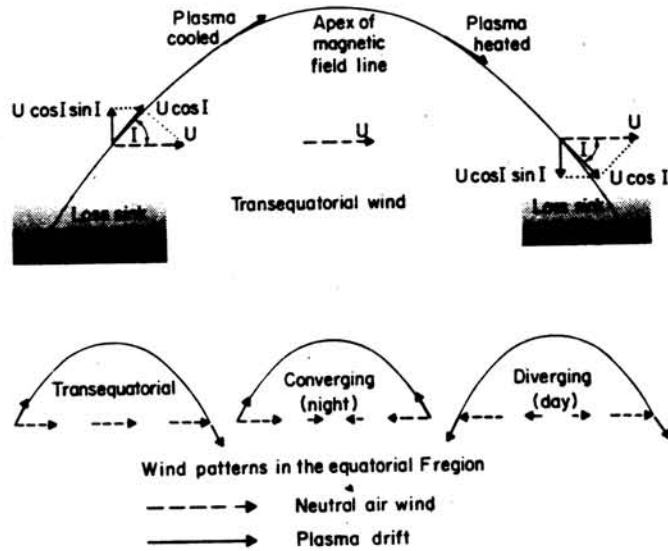


Figure 1.6(a): top: The horizontal wind U produces a vertical drift component $U \cos I \sin I$ as depicted in the top. A transequatorial wind drives the plasma up and over the equator, producing adiabatic cooling and heating. bottom: Three sketches showing patterns of meridional winds in low latitude. (Rishbeth 1977)

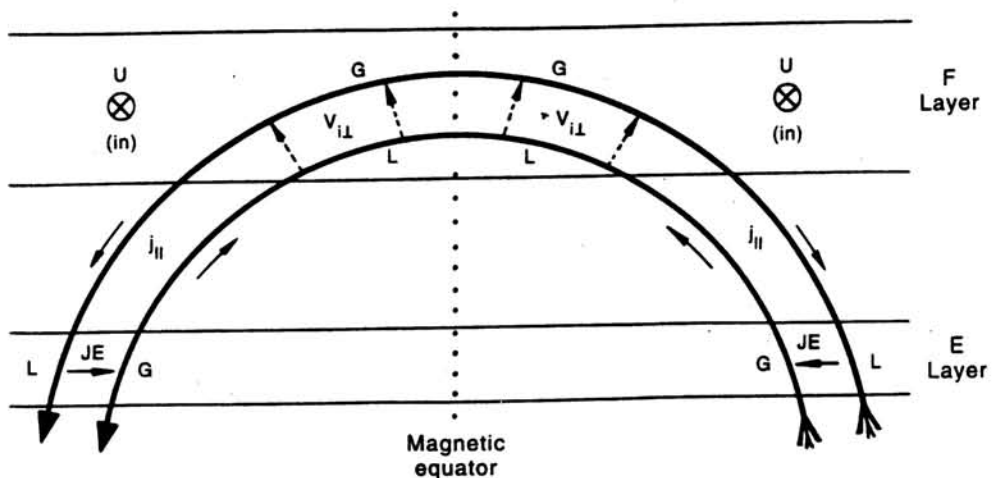


Figure 1.6(b): The current system produced by an eastward wind in the equatorial F-layer, looking eastward. The symbols G and L represent the region where there is a net gain or loss of ionisation. (Rishbeth 1997)

with enhanced thermospheric temperature bring out the importance of strong thermospheric circulation pattern established between high and low latitudes during intense geomagnetic storms. Temporally varying changes in energetics and dynamics are generally found to be associated with fluctuations in thermospheric wind pattern [Roble and Emery 1983, Hernandez and Killen 1988, Hagan 1995, Fuller-Rowell et al. 1997 and references therein]. Therefore, at any time, the thermosphere and the ionosphere are dynamically integrated in such a way that any change in thermospheric parameters representing energetics/dynamics would get registered in the form of changes in ionospheric parameters.

The changes in the TIS system are sought through variations first in thermospheric properties followed by ionospheric changes. But, there exists another important process in which the changes are first observed in ionosphere which are, then, followed by thermospheric changes. This process is the 'ion-drag'. Ion-drag is a very vital coupling force between ionosphere and thermosphere. A brief discussion on ion-drag is provided in the following text.

1.9 Ion-drag

As the name itself indicates, the ion-drag exists in the form of a resistive force experienced by ambient neutral species in motion due to the presence of ions in the vicinity. This arises due to the geomagnetic field confinement of the ambient ionisation. Because of their comparable masses, the collisions between ions and atoms become significant in terms of momentum and energy transfer. The finest example of ion-drag forcing on neutral motion is the formation of 'neutral anomaly' over tropical latitudes, in which the distribution of neutral species also seem to be effected by the presence of magnetic field. During daytime, the eastward electric field causes the plasma to move upwards over

the dip equator only to let it diffuse along the geomagnetic lines to higher latitudes resulting in the phenomenon of EIA. The enhanced ionisation density away from the dip equator causes a drag in the zonal thermospheric flow. This ion-drag on thermospheric species causes a net accumulation of neutral thermospheric constituents at those latitudes, giving rise to the Neutral Anomaly Effect (NA). In another low latitude effect (ETWA), through a significant abatement in the zonal wind flow, the same ion drag effect seems to cause significant loss of momentum to the zonal flow which in turn appears as the localized heating over regions where the reduction in zonal wind flow velocity is maximum. We will come to this in more detail in Chapter 6. Another example of the ion-drag induced changes in thermosphere pertains to high latitudes. Over polar latitudes, the ionic motion is capable of inducing neutral winds and heating through ion-drag. This sort of induced wind dynamo feedback is very important over polar latitudes in deciding the amount of Joule heating and the preferential sunward flow of winds in auroral oval regions [*Hays et al.* 1984, *Rees et al.* 1985, 1986]. Therefore, any change in ionospheric density would also get translated to corresponding changes in thermospheric parameters via ion-drag effect. Thus, ion-drag could be treated as an important feedback mechanism which couples the observed thermospheric effects to the ongoing changes in the ionosphere.

The above description clearly illustrates the fact that, the processes which might arise as purely thermospheric or ionospheric in the beginning, during their subsequent evolution, through a number of intermediate chemical and electro-dynamical interactions, manifest in terms of both the thermospheric and the ionospheric changes indicating thereby of these two regions behaving as a closely coupled system. Since, the interaction mechanism depends on the

chemical, fluid dynamical, and electrodynamical properties of the neutral-plasma medium, the behaviour of the thermosphere - ionosphere system as a whole is looked upon in terms of these properties.

In this context, the low and equatorial latitudes are unique in many ways due to a variety of special geophysical processes occurring therein. These are the consequence of one or more of the above stated mechanisms being operative simultaneously at any given time in this region. Some of the most prominent of these processes are the Equatorial Ionisation Anomaly (EIA), Equatorial Temperature and Wind Anomaly (ETWA), Equatorial Spread-F (ESF) and Midnight Temperature Maximum (MTM). These processes are known to play very important roles in modifying the energetics and dynamics of the low latitude upper atmosphere, but quantitative estimates of their effects are yet to be properly accounted for [Abdu 1997]. The Figure(1.7) displays some of the low latitude processes as a function of time. It would not be out of context to state here that the nonlocal i.e., high latitude and magnetospheric processes can have a significant contribution in perturbing and modifying the low latitude energetics and dynamics at anytime apart from the above stated processes, more so during disturbed geomagnetic conditions.

As mentioned earlier, the EIA, and ETWA associated processes will be discussed in detail in chapter 6. However, a brief account of the other processes like the equatorial spread-F (ESF) and midnight temperature maximum (MTM), mentioned above, which are important in the context of thermosphere ionosphere system behaviour over low latitudes and not dealt with in the later

LOCAL TIME DEPENDENCE OF
THE MAJOR ETIS PHENOMENA

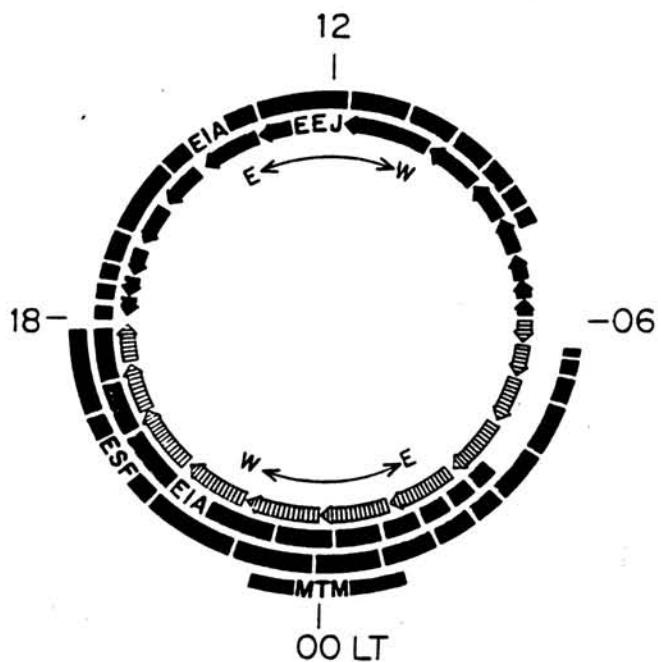


Figure 1.7: The time-dial shows the time of occurrence of various low latitude processes which are also specified along the dial. (Abdu 1997)

1.10 Equatorial Spread-F (ESF)

At times, during nights, a spread is observed in echoed radio signal from F-region heights as seen in ionograms commonly referred to as spread-F [figure(1.8)]. Observations and many theoretical studies have shown it beyond doubt that the occurrence of spread-F can be attributed to the presence of plasma density irregularities of wide ranging scale sizes in the F-region of the ionosphere. The causative mechanisms governing the generation of spread-F over high and equatorial/low latitudes are drastically different. Spread-F in question i.e., equatorial spread-F remains usually confined to the low/equatorial regions in a latitudinal extent of 20° around the dip equator.

It has been shown by experimental and theoretical studies that it is the same electro-dynamical and neutral dynamical coupling that governs the behaviour of the low latitude thermosphere ionosphere system which is also responsible for the observed plasma density irregularities over F-region. The prereversal enhancement of F-region electric field is known to be a prerequisite for the generation of spread-F. The enhanced electric field can push the F-layer to very high altitudes creating steep plasma density gradients in the bottom side F-region. When the plasma density gradient mentioned above is anti-parallel to gravity, a situation analogous to a heavier fluid over a lighter fluid - an unstable condition arises. This particular type of plasma density configuration would give rise to Rayleigh-Taylor (R-T) instability. The role of the parameters like the zonal electrical field, zonal winds and vertical winds in the development of the R-T instability driven by the gravity is demonstrated through nonlinear numerical simulation studies [Zalesak *et al.* 1980, 1982, Ossakow 1981, Sekar and Raghavarao, 1997]. It is precisely this instability which gets generated in the bottom-side F-region and grows nonlinearly encompassing higher altitudes giving rise to irregularities of a wide spectrum of scale

sizes. The fully grown irregularities or instabilities can be of few centimeters to few hundred kilometers in scale size. The signatures of the existence of such irregularities has been confirmed by a number of airglow intensity [*Weber et al.*, 1978, *Mendillo et al.* 1992, *Sinha et al.*, 1996], backscatter radar, and satellite measurements [*Woodman and LaHoz*, 1976; *Rino et al.* 1981, *Patra et al.* 1995] and of course by ground

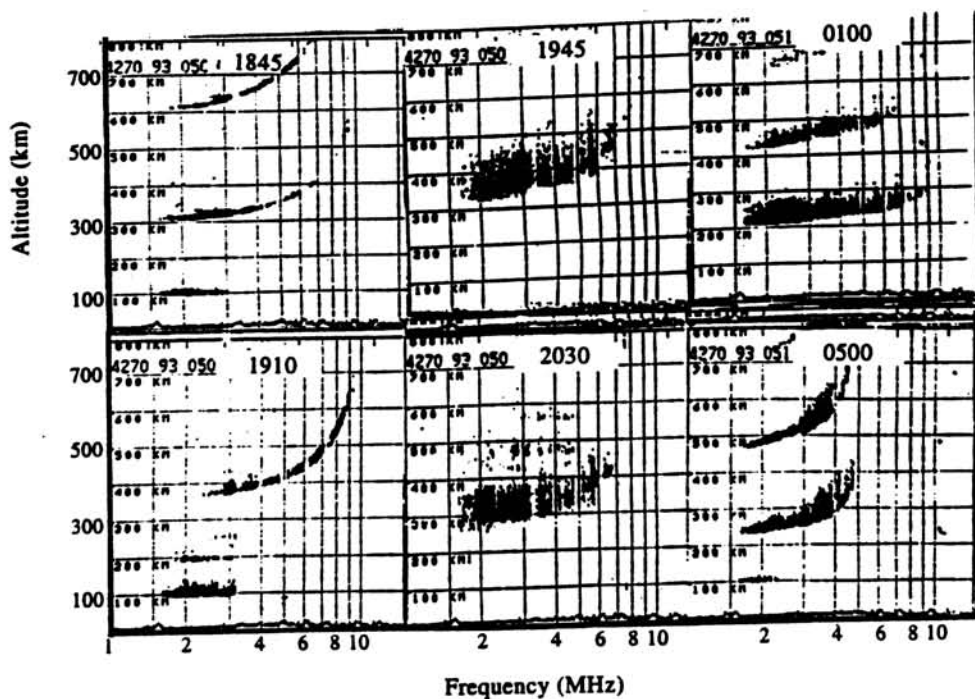


Figure 1.8: The ESF as observed in ionograms.
(Sridharan 1997)

EQUATORIAL SPREAD F MECHANISM

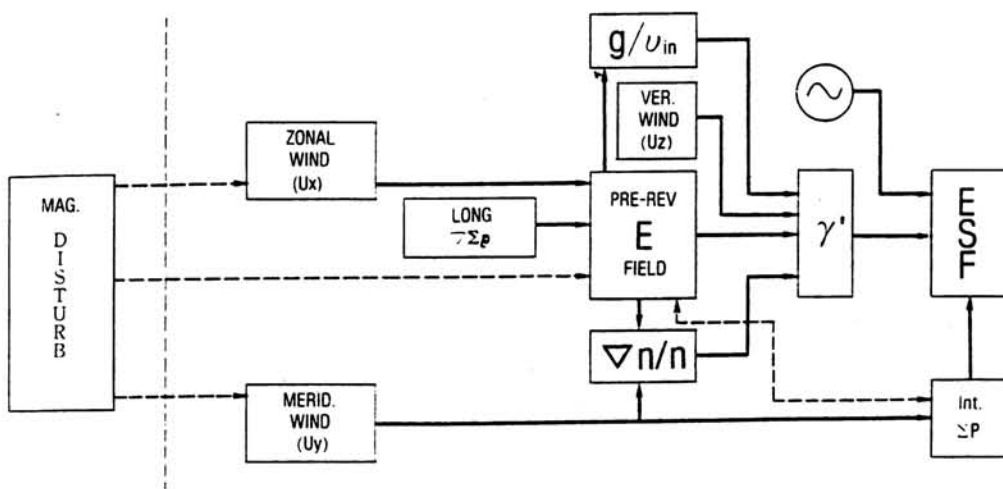


Figure 1.9: The generation mechanism of the ESF.
(Abdu 1997)

based ionosonde and UHF, VHF scintillation too [Kelley, 1989; Chandra and Rastogi, 1972].

However, to know the prevailing ionospheric and thermospheric conditions favourable for the generation of ESF, insitu rocket experiments can be of extreme importance. In the Indian zone, first such campaign was carried out from Sriharikota (SHAR), India, using RH-560 rockets in the year 1981 followed by similar campaigns later [Raghavarao *et al.* 1984, 1987, Sridharan *et al.* 1997]. For the well developed ESF, The Plumex I,II [Narcisi and Szuszczewicz, 1981] and the CONDOR [Kelley *et al.* 1986] experiments are quite successful rocket campaigns which were also very well coordinated with other ground based measurements. The ambient plasma density gradients, ion neutral collision frequencies, the gravitational acceleration and the zonal wind opposing the zonal gradients in addition to eastward electric fields are known to be the parameters which govern the growth rate of above described collisional R-T instabilities in upper atmosphere [Haerendel, 1974 and Ossakow *et al.* 1979].

On the basis of a theoretical simulation study Sekar and Raghavarao [1987] have brought out the importance of vertically downward winds at the onset time of ESF [Sekar *et al.* 1994]. However, the presence of such vertical winds had indeed been shown by other studies as well [Biondi and Sipler, 1985]. The Dynamics Explorer (DE-2) satellite data have also confirmed the presence of such winds and these have been ascribed to circulatory cells that might set up as a consequence of the Equatorial Temperature and Wind Anomaly (ETWA) [Raghavarao *et al.*, 1991, 1993]. Though the morphological features of the equatorial spread-F are broadly understood, the day to day variability of ESF cannot be explained on the basis of our current understanding of the same. It is primarily because of the lack of quantitative estimation on the relative importance of various processes which play the controlling role in the generation of

ESF and its variabilities, eg. the relative importance of plasma density gradients, eastward electric fields, vertical winds etc. in ESF is yet to be understood fully. In this context, *Raghavarao et al.* [1988] showed that the strength of EIA has a good correlation with occurrence of ESF and making use of this fact *Sridharan et al.* [1994] showed from daytime airglow measurements that the nighttime occurrence of ESF can in fact be predicted well in advance (~ 3 hours) of its occurrence. This indicates towards our growing understanding of various individual atmospheric processes and their possible interactions. Figure(1.9) summarises the present understanding of the generation mechanisms of the ESF.

1.11 Midnight Temperature Maximum (MTM)

A combination of insitu measurements and ground based experiments has led to the observation of many new features in low and equatorial thermosphere. Midnight temperature maximum is one such feature which is a consequence of thermospheric dynamics and its interaction with the F-region plasma. The MTM, often observed at F-region heights, is referred to a localized heating (temperature maximum) in the midnight, to levels sometimes greater than the afternoon maximum temperatures.

The first *insitu* observation of MTM was made by NATE neutral wind and temperature experiment onboard AE-E satellite [*Spencer et al.* 1981] figure(1.10). MTM is also accompanied by a minimum in density below 200km and a density maximum over higher heights producing the equatorial midnight pressure bulge. This generation of the secondary maximum of exospheric temperature near midnight hours in the equatorial zone, significantly modifies the thermospheric wind dynamics and the overall low latitude energetics. A very fast collapse of the F-region ionisation at latitudes away from the equator, which

is further confirmed by the enhancements of observed $OI6300\text{\AA}$ airglow, has been observed in connection with the occurrence of MTM over the equator. The descent of the F-layer, leads to increased recombination of O^+ and thereby to enhanced atomic oxygen emission at 6300\AA [Wright, 1971; Nelson and Cogger 1971]. Behnke and Harper [1973] had shown that the equatorward flow of meridional wind actually gets abated before midnight which frequently reverses to poleward after midnight. The consistency of these various observations had highlighted MTM to be a significant energetic process occurring over nighttime low latitude thermosphere. A sort of broad understanding of MTM had evolved in the recent past, in that, the origin of this feature has been attributed to a three dimensional circulation system in which the midnight sector of the equatorial thermosphere below 200 km is heated by compressive flow driven by solar heating on the dayside [Spencer et al. 1979]. Theoretical explanations of the MTM have been proposed by Mayr et al. [1979], and Herrero et al. [1983]. In fact, in a study based on the spectral analysis of MTM, Mayr et al [1979] proposed a complex interaction between the semidiurnal tide from lower atmosphere and the ion neutral momentum coupling associated with the diurnal variation of the ion-density in upper atmosphere to be the cause for midnight temperature maximum figure(1.11). Though, this mechanism seems to explain the MTM reasonably well, all the variations (morphological) involved with MTM are yet to be understood.

Observations based on AE-E and DE-2 satellite data and from a number of ground based measurements from widely separated sites indicate that MTM, alongwith its day to day, seasonal variations has a significant longitudinal character too. Its magnitude has been higher in the Indian sector as compared to the American sector [Rao and Sastri, 1994; Herrero and Meriwether, 1994; Goembel and Herrero, 1995; Colerico et al., 1996]. As a consequence, the

effect of MTM on meridional winds at low and equatorial latitudes seems to depend on the longitude, for instance it is best seen in the December solstice in east Brazil and during equinoxes in the Indian sector [*Batista et al.* 1997]. To investigate possible sources of the MTM, a series of theoretical simulations have been tried by different modeling groups.

The initial efforts to generate the MTM, the National Center for Atmospheric Research (NCAR) thermospheric general circulation model were unsuccessful though the model incorporated ion-neutral momentum coupling and realistic solar forcing. The first successful result, in this context, was obtained only when the effects of waves excited in the lower atmosphere were also included in the general model [*Fesen et al.* 1986]. Recently, a more advanced study was done by the same (NCAR) group involving Atmospheric Research thermosphere/ionosphere/electrodynamics general circulation model (TIEGCM). This study revealed that the MTM is a tidal phenomenon and thus is ultimately due to the thermospheric tidal sources: in situ thermal excitation; ion-neutral momentum coupling; and the tidal waves arising

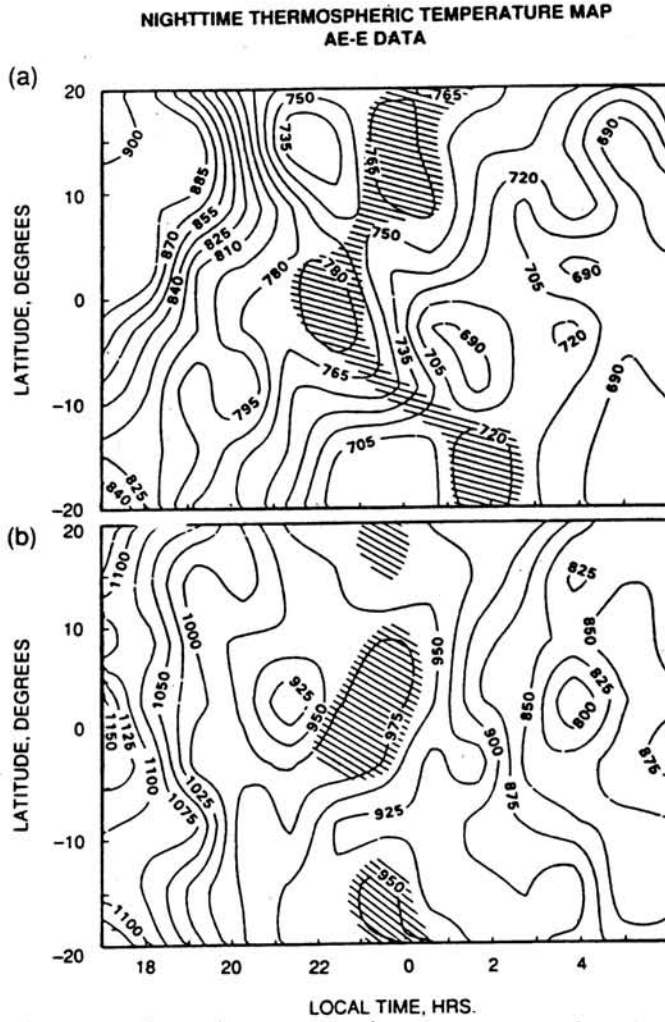


Figure 1.10: The MTM as observed by the satellite (NATE). (Herrero et al. 1993)

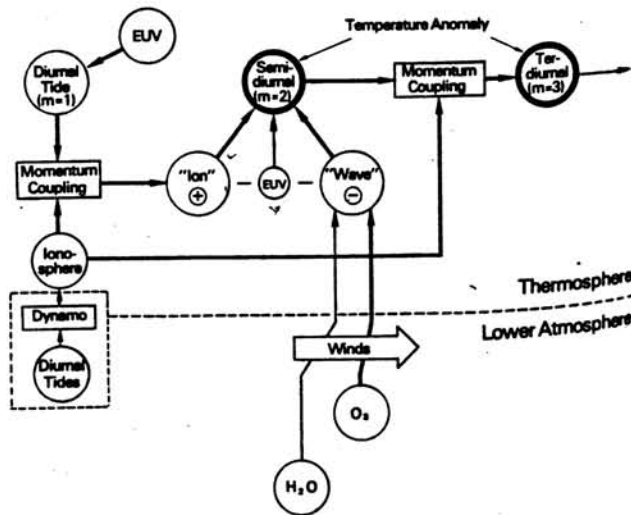


Figure 1.11: The generation mechanism as proposed by Mayr et al. 1979.

in the lower atmosphere which penetrate the thermosphere [Fesen 1996]. For instance, the observed seasonal variation of MTM may be due to the interaction of the 2,2 and 2,3 modes of tides: in summer, the two modes reinforce each other and in winter they offset. In the TIEGCM, the MTM is due to the upward propagating semidiurnal tides. The model suggested that the observed variability in the MTM may be due to the variability in the upward propagating tides. Though, the broad morphological features of these processes are well understood, a complete quantitative information on their energetics and dynamics is yet to be achieved.

In order to be able to study all the energetics and dynamical changes that occur in the upper atmosphere, we must study the variabilities associated with the thermospheric and ionospheric parameters like the thermospheric temperatures and winds. The changes in thermospheric temperatures and winds reflect the changes in the energy and motion of the thermospheric constituents. It is important to have an extended data base to be able to evaluate possible trends and to establish an average reference, against which the variabilities of these parameters can be studied. In this context, the thermospheric model predictions can serve as the standard reference. A brief account of the various thermospheric models widely being used now-a-days is given in the following.

1.12 Thermospheric Models

There are many models in existence today which have been used in different applications depending on the scope of the model. These models range from simple empirical specifications of one or two thermospheric parameters, to highly complex three dimensional (3-D) numerical models. New mathematical techniques have been used in devising these numerical and analytical models.

Each of these models have been designed with the object of elucidating some aspects of the thermospheric physics. The multi constituent spectral models of *Mayr and Volland* [1976], *Mayr et al.* [1978] can be included in this class. *Mayr et al.* devised this model to investigate the time dependent mean and diurnal components of thermospheric circulation and composition over high latitudes. But, in recent years the thermospheric general circulation models (TGCM) and the thermosphere ionosphere electrodynamic general circulation model (TIEGCM) [*Fuller-Rowell et al.* 1987; *Roble et al.* 1988; *Richmond et al.* 1992] have become the state-of-the-art.

These TGCM models have been developed to study the global circulation, temperature and compositional structure. These models have met with exciting results in the recent years. These TGCM use many other empirical models like for instance the empirical ionospheric model [*Chiu et al.* 1975] for its functioning. The National Center For Atmospheric Research TGCM places more emphasis on the accurate aeronomic scheme of the thermosphere, while University College London TGCM concentrates more on the thermosphere ionosphere coupling. These models now are capable of predicting the important time dependent dynamical state of the thermosphere ionosphere system e.g tidal effects on airglow intensity [*Parish* 1990] and electrodynamical effects initiated by thermospheric winds [*Richmond and Roble* 1987]. *Fuller-Rowell et al.* [1990] have added new modified horizontal transport terms for molecular gases and terms for the magnetic activity effects in TGCM. It could be stated that starting from the early work of *Jacchia* [1965] on the development of empirical modeling based on satellite - drag data, the present day coupled thermosphere ionosphere model (CTIM), global circulation models (GCMs) are a giant leap forward in the direction of modeling the thermosphere and ionosphere.

However, a model like NCAR and UCL TGCM require mammoth computational facility and are difficult to use. But the semi-empirical model MSIS [Hedin 1983, 1987, 1991] has proved to be one of the most user friendly models. It is worth mentioning that inspite of its simplicity, the temperature responses predicted by the TGCM and MSIS models were comparable [Roble *et al.* 1987]. The TGCM, of course, could predict more temporal structures than MSIS. In fact, MSIS is very effective in representing the climatological features of the thermosphere. As a reference, MSIS has been used in the present study wherever the base level, average picture is called for. MSIS model can generate thermospheric parameters for particular times and places, without having to generate it for the other times and places. Making use of the wide data base obtained from a number of satellite mass spectrometers and incoherent scatter radar measurements, the MSIS model has been improved to represent the seasonal variations in composition and temperature and also the magnetic storm variations. It has also been adopted as the COSPAR international reference atmosphere whose prediction is based on the four fundamental input parameters namely solar decimetric flux index (F10.7), the geomagnetic activity index (A_p), the local time and the geographic coordinates.

In the present investigation, the temperature measurements are compared with the MSIS model predictions. Observations from low latitude regions consistently point towards the inability of MSIS model in predicting the low latitude temperatures realistically. The reason for this deficiency is because most of the data base used for the development of MSIS model is obtained from mid or high latitudes and the data base from low and equatorial latitudes are sparse. Therefore, it becomes all the more important to attempt to improve the existing MSIS model in order to make it represent the low latitude region better. Because of the extremely dynamical nature of the processes prevalent in low

latitude thermosphere - ionosphere system, it becomes difficult to parameterize the various processes, in order to include them into the model. We have set out a detailed study to parameterize some of these low latitude processes like ETWA in addition to the energy input from the earth's ring current, and to include them into the model. We have dealt with this aspect of study in quiet detail in Chapter 6.

Chapter 2

Instrumentation

2.1 Upper Atmosphere Airglow

As has been discussed in Chapter 1, the Earth's upper atmosphere is an active laboratory in the geospace environment where the dynamical interaction of plasma and neutral species convert the solar radiation energy, primarily, into kinetic energy of the constituents and also channel some part of this energy to produce excited atoms and molecules. These excited atoms and molecules while deexciting emit radiations, which are collectively termed as 'Airglow'. The wavelength of these airglow emissions is governed by the excitation energies of these atoms and molecules. Airglow variations represent the altitude region from where the emission emanates. In this regard, remote sensing of the upper atmosphere using ground based optical techniques has always been considered an important aspect of atmospheric research.

The airglow is distributed over all the latitudes and is present almost all the times. In general, no particular structure can be associated with the airglow. Comprehensive account of the earlier work on airglow has been provided by *Chamberlain* [1961] and the relation between the airglow with the earth's ionosphere has been reviewed by *Thomas and Norton* [1966]. In the last forty years or so, the development in the airglow research had led us to an increasingly accurate knowledge of the airglow spectrum in various wavelength regions;

with the advent of satellite based monitoring of airglow emissions, global coverage of these features became possible [Craven *et al.* 1982, Grechko *et al.* 1982, Hays *et al.* 1982, Torr and Torr 1984, Shepherd *et al.*, 1997]. Traditionally, ground based observers have used the forbidden and the allowed atomic and molecular emissions to characterise the airglow at any particular place. However the lack of appropriate laboratory data on atomic cross-sections, reaction rates and branching ratios leads to uncertainties in explaining some of the airglow observations. With altitude, the decreasing frequency of collisions between the atoms, molecules and the plasma, makes it possible for radiation from metastable species to be observed. These metastable species usually have radiative life time much longer than 10^{-8} sec of the allowed transitions normally observed in the laboratory. These transitions are also referred to as '*forbidden*' because the spectroscopic selection rules for electric dipole radiation is violated.

Some of the important upper atmospheric airglow emissions are the emission lines and bands from atomic oxygen O , N_2 and N_2^+ , which had been the focus of many studies because of their role in thermospheric energy budget. However, other atomic and molecular species emitting airglow are O^+ , N , O_2 , O_2^+ and H . Since the present study deals with the $OI6300\text{\AA}$ airglow, a brief account of some of these important airglow emissions in the visible range is provided here.

2.2 Emission Lines of Atomic Oxygen

The $O(^1D)$ state of atomic oxygen has been studied more than any other metastable species. The existence of this state in the atmosphere was first identified by Sommer [1933] and Slipher [1933] from the 6300\AA nightglow emission. Later, it was shown by Noxon and Goody [1962] that 6300\AA is the strongest emission

feature in the dayglow. This emission results from the $O(^3P - ^1D)$ transition of oxygen atom. The corresponding energy level configuration is shown in figure(2.1). The main source of $O(^1D)$ state in the night sky is through the dissociative recombination reaction of O_2^+ ion. While during daytime, the photodissociation, photoelectron impact and dissociative recombination, contribute to the overall density of $O(^1D)$ in a metastable state. The 6300\AA is quite notable because of the long lifetime (110 sec) of the metastable state. Quenching, mostly by N_2 , deactivates most of the $O(^1D)$ at lower altitudes because of large N_2 abundance, while the low N_2 concentrations at

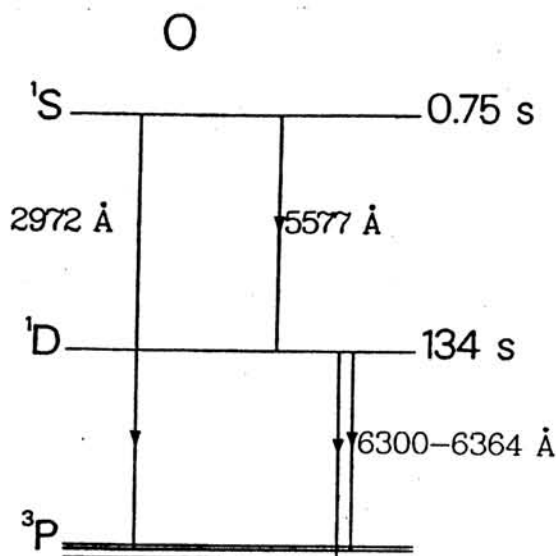


Figure 2.1: The energy level diagram corresponding to Oxygen.

altitude ~ 200 km and above makes the $O(^1D)$ 6300Å transition possible at these heights. Figure(2.2) depicts the volume emission rate of 6300Å dayglow measured by AE-C satellite [Hays et al. 1978].

Further, as shown in the figure(2.1), the 5577Å line, the most prominent lower thermospheric emission, results from the transition $O(^1D - ^1S)$. Rocket photometry estimated the altitude of this emission to be lying between 80 to 115 km [Koomen et al. 1957]. Wallace and McElroy [1966], by means of rocket measurements established that during daytime the 5577Å emission emanates from two distinct layers with an F-region component and a lower peak near 95 km. UARS satellite measurements have confirmed these results. A typical daytime altitude profile of this emission is depicted in figure(2.3). While the excitation to 1S state in the upper thermosphere is similar to that of 1D state in the lower thermosphere it is due to a three body chemical reaction [Barth 1964]. These excited species are generally collisionally quenched by O_2 and N_2 [Torr and Torr, 1982].

It was Chapman [1931] who realised that the association energy of O_2 (5.03 eV) would be adequate to provide the excitation energy of the $O(^1S)$ state (4.02 eV). At the same time, the estimation of $O(^1S)$ from the dissociative recombination of O_2^+ with ambient electrons still continues to be difficult. Apart from 5577Å, 6300Å in

would be adequate to provide the excitation energy of the $O(^1S)$ state (4.02 eV). At the same time, the estimation of $O(^1S)$ from the dissociative recombination of O_2^+ with ambient electrons still continues to be difficult. Apart from 5577\AA , 6300\AA in

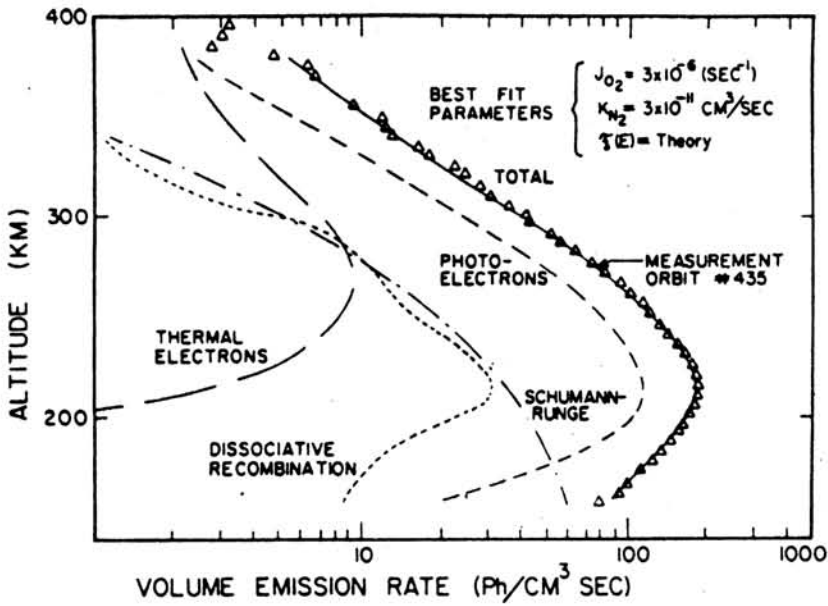


Figure 2.2: Volume emission rate of OI(6300Å) measured by AE-C satellite, compared with different source functions quenched by N₂ (Hays et al., 1978).

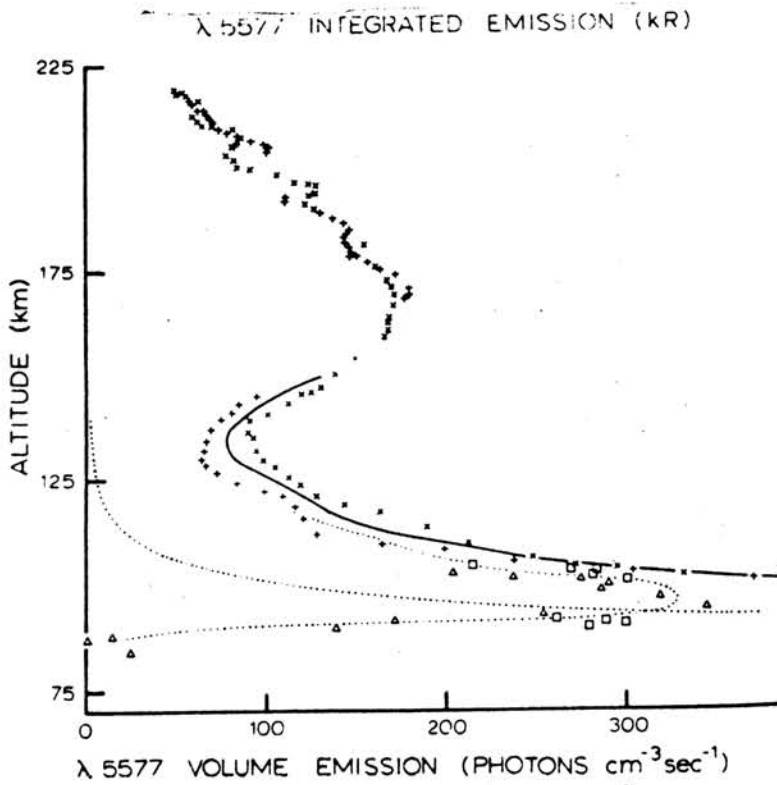


Figure 2.3: The 5577 Å volume emission rate profile obtained by Wallace and McElroy (1966). Squares and triangles represent the low-altitude emission corrected for Rayleigh scattering.

visible airglow spectrum, there are certain other emissions, extremely relevant for the studies of atmospheric thermodynamics and chemistry. Airglow OH emissions in near infra-red region fall in this category. The night glow spectroscopic observations reveal OH emissions to be a band emission emanating from its vibrational levels 1-9. This band emission is found to be extremely useful in estimating the mesopause temperatures. A detailed description on this emission is provided by *Sivjee* [1992]. The description on the airglow emission features is kept minimal here. Nevertheless it is evident that the optical measurements of various emissions from different altitudes are important to study the chemistry and the thermodynamics of the mesosphere, lower thermosphere and upper regions.

All the optical techniques are based upon two fundamental modes of observations. One which deals with total incoming photon flux at a particular wavelength, i.e. *Photometry*, and the other is the *Spectrometry* where variations of flux are observed with varying wavelength. The absolute emission rate combined with excitation cross sections can yield the column density of a species or the intensity of the source that produces the excited state. Vibrational and rotational distributions in molecular bands yield the respective temperatures or provide insight to possible excitation mechanisms. Further, the interconnection between structure, composition, energetics and dynamics in atmosphere would also manifest itself in relationships between various emission features or other spectroscopic details [*Sridharan* 1992]. Conventionally the airglow measurements are restricted only to the moonless periods of the nighttime with clear, cloud free sky conditions.

With the advent of highly improved and ingenious photometric techniques such as Dayglow photometer (DGP) and Multiwavelength daytime photometer (MWDPM) [*Narayanan et al.* 1989, *Sridharan et al.* 1993, 1998], the ground

based photometry is no longer limited to night time conditions only. This has been established on the basis of the important scientific results like the tracking of the equatorial ionization anomaly in its evolutionary phase [*Pallam Raju et al.* 1996] and obtaining a precursor for equatorial spread-F in OI 6300Å dayglow [*Sridharan et al.*, 1994]. These results have opened up a new area for the study of various dynamical processes in the different parts of upper atmosphere during daytime. However, the ground based high resolution spectroscopy has always been a favourite among the atmospheric researchers, as it is capable of determining the kinetic properties i.e. neutral temperatures and line of sight winds. The history of the spectroscopic measurements of dynamical and thermodynamical properties of the upper atmosphere can be dated back to 1923 when *Babcock* [1923] attempted to estimate the Doppler width of the naturally occurring OI($^1D - ^1S$) radiation from the night sky with a Fabry-Perot spectrometer. Though, Babcock was able to infer only an upper limit to the temperatures at the height of the emission (now known to be at ~ 96 km), owing to the limitations in technology available to him, still it was an important development at that time. Since then, ground based spectroscopy has entered into a new era with the development of spectroscopic instruments of high spectral resolving power and large throughput.

All the conventional optical instruments require sufficiently high levels of light intensity for their operation. Among the various optical techniques, the Fabry-Perot spectrometry came to be considered - the instrument of choice for low light level ground based sensing of the upper atmosphere. *Jacquinet* [1954] established that, out of all the spectroscopic devices where interference of light yield the spectrum, the Fabry-Perot interferometer has the highest luminosity for a given spectral resolution along with the Michaelson interferometer. A comprehensive treatise on Fabry Perot devices has been given by *Chabbal*

[1953]. *Hernandez* [1986] further established the usefulness of Fabry-Perot spectrometer by analysing the technical details of the same.

The use of the Fabry-Perot spectrometers to determine temperature and winds prevailing in upper atmosphere is now well established, in part, due to the elegant physical principle upon which this experimental technique is based. A brief discussion on the measurement technique would be presented in the sections to follow.

The natural emissions of the upper atmosphere are normally associated with forbidden electronic transitions of neutrals and ionised species [*Chamberlain*, 1961]. Because of the associated long lifetime with the metastable transition states, the excited species tend to attain thermal equilibrium (statistical equilibrium) due to multiple collisions with the surrounding medium before radiation. The distribution of these species is nearly Gaussian or Maxwellian. The line profile/Doppler profile of the emitted radiation reflects not only the kinetic temperature of the region from where the emission occurs, in terms of profile width i.e.. Doppler width, but also the bulk motion or the wind in that region in terms of Doppler shift [*Hernandez and Killeen*, 1988]. As, the magnitude of the Doppler effects associated with typical wind and temperature magnitudes existing in the upper atmosphere are quite small, a spectroscopic device such as a Fabry-Perot spectrometer, of very high spectral resolution is necessary for their determination. The Doppler measurements are normally made at night to reduce the contamination from the intense scattered background radiation due to Rayleigh-scattered light from the atmosphere illuminated by the Sun. Due to the faintness of airglow, daytime spectroscopic measurements are extremely difficult. The difficulties get enhanced due to the strong Fraunhofer absorption and the telluric absorption features strewn in

the background continuum. Therefore, the photometric and spectrophotometric measurements are usually restricted only to moonless periods of the night with clear sky conditions.

At the same time, with the advancement of technology space borne measurements of upper atmospheric emissions overcome the above difficulty and retrieval of the dynamical parameters during daytime has become a reality. Visible Airglow Experiment (VAE) onboard Atmospheric Explorer-C investigated, while in orbit, the detailed chemistry of $O(^1D)$ atoms in thermosphere [Hays *et al.* 1978]. VAE carried out measurements in various emissions, and also on the variations of height of peak emission with season and magnetic activity. WINDII (Wind Imaging Interferometer) and HRDI (High Resolution Doppler Imaging Interferometry) instruments onboard UARS (Upper Atmospheric Research Satellite) provided information on thermospheric winds and their spatial and temporal variation [Burrage *et al.* 1994, Shepherd *et al.* 1997]. Dynamics Explorer (DE) satellite programme - the most comprehensive programme so far, for the investigation of the thermosphere and exosphere, furnished data on more than 18 thermospheric - ionospheric parameters using different instruments onboard [Hoffman and Schmerling 1981]. All these satellite based measurements have a severe limitation in terms of temporal coverage at any given location over the globe, but they do provide an excellent spatial coverage. Therefore ground based measurements from a given location complement this lack of time sequential data as observed from space-borne instruments.

2.3 Present Study

The desired upper atmospheric parameters for the present study are the nighttime neutral temperatures and winds at F-region altitudes. $OI6300\text{\AA}$ red line

emission originating from an average altitude of 250 km during nighttime is considered appropriate for these measurements. The average OI6300Å intensity levels lie at around 50-100 Rayleigh during nighttime and can even vary by an order of magnitude depending upon the background electron densities in the F-region. A central aperture scanning high resolution Fabry-Perot spectrometer, as described in the following section, is used for line profile measurements of OI 6300Å emission.

The high resolution Fabry-Perot spectrometer is deployed for airglow observations at the Optical Aeronomy Laboratory, Gurushikar, Mt. Abu (24.6° N, 72.7° E geographic; 20° N dip lat.), situated at an altitude of 1697m above sea level. This low latitude laboratory is ideally located, because of very good sky conditions and for the investigation of the dynamics of low latitude and equatorial processes, namely equatorial ionisation anomaly (EIA) and the equatorial temperature and wind anomaly (ETWA) in particular. The equatorial ionisation anomaly can extend as far as 30° latitude on occasions, during solar maximum conditions and the formation of ionisation crests usually occur in the latitude range of 15° – 25°. Mt. Abu falls right under the crest region and therefore, is one of the most suitable locations to investigate the behaviour of the low latitude thermosphere during the passage of crest of the ionization anomaly overhead. The phases of the anomaly moving across zenith, would manifest itself in the variations of observed nightglow intensities. In the following sections, a brief account of the basic optical layout of the Fabry-Perot spectrometer selected for the present study alongwith discussion on the physics involved, is presented. The choice of suitable instrumental parameters, the data analysis technique adopted to recover Doppler parameters from observed interference fringes and the errors involved, are also described.

2.4 Theory of Fabry-Perot Spectrometer

A Fabry-Perot etalon consists of two perfectly parallel, flat, high quality fused silica plates with a thin film coating of $> 85\%$ reflectivity in the wavelength range of interest and separated by a fixed distance (t) between them. A monochromatic light incident upon an etalon at an arbitrary angle (θ) to the normal of the plate undergoes multiple reflections inside the etalon plates. The subsequently transmitted beams, having path differences now, interfere to form an interference pattern when viewed at an extended source. Identical interference conditions exist for incident rays of constant inclination θ . Because of the circular symmetry of the device, the intensity distribution of, interfering beams for both the reflected and transmitted light, is a pattern of bright concentric rings or fringes. These fringes are on a dark background in case of transmitted beams, and an absolutely complementary set of fringes occur for the reflection case. The angular separation or diameter of these fringes is dependent on the spacing between the etalon plates and the wave number of incident radiation. The basic function of this device is to transform wavelength into angular displacement, through interference. In doing so, it introduces broadening to the observed line-profiles, which is purely an instrumental effect. [Hernandez, 1986].

For an etalon consisting of mirrors of reflectivity ' R ' and absorption ' A ' per reflection, the transmitted intensity (I_t) is calculated by summing the amplitudes of each individual light beam, and then squaring the result. Mathematically representing, this expression is called the Airy's function and is given by:

$$I_t = \left(1 - \frac{A}{1 - R}\right)^2 * \left(\frac{1}{1 + R^2 - 2R \cos \delta}\right) \quad (2.1)$$

where

$$\delta = \frac{4\pi \mu t \cos \theta}{\lambda} \quad (2.2)$$

In the expression above, ' μ ' is the refractive index of the medium inside the etalon plates, and ' λ ' the wavelength of the light undergoing interference, and ' δ ' the phase of the transmitted beam. However, the condition for the constructive interference of the transmitted light is given by the following relation:

$$2\mu t \cos\theta = n\lambda \quad (2.3)$$

where n is the order of the interference. It is evident from this condition that for a given wavelength (λ), the interference fringe can be scanned by varying either of the following three parameters. These parameters are ' μ ' the refractive index of the etalon medium, ' t ' the separation of etalon plates and ' θ ' the angle of incidence from normal to the etalon plates.

In an actual experimental setup, if both μ and t are kept constant for a given angle of incidence θ , the necessary change in wavelength to scan the interference pattern by one order is called the Free Spectral Range (FSR) and is given by:

$$\Delta\lambda = \frac{\lambda^2}{2\mu t} \quad (2.4)$$

Conceptually the FSR i.e., $\Delta\lambda$ is the range of wavelength around λ i.e. ($\lambda \pm \Delta\lambda$) which can be displayed without overlapping orders, and is one of the crucial parameters in choosing appropriate Fabry-Perot etalon for the desired application. Another parameter of importance is the 'Reflective finesse' F_R which is a measure of instrument selectivity and represents the extent of the broadening of a monochromatic beam on its passage through Fabry-Perot (FP) etalon. F_R is highly dependent on FP etalon plates and is related to the reflectivity of the plates according to the following expression.

$$F_R = \frac{\pi\sqrt{R}}{1-R} \quad (2.5)$$

Finesse is a dimensionless number, and is defined as the ratio of free spectral range (FSR) to the width of the transmission band at full width at half maximum (FWHM) i.e. $\delta\lambda$.

$$F_R = \frac{\Delta\lambda}{\delta\lambda} \quad (2.6)$$

The overall finesse of an actual Fabry-Perot interferometer can never exceed its Reflective finesse F_R . For very high reflectivity, this limitation comes primarily from the FP plates with finite flatness, surface roughness, finite degree of parallelism and imperfect collimation of the incident light. These factors always tend to contribute towards broadening the output profile, as, the Fabry-Perot plates are never perfectly flat and parallel. This causes a finite loss in the net peak transmission. It is possible to define these limiting finesses as constants of a given FP etalon. The surfaces of the imperfect etalon plates are microscopically inhomogeneous in a random fashion with a root mean square variation which, though, very small in comparison to the size and spacing of the etalon, is still quite significant in relation to the wavelength (λ). Curvature and parallelism defects which usually are associated with polishing defects of the substrate or misalignment, also limit the finesse of the resultant profile. Since these defects are comparable to the wavelength, they can be used to quantify the defect finesse in terms of fractions of wavelength [Atherton *et al.*, 1981] in the following manner:

(i) **Roughness Defect:** The limiting finesse due to the roughness defect, N_{DR} is a constant of the etalon, and is related to the distribution of the defects in the etalon plates in a manner described by the following equation.

$$N_{DR} = \frac{m}{4.7} \quad (2.7)$$

where ' m ' is a mathematical constant having the following relationship with wavelength and the irregularities/defects of the FP etalon.

$$\frac{\lambda}{m} = \sqrt{\text{mean square deviation of irregularities}} \quad (2.8)$$

(ii) **Spherical defect:** Apart from the roughness defects, an etalon has errors of curvature, usually associated with polishing defects of the substrate while coating its plates. The limiting spherical defect N_{DS} , because of this, is given by the following equation:

$$N_{DS} = \left(\frac{m}{2}\right) \quad (2.9)$$

where

$$\frac{\lambda}{m} = \sqrt{\text{mean square variation of defects}} \quad (2.10)$$

(iii) **Parallelism defect:** The nonuniform substrate polishing can give rise to misalignment in parallelism of the etalon plates, which, further, limits the finesse of the etalon. The limiting finesse N_{DP} is given as:

$$N_{DP} = \frac{m}{\sqrt{3}} \quad (2.11)$$

The overall instrument finesse, which is related to the reciprocal of the individual defect finesses, is estimated as per the following relation:

$$\left(\frac{1}{N^2}\right) = \left(\frac{1}{N_R^2}\right) + \left(\frac{1}{N_D^2}\right) \quad (2.12)$$

In the above relation N_D is the overall defect finesse, N_R the reflective finesse and N is the overall finesse of the etalon. The overall defect finesse (N_D), however, is estimated in terms of each defect limited finesse, as per the following relation:

$$\left(\frac{1}{N_D^2}\right) = \left(\frac{1}{N_{DS}^2}\right) + \left(\frac{1}{N_{DR}^2}\right) + \left(\frac{1}{N_{DP}^2}\right) \quad (2.13)$$

As shown in the equation above, the instrument finesse approaches a lower limit determined by the overall defect finesse ' N_D ' as the reflectivity of the etalon plates is increased. The finesse of real spectrometers is further limited by an external component which indirectly depends upon the selected Fabry-Perot constants. This important component is the '*Aperture function*'. An aperture is an area where the light flux after passing through the etalon and the

camera lens is collected through a cone of a finite solid angle. Since the light is integrated over the finite angular spread of the aperture, further broadening of the resultant profile is effected by this process. This aperture limited finesse N_{AP} is given by the following relation:

$$N_{AP} = (FSR) \left[\frac{8 \times f_L^2}{\lambda d^2} \right] \quad (2.14)$$

In the above expression, f_L is the focal length of the camera lens used to focus the light beam on the aperture and d is the diameter of the aperture. The wavelength of the light is represented by λ . Therefore, in the case of a Fabry-Perot, all the broadening factors and corresponding finesse define its response to any incoming emission. Hence, the determination of a line profile requires to have *a priori* information about two factors: (i) a knowledge of the source under consideration and (ii) a knowledge of the integrated instrument response.

2.5 Parameter Selection and Technical Details

The nightglow emission rates vary significantly from solar minimum to solar maximum epoch. The present study deals with extended observations on nightglow during solar minimum. The airglow intensity in the night sky exhibits lot of variability which is produced by variations in the chemistry, abundances of atoms, molecules or ions and their kinetic temperatures. To carry out high resolution spectroscopy on line emissions having low volume emission rates (≤ 100 R), careful selection of the instrument parameters is called for. The following sections deal with this aspect.

2.5.1 Fabry-Perot Etalon

As it is evident from the term, in 'high resolution spectroscopy' a spectral device with high resolving power is required which is necessitated by the width of the emission line to be resolved and the wavelength of emission. A Fabry-Perot with a gap of 1 cm between the etalon plates and plate reflectivity of 85%

and a resolving power of 6×10^5 is considered adequate for the present study. An air gap etalon with optically contacted plates of 100 mm usable aperture has been selected for the present study. The etalon plate parallelism and flatness have been chosen to be $\frac{\lambda}{20}$ and $\frac{\lambda}{100}$ for the wavelength (6300\AA) region of our interest. The spectral scanning of the interference pattern formed by the Fabry-Perot etalon, illuminated by the monochromatic light, is done by altering the refractive index of air between the etalon plates, by changing the pressure of the air between them, for normal incidence.

2.5.2 Static Aperture Size, Field of View and Resulting Luminosity

In the actual spectrometer of the kind used in the present study, changing the refractive index of the medium between Fabry-Perot plates move the projected interference fringes relative to a static aperture and thus facilitate the scanning of the central fringe [Hernandez and Roble, 1979]. The choice of the size of this static aperture is not arbitrary and is very important in deciding the required field of view of the instrument. The size of the aperture limits the amount of useful flux a Fabry-Perot device can collect. The relation between the size of the static aperture ' f ', the order of the central fringe (n_o) and the angle of acceptance $2(\theta)$ is the following:

$$\cos\theta = 1 - \frac{f}{n_o} \quad (2.15)$$

(' f ' is also expressed in terms of order of the interference pattern) This aperture will receive radiation which passes through the etalon between angles 0 and θ i.e. a cone of angle 2θ subtended at the aperture. In other words, the field of view of instrument is ' 2θ '. For a simple circular aperture having inner and outer angular radii of $\theta_1 (= 0)$ and θ_2 respectively. We have:

$$\cos\theta_1 = 1 \quad (2.16)$$

$$\cos\theta_2 = 1 - \frac{f}{n_o} \quad (2.17)$$

So, using the above equation the solid angle Ω associated with the aperture ' f ' becomes

$$\Omega = 2\pi(1 - \cos\theta_2) = 2\pi\frac{f}{n_o} \quad (2.18)$$

The resolving power (R_o) for an ideal etalon, having very high reflectivity is also defined as:

$$R_o = \frac{n_o}{f} \quad (2.19)$$

Combining these two equations, we get

$$\Omega = 2\pi\frac{f}{n_o} = 2\frac{\pi}{R_o} \quad (2.20)$$

$$\Omega * R_o = 2\pi \quad (\text{Jacquinot, 1954}) \quad (2.21)$$

The above equation reveals that the product of the solid angle of acceptance and resolving power is a constant and equals (2π). This relation between angle of acceptance and resolving power forms a part of an important optics theorem, which is known as the **LRP** criterion.

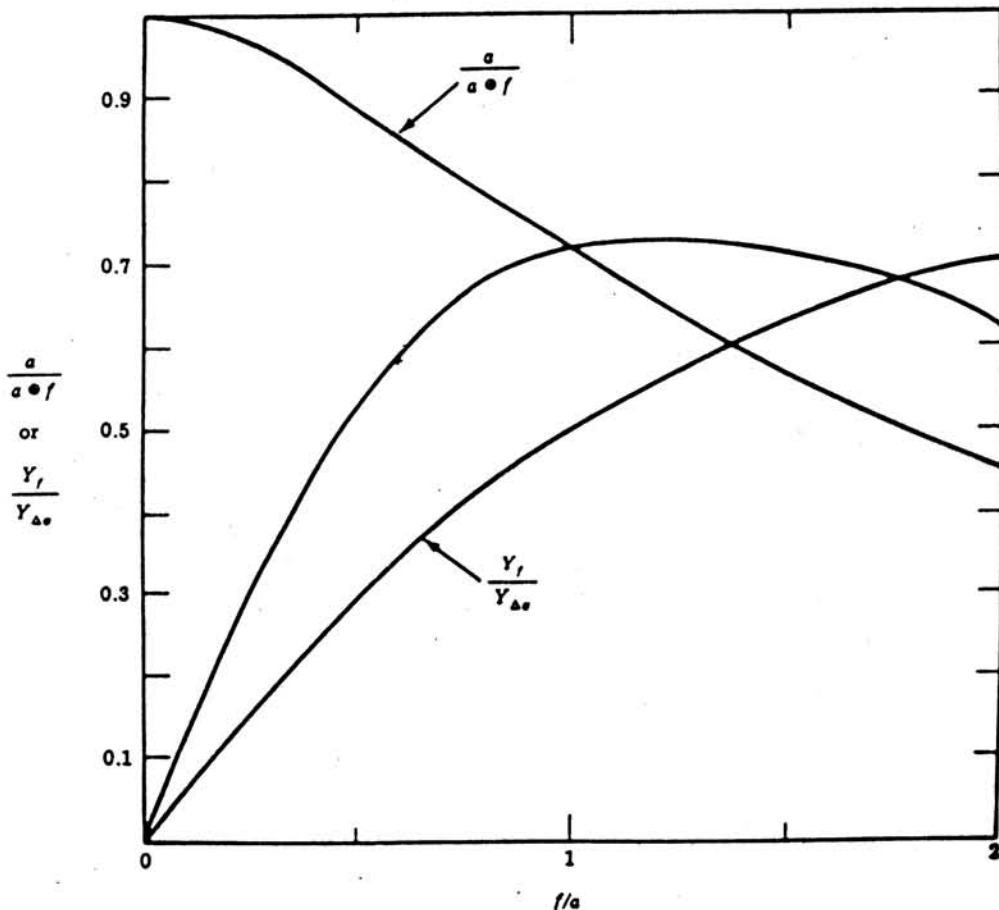
2.5.3 LRP Criterion

In reality, the actual resolving power ' R ' of the instrument is less than R_o and there exists an appropriate aperture size for which the product of flux and modulation (resolving power \times angle of acceptance) is the highest. The maximisation of the above product is the base of LRP or luminosity - resolving power product [Jacquinot, 1954, 1960]. In an important observation, Chabbal [1953] found that the above said product is maximum only when the ratio of the (half width at half maximum) HWHM of aperture (f^*) to the HWHM of the etalon - source combination (e^*) is near unity. However, it has been shown [Bruce, 1966; Hernandez, 1974] that the attainable value of f^* in reality must

always be smaller than 0.5. Thus, for actual observations, the LRP criterion leads to the optimisation between luminous flux, aperture size and instrumental broadening. However, *Hernandez and Roble* [1979] has pointed out towards the limitations of this approach and has derived [*Hernandez* 1986] the conditions for operating a Fabry-Perot spectrometer for detecting line emissions having contamination from a continuous background and noise inherent in signal, limiting its precision. Figure(2.4) depicts the optimum range which corresponds to the broad maximum in the figure. In the present investigation, considering all the etalon parameters and an emission profile of source width ~ 0.1607 (normalised with free spectral range) at a Doppler temperature of 800 K, and using the LRP criterion yields, the optimum value for an aperture diameter in the range of 3.3 mm to 4.3 mm. In this study, we had standardised on a value of 3 mm, keeping in view the possibility of higher temperatures and for this aperture, the estimated field of view for the instrument turns out to be 0.34° .

2.5.4 Interference Filter

In the present investigation, a very narrow band (FWHM- 3\AA) interference filter was used to separate the wavelength of our interest. The tuning for the desired wavelength can be done by tilting the interference filter relative to the optical axis of the instrument or by varying the temperature of the filter. We use the temperature tuning as it can increase or reduce the wavelength of the peak transmission retaining its response characteristics, while tilting the filter shifts the peak transmission wavelength only to lower wavelengths, at the same time broadening the



Figure(2.4): Range of operation of a Fabry Perot Spectrometer. The curves plotted are (i) the ratio of ideal width to resultant width (convolution of ideal function with the aperture broadening function), $a/(a \times f)$, Vs. ratio of aperture width to etalon width (f/a) and (ii) The ratio of flux transmitted over one free spectral range, $Y_f/Y_{\Delta\sigma}$, Vs. f/a . The product $a/(a \times f)$ and $Y_f/Y_{\Delta\sigma}$ is shown as the labeled curve. The optimum range of operation correspond to the broad maximum. (after Hernandez, 1986).

response curve while bringing down the peak transmission. In the actual set up, bipolar temperature controllers employing Peltier elements, capable of doing both heating and the cooling, are used to tune the interference filter which is housed in a chamber kept at the desired temperature [Figure 2.5)]. The filter housing is surrounded by thermo-electric modules i.e., Peltier elements. The bipolar mode of the temperature controller automatically passes the current in a favourable direction to either heat or cool the filter as per the requirement during actual operation. The filter temperature, tuned to the peak transmission, is maintained to an accuracy of better than 0.5°C . This ensures the filter to be functioning at maximum transmission at the desired wavelength, for the given experimental conditions during actual operation of the Fabry-Perot spectrometer.

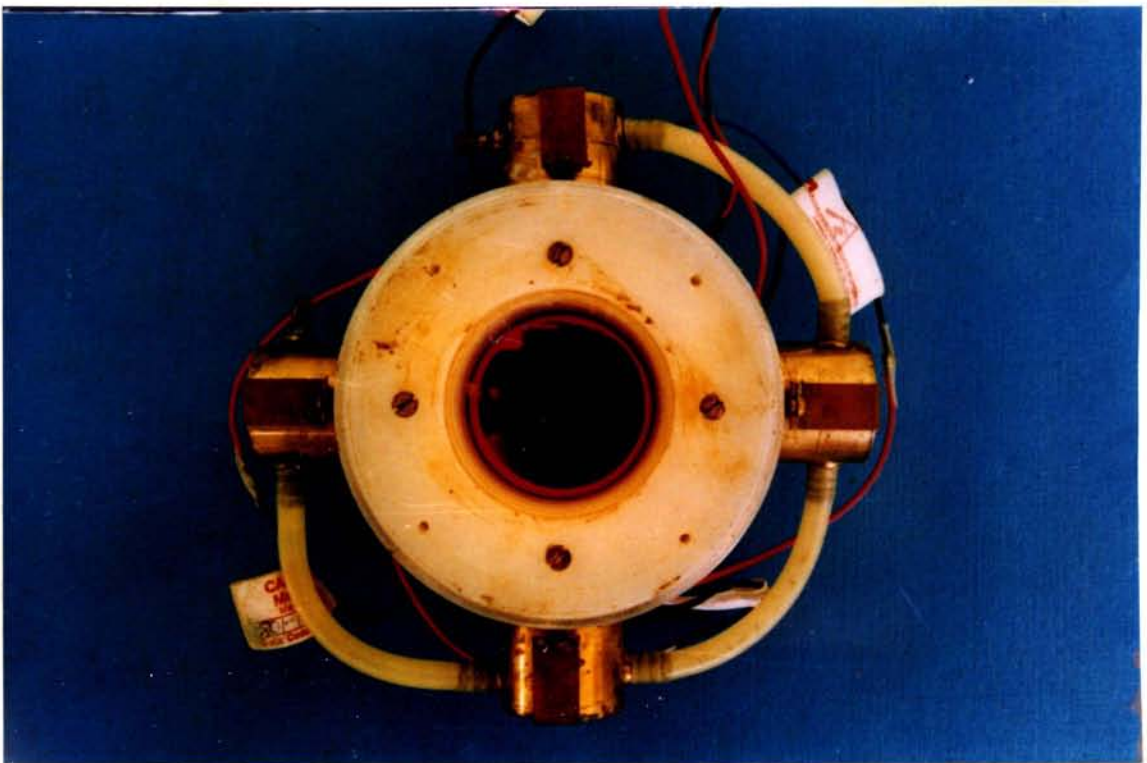


Figure 2.5: The interference filter assembly as used in the present instrument.

2.5.5 Photomultiplier Tube

An EMI 9863 A (14 stage) photomultiplier tube with a cathode sensitivity of at least $200 \mu\text{A}/\text{lumen}$ is used as a detector in the high resolution Fabry-Perot spectrometer. This PMT has a multi alkali (Na_2KSbCs), coated S20 photocathod of 9 mm effective diameter. The photocathod has a quantum efficiency of $\sim 6\%$ for 6300\AA radiation. It has a very small deadtime (10^{-9} sec) and a gain of the order of 10^7 , which is perfectly suitable for our observations. This PMT is operated at ~ -1650 V for maximum signal to noise ratio and is cooled to less than -15°C for reducing the thermal noise to very low levels during actual airglow observations. The PMT output pulses (discrete photon counts) are passed through a pulse amplifier discriminator (PAD) unit in order to discriminate signal below 100 mV which corresponds to thermal noise and amplify the rest beyond the discriminator threshold. The output in the form of counts are fed to the data acquisition system.

2.5.6 Data Acquisition System

The data acquisition system is primarily the necessary electronics and consists of two digital counters. One for the output pulses of the PMT and the other for the pressure monitoring. A PC(486) is also a part of this acquisition system. It helps in faster storage and simultaneous display of the data. However, the functioning of the system such as the integration time, mirror movement and automatic pressure changes etc. are controlled by a software developed completely inhouse. Figure(2.6) depicts the schematic layout of the data acquisition system.

2.6 Working of the High Resolution Central Aperture Scanning Fabry-Perot Spectrometer

The basic optical layout of the high resolution Fabry-Perot spectrometer used in the present investigation is depicted in Figure(2.7). The incoming airglow from the nightsky at fixed elevation is directed into the 100mm FP etalon using high quality front silvered mirror. This mirror goes out of the field of view of the instrument for zenith observation. The etalon (optically contacted) is sealed inside a chamber with an optical window in the front end and a converging camera lens in the rear

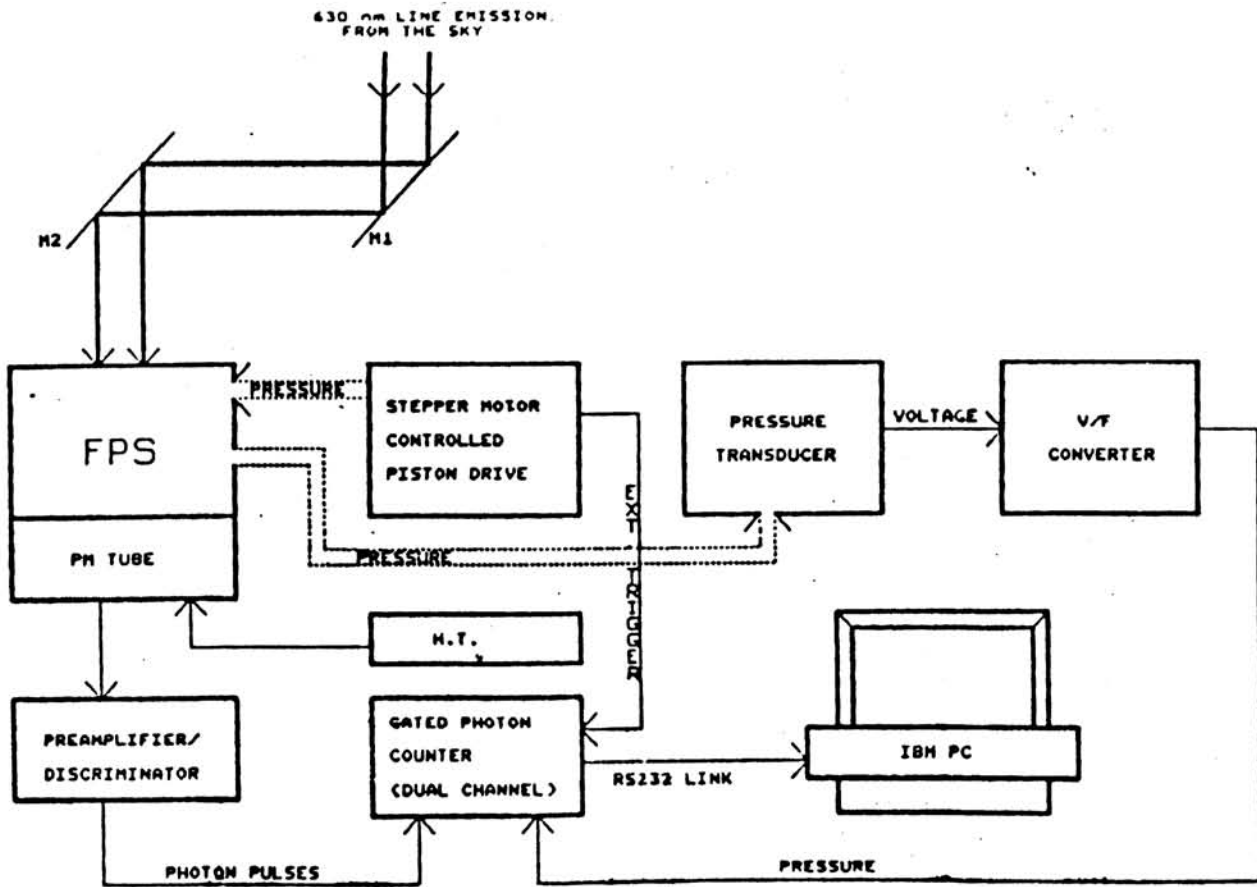


Figure 2.6: Block diagram of the overall data acquisition system with supporting electronics.

HIGH RESOLUTION FABRY-PEROT SPECTROMETER (SCHEMATIC)

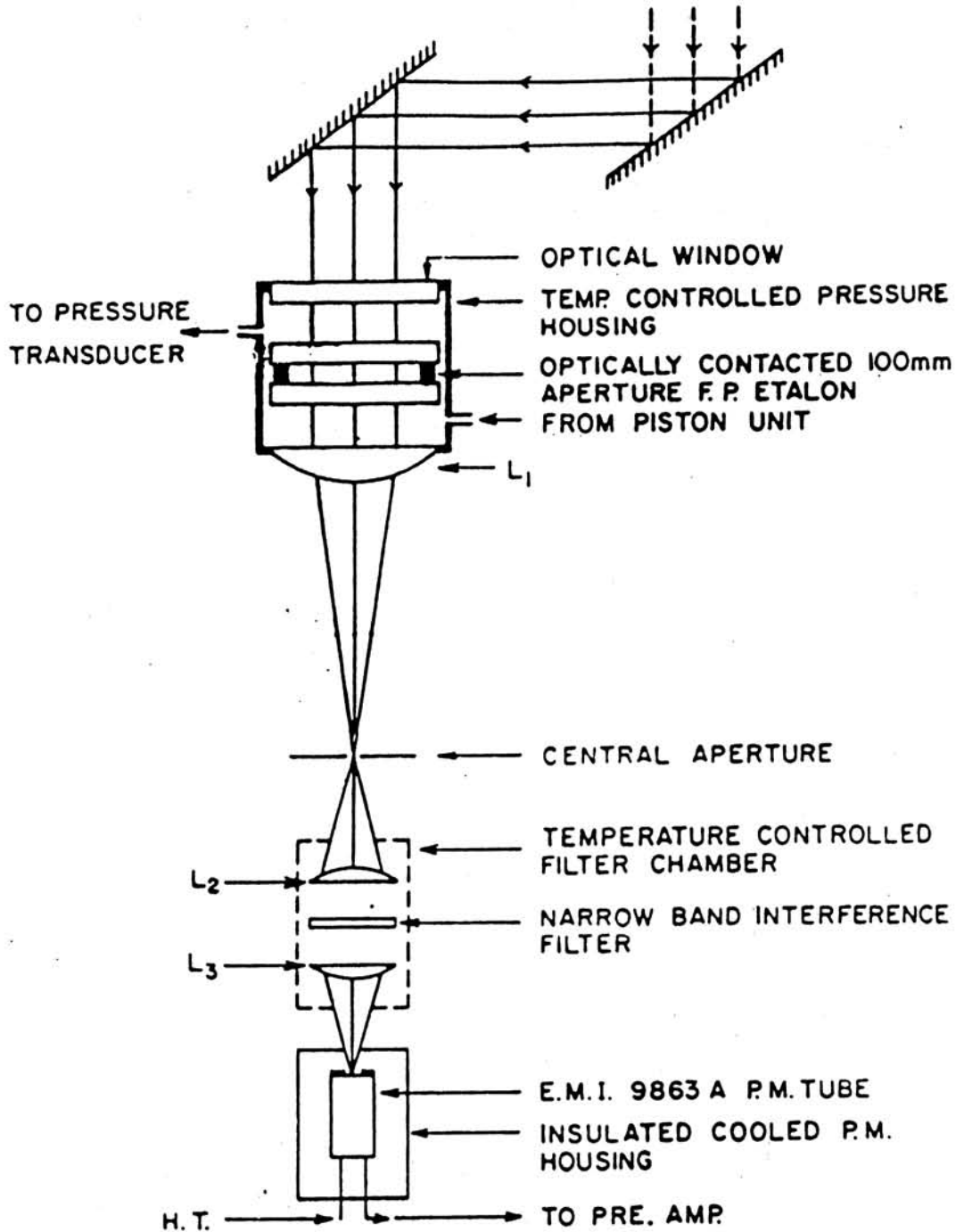


Figure 2.7: Schematic diagram of the central-aperture pressure scanned high resolution Fabry Perot Spectrometer.

end. The light, after multiple reflections inside the etalon, is projected onto the 3.0 mm aperture by means of the lens having a focal length of 50 cm. Therefore, this instrument has $f/5$ optics and 0.34° field of view. The gathered flux at the scanning aperture is collimated and directed into a narrow band (3\AA) interference filter. The filter enables the separation of the flux corresponding to the wavelength of our interest from the rest and the filtered light beam is focussed onto the detector i.e. EMI 9863 A, PMT operating in a photon counting mode. The photons, thus counted are stored and displayed as intensity, in the data acquisition system.

As mentioned earlier, the spectral scanning is accomplished by changing the pressure in the FP chamber. Change in the pressure of the air between the plates of the etalon, causes a change in the refractive index ' μ ' of the medium which in turn, scans the spectral distribution relative to the static aperture. A stepper motor controlled piston drive unit, as per the requirement, varies the pressure. In the present etalon (1 cm gap), a pressure change of ~ 90 torr (1 torr = 1 mm of Hg), with air as the medium, results in scanning of slightly more than two orders of interference. The Free Spectral Range (FSR) in the wavelength domain of interest i.e. 6300\AA is 0.1985\AA . As the nonlinearity in the change of ' μ ' the refractive index, for a pressure change of 90 torr is only to the extent of 10^{-3} [Harnandez, 1986], it is taken as not so significant for our study.

However, the linearity in the temperature dependence of ' μ ' is ensured by maintaining the thermal stability of the etalon to better than 0.1°C during a particular scan; and to an extent of 0.5°C throughout the night. Thermal stability of the etalon becomes more important at places where faster variations are experienced in the outside temperatures as the variation in etalon temperature can cause a shift in the peak of observed Doppler profile, and hence

the precautions. This stability is achieved by means of a dual heating system for the etalon chamber. A resistive heating element is wound on the FP chamber for linear proportional temperature control and a precision temperature sensor (AD590) monitors the temperature of the chamber. In order to provide the right ambient to the proportional temperature controller an outer heating jacket with an on/off temperature control is provided. The chamber outer jacket setting is kept typically $\sim 25^{\circ}\text{C}$ while the chamber itself is kept at $\sim 27^{\circ}\text{C}$. This sort of a dual heating system can maintain the temperature of the etalon to better than 0.1°C .

It has been observed that a shift of 0.0002\AA corresponds to a wind of 10 m/s during the observations. For accurate monitoring of the pressure inside the etalon, a high precision temperature controlled ($<1^{\circ}\text{C}$) absolute pressure transducer is used in the present experimental set up. This device has a Barocel pressure sensing element which acts as a precise and a stable capacitive potentiometer. In this, a thin prestressed metal diaphragm separating two gas tight enclosures is positioned between the capacitor plates. The difference in pressure, deflects the diaphragm and in turn, varies the relative capacitance between the diaphragm and the capacitor plates. The capacitance variations in terms of output voltage, represent the applied pressure. The accuracy of pressure reading is better than $\pm 0.05\%$.

In the actual operational mode, the synchronization between the piston movement and the data acquisition, is of prime importance. The pressure inside the etalon is allowed to stabilise after each step when the pressure is changed (every movement of piston changes the pressure by ~ 1 torr). The counters, for photons and pressure counting, are enabled only after this stabilisation and then the airglow photons are counted for the required integration time which is kept at 10 or 20 seconds depending on the intensity level. A spectral

scan covering one order takes about 18 minutes. The complete operation of the present Fabry Perot Spectrometer (FPS) is now programmable and menu driven which includes forward and reverse scanning of the interference fringe for a given pressure range and changing the direction of observation in elevation and azimuth.

The representative instrument parameters are:

- (i) Typical FWHM of the airglow line profile = $.025\text{\AA}$ (12 torr)
- (ii) FSR = $.1985\text{\AA}$ (91 torr)
- (iii) Contrast = 15
- (iv) Overall instrument finesse of ~ 8 .

The instrument parameters are retrieved from the line profile, obtained from the relative scanning of the central interference fringe with respect to the static aperture, for a standard source i.e. a single mode He-Ne laser operating at 6328\AA . In order to take into account the day to day changes in these parameters because of the change in stability of any of the devices being used in the optical setup, instrumental scans are taken at the beginning of observation each night. The actual instrumental set up in the Optical Aeronomy Laboratory at Mt. Abu is depicted in Figure(2.8)

2.7 Retrieval of Doppler Parameters from Observed Interference Fringes

During actual observations, through the Fabry-Perot spectrometer, the output profile is a distortion of the original source profile by the finite band pass of

the instrument. In a more rigorous mathematical explanation - all the instrument broadening functions get superimposed on the source width and the final result is a broadened representation of the original intensity distribution. In other words it is a convolution of the source function with the instrumental function. The instrument now acts as a window over which each spectral element of the source function is integrated. The output profile, therefore, is expressed as a convolution of the source profile with the instrument function.

$$EO(x) = \int I(x - x') * S(x') dx' \quad (2.22)$$

$EO(x)$ is the expected output profile. $I(x)$ is the Instrument broadening function. $S(x)$ is the source function. The convolution of the individual broadening function with the instrument function has been considered by many workers [Chabbal, 1953; Turgeon and Shepherd, 1962; Hernandez, 1966]. However, in actual observations the intensity of the signal is contaminated by inherent noise, the background continuum and contributions from neighbouring spectral sources if present. So the



Figure(2.8): The actual Experimental setup at Mt.Abu.

actual observed profile $O(x)$ is given as:

$$O(x) = EO(x) + \varepsilon(x) + B \quad (2.23)$$

$\varepsilon(x)$ and B are the noise and background continuum respectively. Therefore, in order to retrieve the Doppler parameters, the source function $S(x)$, is to be obtained first, from the observed, convolved, nightglow intensity profile.

Its clear from the convolution integral above, that one obvious way to obtain the source function $S(x)$ would be to go for a deconvolution process in the Fourier domain. But, for signals having inherent noises, this process of deconvolution becomes ill conditioned and hence cannot reproduce the source function without having added some side effects [Cooper, 1977]. Anandarao and Suhasini [1986] also have shown results confirming the above aspects of a deconvolution approach. A new method to retrieve the Doppler parameter was developed which is largely based on the work of [Gurubaran, Ph.D. thesis, 1993] taking into account not only the noise inherent in the signal but also the various limitations faced during the observations.

The approach adopted in the the present analysis, is discussed in the following sections.

2.8 Spectral Line Shape

In the upper atmosphere, the fraction of atoms emitting airglow at a certain wavelength and intensity under thermal equilibrium at temperature are represented by the Gaussian distribution in the following way:

$$I(\lambda) = \frac{I_o}{d\lambda} \exp\left[-\frac{(\lambda - \lambda_o)^2}{d\lambda^2}\right] \quad (2.24)$$

This Gaussian distribution is centered about λ_o and the width of the Gaussian distribution ($d\lambda$) arises because of the distribution of velocities of atoms contributing towards the particular spectral emission. The Doppler width of the

emission profile is related to the full width at half maximum ($\delta\lambda$) by

$$\delta\lambda = (2\sqrt{\ln 2})d\lambda \quad (2.25)$$

and to the kinetic temperature T_n by:

$$\frac{\delta\lambda}{\lambda_o} = 7.16 \times 10^{-7} \sqrt{\frac{T_n}{M}} \quad (2.26)$$

M is the molecular/atomic weight of the emitting species in atomic mass units (amu).

The same (Gaussian) emission line profile as observed by our Fabry-Perot spectrometer could be written as:

$$EO(X_i, P_j) = \sum_{k=1}^n I(X_i, X_k)S(X_k, P_j) \quad (2.27)$$

The functions $EO(X_i, P_j)$, $I(X_i, X_k)$ and $S(X_k, P_j)$ are the expected output profile, instrument function and the source function respectively. The above expression represents the scanning of interference fringes, the data taken in terms of discrete steps in the parameter X_i i.e. pressure in our case. In this scanning technique, the net result of a scan over a free spectral range is a set of sample points. The parameters of the Doppler profile to be determined are P_j 's, i.e. P_1, P_2, P_3 which are peak line intensity, the line center and the line width respectively. In terms of P_1, P_2, P_3 (the required parameters) the source profile becomes:

$$S(X_k, P_j) = \left(\frac{P_1}{P_2}\right) \exp\left[-\frac{(X_k - P_2)^2}{P_3^2}\right] \quad (2.28)$$

2.8.1 Determination of P_j 's

Since the form of the expected output profile $EO(X_i, P_j)$ is known, an approach of linearizing the fitted curve function $EO(X_i, P_j)$ in the parameter space close

to the optimum values of P_j 's is adopted for the determination of P_k 's [Draper and Smith, 1966; Bevington, 1969]. The linearization process uses the results of linear least squares which is an iterative procedure based on Taylor series expansion about the approximated required solution of P_j 's. As the first step, the profile function $EO(X_i, P_j)$ is expanded in a Taylor series about P_j 's (a set of initial approximate solutions).

$$EO(X_i, P_j) = EO(X_i, P_j^o) + \sum_{j=1}^3 \left(\frac{\partial(EO)^o}{\partial P_j} \right)_i P_j' \quad (2.29)$$

where

$$P_j = P_j^o + P_j' \quad (2.30)$$

and

$$EO = EO(X_i, P_j^o) \quad (2.31)$$

The higher order dependence of P_j' is neglected in the Taylor expansion. The initial value of P_j 's correspond to the observed profile $O(X_i)$ assuming the $O(X_i)$ follows Gaussian distribution. Sum of the squares of deviation (χ^2) becomes:

$$\chi^2 = \sum_{i=1}^n W_i [O(X_i) - EO(X_i, P_j^o)] \quad (2.32)$$

Minimisation of the above term would lead to three equations which are to be solved for P_j' . Thus found P_j 's, give the estimate of the parameters to be used as initial value for the next iteration. In our case, the convolved output or the Doppler Broadened profile is given by

$$EO(X_i, P_j) = \sum_{k=1}^n I(X_i - X_k) \left[\frac{P_1}{P_3} \exp \left(\frac{(P_2 - X_k)^2}{P_3^2} \right) \right] \quad (2.33)$$

For the minimisation of sum squares of deviation, the deviations with respect to P_j' should be zero i.e.

$$\frac{\partial}{\partial P_k'} \left[\sum_{i=1}^n W_i \left\{ O(X_i) - EO(X_i, P_j^o) - \sum_{j=1}^3 \left(\frac{\partial EO^o}{\partial P_j} \right)_i P_j' \right\}^2 \right] = 0 \quad (2.34)$$

$$2 \times \sum_{i=1}^n W_i \left[O(X_i) - EO(X_i, P_j^o) - \sum_{j=1}^3 \left(\frac{\partial EO^o}{\partial P_j} \right)_i P_j' \right] \left(\frac{\partial EO^o}{\partial P_k'} \right)_i = 0 \quad (2.35)$$

second and higher order derivatives are neglected. However, the derivatives are

$$\frac{\partial(EO)}{\partial P_1} = \frac{(EO)}{P_1} \quad (2.36)$$

$$\frac{\partial(EO)}{\partial P_2} = \frac{2(X_k - P_2)}{P_1^2} EO \quad (2.37)$$

$$\frac{\partial EO}{\partial P_3} = \left[\frac{2(X_k - P_2)}{P_1^2} - \frac{1}{P_3} \right] EO \quad (2.38)$$

For brevity, function $EO(X_i, P_j)$ is written as only EO in expression above. Equation (2.39) below provides the normal equation.

$$\sum_{i=1}^n W_i O(X_i) \left(\frac{\partial EO^o}{\partial P_k'} \right)_i - \sum_{i=1}^n W_i EO(X_i, P_j^o) \left(\frac{\partial EO^o}{\partial P_k'} \right)_i - \sum_{j=1}^3 W_i \left(\frac{\partial EO^o}{\partial P_j'} \right)_i \left(\frac{\partial EO^o}{\partial P_k'} \right)_i P_j' = 0 \quad (2.39)$$

The important thing here is, that, the derivatives $\frac{\partial EO^o}{\partial P_k'}$ are numbers and the above equation gives a set of simultaneous equation to be solved for P_1, P_2 and P_3 . If

$$\sum_{i=1}^n W_i O(X_i) \left(\frac{\partial EO^o}{\partial P_k^o} \right)_i - \sum W_i EO^o \left(\frac{\partial EO^o}{\partial P_k^o} \right)_i = C_k \quad (2.40)$$

The normal equation becomes:

$$C_k = \sum_{i=1}^n W_i \left[\sum \left(\frac{\partial EO}{\partial P_j} \right)_i \left(\frac{\partial EO}{\partial P_k} \right)_i P_k' \right] = 0 \quad (2.41)$$

so

$$C_1 = \sum W_i \left[\left(\frac{\partial EO}{\partial P_1^o} \right)_i + \left(\frac{\partial EO}{\partial P_2^o} \right)_i + \left(\frac{\partial EO}{\partial P_3^o} \right)_i \right] \left(\frac{\partial EO}{\partial P_1^o} \right)_i \quad (2.42)$$

similar solutions for $k= 1, 2, 3$ can be written as:

$$C_1 = A_{11}P_1 + A_{12}P_2 + A_{13}P_3 \quad (2.43)$$

$$C_2 = A_{21}P_1 + A_{22}P_2 + A_{23}P_3 \quad (2.44)$$

$$C_3 = A_{31}P_1 + A_{32}P_2 + A_{33}P_3 \quad (2.45)$$

Or in matrix form, the above equation can be written as

$$\begin{pmatrix} C_1 \\ C_2 \\ C_3 \end{pmatrix} = \begin{pmatrix} A_{11} & A_{12} & A_{13} \\ A_{21} & A_{22} & A_{23} \\ A_{31} & A_{32} & A_{33} \end{pmatrix} \begin{pmatrix} P_1 \\ P_2 \\ P_3 \end{pmatrix} \quad (2.46)$$

In other words,

$$C = A * P \quad (2.47)$$

C , A and P are general terms used for the above mentioned matrices. To obtain P we used matrix inversion technique.

$$P = C * A^{-1}$$

and the estimates of P_j 's are obtained by adopting Gauss - Jordan elimination processes for coefficient matrix A^{-1} . Thus estimated P_j 's serve as the initial values for the next iteration, and the whole procedure is repeated till the solution converges.

2.8.2 The Noise Reduction and Estimation of Background

All the data points observed during a scan consist of the desired signal and some superimposed noise, which is random in nature. It is to be noted that this noise becomes more dominant when the signal strength becomes low. However, the frequency spectrum of the noise is rather flat compared to that of the fringe peak [Hays and Roble, 1971]. The photons falling into the detector during a real time observation follow Poisson distribution [Bevington, 1969; Hernandez, 1986]. In other words, if the detector observed N photons having inherent noise for a given time, then the variance of this distribution i.e. $\sqrt{(N)}$ is a measure of the statistical observational uncertainty. The importance of these uncertainties in actual conditions is highlighted and quantified by Hernandez in a series of papers [1978, 1979, 1982, 1985]. Hays and Roble [1971] have clearly shown that the Fourier decomposition technique can efficiently

filter out the high frequency component i.e. noise, from the incoming signal photon fields, by using only the first five coefficients. We have adopted the above said Fourier decomposition technique to minimise the random errors associated with photon noise. The airglow profile which is a function of pressure (wavelength) and is Gaussian in shape and can mathematically be written as the superposition of even (cosine functions) and odd (sine) functions of various orders (m). If $Y_s(x)$ is the actual airglow profile then in terms of Fourier components it can be written as

$$Y_s(X) = \frac{Y_{co}}{2} + \sum Y_m \cos(mX + \alpha) \quad (2.48)$$

here Y_{co} is the zeroth order transform of the data. In the analysis $m = 4$ is our limit for coefficient order, as explained above. The amplitude is defined by $\sqrt{(Y_{cm}^2 + Y_{sm}^2)}$ and α as $\tan^{-1}(\frac{Y_{sm}}{Y_{cm}})$ are the odd and even (Sine and Cosine) Fourier transform of the data. This method enables us to treat the data free of inherent random noise. However, there remains one more component of noise to be removed from the observed data that is in the form of background continuum.

There is no qualitative definition, describing the background, but the lowering of contrast in observed profiles is associated with the presence of background radiation during observations. It has been shown [Chabbal, 1953] that the observed contrast (C_{act}) of the airglow profile is always less than the instrument contrast (C) and is related to the product of the instrument contrast and the transmission of the etalon (τ). He also gave a theoretical response curve for the instrument as variation of transmission for the etalon for different source width(s) compared to etalon widths (E), where the transmission actually is:

$$\tau = \frac{C_{act}}{C} \quad (2.49)$$

C is the resultant contrast for an ideal monochromatic source (zero width) and

C_{act} is the contrast for assumed source widths. The observed contrast C_{act} is given by

$$C_{act} = \frac{I_{max} - BG}{I_{min} - BG} \quad (2.50)$$

I_{max} , I_{min} , BG , represent the maximum and minimum and background intensity levels respectively.

Using the above expressions (2.49) and (2.50) and the transmission curve, the background can be estimated for any source (i.e. source widths under consideration). The estimated background is subtracted from the observed (data) and then the profile is subjected to the analysis for determination of the Doppler parameters. Figure(2.9) shows the deconvolved airglow profile after applying the Fourier decomposition technique for noise reduction and due correction for the background. A theoretical profile determined for the estimated temperature from the former profile is also shown for comparison.

2.8.3 Estimation of Errors in the Evaluation of Doppler Parameters

Owing to the nature of the distribution of observed photons and inherent noise in our measurements, the uncertainty associated with the determination of P_j parameters is the root sum square of the products of the standard deviation of each data point (σ_i) multiplied by the effect that the data point has on its determination [Bevington, 1969].

$$\sigma_{P_j}^2 = \sum_{i=1}^n \left[\sigma_i^2 \left(\frac{\partial P_j}{\partial O X_i} \right)^2 \right] \quad (2.51)$$

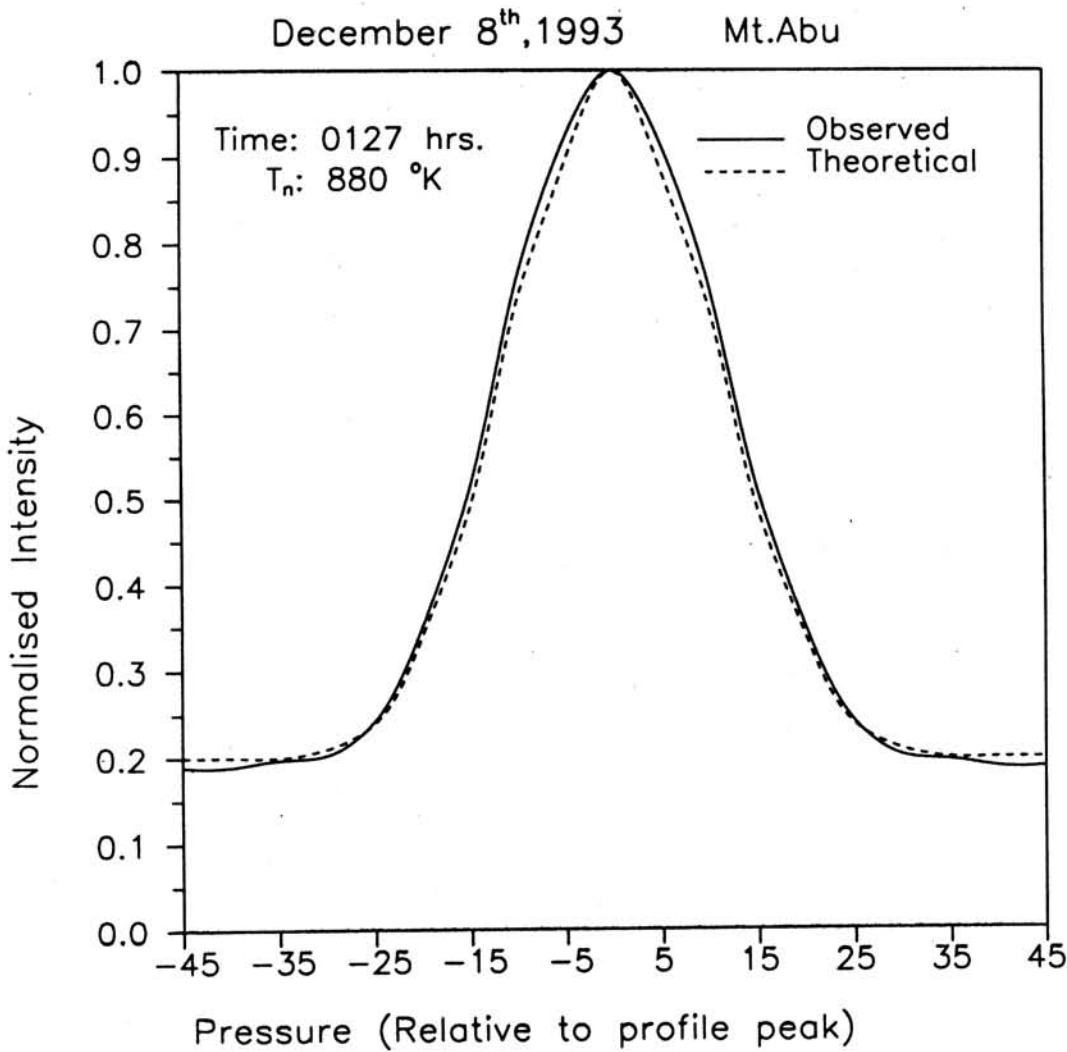


Figure 2.9: The deconvolved airglow profile after noise reduction and due correction for background. A theoretical profile determined for the measured temperature is also shown.

However, the fluctuations are statistical and so, the uncertainties σ_i are given by $\sqrt{O(X_i)}$ which is the observation corresponding to variable X_i [Hernandez, 1978]. As it is clear eqn(2.51) that for the determination of the uncertainties, the deviation of P_j with respect to the observation $O(X_i)$ is to be estimated; while P_j 's are obtained from the solution of the normal equations.

$$P = A^{-1} * C \quad (2.52)$$

$$P_j = \sum_{k=1}^n (A^{-1})_{jk} \left[\sum W_i \{O(X_i) - EO(X_i, P_j^o)\} \left(\frac{\partial EO^o}{\partial P_k} \right)_i \right] \quad (2.53)$$

where $(A^{-1})_{jk}$ are the elements of the inverse matrix A^{-1} . The derivative $\frac{\partial P_j}{\partial O(X_i)}$ is

is :

$$\frac{\partial P_j}{\partial O(X_i)} = \frac{\partial}{\partial O(X_i)} \left[\sum_{k=1}^3 (A^{-1})_{jk} \sum_{i=1}^n (A^{-1})_{jk} \sum W_i \{O(X_i) - EO(X_i, P_j^o)\} \right] \quad (2.54)$$

$$\frac{\partial P_j}{\partial O(X_i)} = \sum_{i=1}^3 (A^{-1})_{jk} W_i \left(\frac{\partial EO^o}{\partial P_k} \right)_i \quad (2.55)$$

So the uncertainty

$$\sigma_{P_i}^2 = \sum_{k=1}^3 \sum_{l=1}^3 (A^{-1})_{jk} (A^{-1})_{jl} \sum_{i=1}^n \left[W_i \left(\frac{\partial EO^o}{\partial P_k} \right)_i \left(\frac{\partial EO^o}{\partial P_l} \right)_i \right] \quad (2.56)$$

The above expression is a matrix, whose diagonal elements are the uncertainties of the parameters P_j 's. This method is based on the earlier formulation used to determine the Doppler parameters [Sridharan *et al.* 1991; Gurubaran 1993].

2.9 Limitations in the Retrieval of Doppler Parameters

The data reduction technique described above was developed taking all the instrumental parameters and the stability factors into account, including the limitations imposed by variations in the airglow source region itself. Some of the factors which limit the precision of the retrieved Doppler parameters are,

- (i) Tilt in the static aperture.
- (ii) Fast airglow intensity variations.
- (iii) Extremely low signal strength.
- (iv) Shears present in the winds in the emitting region.
- (v) Contamination from other spectral sources in the nearby wavelength region.

As most of these factors cannot be dealt with directly, except (i); only their effects on the estimation of parameters can be minimised. The merits of alternative approaches adopted by us to minimise these effects, in the present investigation are discussed below:

2.9.1 Aperture Tilt

As in the present Fabry-Perot spectrometer, the central interference fringe is being pressure scanned over the static aperture, any tilt with respect to the optic axis in the aperture plane would cause an asymmetry in the observed profile. The effect of such a tilt can be seen during the scan only when the central fringe crosses the aperture boundary while going out or converging in. Hence, the asymmetry would appear on the scanned profile on the left or the right half, depending on the direction of the scan. To eliminate any ambiguity in the profile because of asymmetry; we swap that half of the profile which is unaffected by the tilt of the aperture in order to get a complete smooth profile. The resulting profile, thus obtained is relatively free of any distortions or asymmetry and is analysed using the procedure described in the previous sections. This method had been found to be successful for a variety of profiles with varying intensities.

2.9.2 Airglow Intensity Changes

Faster variations in observed airglow intensity levels can be caused by many processes which can be both local and non local in origin. One such local process which is known to cause such changes in nightglow is the Equatorial Ionisation Anomaly (EIA). This process will be discussed in detail in the following chapters. Such fast intensity variations due to processes like EIA can cause large distortions in the profile shape and width leading to large uncertainties in the estimated Doppler parameters when the airglow intensities are low. It has been seen during the present investigation, that, if the intensity changes are more than 25% during a scan, significant fluctuations in estimated temperatures are experienced. So the profiles with such drastic changes in intensity are not included for the estimation of Doppler parameters. At the same time, very low levels of airglow intensity have significant noise level merged in the

signal, which yields a very low signal to noise ratio not adequate enough to obtain reliable Doppler temperatures and winds [Hernandez and Roble, 1976, 1978]. For Mt. Abu, airglow profiles having peak photon counts less than 100 are rejected. Unfortunately, such low count levels are quiet frequent during solar minimum epoch rendering a limited optical data base to derive neutral parameters i.e. temperature and winds.

2.9.3 Velocity Gradients and Gross Motions

As it has been pointed out earlier, the distribution of atoms/molecules emitting the airglow follow a Maxwellian distribution. The fundamental assumption in this is that the region from where the emission originates is more or less in uniform motion or there are no vertical velocity gradients therein. *Biondi and Fiebelman* [1968] have shown during their observations from Laurel mountain, Pennsylvania, sharp gradient in wind velocity within the emitting region were possible at least on occasions. These gradients would distort the observed airglow profiles causing marked asymmetries. However, the rocket cloud experiments in Indian zone [Sridharan *et al.* 1989, 1993] clearly suggested that such gross motion or shears are not a common occurrence. Irrespective of the cause, severely distorted profiles are screened out and not included in the analysis.

2.9.4 Contamination from Nearby Emissions

The analysis procedure described in earlier sections applies to Doppler broadened emission lines which are free from the contribution of the overlapping orders of nearby emissions. However, the $OI(^1D - ^3P)$ transitions at 6300\AA may get influenced by the overlapping orders from the nearby $OH(9, 3)$ and $OH(5.0)$ vibration bands if their intensities are above certain levels [Armstrong, 1969]. The presence of these vibrational lines ($6287.5, 6297.9, 6307\text{\AA}$) in the vicinity of 6300\AA is well identified but the effect of their contamination to 6300\AA is not understood properly. Nevertheless, it has been established that

at certain times when the airglow emission rate goes below 20R, the *OH* contribution has been observed to be significant [Hernandez 1974]. These emission bands are usually weak and proper instrument design and appropriate selection of filters would minimise their effect on Doppler parameters. The narrow band interference filter used in our instrument can effectively remove these lines except the one centered at 6297.9\AA . In order to minimise the effect of this line, the Fabry-Perot etalon (1 cm gap) is so chosen as to make this emission feature, which lies at the falling edge of the filter transmission, appear right in the middle of the 6300\AA airglow profiles corresponding to adjacent orders. At this position where the contribution from other orders is least, 6297.9\AA *OH* line is not significant in contaminating the observations of 6300\AA emission in the nightsky. However, the possibility of *OH* contamination cannot totally be ruled out on occasions when the molecular emission intensity becomes high, as the overall operating finesse of the system is kept only at ~ 8 in order to be able to maintain the luminosity requirement of the spectrometer.

The results presented in the following chapters are based on the Doppler parameters obtained using the central aperture scanning high resolution FP spectrometer and following the data analysis procedure, discussed in this chapter.

Chapter 3

Low Latitude TIS During Quiet Times

3.1 Introduction

The emphasis in the present study is on the self-consistent physical description of the relevant processes prevalent in the thermosphere-ionosphere system (TIS). Since, the physical, chemical, radiative and dynamical processes occurring within the whole of upper atmosphere depend upon altitude, location on the globe, time and season characterized by the temporal and spatial variations in temperature, composition and dynamics, it is extremely complex to address any particular problem taking all these factors into account simultaneously. So, we have restricted our investigation to that part of the upper atmosphere which is predominantly neutral, but has plasma immersed in it i.e. the thermosphere and the ionosphere. In the following sections, a detailed description of our present study on different coupling aspects of the low latitude thermosphere - ionosphere system, which is based on observational data on neutral temperatures, winds, F-region heights and densities obtained from Mt.Abu (24.6° N, 72.7° E geographic; 20° N dip lat.) and Ahmedabad (23° N, 72.1° E geographic, 18.4° diplat.) during geomagnetically quite times, is provided.

The thermosphere - ionosphere, a complex, chemically and physically integrated system (TIS) is closely connected to activities in the sun through the

interplanetary medium, to the magnetosphere higher above and also to the lower atmosphere. Under normal conditions, a dynamical equilibrium persists between the neutral and ionized species characterized by their production, loss and transport. The ionosphere is constantly under the influence of electromagnetic drifts, thermospheric neutral winds and diffusion. Since gravity and pressure gradients also contribute to the overall motion, it becomes difficult to unambiguously interpret the behaviour of this dynamic system as a whole, at any given time. During the day, production of ionisation results in creating horizontally stratified plasma layers known as E and F-regions. During the night, while the E-region plasma content disappears as a result of increased recombinations; the F-region plasma density, though decreasing, remains significant enough to participate and influence the overall energetics and dynamics. Expectedly the plasma drifts have a strong dependence on the geometry of the magnetic field lines, as, all the electrodynamic processes depend on the orientation of interacting magnetic and electric fields. However, for a comprehensive understanding of the ionospheric processes, one should know how the ions and electrons move in response to neutral winds, electrical conductivity, polarization fields, atmospheric impedances resulting into 'voltage and current generators', field aligned currents and the interaction of conjugate ionospheres [Rishbeth, 1997]. The processes, which control the ionic motion resulting in transferring energy and momentum to neutrals thereby influencing the neutral dynamics and vice-versa, are of chemical, fluid dynamical and electrodynamic origin. The movement of ionisation, especially the F-layer of ionisation, under the influence of the above stated processes, serves as an excellent indicator in the investigation of the very nature of the mutual coupling in the thermospheric-ionospheric system (TIS) [Rishbeth et al., 1978].

As a system, TIS displays large variabilities with altitude, latitude, longitude,

local time, season, solar and geomagnetic activity. The early works of *Rishbeth* [1969, 1978, 1979, 1985] provide a very useful insight into the various physical mechanisms operating in the low latitude or equatorial F-region. Beginning from the earlier works on ionospheric conductivity [*Cowling* 1945; *Baker and Martyn* 1953; *Chapman* 1956], to comparatively recent topics of E and F region dynamics [*Matsushita* 1969; *Rishbeth and Garriot* 1969; *Kelley* 1989; *Crain et al.* 1993]; and unique geophysical phenomena like the Equatorial Temperature and Wind Anomaly (ETWA) [*Raghavarao et al.* 1991]; formation of additional F3 layer near geomagnetic equator [*Balan and Bailey* 1995] and plasma temperature anomaly [*Balan et al.* 1997], there has been a tremendous growth in our understanding of the nature of the low and equatorial thermosphere-ionosphere system.

As discussed in chapter 1, it is recognized now that some of the important ionospheric parameters namely electric fields and the consequent plasma drifts as well as height distribution of plasma density are governed to a large extent by the magnitude and the direction of the thermospheric winds. The zonal wind flow leads to the generation of polarization electric fields by pushing the ionospheric plasma across the magnetic field lines. For the thermally driven wind system, the collisions between the neutrals and the ambient ions which are confined only to move along the magnetic field lines, results in the 'ion-drag' which in turn limits the movement of the neutrals. Ion-drag also provides the momentum coupling to large scale atmospheric motions e.g. thermospheric tides [*Rishbeth* 1979, *Forbes et al.* 1982].

Further, the F-region dynamics is also controlled by the interplay between the chemical and plasma diffusion processes. The winds and electric fields can move the F-layer to altitudes where the recombination and diffusion coefficients are different. This would cause a change in plasma density distribution

which in turn can affect the 'in situ' wind and electric field. This sort of feedback mechanism in the complex web of interacting processes in TIS is referred to as '**servo mechanism**'. *Rishbeth* [1967], observing the perturbations of F layer from equilibrium distribution under the influence of external forces, proposed this motion to be a part of the servo mechanism. The effect of the external forces, especially the winds in both day and night equilibrium layer was investigated for the first time. Followed by this, *Rishbeth et al.* [1978] put forward a model known as 'servo model' to investigate the basic interactive nature of thermosphere - ionosphere system. The servo model offers possibilities of examining the behaviour of the ionic species i.e. the F-layer and its response to applied perturbations in the presence of neutral species. This model has found its real use in a number of studies reported in the literature [*Yagi and Dyson, 1985; Miller et al. 1986; Buonsanto 1989; Forbes and Roble, 1990; Sridharan et al. 1991; Gurubaran et al. 1993; Pant and Sridharan 1998*]. The servo model treats the F-layer as a unit, and therefore cannot provide any information about the height variations taking place within the layer. In spite of this limitation, it is a convenient tool to investigate the thermosphere - ionosphere system as it couples the thermospheric parameters like temperature and winds with ionospheric parameters such as peak density and height of the layer i.e. N_{max} and h_{max} . In the following section, a brief description of the servo model is given followed by a discussion on the behaviour of the thermosphere and ionosphere as a servo system from a low latitude station Mt. Abu.

3.2 The Servo Mechanism

As per the general definition, the servo mechanism is a feedback control system in which the controlled variable is the position. The steady-state can be interpreted as a steady dynamic condition of the system. In similar lines, the F-layer was envisaged as behaving like a servo-system in which the system

equilibrium is the altitude location of F2-peak which is disturbed by time varying external perturbations i.e. the drifts. The servo mechanism gets operative and the system responds by seeking new equilibrium position with finite time constants [Rishbeth, 1967]. The 'feedback' channel to this system is facilitated by the ion-neutral interactions. The most intriguing feature of the F-layer is the large variabilities in its vertical motion. *Martyn* [1956] postulated the electro dynamical forces and winds associated with ionospheric current systems to be responsible for the F-layer vertical drifts over the equator. The thermospheric wind system which is set up by diurnal heating and cooling of the thermosphere were also invoked to explain the vertical drifts experienced by the F-layer [Giesler, 1966]. However, these studies pertain to mid latitudes.

The contribution of diffusion to overall motion of the F2-layer (plasma) was illustrated clearly by *Shimazaki* [1957]. Both the 'day equilibrium layer' and 'night stationary layer' were investigated by *Rishbeth* [1967], in terms of the effect of winds on them. It became clear from these studies that large thermospheric winds cause significant day to night changes in the heights of the peak electron density of the F2-layer. It is important to note that the ionization within the thermosphere - ionosphere system is tied up with the magnetic field lines, and the diffusion of ionisation along the magnetic field lines in the vertical direction would only be possible if the field lines have a finite magnetic dip angle. The plasma diffusion velocity is known to be proportional to $\sin^2 I$ where ' I ' is the magnetic dip angle, which means that, the vertical diffusion gets inhibited over the dip equator. Therefore the electro dynamical processes control the dynamics of the F-region and the associated variabilities. In short, the dynamical behaviour of the F-layer at any given instant of time is governed to a large extent by transport of ionisation, apart from production and loss. The realistic physical description of the F-layer is brought out by the

continuity equation. In the following section, the importance of the continuity equation for F2 layer, in the context of servo model is discussed in detail.

3.3 The F-layer Movement and the Continuity Equation

As has been discussed already, the solar radiation provides the necessary energy to maintain the thermal budget of thermosphere and to produce ionisation to a large extent. The major loss processes for the ionisation are the recombination processes. From the discussion above, the variation of F-layer height is not just a result of the production and loss processes, instead, it is dependent on the transport processes too, which operate almost simultaneously. The continuity equation for the F-layer is given by:

$$\frac{dN}{dt} = q - L - \nabla \cdot (Nv) \quad (3.1)$$

The left hand term of the equation is the rate of change of plasma density ' N '. ' q ' is the production rate of plasma and L the loss rate. The transport processes result in a net drift velocity ' v '. The change due to the transport term is represented by the divergence of the plasma flux which is ' $\nabla \cdot (Nv)$ '. It is important to note, that for the study of motion of individual species i.e. electrons and ions, the same continuity equation holds true. During daytime, the ionosphere (F-region) below 200 km is found to be in 'photochemical equilibrium'. In this quasi-equilibrium state, the transport term is treated only as a small perturbation and is usually neglected. Under equilibrium, the production is balanced by the loss i.e. $q = L(N)$. The rate of ionisation loss takes a linear form given by ' βN ' (β being the effective loss coefficient). During nighttime, the situation changes drastically with the production term becoming zero. The average life time of the ambient ions increases considerably due to the decreased densities, thus making the F-region plasma sensitive for any external perturbation and as a result the term $\frac{d(N)}{dt}$ becomes significant. A very comprehensive discussion

of all these processes is given by *Rishbeth* [1969, 1986]. The important transport processes are enumerated below.

3.4 Wind Induced Drifts

As discussed earlier, the plasma can be moved along the field lines by neutral meridional winds. The resulting vertical drift velocity induced on the plasma by steady thermospheric wind vector \vec{U} , is given by the following equation.

$$V_w = \frac{(\vec{U} \cdot \vec{B})\vec{B}}{|\vec{B}|^2} = \vec{U} \cos I \sin I \quad (3.2)$$

Figure(3.1) clearly depicts the component of vertical drift to be $U \cos I \sin I$. Over low and mid latitudes, the wind can push the F-region plasma up and down along the field line, depending upon its polarity i.e. whether it is equatorward or poleward. It could easily be seen through figure(3.1) that the effect of meridional winds on the F-region maximises at 45° dip angle corresponding to 22.5° dip latitude.

3.5 Electromagnetic Drifts

The plasma can also be moved up and down by electromagnetic forces in the presence of an electric field \vec{E} . However, the generation of these fields depends upon the atmospheric dynamo and other external processes. The combined interaction of electric and magnetic field induces an $(\vec{E} \times \vec{B})$ drift to the charged particles [fig. (3.2)], and is given by the following formula.

$$V_E = \frac{(\vec{E} \times \vec{B})}{|\vec{B}|^2} \quad (3.3)$$

The electromagnetic drift is independent of charge and mass of the drifting particles. Thus, under the influence of this electromagnetic drift, the electrons and

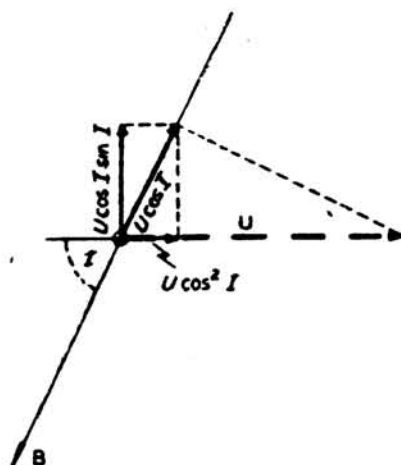


Figure 3.1: The meridional wind induced motion to the plasma. A southward neutral wind U will impart velocity $U \cos I$ to the plasma along the field lines. An upward component $U \cos I \sin I$ will also act. (Rishbeth and Garriott 1969)

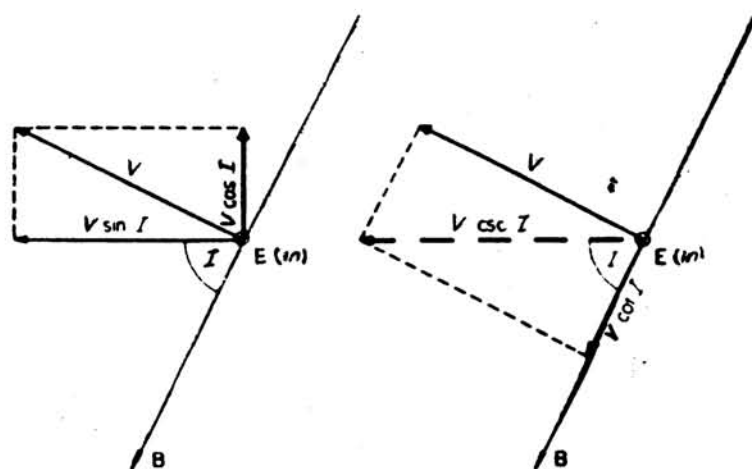


Figure 3.2: The geometry of the magnetic field and the electromagnetic drift. The plasma drift $\frac{\vec{E} \times \vec{B}}{|\vec{B}|^2}$ has an upward component $V \cos I$ and a northward component $V \sin I$ (Rishbeth and Garriott 1969)

ions move together and do not produce any net current. However, the ion-drag or ion neutral collisions tend to reduce the magnitude of drift term.

3.6 Diffusion

The plasma, like any other gas, diffuses under the action of gravity and of its own partial pressure gradients. The generation of polarisation electric field between the electrons and ions does not allow the particles to diffuse independently, therefore, both the species diffuse together which is known as 'ambipolar diffusion'. Diffusion proceeds rapidly in the upper thermosphere i.e. in the F-region heights. Therefore, above 250 km the transport terms become more significant than the production and the loss terms. While *Chapman and Cowling* [1952] gave the theory of diffusion in its mathematical details, *Rishbeth* [1969] derived the plasma diffusion velocity based on simple force balance equations. As per his derivation, the plasma diffusion velocity, in the absence of thermal diffusion is given by:

$$-V_D = D(h) \left[\frac{1}{N} \cdot \frac{\partial N}{\partial h} + \frac{1}{T} \cdot \frac{\partial T}{\partial h} + \frac{\mu}{H} \right] \sin^2 I \quad (3.4)$$

In this expression T is the neutral temperature, H is the scale height. The mean molecular weights of the plasma and the ionized gas becomes 1/2 if both are chemically the same. $D(h)$ is the diffusion coefficient at an altitude h . [*Shimazaki*, 1957; *Rishbeth and Baron*, 1960]. *Martyn's* [1956] derivation of diffusion velocity was based on a single particle diffusing through the surrounding gas undergoing collisions as it did so. Supposing that the mass of the particle is m_i , collision frequency is ν_i , the force causing the motion is gravitational i.e. $m_i g$ and the pressure gradient which is $-\frac{\partial P_i}{\partial h}$ where $P_i = P_e = NkT$ (k is the Boltzmann constant). The net force ' F ' is:

$$F = -m_i g - \frac{2kT}{N} \times \frac{\partial N}{\partial h} \quad (3.5)$$

and the drift velocity V_D should be $= \frac{F}{m_i \nu_i}$

$$V_D = -\left[\frac{g}{\nu_i} - \frac{2kT}{m_i \nu_i N} \frac{\partial N}{\partial h}\right] \quad (3.6)$$

If the magnetic dip angle is also taken into account, then

$$V_D = -\left[\frac{g}{\nu_i} - \frac{2kT}{m_i\nu_i N} \frac{\partial N}{\partial h}\right] \times \sin^2 I \quad (3.7)$$

$$V_D = -\left[1 + \frac{2H}{N} \frac{\partial N}{\partial h}\right] \frac{g}{\nu_i} \times \sin^2 I \quad (3.8)$$

Comparing equations(3.4) and (3.8) and neglecting the vertical temperature gradients, the 'diffusion coefficient' $D(h) = \frac{2gH}{\nu_i}$ and the diffusion velocity ' V_D ' at the height of maximum electron density in terms of diffusion coefficient becomes:

$$V_D = -\frac{D_m}{2H} \sin^2 I \quad (3.9)$$

3.6.1 Solar Heating Effects

Apart from the above stated transport processes, large scale phenomena which affect both the neutral air as well as the charged particles or the plasma, is the diurnal cycle of solar heating which causes expansion and contraction of the atmosphere. The changes in the thermospheric temperature affect the energetics of plasma and neutrals which in turn lead to changes in the height of the constant pressure levels. Apart from this, temperature dependent parameters like diffusion coefficient ' D ' and chemical recombination coefficient ' β ' can alter the net effect of transport with the variation of thermospheric temperature. It is quite clear from the above that the study of the F2-layer movement, under the influence of production, loss, diffusion and drifts is an important aspect in the investigation of the coupling mechanisms in the TIS.

The F2 peak is moved over to a new position (altitude) under the action of the above stated forces, thus, in turn affecting the very processes which caused the drift. However, the dip angle dependence of diffusion leads to a natural question-to what extent the servo model holds true for low and equatorial latitudes. Therefore, in order to study the low latitude TIS, it becomes

important not only to test the validity of servo model over these latitudes but also to investigate the very nature of different processes. Such an investigation is complex due to the presence of many large scale processes like the Equatorial Ionisation Anomaly (EIA) [Appleton 1946, Moffett, 1979], Neutral Anomaly [Hedin and Mayr, 1973], Equatorial Temperature and Wind Anomaly (ETWA) [Raghavarao *et al.* 1991], Equatorial spread-F [Fejer and Kelley, 1980] and Midnight Temperature Maximum (MTM) [Spencer *et al.* 1979]. Their contribution in terms of energy and dynamics to the TIS are largely unknown, especially the newly discovered ETWA which has a direct bearing. All the relevant low latitude processes have been comprehensively reviewed by Abdu[1997] and have already been dealt with in the introduction.

In the present investigation, we have dealt with both the validation and extension of servo model to low latitudes for different geophysical conditions and have attempted to quantify and incorporate the energetic changes due to ETWA in low latitude model representation of TIS. Chapter 5 deals with the second aspect in detail. The present chapter deals with the first aspect restricting to magnetically quiet, solar minimum periods. Coordinated measurements on thermospheric parameters namely temperature and wind are used in conjunction with the peak height of the F2-layer obtained from the ground based ionosonde, during nighttime. The Servo model, proposed by Rishbeth [1978], is used as a tool in a way similar to the one adopted by Gurubaran *et al.* [1993]. In the following section, a description of the servo model followed by its application to low latitudes in the context of the 'night stationary layer' i.e, the F-layer peak during nighttime is given.

3.7 The Servo Model

The continuity equation for ion or electron concentration (N) at the F2-peak is the basic servo equation, which has already been discussed in previous sections. The servo equation is of the form:

$$\frac{\partial N}{\partial t} = q - \beta N - \frac{1}{H} \frac{\partial(NV_z)}{\partial z} \quad (3.10)$$

Here the representation is in terms of reduced height ' z ' which is measured in terms of scale height ' H ' of neutral ionizable gas. The reference for the reduced height i.e., $z = 0$ is defined to be the altitude of the F2-peak at which it remains in the absence of applied drifts. It is also defined as the 'balance height'. The terms t , q , β , V_z used in the servo equation are time, production rate, loss coefficient and vertical upward plasma velocity respectively. The servo model [Rishbeth *et al.* 1978] obeys the following laws:

- (a) In the absence of any applied drift, the F2-peak lies at a 'balance height' determined by diffusion and loss.
- (b) Vertical drifts due to electric fields or neutral air winds displace the equilibrium position of the peak to a new level, which is time-varying if the drift is time-varying.
- (c) At any instant the actual height of the peak approaches its equilibrium value at a rate determined by diffusion and loss.
- (d) The rate of change of peak electron density is determined by local values of the production rate and loss coefficient.

The servo equation incorporates the fourth law (d) directly in equation(3.10) in the form of a continuity equation. Based on the above laws, the transport effects are assumed to arise only in vertical direction. For simplicity, any parameter associated with the F2-peak at any instant is denoted by using a suffix ' m ' with the notation. To estimate the time rate of change of plasma content

from the F2 peak i.e. from $z = z_m$ to $z = \infty$; the servo equation is integrated from $z = z_m$ to ∞ on both sides.

$$H \frac{\partial}{\partial t} \int_{z_m}^{\infty} N dz = H \int_{z_m}^{\infty} (q - \beta N) dz - \Phi_{\infty} + N_m V_{z_m} \quad (3.11)$$

Φ_{∞} corresponds to the plasma flux flowing outwards along the magnetic field lines at the top of the ionosphere (i.e. $z = \infty$). Accounting for the relative vertical velocity of the plasma and the peak. the above equation becomes:

$$H \frac{\partial}{\partial t} \int_{z_m}^{\infty} N dz = H \int_{z_m}^{\infty} (q - \beta N) dz - \Phi_{\infty} + N_m (V_{z_m} - H \frac{dz_m}{dt}) \quad (3.12)$$

However, equation(3.12), at altitudes much higher above the F2 layer peak, takes a simpler form as a limiting case if the following few assumptions about the F-region are made, which once again are based on the results from earlier experimental work. These assumptions are:

- (i) In order to treat the variation in ionisation to be associated with layer movements, it is assumed that the topside of the layer maintains a constant shape, such that the height - integrated ion content can be related directly to density at peak of the layer i.e., the ion-content is aHN_m , where ' a ' is the Chapman's layer shape factor ($a = 2.282$), ' H ' is the scale height and N_m the peak plasma density.
- (ii) The F2-peak is well above the production peak, so that

$$q \propto e^{-z} \quad (3.13)$$

- (iii) The dominant ion is O^+ which decays by reacting with N_2 and O_2 . Since N_2 density decreases exponentially with increasing altitude, the loss coefficient ' β ', which is dependent on molecular density, can be assumed to follow an exponential trend i.e., $\beta \propto e^{-\kappa z}$ where $\kappa (= 1.75)$ is a constant.

Under these assumptions, the equation(3.12) at F_2 heights becomes

$$aH \frac{dN_m}{dt} = q_m H - a' \beta_m N_m H - \Phi_\infty + N_m (V_{zm} - H \frac{dz_m}{dt}) \quad (3.14)$$

the constant a' , which arises from the weight integral of βN , can be approximated to κ in assumption (iii) above.

According to equation(3.14), the variation of ion content at greater heights depends on the vertical plasma velocity ' V_{zm} ' factor, apart from production and loss. To make the treatment simpler, the layer is assumed to be isothermal. ' V_{zm} ' as explained in the previous section, can be written alternatively as:

$$V_{zm} = W - \left(\frac{g}{\nu_m}\right) \sin^2 I = W - \left(\frac{D_m}{2H}\right) \sin^2 I \quad (3.15)$$

Here ' W ' represents the drifts caused by the thermospheric wind and electric field, while the second term is associated with gravity. ν with any suffix denotes the ion-neutral collision frequency. It is important to note that the diffusion coefficient ' D ' which has an inverse relation with collision frequency, varies as $D \propto e^z$. Substituting these terms in equation(3.14) and dividing by $N_m H$ and rearranging,

$$\frac{dz_m}{dt} = \frac{q_m - \Phi_\infty/H}{N_m} - \frac{a}{N_m} \left(\frac{\partial N_m}{\partial t}\right) - \frac{\beta_m}{\kappa} - \frac{D_m \sin^2 I}{2H^2} + \frac{W}{H} \quad (3.16)$$

Equation(3.16) incorporates the first three laws of the servo model. The term $\left(\frac{\partial N_m}{\partial t}\right)$ in the above equation could be accounted for through the continuity equation, i.e.

$$\frac{dN_m}{dt} = \left(\frac{\partial N}{\partial t} + \frac{\partial N}{\partial z} \frac{dz}{dt}\right)_{z_m} = q_m - \beta_m N_m - \frac{V_z}{H} \frac{\partial N}{\partial z} - \frac{N_m}{H} \frac{\partial V_z}{\partial z} \quad (3.17)$$

The treatment of this equation becomes deficient due to two factors. One is the lack of a term describing the height dependence of V_z . The other factor is the lack of knowledge about the flux exchange (Φ_∞) which is occurring on the topside of the F layer, which in turn has a significant effect on the ion-content. We do not have any explicit term representing these two factors in

the above equation. To overcome this difficulty, it was assumed that the flux (Φ_∞) is uniformly distributed over the 'equivalent thickness aH ' of the topside layer [Rishbeth, 1978]. Also assumed was that the transport processes, indirectly representing ($\frac{\partial V_z}{\partial z}$) at the peak, are related to the loss processes through an empirical constant ' c ' of order unity. These assumptions considerably simplify the above equation, which can now be written as:

$$\frac{dN_m}{dt} = q_m - c\beta_m N_m - \frac{\Phi}{aH} \quad (3.18)$$

The complete diffusion equations with their idealized solutions provided the value of c [Rishbeth, 1967]. However, the dependence of ' c ' on drift term ' W ' is ignored, which in fact would be appreciable only if the induced upward drift is very large. Replacing ($\frac{dN_m}{dt}$) in equation(3.16) by equation(3.18), we get

$$\frac{dz_m}{dt} = (1 - a)\frac{q_m}{N_m} + \frac{(\kappa ac - 1)}{\kappa}\beta_m - \frac{D_m \sin^2 I}{2H^2} + \frac{W}{H} \quad (3.19)$$

3.8 The Night Stationary Level

During nighttime, the production of ionisation ceases i.e., $q_m = 0$. If the drift ' W ' is also absent, then the layer would be balanced at a height called the 'Night stationary level'. Therefore, for night stationary level, the local values of various parameters represented in equation(3.19) are related by:

$$\beta_s = \frac{D_m \sin^2 I}{2H^2} \frac{\kappa}{(\kappa ac - 1)} \quad (3.20)$$

Subscript ' s ' represents the night stationary level. If the layer moves from this position under the influence of external drift, this level would in turn serve as the reference. In other words, if z_m is measured from this level, the servo equation governing the nighttime F-layer would become:

$$\frac{dz_m}{dt} = \frac{D_m \sin^2 I}{2H^2} [e^{-\kappa z_m} - e^{z_m}] + \frac{W}{H} \quad (3.21)$$

The exponential nature of D was made use of in obtaining the above equation. The above expression provides a physically simple picture of the F-layer behaviour and the effects of various perturbing forces on it. In fact, the servo model proved to be a very useful tool in the investigation of the motion of ions which is parallel and perpendicular to the magnetic field in a coupled system of plasma and neutral air. The imposed vertical velocity to the F2-layer by the thermospheric wind, diffusion and electric fields and the newly attained peak height are the servo feedback elements in the coupled system. It is important to mention here that apart from winds and electric fields, the local changes of neutral temperature would also cause changes in neutral composition, which in turn would alter the height where the peak ionization density of the F2 layer occurs.

Therefore, in the present investigation, the response of the F-layer is studied by using spectroscopically measured thermospheric temperatures and winds in conjunction with the servo model. The details are furnished in the following section.

3.9 The F-peak Position Vs. the Temperature, Winds and Electric Fields

As has already been mentioned in the earlier section, the change of neutral temperature causes variations in the altitude of the F2 peak through neutral composition, while, winds and electric fields cause changes by imposing an external drift. Any change in layer height which is to be studied using the servo model will be through changes in ' β ' and ' D ' parameters which are altitude, temperature and composition dependent. Further, the F-layer, during nighttime and in the absence of any production of ionisation, decays as per the following relation.

$$N_e = (N_e)_0 \exp(-\beta t) \quad (3.22)$$

$(N_e)_o$ being the ionisation at the time when production ceased, ' β ' is the effective recombination coefficient and t represents the time. The external forces can move this layer to very large heights where ' β ' becomes very small thereby retaining the plasma from further decay. This would sustain the layer for a long time during the night even in absence of further production of ionisation [Hanson and Patterson, 1964].

Therefore, the dependence of the layer height on temperature can be investigated by studying the variation of β and D with altitude. In the present investigation an iterative method is used for this purpose. In this approach, an initial reference height of 200 km is assumed, and the deviations between ' β ' and ' D ' are minimized for each iterative increase of height from the initial height of 200 km. Servo relation between ' β ' and ' D ' for the night stationary layer is worked out at each stage. This method was successfully used, earlier, by Yagi and Dyson, [1985], Miller et al. [1989] and Gurubaran and Sridharan [1993]. The following expressions were used for evaluating ' β ' and ' D ' to determine the 'night stationary height' of the F2-peak.

$$\beta = 10^{-18} [N_2] \quad (\text{sec}^{-1}) \quad (3.23)$$

$$N_2 = 3.22 \times 10^{15} \exp\left[-k \frac{(h_s - 200)}{H}\right] \quad (\text{m}^{-3}) \quad (3.24)$$

and for diffusion coefficient:

$$D = \frac{2gH}{\nu} \quad (\text{m}^2\text{s}^{-1}) \quad (3.25)$$

$$\nu = 7.3 \times \left(\frac{T_\infty}{1000}\right)^{1/2} [O] \quad (\text{s}^{-1}) \quad (3.26)$$

$$[O] = 4.07 \times 10^{15} \exp\left[-\frac{(h_s - 200)}{H}\right] \quad (\text{m}^{-3}) \quad (3.27)$$

$$H = \frac{0.93T}{M} \quad (3.28)$$

These empirical relations are based on the earlier work of Dalgarno et al. [1964], Banks and Kockarts [1973], Rishbeth et al. [1978], and Yagi and Dyson, [1985].

Substituting the above values in equation(3.20) and simplifying one gets,

$$h_s = 200 \times 10^3 + 21.23 T_n [1.5 \ln T_n - \ln \sin^2 I - 4.85] \quad (3.29)$$

The dependence of h_s i.e. the night stationary layer on the dip angle ' I ' clearly illustrates the increasing importance of T_n to h_s changes as the dip angle decreases, i.e., over low and equatorial latitudes. A change in h_s of ~ 25 km is envisaged for a 100 K change in neutral temperature at around $I = 5^\circ$. The decreasing influence of diffusion with dip might account for such a rise in the F-layer height but the very validity of servo principle would be questioned at very low and equatorial latitudes. Further, such large drifts would cause changes in layer shape too invalidating some of the basic assumptions of the servo model. As a result, equation(3.20), which is based on the assumption of constant layer shape, might not represent the actual balance height. However, the validity of the servo-model at mid latitudes is proven beyond doubts. The prediction of servo model was found to be agreeing well with the night-time behaviour of the F layer in response to temperature and winds [Yagi and Dyson, 1985]. They found that the 'night stationary level' changed by (13 ± 6) km per 100 K change in temperature. They have made use of coordinated measurements of temperatures and winds using high resolution Fabry-Perot spectrometer and base height and density from ground based ionosondes located at Canberra ($35.4^\circ S, 149.2^\circ E$) and Hobart ($42.9^\circ S, 147.2^\circ E$), respectively in Australia. According to Yagi and Dyson (1985), almost 60% of the variation in the F-layer height can be accounted for by the variation in neutral temperature.

On the other hand, Sridharan *et al.* [1991] provided the first experimental proof for the applicability of servo principles over low latitudes. Coordinated measurements of thermospheric temperature and meridional winds obtained from a low latitude station Mt.Abu ($24.6^\circ N, 72.7^\circ E$ geographic, $20.3^\circ N$ dip lat.)

and ionospheric parameters such as layer height deduced from ground based ionosonde at Ahmedabad ($23^{\circ}N$, $72.1^{\circ}E$ geographic, 18.4° dip lat.) were made used of in the above study.

It is important to delineate the actual movement from the apparent movement of the layer which, during postsunset times, would be seen in the case of faster plasma neutralization in the base of F-region due to the recombination processes. After accounting for the recombination effects, *Sridharan et al.* [1991] and *Gurubaran* [1993] dealt with a number of cases from Mt. Abu and studied the temporal evolution of the base height of F-region for the nights along with measured thermospheric temperature (T_n). They showed that for Mt. Abu the F-layer undergoes an altitude change of 11 ± 4 km per 100 K change of temperature. However, the effects of electric fields were not taken into account in the above study while estimating the peak height of F-layer. Nevertheless, this study ascertained the role of neutral temperature in the dynamics of F-region in the context of the servo model. The action of external forcings such as winds and electric fields on the F-region was brought out and discussed by them in a later exercise in the following manner. For smaller magnitude of wind and electric field, it had been shown that the changes in wind speed and the corresponding changes in layer heights exhibit a linear dependence [*Rishbeth and Baron, 1960; Rishbeth, 1966; Buonsanto et al. 1989*]. Taking the servo equation for 'night stationary layer' and writing it in terms of real height (h) instead of reduced height z . The equation for vertical drift velocity becomes:

$$\frac{dh_m}{dt} = \frac{D_m \sin^2 I}{2H} \left\{ \exp\left[-k \frac{(h_m - h_0)}{H}\right] - \exp\left[-\frac{(h_m - h_0)}{H}\right] \right\} + W \quad (3.30)$$

' W ' denotes the drift because of wind and electric field. Taking a cue from *Buonsanto et al* [1989] that the effects of the time rate of change of layer height and also the exponential terms in most of the F-region conditions are small, the

above expression can be rewritten as:

$$W = \frac{(k+1)}{2H^2} D_m \sin^2 I (h_m - h_0) \quad (3.31)$$

In other words, 'W' which is a combination of vertical drift due to meridional wind up and east-west electric field E_E , can be written as:

$$W = -U_p \cos I \sin I + \frac{E_E}{B} \cos I \quad (3.32)$$

equating equation(3.29) and (3.30) we obtain the layer displacement

$$h_0 - h_m = \alpha \left[U_p - \frac{E_E}{B \sin I} \right] \quad (3.33)$$

$$\alpha = \frac{2H^2 \cos I}{(k+1)D_m \sin I} \quad (3.34)$$

Equation (3.33) yields the extent of changes in the F-layer altitude as the wind and electric field changes their magnitude or direction; and it takes a relatively simplistic form if the electric fields are small.

$$h_0 - h_m = \alpha U_p \quad (3.35)$$

The upward drift of the layer due to equatorward winds is opposed by the increased downward diffusion thus limiting it from continuously moving up and the downward drift of the F-layer due to poleward winds is restricted due to the enhanced recombination in the base of the F-layer which stops its further downward movement, thereby leaving it to approach an equilibrium level depending on whichever i.e. diffusion or the recombination time scale is shorter than the time rate of variations in the drift [Forbes and Roble, 1990]. The meridional wind component along the magnetic field line would push the layer height h_o to a new height h_m , which can be estimated using equation(3.30) and (3.33) if the parameters T_n and U_p are available, and also the E_E . Thus estimated heights are compared with the independently observed peak heights from ground based ionosonde. Gurubaran and Sridharan [1993]

while discussing the applicability of servo model to low latitudes (Mt.Abu) using the experimentally observed thermospheric parameters adopted the above approach. Their results represent a fairly good agreement between the observed and estimated h_{max} indicating towards the strong coupling between the thermosphere and the ionosphere. From the small differences, between the servo model-estimated h_{max} and the independent measurements on several occasions, *Gurubaran and Sridharan (1993)* were able to make a first order estimate of the electric fields also.

Apart from this, few more studies have been reported in the literature bringing out the different aspects of these forcings on the F-region [*Rishbeth and Barron, 1960, Rishbeth, 1978; Forbes and Roble, 1990; Buonsanto,1990; Abdu 1997* and the references cited therein]. In these studies the independent nature of thermospheric and ionospheric parameters was stressed upon and useful relationships have been obtained and reported in the literature [*Miller et al. 1986, 1987; Buonsanto et al. 1989; Krishnamurthy et al. 1990*]. In this chapter we present the behaviour of the system during magnetically quiet geophysical conditions and low solar activity with special emphasis given to the temporal variabilities of temperatures and winds, before proceeding to investigate magnetically disturbed periods in the later chapters. It is well known that the measured temperatures (spectroscopically and otherwise) show significant deviations from the models eg. the MSIS model on several occasions. Also, it is well appreciated that most of the models are initially designed to yield only the climatological rather than bringing out shorter term variabilities. Keeping this limitation in mind the measurements are compared with the MSISE-90 model and representative results for a few days are presented below.

3.10 Variations of Thermospheric Parameters over Mt.Abu

In this section, we deal with the variations shown by thermospheric nighttime temperatures and corresponding meridional winds. The measured thermospheric temperatures and winds for a few days, are shown in figure(3.3) to figure(3.6). Each figure consists of two panels. The top panel depicts the variation of measured temperature as a function of time, the lower panel shows the corresponding variations in the meridional wind. The value of the magnetic index ' A_p ' representing the average geomagnetic condition of that day is also given at the top of the panels. A comparison of the measured temperatures with MSIS model predictions is also shown in the top panel.

The definition of a quiet day for the present study is based not just on the value of the average planetary magnetic index A_p for the day, but also on another important index ' D_{st} ' which is a low latitude ring current index. Since, the ring current plays an important role in the low latitude energetics as would become clearer in the later chapters, the ' D_{st} ' which represents largely the classical ring current system is given special importance in the present investigation. Therefore, we have based our definition of a quiet day on the trend of variation of ' D_{st} ' rather than the corresponding A_p index. If the ' D_{st} ' is closer to zero or remains steady for an extended period of time then, the day is taken to be representative of geomagnetically quiet day. The sample days meeting the above requirement and included in the present study are 14th December '93.

December 14th, 1993 is a very good example of a quiet day with daily average A_p index of 4 and average D_{st} value near -3nT. The relevant A_p and the D_{st} variations for December month are shown in the figure(3.7). As is clear from this figure, the daily average index A_p decreased sharply to a value ~ 4 immediately after from a maximum of ~ 47 on Dec. 8th. The corresponding D_{st} index also came close to zero

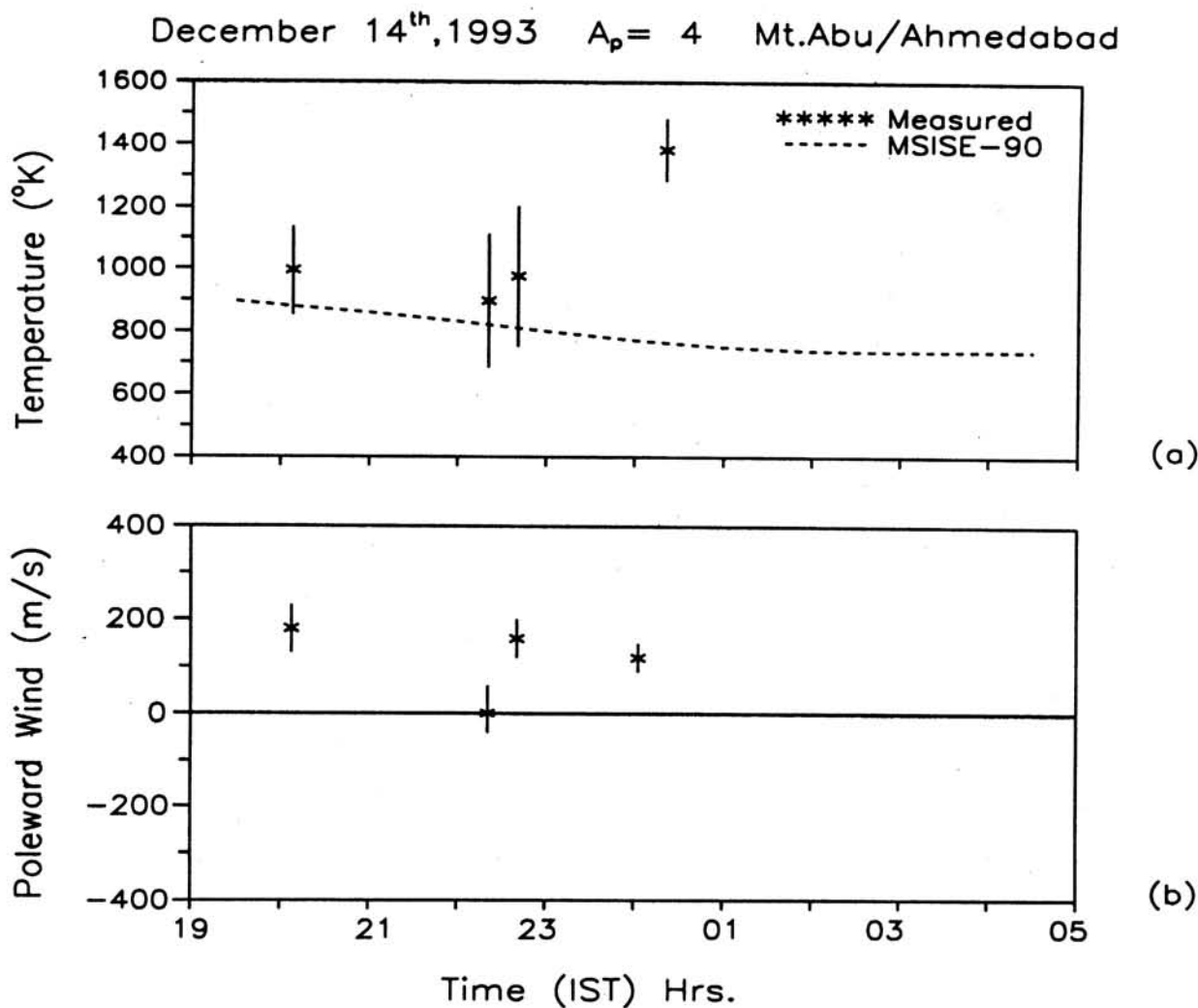


Figure 3.3: The measured thermospheric temperatures and winds on 14th Dec. 1993

on this day. Dec. 14th happens to be the quietest day after Nov. 29th and during the whole Dec.'93 period. As seen in the figure(3.3a), the F-region of thermosphere on this night seemed to be at a temperature of $\sim 1000\text{K}$ as measured at $\sim 2000\text{hrs}$ and later at $\sim 2230\text{hrs}$. There were no temperature measurements in the time span of 2000-2330hrs due to the extremely low airglow intensities. The temperature showed a marked increase by almost 400K at midnight. The simultaneously measured neutral wind figure(3.3b) revealed it to be poleward in the early hours around 2000hrs, became close to zero at around 2230hrs, whereas the average poleward wind magnitude was quite significant $\sim 175\text{m/s}$. The wind vector on this night which is predominantly poleward indicated towards the contribution of diurnal heating over low latitudes to be more in comparison to the energy input

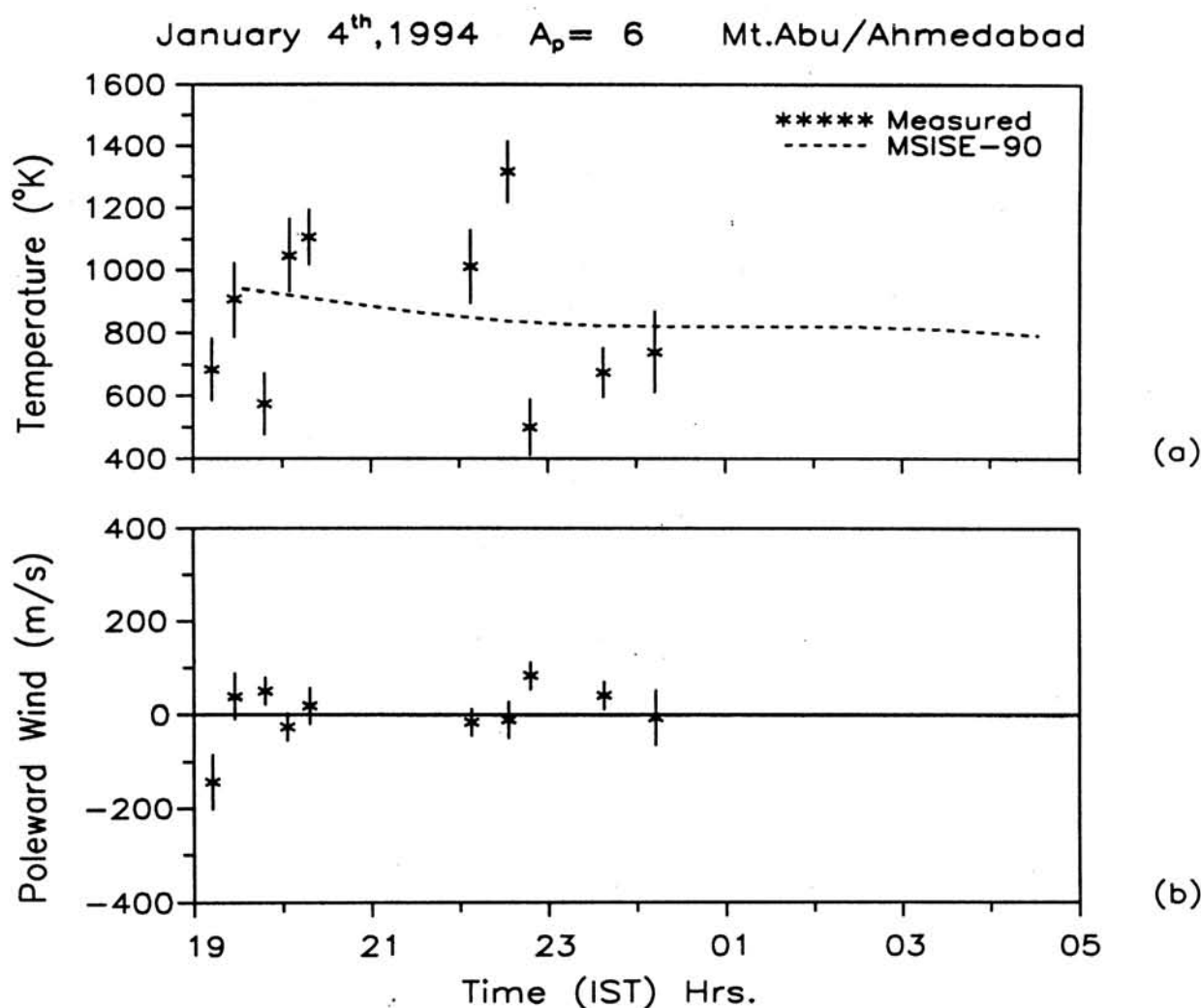


Figure 3.4: The measured thermospheric temperatures and winds on 4th Jan. 1994

over the poles. At the same time, the seasonal dependence of the wind structure would also get reflected in the wind variation in the present case. For instance, the hemispheric asymmetry in solar energy distribution during any particular season would cause a small transequatorial flow across the equator at thermospheric heights. At Mt. Abu, during winter months, the equatorward flow of the wind can be reduced by the opposite transequatorial flow.

Another interesting day was Jan. 4th 1994 (figure 3.4). The A_p on this day was 6 and average ' D_{st} ' around -20nT. The daily average A_p index alongwith the D_{st} variations for Jan'94 are depicted in figure(3.8). The observed thermospheric temperatures exhibit large fluctuations by varying between ~ 500 K to ~ 1300 K as can be seen in the figure. The temperature in the early evening hours i.e. ~ 1930 hrs

hours i.e. ~ 1930 hrs was around ~ 600 K followed by a slow increase. The temperature seemed to have reached a maximum of ~ 1300 K at ~ 2230 hrs followed by a downward trend with an indication of asymptotically reaching towards the model value at around 0000 hrs. Earlier studies from Mt.Abu had also reported considerable variation in the thermospheric temperatures over a night [Gurubaran 1993] on several occasions. In the present case, the overall temperature modulation has been to the tune of ~ 800 K from nearly 500 K at 1900 hrs to 1300 K at 2230 hrs.

During low solar activity and geomagnetically quiet periods, the temperature variations of this magnitude cannot be attributed to the changes in the solar flux alone. This is evident from the deviations exhibited by the measured temperatures from the MSIS model predictions figure(3.4a). The model presents the average atmospheric conditions estimated on the basis of solar flux and magnetic activity changes. Therefore, the variabilities observed in thermospheric temperatures in terms of both time and magnitude during low solar activity period had remained rather unexplained. As depicted in the figure(3.4b), the meridional wind structure on this night, seem to have undergone a periodic change from poleward to equatorwards and vice versa with their respective magnitude remaining low. The meridional wind vector exhibits a strong equatorward wind ~ 150 m/s during early evening hours (~ 1930 hrs.), which very soon changed over to a weak poleward flow (~ 50 m/s). The wind maintained both the direction and magnitude for nearly one and half hour, to become equatorward again at 2030 hrs. No wind and temperature data were available for the time interval $2030-2200$ hrs and beyond midnight. At 2200 hrs, the equatorward wind once again changed its direction turning into a weak poleward flow only to turn equatorward at around midnight 0000

hrs. Apart from the wind at 1930hrs and irrespective of the direction of meridional flow, the wind magnitudes remained small unlike on Dec. 14th. The large equatorward wind (~ 150 m/s) at a 1950hrs, however, corroborates with the corresponding ionospheric variations, and these would be discussed in the next section.

Jan. 5th was yet another quiet day. The average planetary index A_p for this day was 4 and the average 'D_{st}' index lied at -11nT. The observed thermospheric temperature on this night also exhibited significant variations [figure(3.5a)].
Except

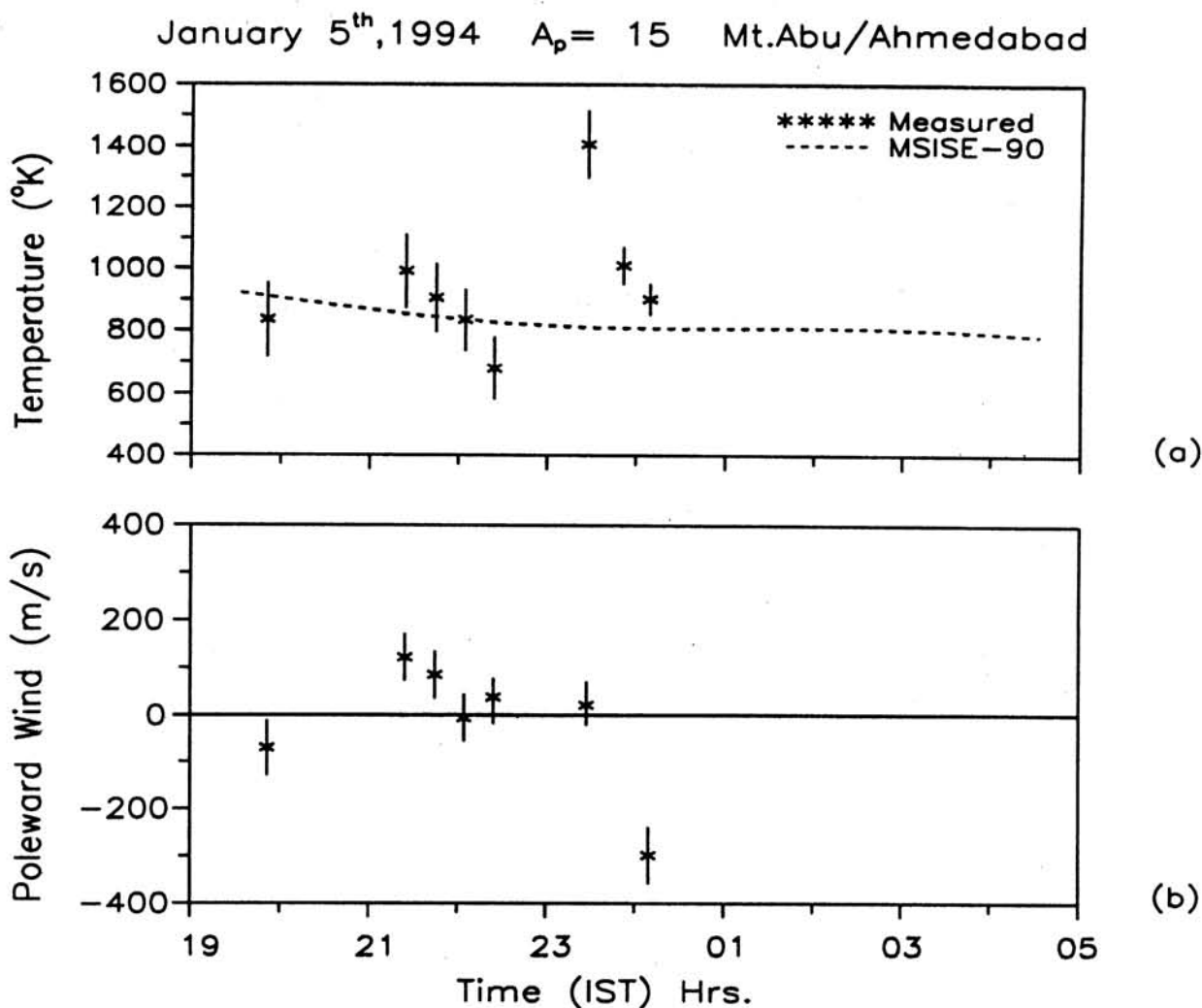


Figure 3.5: The measured thermospheric temperatures and winds on 5th Jan. 1994

for the high temperature at 2330hrs, the overall temperature variation was in the range of $\sim 700K$ to $\sim 1000K$. As is obvious from the figure(3.5a), the measured temperatures were close to model predictions. Unlike Jan.4th, the observed temperature structure on this night was devoid of large temporal variabilities. The simultaneously measured neutral wind on this night [figure(3.5b)], like Jan. 4th, also showed an initial equatorward flow i.e. at 2000 hrs., which gradually became poleward 100 m/s at 2130 hrs and reverted back to equatorward again at 2330hrs. The equatorward component of neutral wind at 0000hrs was quite large $\sim 300m/s$. Such winds can be generated only by the presence of active energetic sources sufficiently away from low latitudes which is more common during geomagnetic storms.

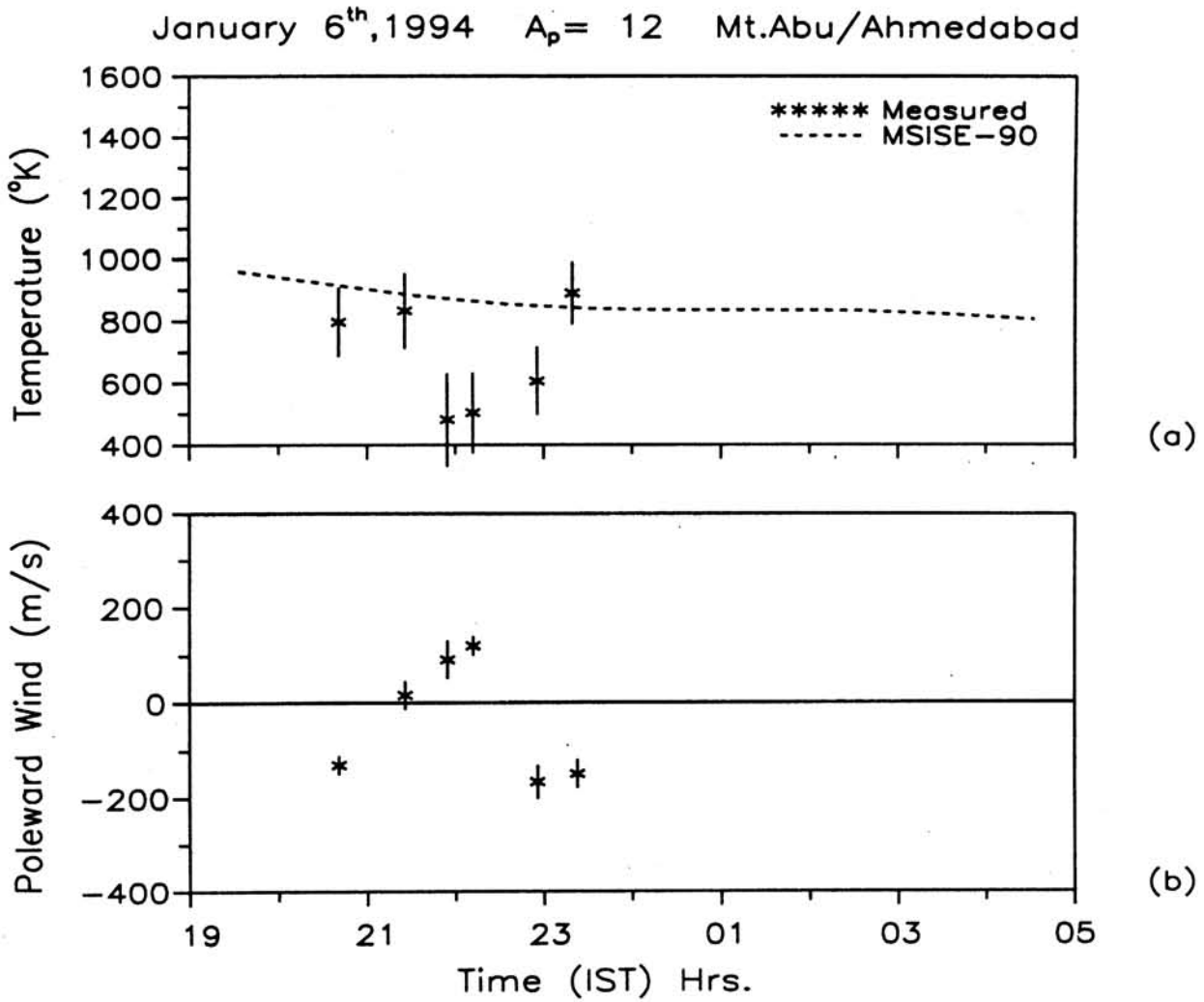


Figure 3.6: The measured thermospheric temperatures and winds on 6th Jan. 1994

The existence of such strong winds during quiet periods like the one under discussion can be validated on the basis of corresponding ionospheric variations which indeed confirms the presence of such large magnitude wind.

Jan.6th, another sample day was comparatively less quiet than the rest of the days, as was evident from the corresponding A_p value [figure(3.8)]. A_p value was 12 and the D_{st} underwent a sudden fluctuation on this day. The D_{st} became positive ($\sim 10nT$) on 6th for a brief period of time from where it steadily went down to $\sim -30nT$ in around 12hrs. Contrary to the other days, the observed neutral temperatures on this day were relatively lower. It is clearly seen in the figure(3.6a) that the temperatures, though remained low $\leq 900K$, showed the presence of a wavelike modulation. The temperature was lowered to $\sim 500K$ at ~ 2200 hrs under

to $\sim 500K$ at ~ 2200 hrs under the effect of this wavelike modulation. The observed meridional wind pattern is typical to that of Jan. 5th. It can be seen in the figure(3.6b), that the meridional flow was equatorward in the early evening hours i.e. ~ 2000 hrs, changed to poleward at around ~ 2130 hrs and remained poleward for next one hour and became equatorward again at 2300hrs. The velocity of equatorward flow is comparatively large i.e. ~ 200 m/s than the corresponding poleward flow ~ 100 m/s. Unlike previous days, the equatorward wind velocity was quite significant on this night. This day being geomagnetically more active, can have stronger energy sources over high latitudes. Since, the D_{st} exhibited a sudden change, there can be an associated change in the relative strength of the other magnetospheric currents which close in the polar ionosphere. This in turn, would appear as the variation in the overall joule heating rate at polar latitudes. The increased joule heating rates can cause enhancements in the equatorward velocity of the meridional winds. At the same time, the observed lowering of the thermospheric temperature on this night seems to be due to the presence of gravity waves in the thermosphere. The presence of such waves indeed gets confirmed on the basis of observed airglow intensity variations. Corresponding results and discussion are provided in the following text.

So far, examples were presented on the neutral thermospheric conditions during geomagnetically quiet and low solar activity periods. The important result of the above study is that the night time measurements, all selected for such conditions, show a considerable variation in the thermospheric temperatures, but a relatively smaller variation in the meridional winds. It is also seen that the measured temperatures do not agree with MSIS model predicted temperatures. However, to study the ionosphere-thermosphere interactions and the extent of coupling between the two, both need to be studied together. In

the present investigation, the observed thermospheric temperatures and winds were used to estimate the height of the peak of F-layer of ionisation i.e. h_{max} by means of Rishbeth's servo model. Initially, the height is estimated considering only the observed thermospheric temperature and the variation due to winds are later added on to this height. To estimate the altitude of the F-layer ionisation peak, following sequence of operations were followed. At first, using the observed thermospheric temperature as the

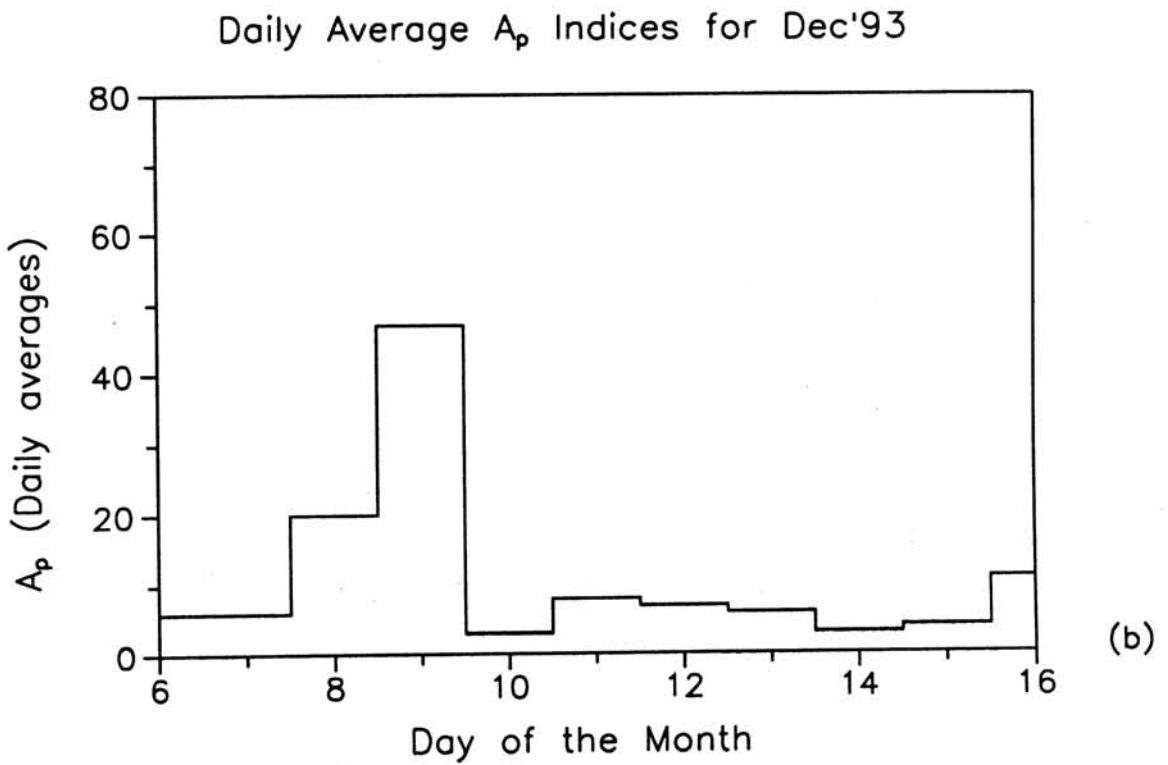
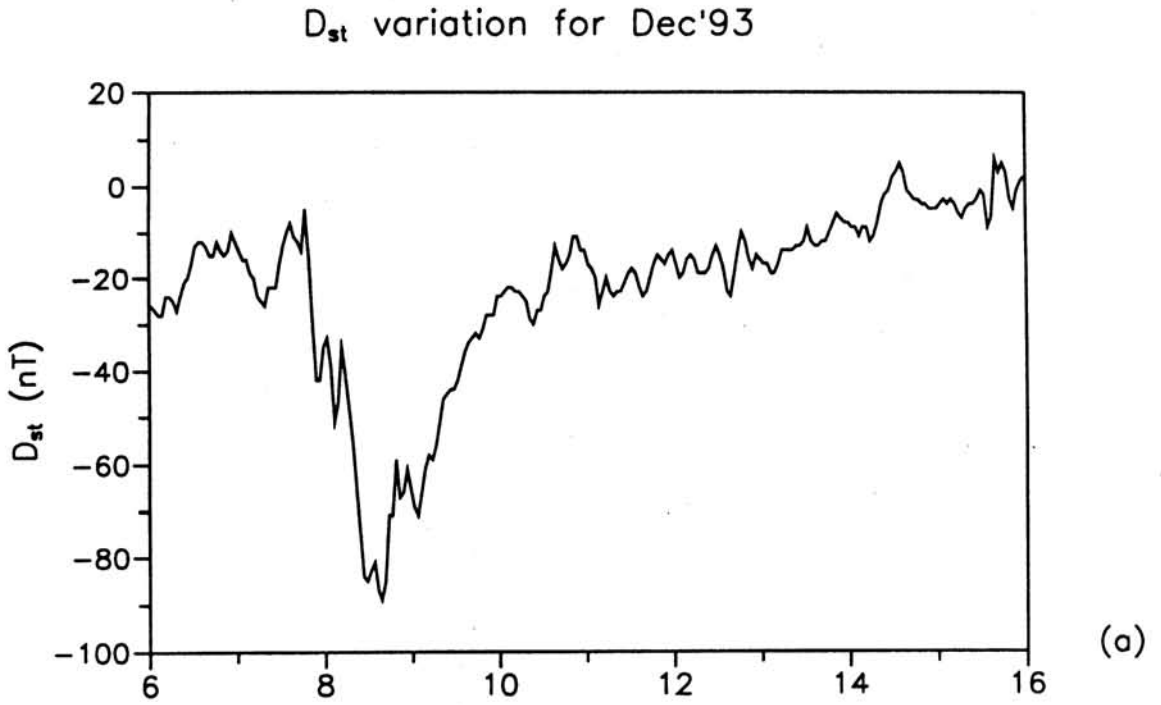


Figure 3.7: The variation of D_{st} and A_p for December 1993

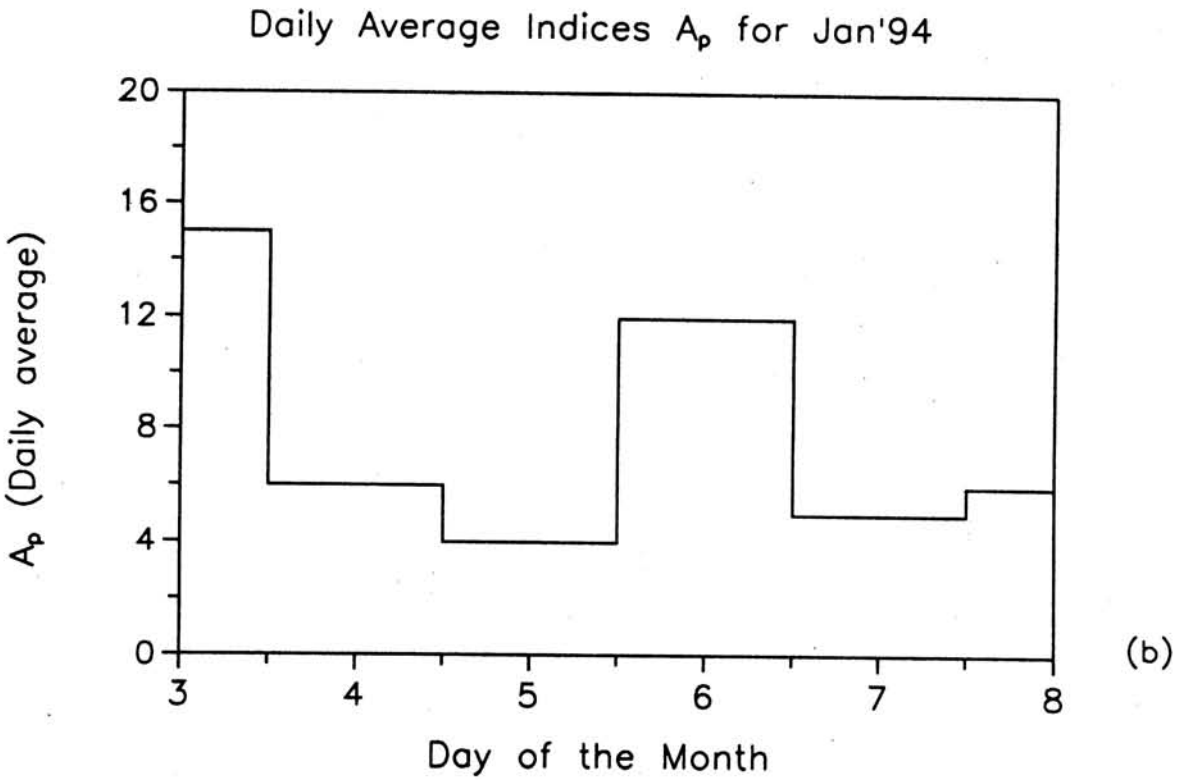
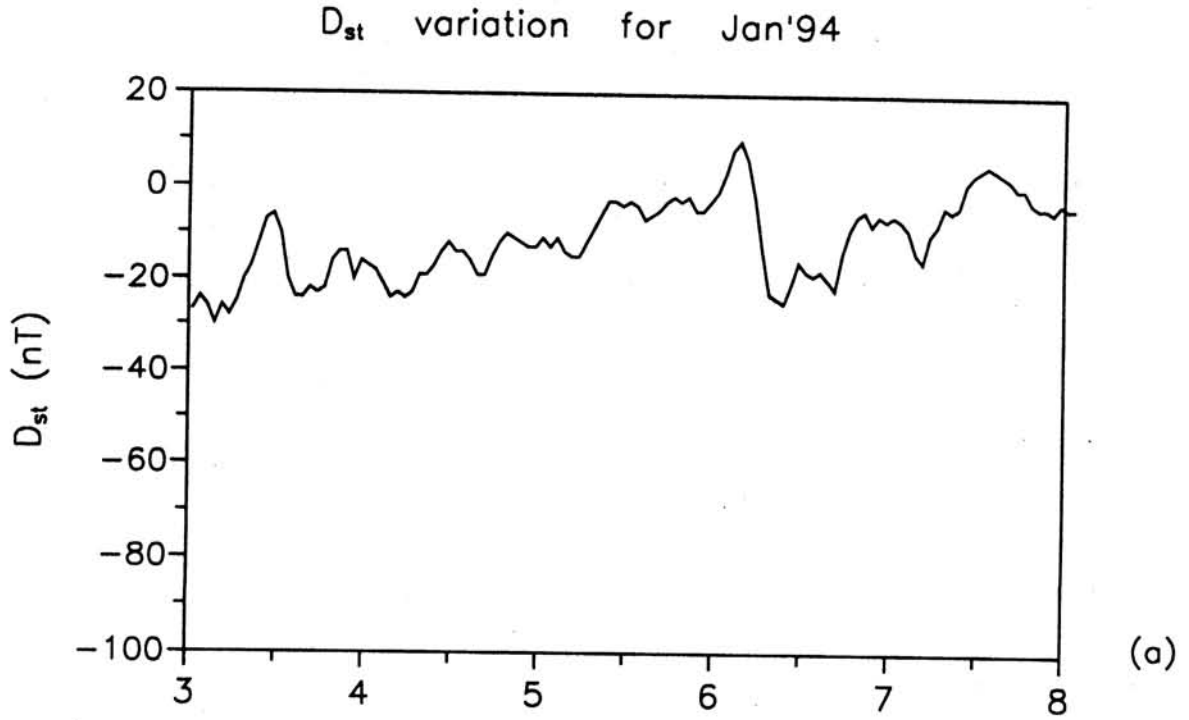


Figure 3.8: The variation of D_{st} and A_p for December 1993

input to the MSIS model, corresponding exospheric temperature and the composition is estimated. Thus estimated composition is used to find the initial values of the diffusion coefficient D and the loss coefficient β . An initial height of 200km is assumed to begin with. The deviations between the D and β are worked out for this height using Servo expression, and an iteration is started incrementing the height by 1km each step. The deviations between the two are worked out every time, till the deviation becomes minimum and the height converges to the altitude where the servo balance of the F-layer occurs. The effects of F-region electric fields were not considered in this analysis.

The following section deals with the behaviour of the low latitude TIS the same four days as representing the low solar activity magnetically quiet periods..

3.11 The Low Latitude Thermosphere Ionosphere System

All the parameters used in the present study are depicted in the figures(3.9) to figure(3.12). The top two panels in each figure depicts the observed thermospheric temperature and wind for given geomagnetic condition of that day and had already been presented and discussed but are repeated here for the sake of completeness.

The third panel (3.9c) depicts the airglow intensity alongwith the electron density at 250km and it clearly shows that the observed electron density remained nearly constant in the premidnight hours during 1900hrs to 2230hrs. Only minor fluctuations in densities were seen in that period. At 2230hrs the density started decreasing, reaching a minimum at around 2330hrs. It increased monotonically afterwards attaining almost the premidnight level of ionisation at \sim 0330hrs in the morning. This slow variation of existing ionisation density is clearly reflected in observed airglow (6300\AA) intensity. During nighttimes, the airglow intensity depends upon the existing F-region electron density, which

in the absence of any further production, decays exponentially. The observed airglow intensity variations followed the ongoing changes in electron density. The observed F-layer of ionisation [figure(3.9d)] remained at around same altitude ($260 \pm 50\text{km}$) during 1900hrs

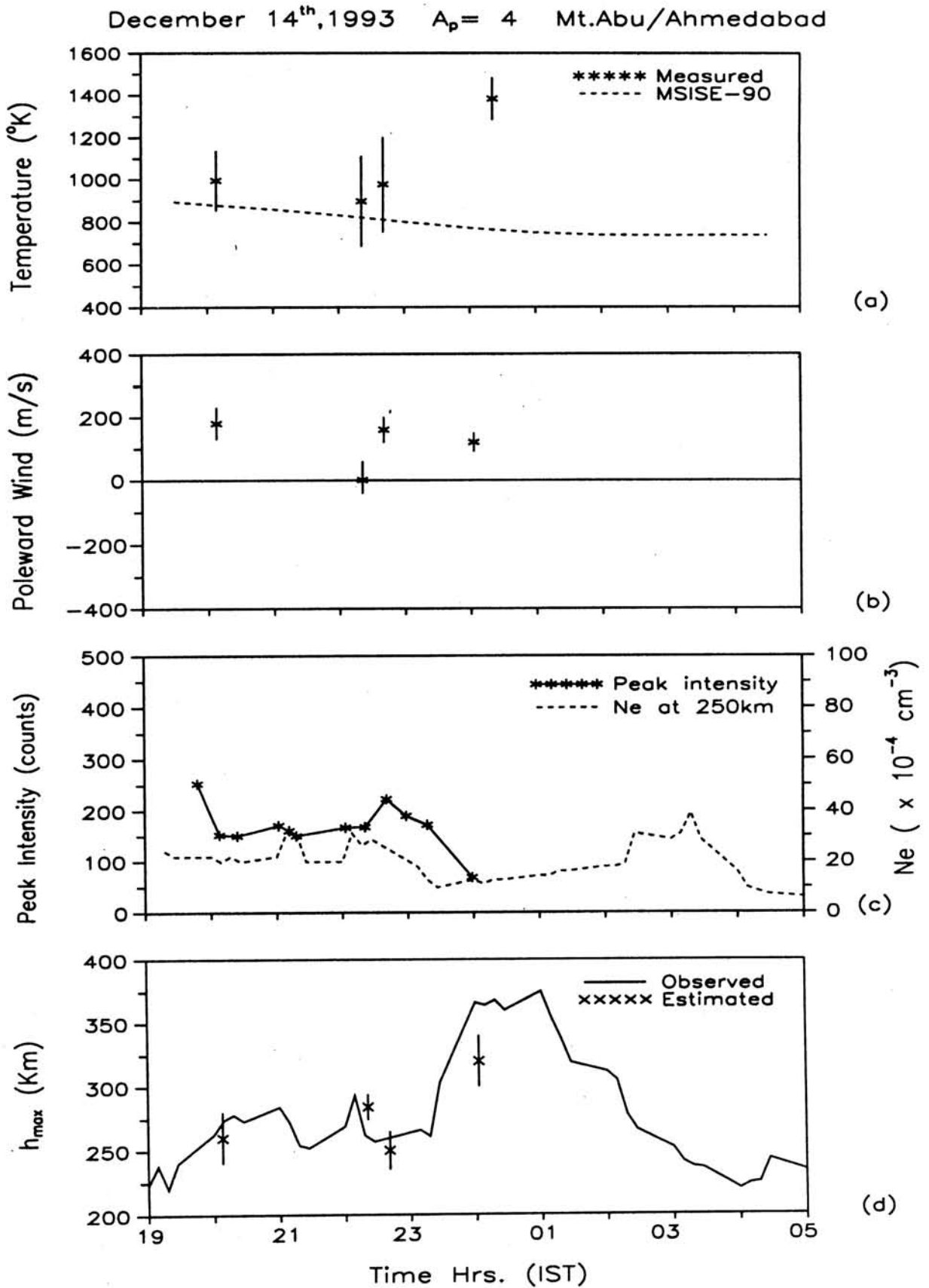


Figure 3.10: The thermosphere ionosphere system (TIS) behaviour on 14th Dec. 1993

and 2330hrs, after that an increase in the F-layer peak altitude followed. The layer attained a new equilibrium height at $\sim 370km$ changing from 260km within half an hour. The peak of F-layer remained at that altitude till 0100hrs, afterwards decreasing to 225km at 0400hrs. Once the F-layer gets lifted up beyond 350 km there would be a steep depletion in the plasma densities causing very low level airglow intensities. Hence no useful data could be retrieved beyond 2330 hrs.

During nighttime, at heights above and around 250 km, the life time of ionisation is quite large (in hours), therefore the height and density of F-region is controlled largely by the thermospheric dynamics i.e. due to wind and temperature. Figure(3.9d) shows the comparison of ionosonde observed h_{max} altitude, alongwith the servo model estimated peak heights. The agreement between the two is very good, inspite of the electrodynamic forcing not being taken into account. The close agreement also points out that the low latitude electric field induced motion to F-layer is relatively insignificant on this occasion. However, at times the reported strength of electric fields over low latitudes is quite significant [Woodman, 1970; Namboothiri et al. 1989]. In the present study, the contribution of electric fields in altering the layer equilibrium height can be indirectly inferred by comparing the observed h_{max} with the servo model estimated heights. For instance, the difference between the estimated and observed h_{max} at 0000hrs can be due to the electric field induced variations which are not accounted for in our formulation as stated earlier.

In the absence of simultaneous electric field measurements, it is difficult to differentiate between the relative contribution to the observed h_{max} altitude by electrodynamic and neutral dynamical processes. However, at any given

time, the ionic motion can be set by the low-latitude east-west electric field arising mainly from the global ionospheric wind dynamo and also from the magnetospheric dynamo which becomes active primarily during geomagnetically disturbed times [Richmond, 1995]. Apart from this, the low latitude ionosphere - thermosphere is also replete with many large scale local processes which can play a partial role in inducing vertical motions to the ionisation layer. Since, the present study concerns quiettime low solar activity epoch, the effects of such large scale local processes and magnetospheric dynamo induced electric fields are assumed as minimal and negligible and therefore the coupling between the F-region and the thermosphere could be considered to have been brought out in terms of h_{max} altitude variations on this night.

On Jan 4th, the night stationary layer (h_{max}) lied at a very high altitude ~ 350 km at ~ 1930 hrs (figure(3.10d)), coinciding with the phase when meridional wind showed strong equatorward velocity (~ 150 m/s) (figure(3.10b)). Later, the layer experienced a downward movement which became steady after it reached an altitude of ~ 275 km for an extended period of time i.e., till 0100 hrs. The h_{max} showed a sudden upward excursion at 0100 hrs, reaching ~ 400 km in just about 0.5 hrs. The phase where h_{max} remained more or less at the same altitude, the wind magnitudes were also quite small irrespective of the direction. The initial high altitude i.e. at 1930hrs of night stationary layer can be attributed to the large meridional wind existed at that time. At the same time, the post-sunset enhancement of vertical drifts because of enhanced zonal electric field due to F-region dynamo can also cause such a rise in h_{max} height. The generation of such fields involves significant gradients of the conductivities (east-west), currents and fields. A brief overview of the various electro-dynamical processes responsible for equatorial electrical field presented in the introduction, has been comprehensively dealt by Richmond *et al.* [1995]; Fejer

[1997]; *Abdu* [1997]. Therefore, the early evening rise of the F-layer as illustrated in figure(3.10d) is believed to be a result of both the meridional winds and the electric fields in the low latitude thermosphere/ionosphere system.

The existence of such winds and the temperatures over Mt.Abu is indeed confirmed when h_{max} on the basis of these were estimated and compared with observed h_{max} altitude. A remarkably good agreement between the two was found on this day. As seen in the figure(3.10c) the observed airglow intensity shows a slow monotonic decrease with time on this night. This variation in airglow intensity corroborated reasonably well with corresponding peak electron density variations highlighting the role of F-region recombination chemistry. The dominant role of neutral temperature and wind in the low latitude TIS coupling is further established by the observations on Jan 5th and 6th. The airglow intensity during both of these nights were significantly larger than the other days. On Jan 5th the

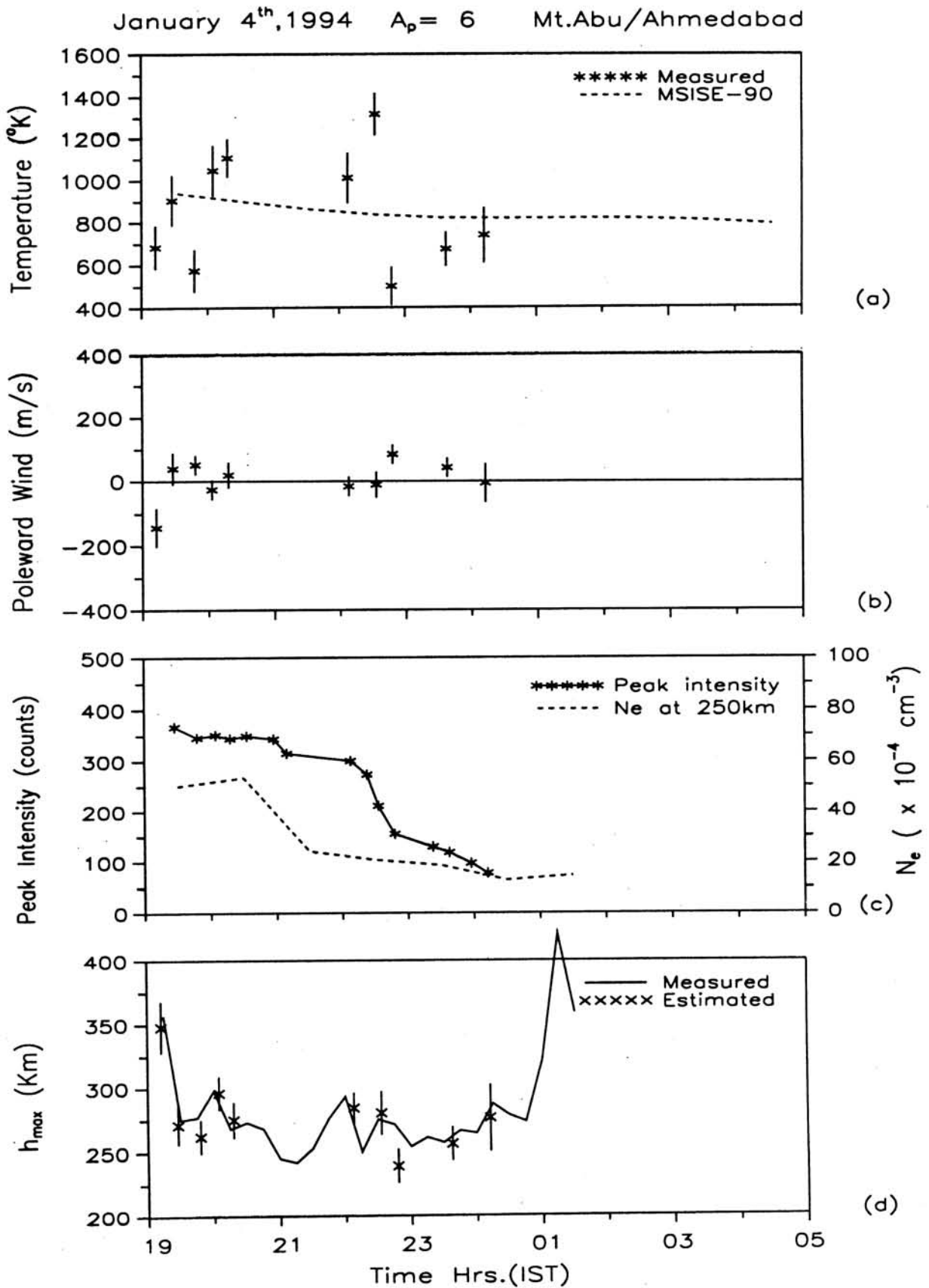


Figure 3.10: The thermosphere ionosphere system (TIS) behaviour on 4th Jan. 1994

airglow intensity variations followed the changes in electron density at ~ 250 km [figure (3.11c)]. The observed h_{max} displayed fast temporal changes in the peak altitude on this night [figure(3.11d)]. These changes occurred in the altitude range of 280 ± 50 km till 2330hrs. The large equatorward meridional wind component, at 2330 was concurrent with the excursion phase of h_{max} to higher altitude. The servo model predicted h_{max} heights at Mt. Abu [figure(3.11d)] were in good agreement with the observed h_{max} except at ~ 2130 hrs and ~ 2330 hrs. Both of these occasions, happened to be when the h_{max} experienced a sudden change in altitude. These faster variations could be due to dynamical changes like propagation of waves within the layer, which otherwise are assumed to be minimum in the servo model formulation or of electrodynamical origin.

Similar fast temporal changes with periodicities ~ 40 min. were also recorded in the altitude of the nighttime F-layer peak on Jan 6th (3.12d). Apart from these short period fluctuations, the h_{max} remained stationary at the same altitude till 2200hrs. After 2200hrs, h_{max} experienced an excursion upto an altitude of ~ 370 km. This upward excursion was followed by a slow decrease in altitude till 0300hrs with superposed oscillatory features. These variations in h_{max} were explained by the meridional wind flows. Significant differences between the observed and servo model estimated F-layer heights were seen at three occasions on this night i.e. at around 2000hrs, 2215hrs and 2330hrs presumably due to the unaccounted dynamical parameters. The agreement between the two was very good for rest of the times. The observed airglow intensity on this night also showed an anomalous feature. As in the figure(3.12c), the airglow intensity before 2130hrs, follows the F-region peak electron density variation i.e. both experience a decrease with time. The h_{max} remained at an altitude of ~ 250 km during that time. After 2130hrs, the airglow intensity got enhanced

and remained so, for the next one hour while the electron density at ~ 250 km continued to decrease with the same rate. Also associated, is a simultaneous rise in h_{max} altitude from 200km to 400km and a strong equatorward wind. The airglow intensity corroborated well with the electron density at 250km before 2130hrs and after 2215hrs. There was a steady increase in airglow intensity between 2100-2215hrs, electron density showed a decrease. This

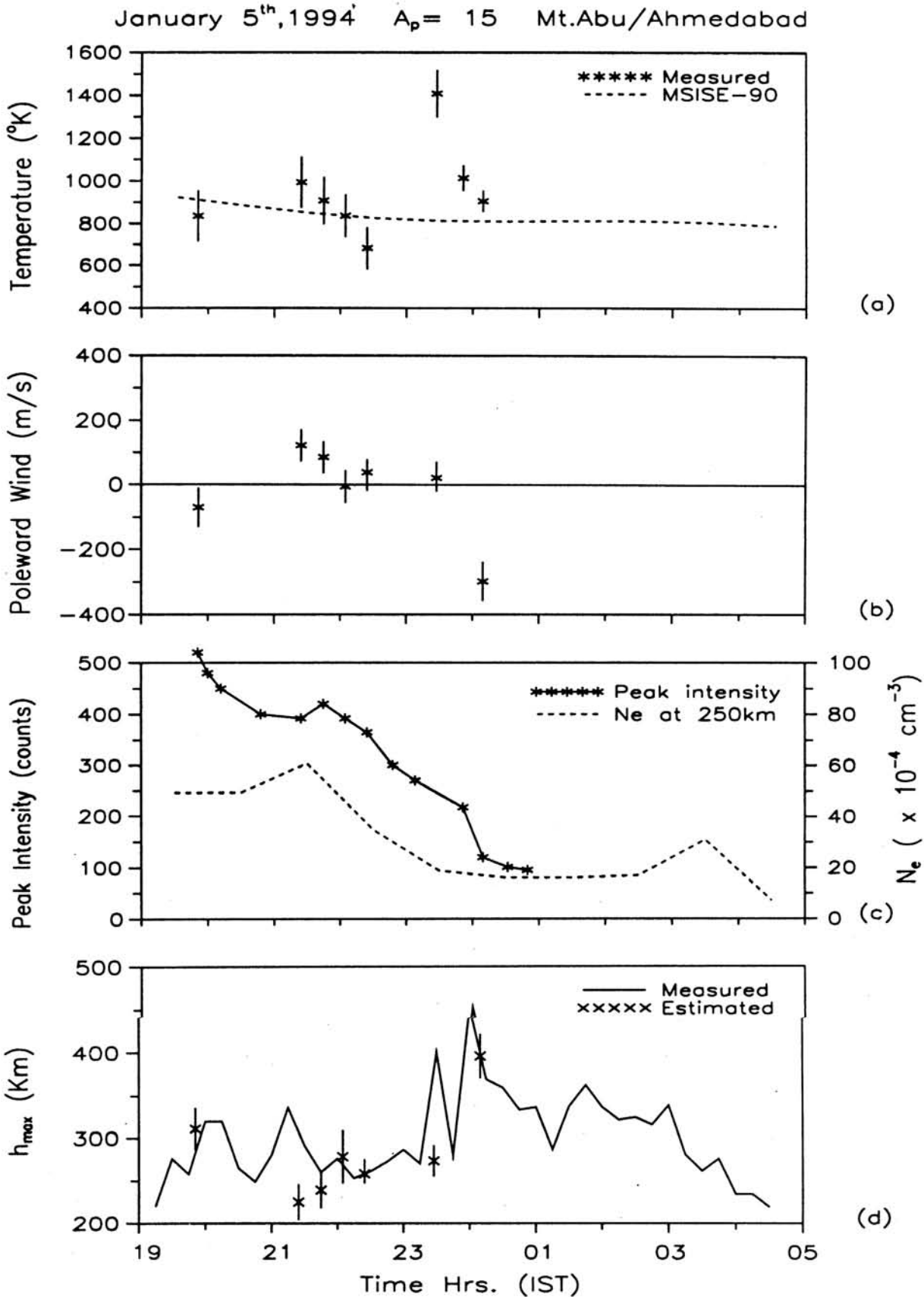


Figure 3.11: The thermosphere ionosphere system (TIS) behaviour on 5th Jan. 1994

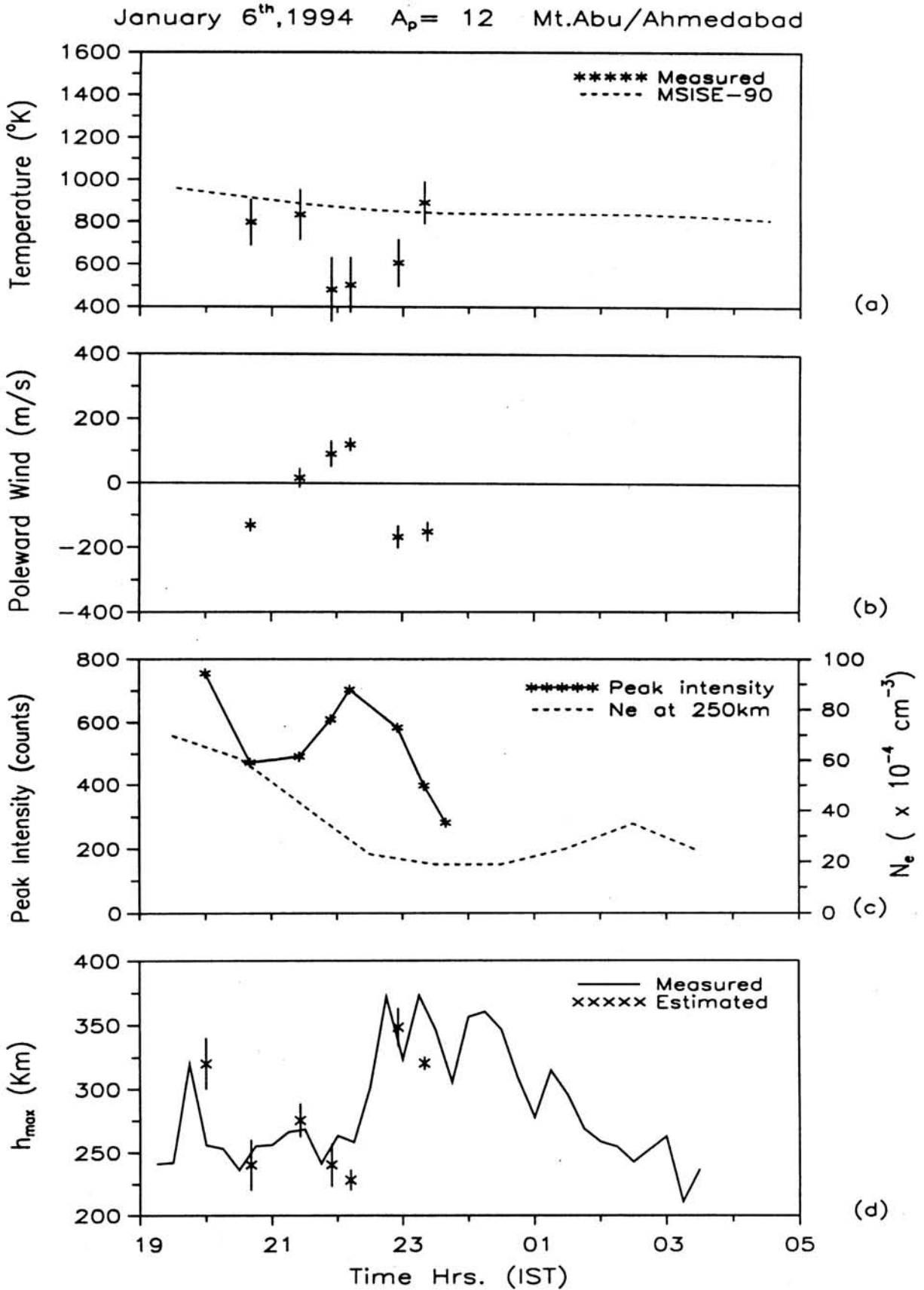


Figure 3.12: The thermosphere ionosphere system (TIS) behaviour on 6th Jan. 1994

increase in the airglow intensity could be attributed to the additional ionisation available due to the F-region peak which was lying in the airglow emission region (250km). The airglow intensity started decreasing as soon as the F-layer moved away from 250km, indicating above scenario to be true. However, the thermospheric temperature seemed to be undergoing modulations which could as well be due to traveling atmospheric disturbances or gravity waves.

The examples discussed above, provide us clear insight into the coupled thermosphere ionosphere dynamics and electrodynamics. It also demonstrates the relative importance of these processes in the coupled TIS. Though, the contribution of low latitude electric fields still remains to be quantified during low solar activity epoch and quiet geophysical conditions, the electric field induced dynamical effects are comparatively less significant.

3.12 Conclusions

Though, the investigation of the coupled behaviour validates both the temperatures and winds alongwith their variabilities. The causative mechanism which is responsible for these variabilities are not well understood, in particular, this applies to the temperature and its variabilities. The possible causes and plausible approach to account for them are discussed in detail in the following chapters.

The important conclusions that could be drawn from the results presented so far are: (a) The neutral temperatures and winds are the dominant factor that control the overall energetics and dynamics of the low latitude TIS with the electric field playing a less significant role especially during geomagnetically quiet time in the solar minimum epoch. (b) The heights of the F-layer could conveniently be used as an indicator of the thermosphere ionosphere dynamics, while the densities control the chemistry. (c) There are limitations in

the existing models like MSIS with regard to its representation of the variabilities most of the time and the absolute magnitude itself on several occasions. The models by themselves are designed only to represent the climatology of the thermosphere and improvements would be called for, for a realistic representation including the variabilities. These aspects would be covered in the chapters to follow.

Chapter 4

Low Latitude TIS During Storm Times

4.1 Geomagnetic Storms

The sun, in addition to the electromagnetic radiation, is also a source of hot plasma in the form of solar wind. It has been realised that these plasma emissions are capable of influencing significantly the solar terrestrial environment. These influences generate disturbances known as 'geomagnetic storms' in earth's magnetosphere - ionosphere - thermosphere system. Understanding the energetics and the dynamic nature of these geomagnetic storms in terms of both the cause and the effects is fundamental to the global issues like the 'Space weather'. In the following sections, various aspects of geomagnetic storms, their generation mechanisms and their effects in terms of thermospheric - ionospheric energetics/dynamics over high and low latitudes are discussed in detail.

4.2 Sun as a Source of Energetic Plasma

Some of the most spectacular, yet poorly understood terrestrial phenomena are a direct consequence of the interactions of solar wind with the earth's atmosphere. Sun's outer atmosphere, the corona, is the source of the solar wind, though there are questions about how these winds are generated. Some of

the recent space missions like the Solar Maximum Mission (SMM) has concentrated on these aspects. The measurements made on the total solar irradiance and its variation over 11 year period encompassing solar cycle No. 21 and 22; by the Active Cavity Radiometer Irradiance Monitor (ACRIM) onboard the SMM has shown that the solar magnetic activity has a positive correlation with the number of sunspots and bright faculae and plages in the solar disk [*Willson and Hudson, 1991; Foukal and Lean, 1990*]. Some more results on the measurements made by the 'Earth Radiation Budget' experiment onboard Nimbus-7 satellite have been summarized by *Hoyt* [1993] supporting the above results. Apart from irradiance variations, there are important observations and also questions about the acceleration of transient solar wind arising from explosive solar events called 'Coronal mass ejections'(CMEs) and flares. CMEs are capable of producing large fluxes of energetic particles, and the CME associated solar flares are capable of generating impulsive bursts of energetic particles, hard X-rays and gamma rays. They are distinct structures of solar plasma in interplanetary space that open and carry out magnetic fields from the solar corona [*Roederer, 1995*]. This magnetic field is referred as the Interplanetary magnetic field (IMF). Though not much is known about the CMEs beyond the rudimentary levels, it would suffice to say that the CMEs projected towards earth produce geomagnetic activity on earth's atmosphere when the shock front arrives. The severity of the disturbance depends upon the polarity of north-south component of the IMF as well as, the velocity of the incoming solar wind. However, all storm events cannot be associated with solar flares [*Gosling, 1993*]. It is CMEs, not flares, that are now considered to be linked with observed phases of geomagnetic activity. The energy, in most of the CMEs, is associated mainly with the ejected plasma. The kinetic energies range from

10^{22} to 10^{24} Joule [Howard *et al.* 1995, Richardson, 1994]. Current efforts are focussed on studies indicating the topology of ejected magnetic fields [McComas, 1995].

Recently, in the month of Jan'97 there occurred a CME event which, for the first time ever, was covered throughout its evolution and final interaction with earth's *magnetosphere* by a series of satellites. The detailed results of these observations are still awaited and will definitely shed some light on the important aspect of CME generation and its interaction with terrestrial environment. Solar wind mainly consists of protons (H^+) $\sim 95\%$, $\sim 4\%$ of Alpha particles (He^{++}) and $\sim 1\%$ of minor ions, of which carbon, nitrogen, oxygen, neon, magnesium, silicon and iron dominate. Solar wind velocity in the ecliptic plane is measured in the range of 300 to 600 km/s which under some conditions can even exceed 1000 km/s. The density of solar wind particles is between 1-10 / cm^3 and the kinetic temperature of particles is in the range from $10^4 - 10^6$ K [Ogilvie *et al.* 1995]. The charge energy mass (CHEM) instrument aboard AMPTE spacecraft has provided number of composition measurement of high speed solar winds [Gloecker *et al.* 1986]. The important energetic coupling between the solar wind and the earth's atmosphere is facilitated by the interaction of the IMF with the geomagnetic field.

The interplanetary magnetic field remains 'frozen' into the solar wind plasma by its very high electrical conductivity, and as the solar wind plasma velocity, away from the sun, becomes faster than the Alfvén speed, the solar wind and its 'frozen in' magnetic field cannot contract back to the sun and it spreads out into the interplanetary medium, interacting with planetary atmospheres and their respective magnetic fields. The IMF is generated, primarily by the magnetic dynamo inside the sun; and is directed radially inward or outward near the sun. Out into the space, the field, because of the motion/rotation of the

sun, gets wrapped around at an angle in the form of an Archimedean spiral or a Ballerina's skirt [Parker, 1958]. Figure(4.1) depicts this special field orientation of magnetic field associated with sun. The total amount of magnetic flux extending into the interplanetary space along with the solar plasma is quite variable. Recent analyses have indicated a substantial ($\sim 60\%$) variation in the IMF magnitude [Slavin *et al.* 1984, 1986]. Though, the instantaneous magnetic field directions deviate significantly from the ecliptic plane, on an average, the IMF lies in the ecliptic plane. The more fundamental questions regarding the origin and time evolution of IMF at the solar surface are beyond the scope of present discussion. However, the important aspect of solar winds, IMF, shocks and their connection with geomagnetic disturbances is briefly discussed in the following sections.

4.3 Interaction of Earth's Magnetosphere with the Solar Wind

The earth crosses in and out of the solar wind associated interplanetary magnetic field sectors as the sun rotates throwing highly energetic plasma from its corona. Wilson, [1987] has shown a strong association between the initiation of geomagnetic storms and the magnetic clouds associated with the ejected plasma or the solar wind. Some very important results had been arrived at by the study of statistical correlations between source parameters characterizing earth's magnetosphere and some of the interplanetary fields (eg. IMF B_z component). However, more detailed information is obtained only by the study of the various magnetospheric processes following ongoing variations in the interplanetary field and solar wind speed [Farrugia *et al.*, 1993].

According to the classical definition, the earth's magnetosphere is a vast magnetic cavity in which the earth resides, and the source of this mainly dipole field is believed to be a giant dynamo set up by the ponderous flow of matter inside the core of the earth. The dipole field which behaves as a compressible

fluid, on interacting with the solar wind gets distorted, compressing the geomagnetic field to $10R_E$ in the sunward side and extending it to several hundred earth radii (R_E) in the nightside. The cavity boundary i.e. the *magnetopause*, is in dynamic equilibrium and is highly variable depending on the dynamic pressure exerted by the solar wind. Inside the magnetopause, is the region called the magnetosphere. However, it is important to mention that the dipolar field of the magnetosphere is only one component of the field, there are other important components owing to the electrical currents replete in the ionosphere and magnetosphere. The highly energetic solar wind plasma being unable to directly penetrate deep into the magnetosphere through magnetopause, sweeps around the earth surrounding the cavity by dragging the field along in the anti-sunward side resulting in a long active tail like structure, appropriately called the magnetotail. Figure(4.2) schematically illustrates the interaction of solar wind with earth's atmosphere. During the solar wind magnetospheric interactions, a preferential flow of plasma, energy and momentum takes place from the solar wind to the magnetosphere. Two fundamental processes which had been considered to be providing the conversion mechanism for energy stored in the field, are the viscous interaction [Axford and Hines, 1963] and magnetic reconnection or Flux Transfer Events (FTE) [Dungey, 1961]. The energy transfer efficiency during a reconnection event is of the order of 10% [Gonzalez et

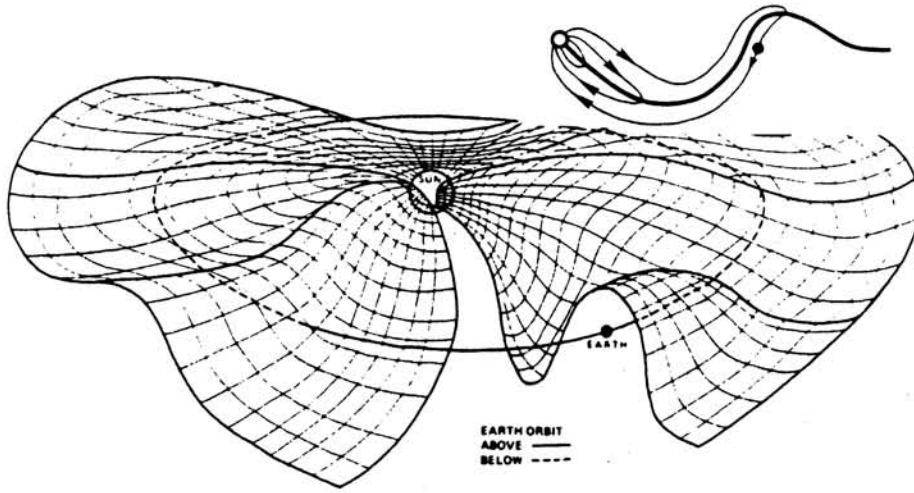


Figure 4.1: Three dimensional sketch of the solar equatorial current sheet and associated magnetic field lines. (courtesy of S. I. Akasofu)

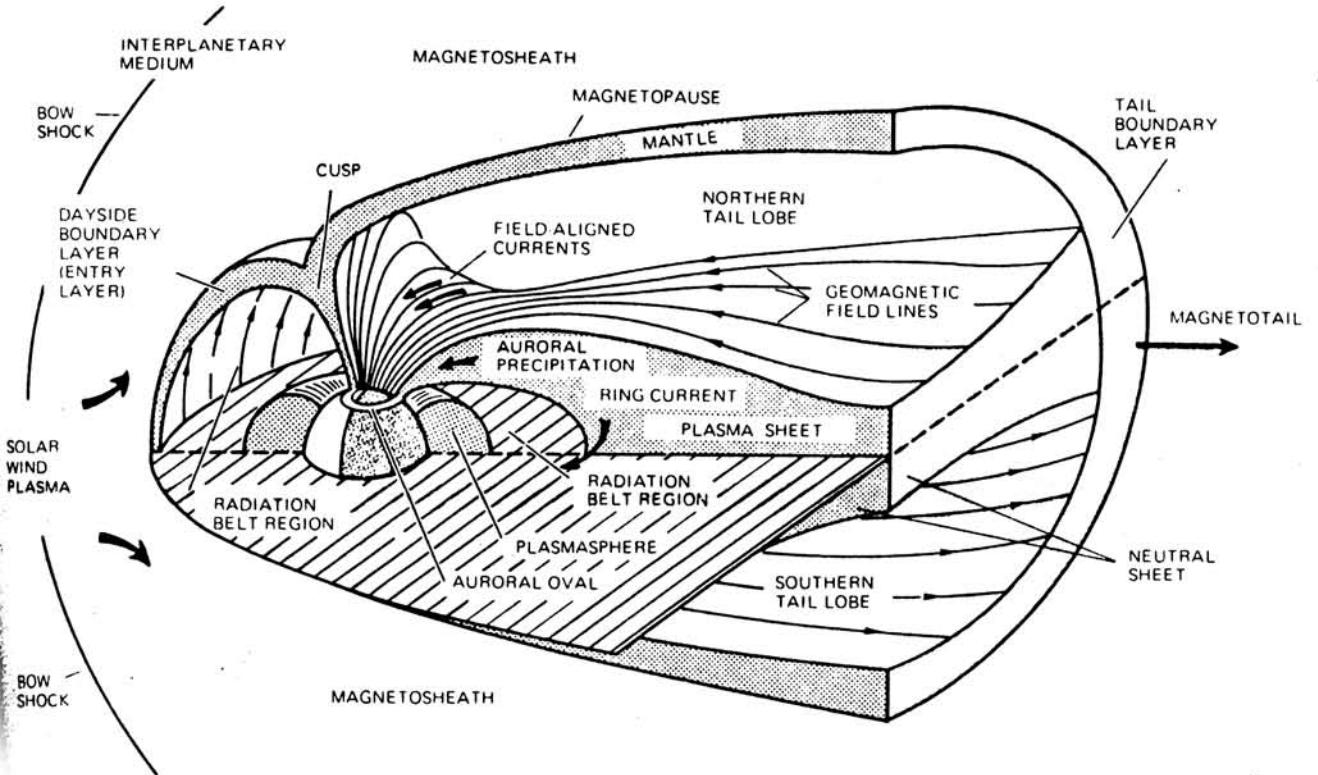


Figure 4.2: Schematic representation of the magnetosphere. (courtesy of J. Roederer)

al., 1989] while it is only 1% for viscous interaction through micro instabilities and their resonant interaction in a collisionless plasma [Sonnerup, 1984] during intense northward IMF phases [Tsurutani *et al.* 1992]. Magnetic reconnection is thought to be the most effective mechanism for the energy exchange between the solar wind plasma and terrestrial atmosphere.

4.4 Magnetic Reconnection and Flux Transfer Events

Magnetic reconnection processes are essentially the magneto hydrodynamic interaction between the 'frozen in' field associated with the solar wind plasma and the geomagnetic field at the magnetopause, causing influx of energy and mass to the earth's atmosphere. As the incoming solar wind plasma impinges on the magnetosphere and compresses it, in some regions the solar wind (SW) associated IMF and magnetospheric field (antiparallel to each other) become so close that the geomagnetic field diffuses through the SW plasma and gets connected with IMF (B_z component). The newly reconnected field lines move away from each other joining the general solar wind flow in the antisunward side, allowing the solar wind plasma to enter into the magnetosphere and to the ionosphere lower below.

These reconnected field lines are swept back into the geomagnetic tail, where a second reconnection process takes place, producing field lines which are closed again and subsequently convect back towards earth. This, accelerates simultaneously (Fermi acceleration) the plasma or the flux associated with the closed field lines. Figure(4.3) depicts this process in a simplistic way. Usually the reconnection and the Flux Transfer Events (FTE's) are a short lived phenomena, the duration being decided by the kinetic processes and large scale dynamics [Lockwood 1993, Elphic 1979; Harendel 1978]. On the whole the

magnetic reconnection and FTE's are quite complex, as revealed by the satellite missions [Otto, 1995] and are extremely important in the investigation of magnetosphere-ionosphere-thermosphere system. As these are threaded by the same magnetic field lines, large amount of momentum and energy is exchanged among them during geomagnetically disturbed periods. Some of this energy is directly transferred to the ionosphere over polar latitudes through cusp regions and also via field aligned currents

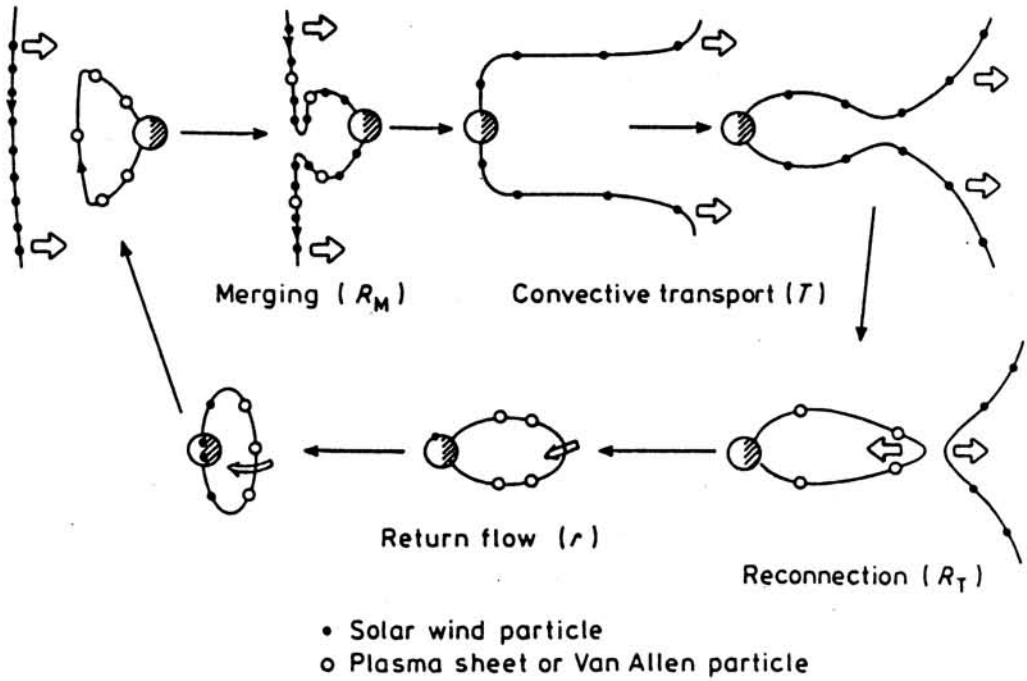
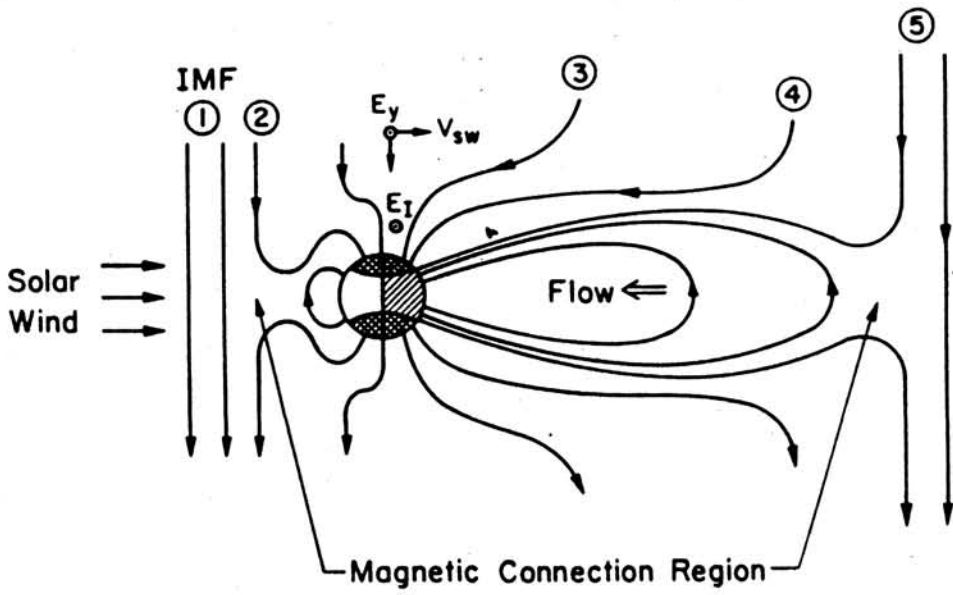


Figure 4.3: History of the field line after reconnection with IMF B_z on sunward side and subsequent convection anti sunward side. (Akasofu, 1973)

where it is dissipated by Joule heating. Another major part of the solar wind energy, stored in the magnetotail region in the form of kinetic and thermal plasma energy as well as magnetic field energy is transferred to inner magnetospheric ring current, direct particle precipitation and a complex web of other magnetospheric currents and their associated Joule heating. Some part of this energy is also released back into the space in the form of plasmoids. The regions namely (i) the polar ionosphere (ii) the ring current and (iii) magnetotail are the main consumers of solar wind energy. So, the enhanced solar wind energy input, especially following the periods of geomagnetic disturbances is a phenomenon whose manifestations can be registered in nearly all regions of the magnetosphere, ionosphere, and thermosphere globally, modifying their mean thermal budget.

4.5 Current Issues of Magnetosphere - Ionosphere Coupling

Since, the magnetosphere and the ionosphere are coupled in many different ways, it is extremely difficult to study the processes occurring in upper atmosphere taking only one of these regions into account. All the ionospheric plasma processes are in some way controlled by the state of the magnetosphere; and, the magnetospheric plasma processes are driven by the electrodynamics in the ionosphere. The magnetosphere and the ionosphere form a coupled feedback system through magnetic field lines via field aligned currents called the Birkland currents and the Alfvén waves. The energy generated by the solar wind-magnetospheric dynamo causes earthward convection of field and plasma in the magnetotail and is transmitted to the ionosphere via field aligned currents which close in the polar ionosphere. The dissipation of these currents causes heating in the high latitude ionosphere.

In reality, the current system that connects the magnetosphere and ionosphere

is complex, consisting of many primary and secondary currents [Iijima and Potemra, 1976]. Figure(4.4a) shows these different current systems. These currents also give rise to large potential differences along the magnetic field, causing tremendous energization of the particles and generation of a range of plasma waves [Knight 1973, Rolef et al. 1991]. Figure(4.4b) show the basic potential structure responsible for the energisation of charged particles inside the magnetosphere. The energetic particles are capable of dissociating, ionising and exciting the atoms and molecules in the polar upper atmosphere, which, while deexciting emit intense radiation known as Aurora. It is well known that aurora does not occur randomly over the polar regions, but restricted to an area, which is the locus of the feet of field lines which are connected to IMF B_z component above the magnetopause, and is referred to as the Auroral oval. In relation to the structure of the magnetosphere, the auroral oval is the region which marks the division between open and closed field lines. Variation in the luminosity of aurora (10% to a factor >2) is a good indicator of the extent of geomagnetic disturbance and the intensity of solar wind - magnetosphere interaction [Vorobyev, 1974; Craven et al. 1987]. As mentioned earlier, significant amount of storm energy is received in the form of energetic particle precipitation over polar latitudes but the precipitation of auroral particles into ionosphere is highly discrete and localised.

During strong geomagnetic disturbances, the electrical conductivity is high along the geomagnetic field lines and to a very good approximation the field lines can be treated as equipotentials. Owing to this, the magnetospheric electric fields get mapped along these equipotential field lines on to the polar ionosphere where the field lines penetrate and; at the same time, the electric field is enhanced a great deal because of the closing distance between the field lines

from magnetopause to polar ionosphere resulting in strong dawn to dusk electric fields. In the following sections a brief account of the temporal evolution of a geomagnetic storm, its representation and the energetics with regard to the polar latitudes are provided in the backdrop of which the response of the low latitude region would be discussed and results presented.

4.6 Evolution of a Geomagnetic Storm

True to the nomenclature, 'geomagnetic storms' are periods of extraordinary geomagnetic disturbances, usually lasting for about 5-6 days and sometimes even more depending upon the storm intensity. As mentioned earlier, strong geomagnetic storms are caused by 'coronal mass ejections' and intense shocks originating

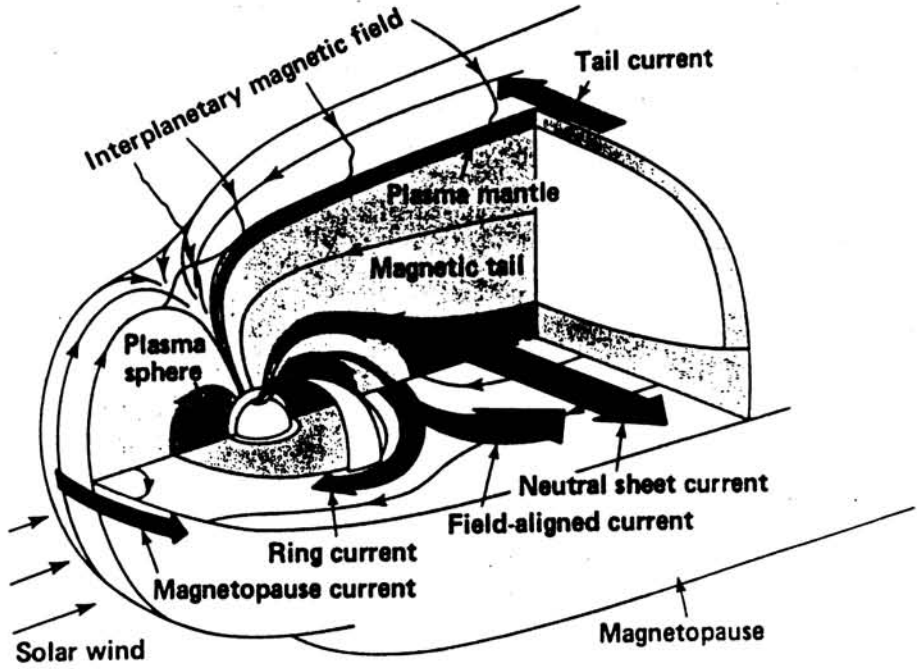


Figure 4.4a: Three dimensional sketch of the different current systems in magnetosphere. (T. A. Potemra, JHAPL Tech. Digest, 1983)

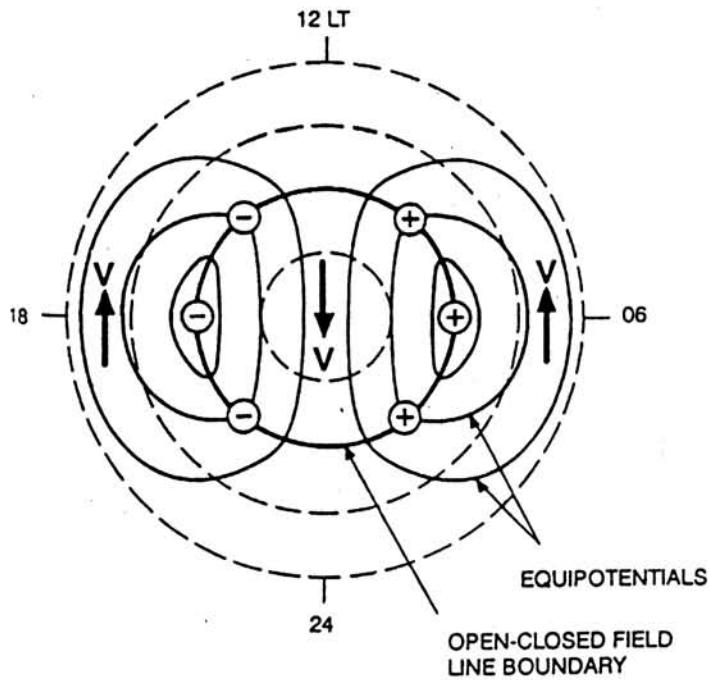


Figure 4.4b: Mapping of magnetospheric electric Potentials and plasma flows to the ionosphere as seen looking down over the northern polar cap. (Lyons 1993)

at the sun [Gosling, 1991]. Shortlived intense magnetic disturbances in the nightside are known as 'substorms' [Akasofu and Chapman, 1961]. In reality, a substorm is a systematic sequence of physical processes that occur over high latitudes, causing Auroral and magnetic disturbances. On the other hand the 'Magnetic storm' differs from the substorm in the activity duration, intensity/strength and effects, and is global in nature. However, in principle, magnetospheric substorm can occur quite independently of a magnetic storm [Akasofu *et al.*, 1968], but it is important to mention here that no magnetic storm has been observed in the absence of magnetic substorm. The 'geomagnetic storm' is a linear superposition of intense substorm disturbances. Though, no major differences exist between the two in terms of effects on auroral atmospheres, Kamide *et al.* (1977) found while discussing the dependence of substorm occurrence probability on IMF that substorms are sure to occur whenever IMF B_z had a value $\leq -3\text{nT}$ sustaining for atleast one hour. And the necessary condition for the magnetic storms to occur emerged out to be a southward IMF B_z ($\sim -10\text{nT}$) for more than 3 hours. However, northward IMF B_z also can initiate great storms at times. At present we are still far from a comprehensive understanding of these storm/substorm events.

Nonetheless, it is generally accepted that the solar wind energy reaching the magnetosphere during storms, is stored and dissipated by three main processes. These are generation of 'ring current' and its dissipation by charge exchange; enhanced Joule heating in the ionosphere and thermosphere; and energetic particle precipitation. The ratio of energy, transferred into the ring current is usually more than the other two. The characteristic feature of a geomagnetic storm, i.e. an unmistakable decrease in the strength of horizontal magnetic field of earth and its subsequent recovery, is now identified to be mainly due to ring current evolution. The electromagnetic drifts, imposed on

the trapped magnetospheric particles, due to radial magnetic field gradient and curvature lead ions to move from dawn to dusk and electrons from dusk to dawn, forming an overall ring current surrounding the globe. Strengthening of the ring current is, therefore, regarded as a sure sign of the onset of a storm. The induced magnetic field on the surface of the earth opposes the horizontal component (H) of geomagnetic field, causing a decrease in 'H'. Studies have shown that the extent of the depression in geomagnetic field strength is a useful proxy for the level of geomagnetic disturbance. The 'ring current' will be dealt with later.

4.7 Geomagnetic Storm and the Use of Indices

Bartels (1940) made the first attempt to represent the variations on the terrestrial magnetic field through indices. *Sugiura and Chapman* [1960] assigned a numerical intensity index to individual storms by measuring the differences in daily mean value of horizontal magnetic field, and categorised the observed storms as: weak, moderate and great. Initially, the use of such indices was for a point of reference only to infer the presence or absence of disturbances/activity. One important aspect of the 'indices' is that if the index series is homogeneous in time representing the phenomena well, then it could be used as a tool for statistical studies concerning its time variation, and its relationship with other phenomena [*Mayaud*, 1980].

The fundamental problem in defining a geomagnetic index is the separation of geomagnetic variations observed at any given time, at any place, caused by permanent sources of field, from those which are not permanent. These irregular or non permanent variations were classified into two sets [*Mayaud*, 1978a]. The first, consists of variations due to equatorial ring current effects, storm

sudden commencements, sudden impulses and fluctuations etc; while the second belongs to a class of localised effects namely polar cap variations, auroral pulsations etc. The present indices recognised by IAGA (International Association of Geomagnetism and Aeronomy), also constitute two distinct families of indices. One aiming at monitoring a single and well defined phenomenon i.e ring current variations or the auroral variations while the second type of indices characterise the planetary level of the variations as a whole.

The most frequently used indices are K_p and ap (the planetary indices) and; D_{st} , a nonplanetary index for equatorial ring current). The K_p index, determined to an accuracy of 1/3 of a unit, is obtained by combining index K, which runs from 0 to 9 related to the amplitude of field variation by a quasi-logarithmic scale, from twelve observatories around the world. Typically the qualification $K = 9$ is a geomagnetic disturbance of 300 nT for low latitude, 500 nT for mid latitudes and 2000 nT for stations in the auroral zones. And for index ap , the field variations of each magnetic field components i.e. horizontal H, vertical Z and dip (D) recorded every three hour at any station are considered. The greatest of the three deviations is called the amplitude (a). The amplitude 'a' for twelve observatories are combined and averaged, after removing the solar quiet day (Sq) and lunar (L) variations, to define the index ap .

These indices especially ap is used as an input to the modern day thermospheric - ionospheric models for representing different geophysical conditions. On the other hand, the ' D_{st} ' is purely a ring current index obtained from low latitudes, sufficiently away from the equatorial electrojet current region. Notwithstanding the fact that all the sources and variations involved in the observed field fluctuations of D_{st} , are not fully understood, D_{st} is the only index which describes the event with maximum accuracy. Figure(4.5) shows how a

typical magnetic storm is recorded in terms of K_p and D_{st} . The panel showing the D_{st} variations clearly registers three different phases of the magnetic storm (as marked in the figure). These are (a) an increase of magnetic field lasting a few hours, marking the first impact of the shock associated with solar wind plasma with earth's magnetosphere (initial phase) (b) A large decrease in horizontal component 'H' of earth's magnetic field building upto a minimum in about a day (main phase) characteristic of the developing ring current and its induced magnetic field strength on ground. (c) A slow recovery of the field strength to pre-storm levels, This phase is characterised by the decay of storm time ring current. This phase usually is the longest, depending on the extent of disturbance, and is known as the recovery phase.

A statistical study performed over a large number of storm events reveals that very great magnetic storms ($H \sim 500$ nT and more) occur only two to three times per solar cycle, while great magnetic storms ($H \sim 300$ nT) are relatively more frequent i.e. about 8 to 10 times per solar cycle. Smaller storms ($H \leq 300$ nT) occur about

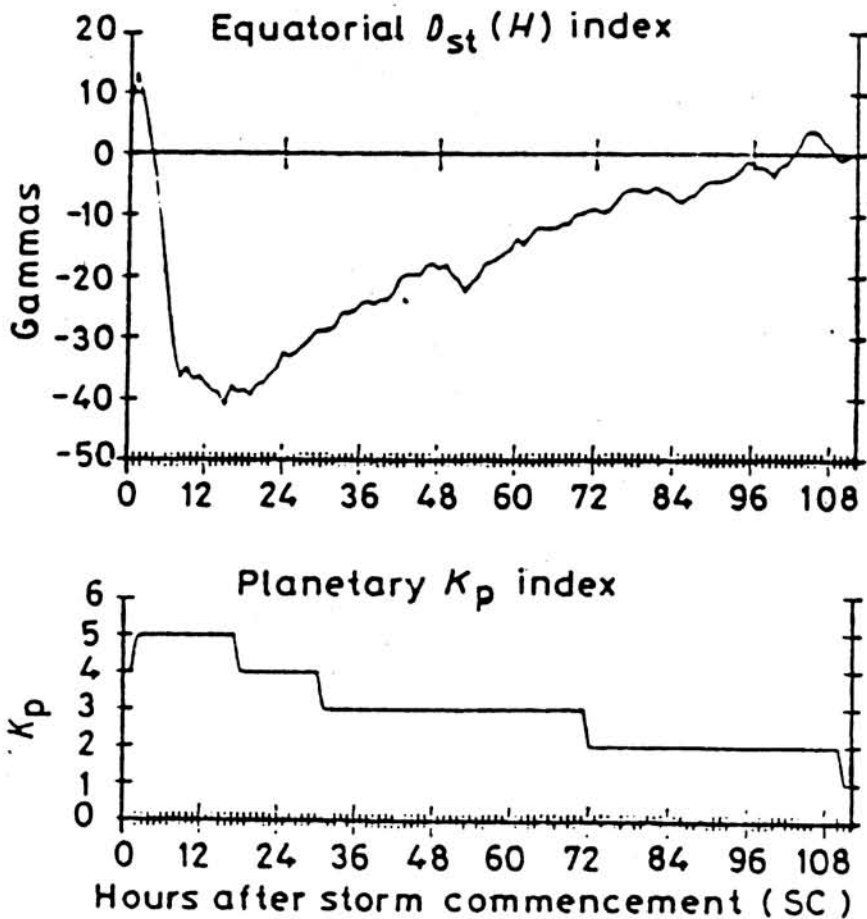


Figure 4.5: Average storm-time variations of equatorial magnetic index D_{st} and K_p . (M. Mendillo, *Planet. Space Sci.*, 1973)

400 times per cycle [Russle and McPherron, 1973]. Modern magnetometric observations and data acquisition techniques have made it possible to evaluate the ' D_{st} ' (storm time index) in real time. A very comprehensive review on the importance of these indices, is given in the classical books on 'Geomagnetism' Vol. I and II [Chapman and Bartel, 1962 and 'Derivation, Meaning and use of geomagnetic indices' [Mayaud, 1980].

Figure 4.5: Average storm-time variations of equatorial magnetic index D_{st} and K_p . (M. Mendillo, *Planet. Space Sci.*, 1973)

400 times per cycle [Russle and McPherron, 1973]. Modern magnetometric observations and data acquisition techniques have made it possible to evaluate the ' D_{st} ' (storm time index) in real time. A very comprehensive review on the importance of these indices, is given in the classical books on 'Geomagnetism' Vol. I and II [Chapman and Bartel, 1962 and 'Derivation, Meaning and use of geomagnetic indices' [Mayaud, 1980].

4.8 The Atmospheric Energetics and Dynamics during Geomagnetic Storms

Several ground based and advanced satellite observations of global ionospheric, thermospheric, plasmaspheric and magnetospheric processes have provided

an important framework to understand the true global nature of the geomagnetic disturbances. They have shown clearly that the structure, composition and dynamics of the ionosphere and thermosphere are altered in or near the auroral zone during these periods. The auroral zone is known to expand away from the geomagnetic poles with the increasing geomagnetic and magnetospheric activity levels. Also, the regions of strong magnetospheric electric fields mapped into the polar ionosphere undergo a similar equatorward expansion [Foster *et al.* 1986; Heppner and Maynard, 1987]. The direct heating effects of precipitating ions and electrons are however, limited to mainly the dayside cusp. These energetic electrons and ions enhance the plasma density by ionising the neutral atoms and molecules in the thermosphere.

During geomagnetic storms, the convection electric field drives the enhanced ionospheric plasma of the auroral oval and around the polar cap to high velocities ($\vec{E} \times \vec{B}$ drift, \vec{E} representing the convection electric field and \vec{B} the magnetic field intensity). The moving ions impart significant amount of momentum to neutrals via 'ion-drag', while at the same time, the resistance offered by the neutral atoms and molecules causes the dissipation in Pederson current component through increased Joule heating. Outside the oval and over the polar cap regions the electrodynamic heating is effective depending upon the electrical conductivity in that area [Fujii *et al.* 1981]. The efficiency of momentum transfer and Joule heating increases linearly with ionospheric plasma density and is more important than heating by particle precipitation [Baumjohann and Kamide, 1984], though, at times, particle precipitation may become comparable. Statistical studies indicate that both the electro-dynamic and particle heating maximises in the annular regions around poles which are roughly colocated [Fieldstein and Starkov, 1967; Holzworth and Meng, 1975; Iijima and Potemra, 1976]. The electrodynamic heating is known to peak at about ~ 130

km [Banks 1977; Brekke and Rino, 1978] while the maximum particle heating occurs at an altitude of ~ 110 km [Spiro *et al.* 1982; Rees *et al.* 1983].

The lower ionospheric region, around ~ 150 km, over high latitudes responds directly to the 'auroral input'. Large scale advection and convection forced upon the thermosphere by geomagnetic heating causes the high latitude F-region neutral gas composition to change dramatically [Rees *et al.* 1985a; Fuller-Rowell *et al.*, 1987b], as a part of the thermospheric response to Joule and particle heating. The varying composition structure with altitude during geomagnetic disturbances is the consequence of the convection of these horizontal winds with the mean vertical wind flow, as a part of global wind system. It was Jacchia [1959] who first inferred the changes in the neutral densities through the increased satellite drag. Later on, neutral composition measurements by OGO-6 [Taeusch *et al.* 1971] and ESRO-4 [Trinks *et al.* 1975] confirmed this aspect. Significant enhancement of molecular nitrogen (N_2) density, and a corresponding decrease of atomic oxygen density are seen in the high latitudes during intense storms [Fuller-Rowell *et al.*, 1988]. Enhanced molecular concentrations cause significant depletions in F-region plasma density by greatly increasing the effective recombination rates, while the ionisation rates are only slightly modified by auroral precipitation. However, atomic oxygen (O) the dominant thermospheric species, usually registers a depletion below 300 km and a slight increase above. The E-region wind velocities are typically lower than that of the F-region, and the basic wind pattern follows the ion convection over high latitudes [Johnson and Wickwar, 1987]. Further, the temporal variabilities in the energy injection at high latitudes trigger a broad spectrum of atmospheric waves, namely Traveling Atmospheric Disturbances (TADs). As a part of global-scale disturbances, the low latitude, thermosphere - ionosphere system follows the initial high latitude geomagnetic forcing; and it is

known to show distinctive storm time features in composition, dynamics and energetics.

4.9 Geomagnetic Storms-The Low Latitude TIS during Geomagnetic Storms

One of the least explored aspect is the behaviour of low and equatorial latitude Thermosphere-Ionosphere System during geomagnetic storm and how the large amount of energy that gets dumped into high latitude regions during storms gets redistributed to low latitudes. The magnetosphere - ionosphere - thermosphere coupling is believed to be the only route through which the magnetospheric disturbances get propagated to low latitudes. Three main processes which play important roles in the redistribution of storm energy and momentum to low latitudes are (i) large scale meridional wind circulation; (ii) gravity wave or TADs; and (iii) Ring current [*Prolss, 1982*].

The thermospheric composition and temperature are essentially controlled by vertical and horizontal advection and molecular diffusion. Due to the large energy input during the geomagnetic storms over high latitude regions, the atmosphere gets heated up that cause the air to move upward and outwards i.e., away from the source region. In its upward expansion, the air undergoes adiabatic cooling but the air is, nevertheless, hotter than the normal (even during geomagnetically quiet periods) as it flows equatorwards *Roble and Dickinson, [1970]*. As a result of the pressure gradients between the equatorward/low and high latitude regions, a strong meridional circulation gets established, which produces some heating because of the relative motion between ions and neutrals i.e. ion-neutral collisions [*Stubbe and Chandra, 1970*]. On the descending part of the meridional circulation over low latitudes the air undergoes adiabatic compression which heats the air further. The wind flow and the pressure

differences constantly modify each other, as the flow is continuous spatially [Rishbeth, 1975]. Existence of such circulations during storms, has indeed been observed and confirmed by the presence of strong winds over mid latitudes [Armstrong *et al.* 1969; Hays and Roble 1971; Hernandez *et al.* 1980]. However, there have been relatively few direct observations on the thermospheric dynamics at low and equatorial latitudes [Hernandez *et al.* 1975; Bittencourt *et al.* 1976; Sipler and Biondi, 1978; Hernandez *et al.*, 1980; Meriweather *et al.* 1986; Sridharan *et al.* 1989, 1991; Gurubaran, 1993; Pant and Sridharan, 1998]. In an important observation it has been seen that at times during storms, because of the hemispheric asymmetry and the shape of energy input function with time, poleward winds also can get setup over low latitudes [Fagundes *et al.* 1995]. All these meridional wind circulations would affect the composition, dynamics and energetics. The model estimated and actually observed time lag between the setting up of the meridional circulation cell from the time of intense high latitude heating during a storm, is around 8-10 hrs.

The temporal variations of energy injection at high latitudes during disturbed periods generally triggers a broad spectrum of waves which may combine to form a Traveling Atmospheric Disturbances (TAD) or gravity waves. These TADs are pulse like superposition of atmospheric waves. TADs move away from the source regions i.e. high latitudes, towards middle and lower latitudes and dissipate their energy through molecular viscosity, thereby transporting energy [Richmond, 1978; Hunsucker, 1982]. At low latitudes, the energy dissipation of the two TADs launched in both the hemispheres cause an increase of the temperature and densities. One essential feature of TADs is that they are associated with an equatorward meridional wind of moderate magnitude. It is this transient increase of meridional wind velocity which is believed to be responsible for the generation of positive ionospheric storms at middle latitudes

[*Testud et al.* 1975; *Prolss and Jung*, 1978; *Roble et al.* 1978; *Prolss* 1993, *Prolss et al.* 1991, *Crowley et al.* 1989b]. TADs, also continuously lose energy by heat conduction and ion drag, and they may cause compressional heating too. It is this energy dissipation which appears as geomagnetic activity effect at low latitudes [*Klostermeyer et al.* 1973; *Richmond*, 1979; *Cole and Hickey*, 1981; *Prolss*, 1982; *Forbes et al.* 1987; *Burns and Killeen*, 1992]. These TAD effects can be seen even after a prolonged time i.e. 24-30 hrs. and as early as 10hrs. after the main energy dissipation.

An additional energy source that is active during storm time is the ring current formed in the magnetosphere. During geomagnetic storms, large amount of energy is contained in ring current in the form of trapped particles. This trapped energy is released directly into the thermosphere by means of neutral particle precipitation, produced due to resonant charge exchange process and also by field aligned charged particle precipitation over high latitudes. At middle and lower latitudes some of these trapped ring current ions are dumped directly into the thermosphere if their mirror height is lowered to the thermosphere sufficiently fast. There is also a more continuous flux of energetic neutrals showering from higher altitudes in all directions due to the charge exchange with the exospheric constituents over a much greater range of mirror heights. The heating effect [*Prolss et al.* 1973; *Tinsley et al.* 1981] at middle latitudes [*Torr et al.* 1974; *Kozrya et al.* 1982; *Ishimoto et al.* 1986; *Schroder and Prolss et al.* 1991] and ionospheric perturbations at low and middle latitudes due to these currents have been dealt with in the literature. The first ever Energetic Neutral Atom (ENA) image of earth's ring current was reported by *Roelef et al.* (1987), using ISEE-1 energetic particle data. Recently *Lui et al.* [1996] reported ENA detection by energetic particles and ion composition (EPIC) instrument onboard Geotail spacecraft during a magnetic storm on Oct. 29-30, 1994. The

ENA fluxes and the rate of recovery of D_{st} were found to be consistent with charge exchange, implying that ENA precipitation is a significant energy loss process for storm time ring current.

4.10 Temporal Evolution of Storm Effects over Low Latitude Regions

As has already been stressed upon in the earlier sections, the processes which redistribute the storm energy to lower latitudes take some time to become operative after the initial deposition over high latitudes. A case study was performed to study the temporal evolution of the temperatures during a storm on 21st Sept. 1982, over low latitudes. The recovery started on 22nd Sept'82. Temperature measurements from the WATS instrument onboard DE-2 satellite were used for this case study. Figure(4.6) shows the variation of thermospheric temperatures with latitude at different times during the recovery phase. It is clearly seen that the temperatures, observed after 3.8hrs in the recovery, were steady at $\sim 1100\text{K}$ at all latitudes upto

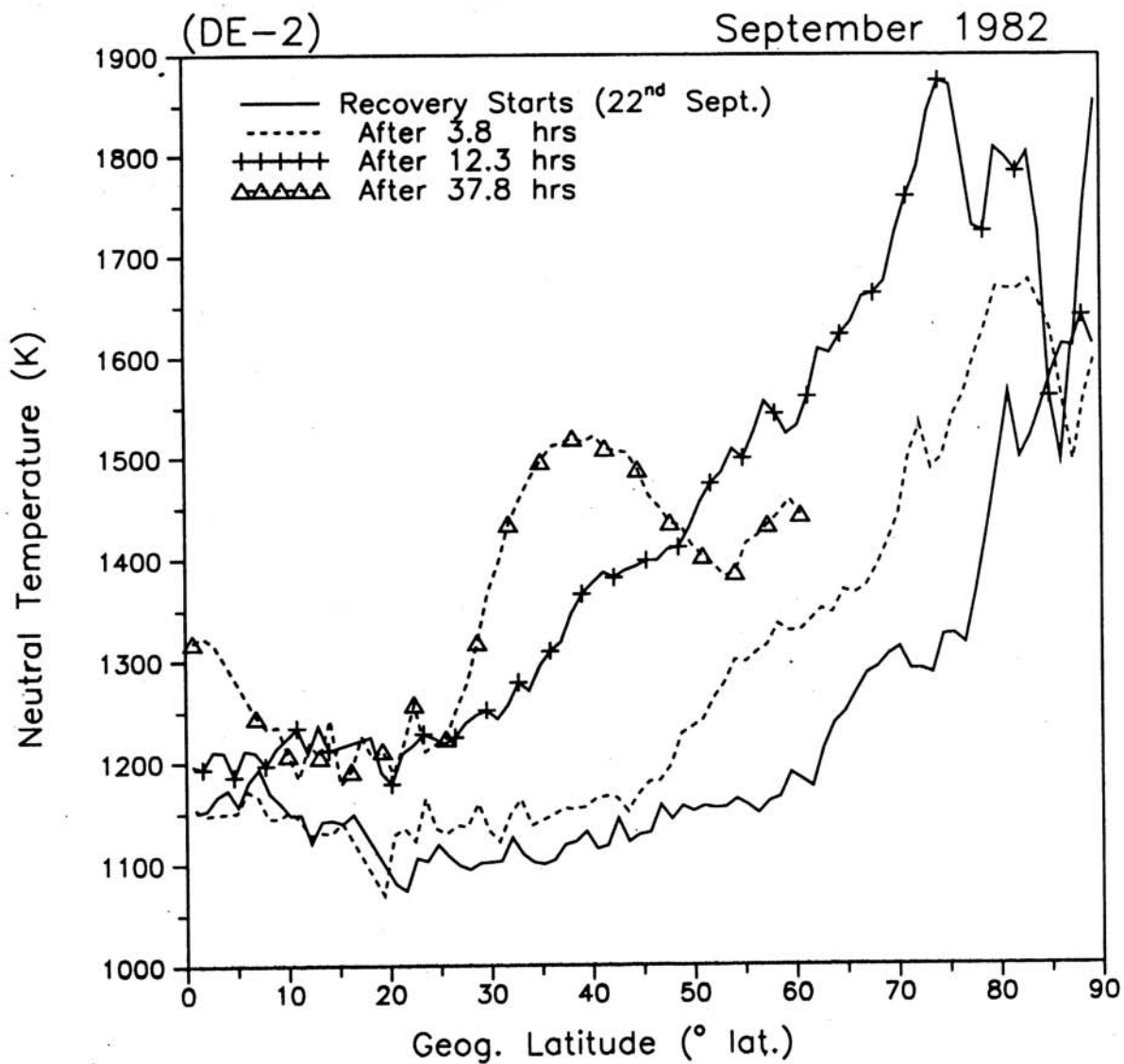


Figure 4.6: The variation of WATS (DE-2) measured thermospheric temperatures with latitude during the recovery phase of the storm in the month of September 1982.

60° latitude. They were seen to rise monotonically beyond 60° latitude signifying that the polar region received the maximum flux of storm energy. And, the steady temperature below 60° latitude indicates that the effect of enhanced storm energy has not yet been communicated to lower latitudes. Incidentally, after 12-13hrs. the temperature over midlatitudes also started registering an enhancement. At the same time, the corresponding increase in temperature at 20° latitude was only by ~50-100K. The meridional stormtime circulation which takes about 8-10 hrs to become operative after the heating over high latitudes, seem to be appropriately explaining the observed latitudinal pattern

of temperature, after 12.3 hrs. However, after 37.5hrs. there was a significant increase in thermospheric temperatures ($\sim 1300\text{K}$) over the low and equatorial latitudes also. Prominent wavelike fluctuations which were not that significant in the earlier hours were clearly seen in the latitudinal profile of the temperature. This indicated towards the possibility of the presence of gravity waves, which are generated over high latitudes as a result of the time variation in storm energy input.

As discussed in earlier sections, the time lag for these gravity waves to appear at low latitudes is typically more than 12hrs. and their effects are known to persist for long time durations which can, at times, be few days. The temperature after 37.8hrs seemed to be approaching the prestorm values over almost all the latitudes. Figure(4.7) is another representation of the temperature variations during the storm. In these four surface plots the longitudinal variations are also shown alongwith the latitude. Significant modulations were observed in temperature with latitudes, but no corresponding longitudinal variations were seen. This showed that, during geomagnetic disturbances, the coupling between the low and the high latitudes becomes prominent, and manifests itself in the form of the variation of the thermospheric temperatures which are more pronounced only as a function of the latitude.

Apart from this, under the influence of the various energy and momentum sources during a geomagnetic storm, the neutral composition as well as the ionospheric densities also undergo significant changes over low latitudes. While O_2 and N_2 enhancements have been reported by *Prolss* [1982] over low latitudes, *Mayr et al.* [1978] showed some sort of a uniform increase in all the constituents. The effect on atomic oxygen density was somewhat less pronounced over low latitude regions. Both enhancements and depletions of ionisation

densities are possible at any altitude within the low latitude thermosphere depending upon the dominant processes in that region. The height of the F-layer also had been observed to increase on occasions [*Matuura et al.* 1972; *Prolss*, 1980; *Miller et al.* 1984]. Extending the above mentioned case study, more systematic investigation of the low latitude thermospheric response to geomagnetic storms were carried out from Mt.Abu, wherein,

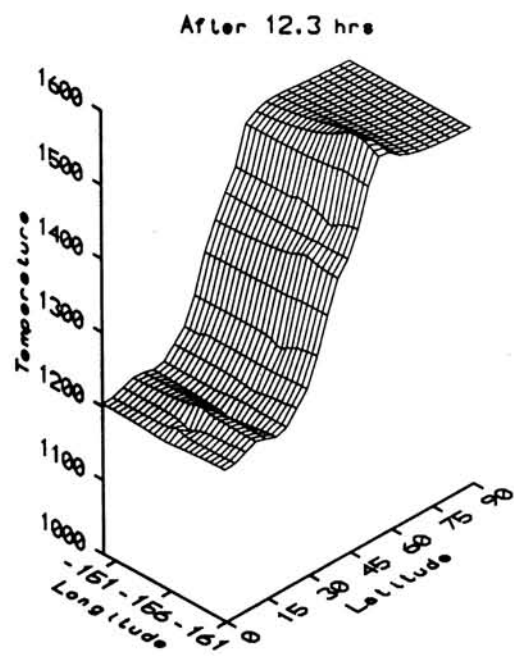
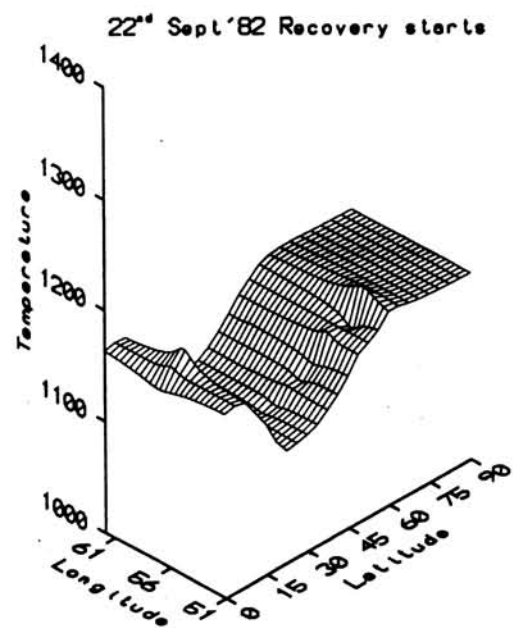
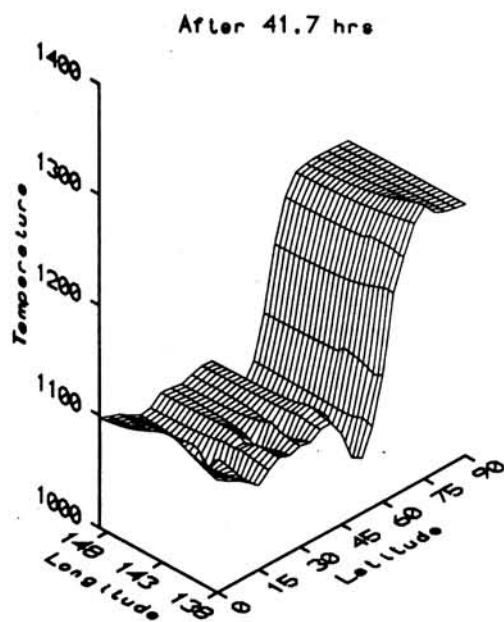
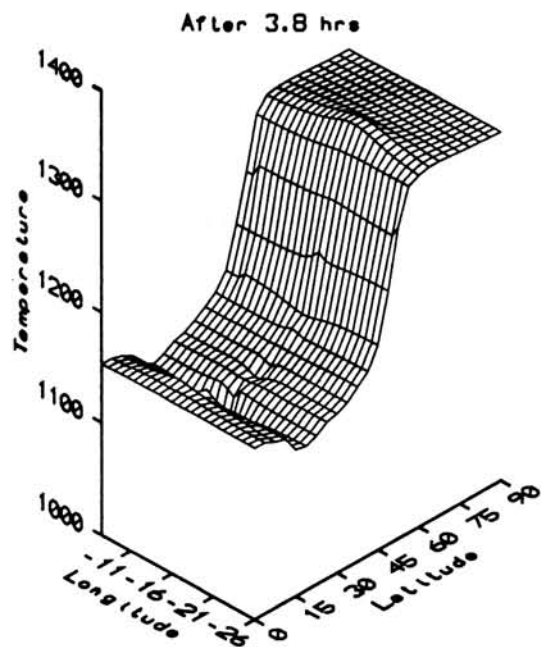


Figure 4.7: The surface plots of the variation of in situ measured thermospheric temperatures.

an attempt is being made to show the variabilities of neutral temperature and meridional winds with respect to changes in the solar wind energy input are presented and discussed.

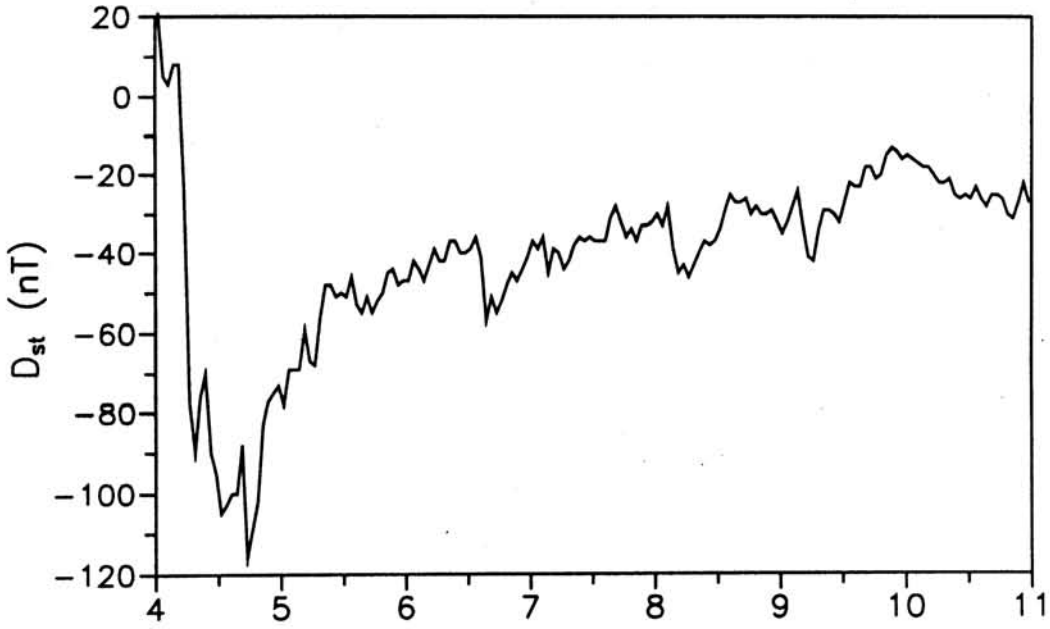
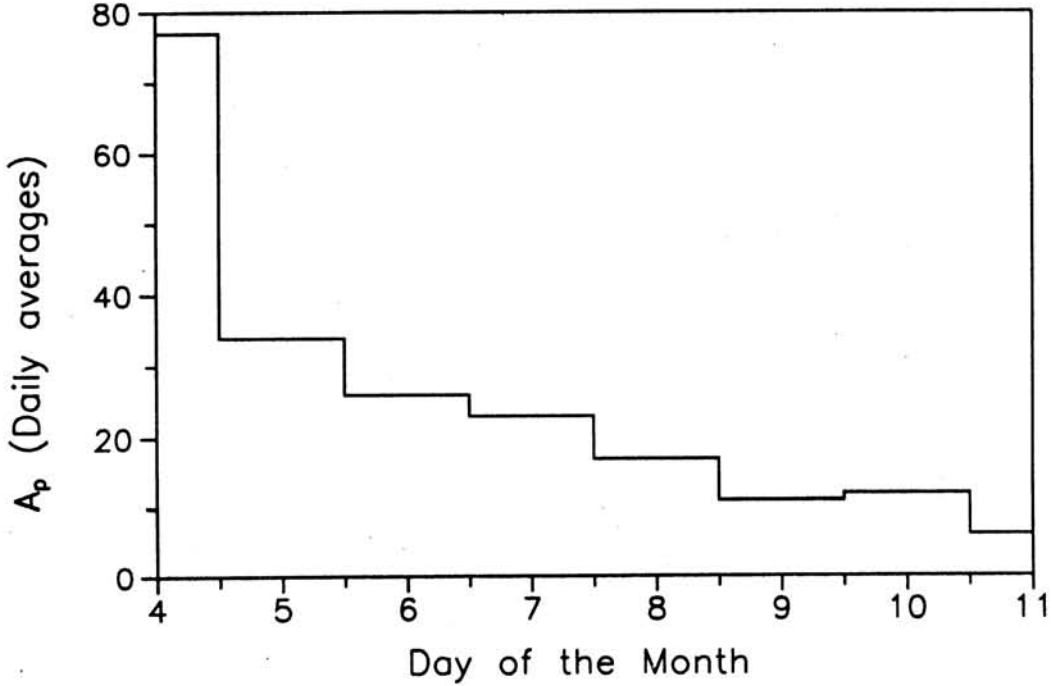
4.11 Data Presentation

Three moderate geomagnetic storms, during November 4-10, 1993, December 6-10, 1993 and during February 5-14, 1994; have been chosen for the present study, as spectroscopic line profile measurements at OI 6300\AA from Mt. Abu during these events were available. Figure(4.8) to Figure(4.10) depicts the D_{st} values for all the three events.

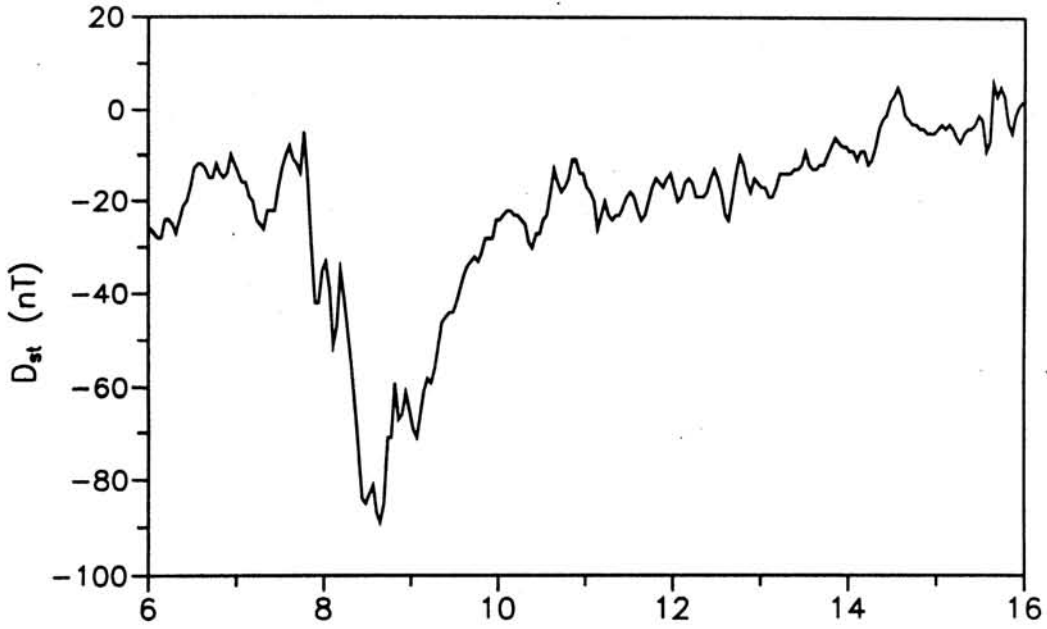
Figure(4.8) shows a moderate geomagnetic storm, which commenced on 4th November, 1993. As seen in the figure, the main phase of the storm remained active for more than 20 hrs and then the recovery of the storm set in. The recovery lasted six days. The D_{st} reached its prestorm levels only after 10th Nov'93. A sort of oscillatory behaviour was observed in D_{st} values between 6 to 10th Nov. Figure (4.9) shows a classical storm sequence with the main phase of the storm during 6-8 December 1993. The recovery phase started during 8-9 extending upto 10-11 December, beyond which a slow recovery is seen upto December 15. Figure(4.10) represents the third storm event, the intensity of which was nearly double that of the previous storms. Very large oscillatory features were seen for the whole period from 5 February to 14 February. The recovery on this occasion had been rather slow and it could well be a recurring storm, in which case it represents a complex dynamic event.

The storm during the December'93 period was unique in the sense that it created lot of unusual features over high latitudes. F-region patches in 6300\AA were observed over the polar cap for a period of over 9 hours on December 8th at Eureka ($70^{\circ}N, 80^{\circ}W$) northwest territories, near the geomagnetic north

pole [*Steele and Cogger, 1996*]. The solar wind speed was measured to be 490 km/s, and its number density varied slowly between 3 and 14/cm³. The interplanetary magnetic field IMF B_z component remained southward for an extended period of time (-7nT) providing an ideal situation for the generation of F-region patches. The auroral

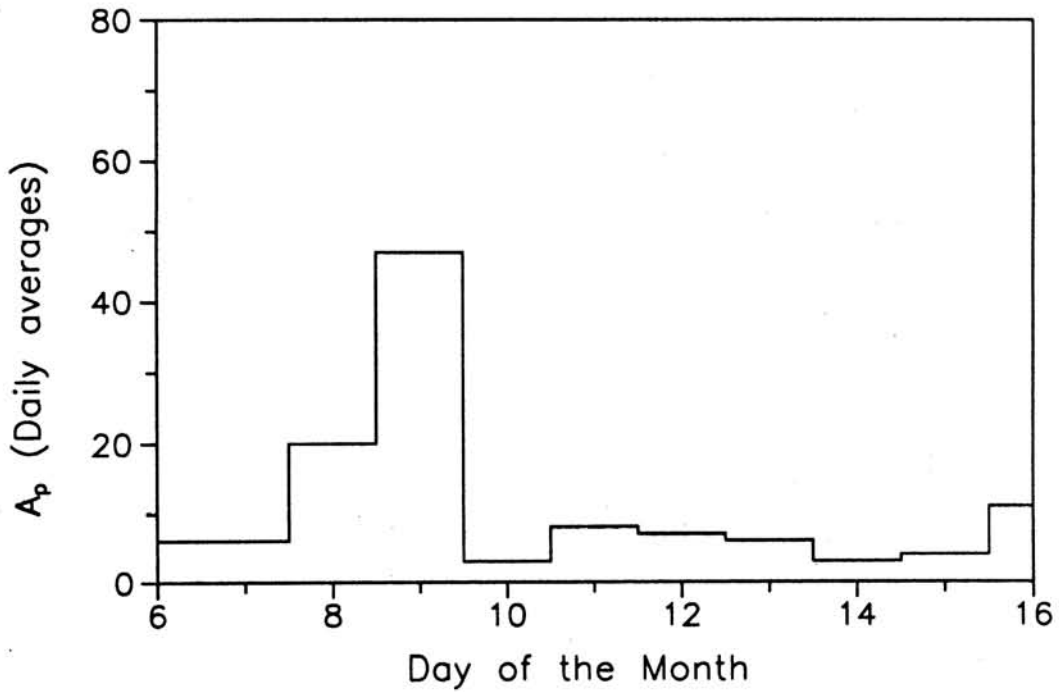
D_{st} variation for Nov'93Daily Average Indices A_p for Nov'93Figure 4.8: The variation of D_{st} and A_p for November 1993

D_{st} variation for Dec'93



(a)

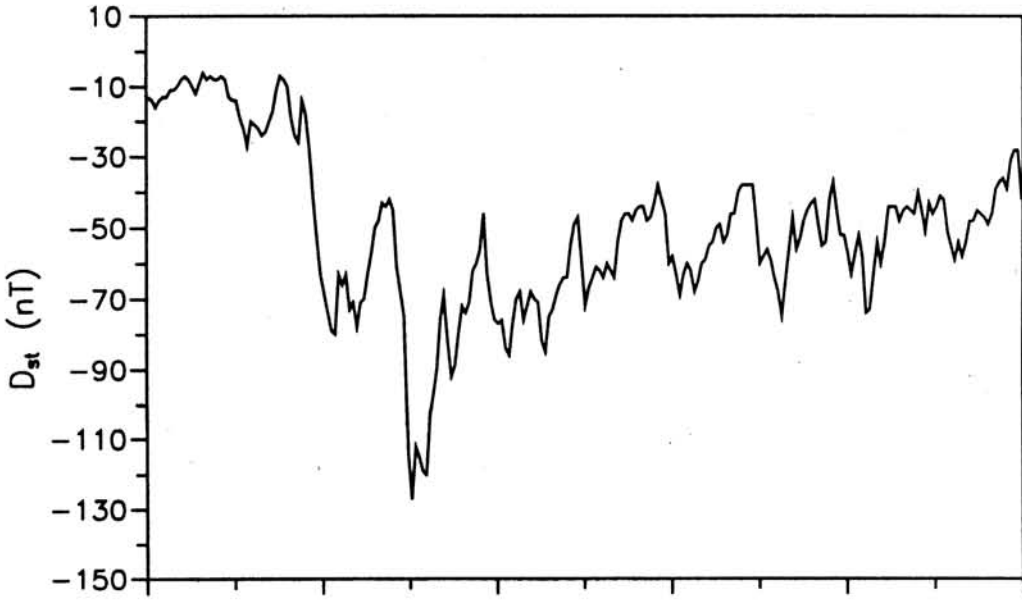
Daily Average A_p Indices for Dec'93



(b)

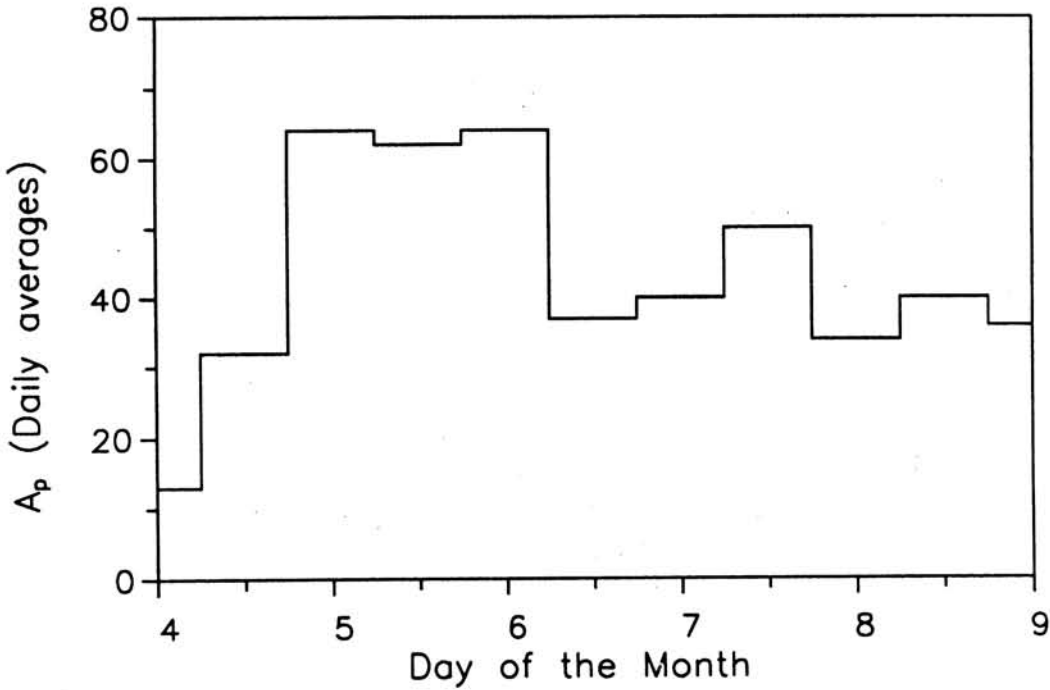
Figure 4.9: The variation of D_{st} and A_p for December 1993

D_{st} variation for Feb'94



(a)

Daily Average Indices A_p for Feb'94



(b)

Figure 4.10: The variation of D_{st} and A_p for February 1994

oval was severely displaced as the Defence Meteorological Satellite Program (DMSP) F10 satellite observed the low-latitude particle cusp at $\sim 70^\circ$ corrected geomagnetic latitude.

4.12 Temperature variations over Mt.Abu

Figure(4.11) shows three panels, exhibiting the variation of the observed thermospheric temperatures on November 7th, 8th and 9th, 1993. The average daily A_p indices representing the geomagnetic level of the day is also given at the top of each panel. The temperatures on the 7th night showed large temporal fluctuations. The lowest observed temperature on this night was $\sim 900\text{K}$ at $\sim 2200\text{hrs}$, and the maximum was observed at $\sim 2130\text{hrs}$ and $\sim 0000\text{hrs}$ to be $\sim 1400\text{K}$. The temperatures on an average, showed large deviation ($\geq 300\text{K}$) from the MSIS model predictions. Contrary to the observations on 7th, the temperatures on 8th and 9th night underwent changes which were more gradual. The temperatures on 8th, between 2030 to 2200hrs displayed a steady decrease from 1100K to 700K. Within next one hour or so, it increased to $\sim 1500\text{K}$. An equally fast recovery back to 900K at 0030hrs seemed to have taken place after 2330hrs. However, after 0030hrs the temperatures exhibited the steady increase once again, rising to new levels of $\sim 1400\text{K}$.

The MSIS model grossly underestimated the temperatures, except at around $\sim 2145\text{hrs}$. As explained in earlier sections, TADs can be a very significant source of energy for thermosphere over low and equatorial latitudes during late recovery phases of the storms. The slow temporally changing energy input over polar latitudes can launch these TADs. The observed temperature variation on 8th could be due to the presence of the TAD over Mt.Abu on this day and also on the next day. The slow oscillatory feature seen on 9th Nov., indicated towards the presence of large scale gravity wave features. Similar

rise and fall of temperatures as seen on 8th were observed though the modulations were more gradual. The temperatures remained at $\sim 800\text{K}$ for nearly one hour from 2130hrs to 2230hrs. Afterwards, it increased to $\sim 1500\text{K}$ at 0000hrs, followed by a gradual decrease for the next three hours. The temperature at 0230hrs was measured to be at $\sim 880\text{K}$. Figure(4.12) shows the variation of the thermospheric temperatures on the nights of Dec.8th,

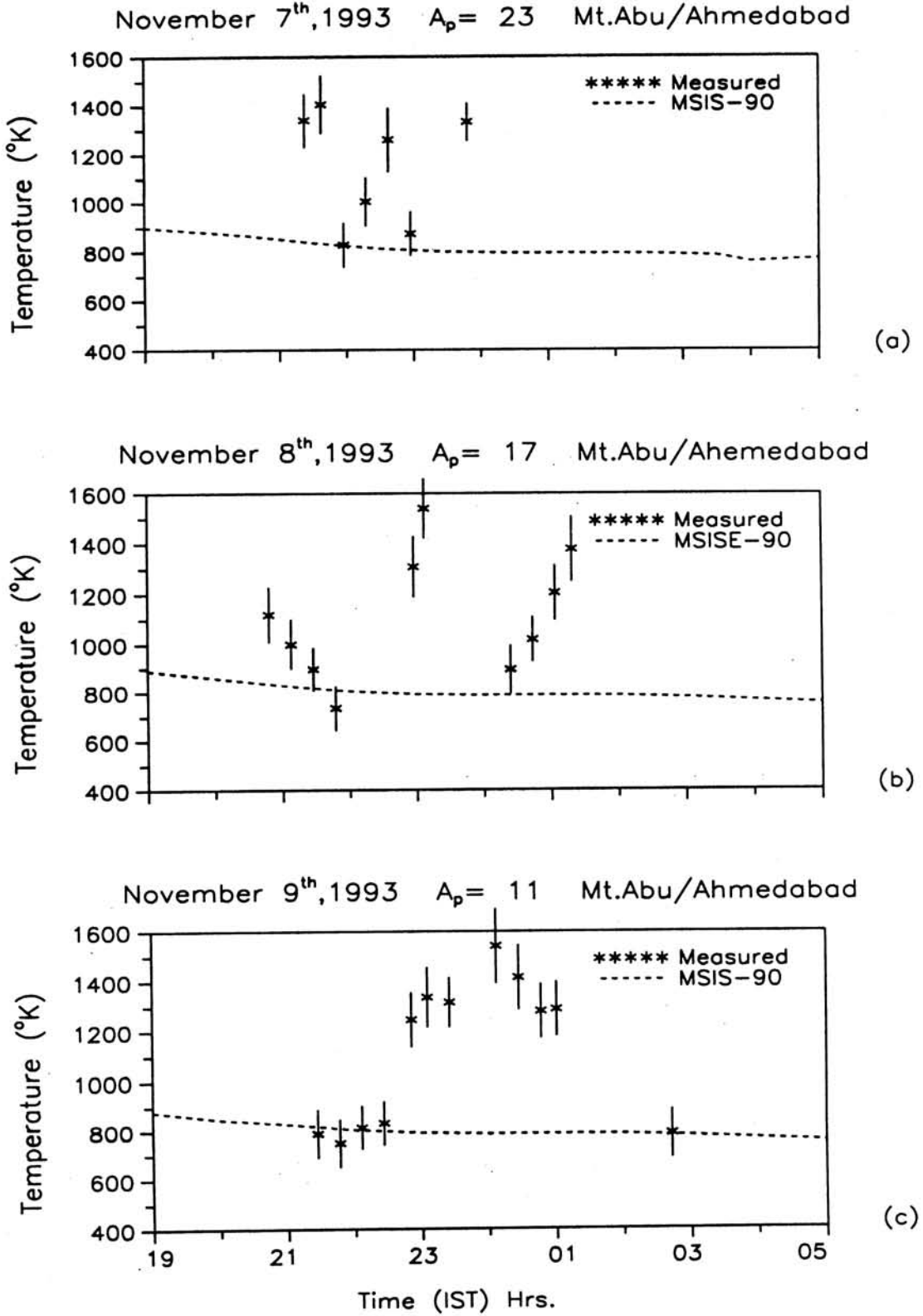


Figure 4.11: The thermospheric temperature variation over Mt.Abu on November 7th, 8th and 9th, 1993.

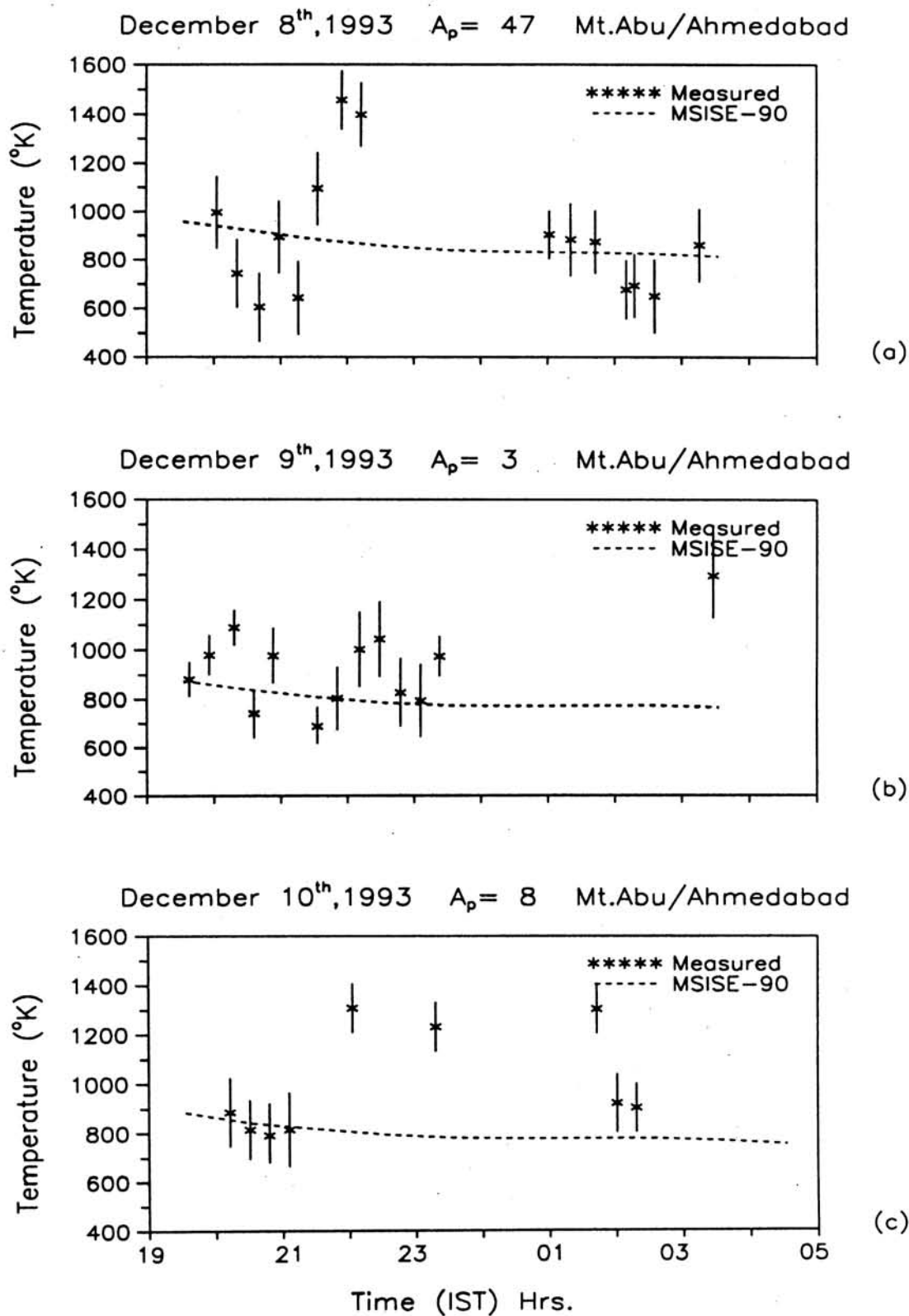


Figure 4.12: The thermospheric temperature variation over Mt.Abu on December 8th, 9th and 10th, 1993.

9th and 10th, 1993. They exhibited an oscillatory pattern indicating the presence of wave like disturbances. The periodicity of these wave like features was approximately 2.5 to 3 hrs, which is close to the periodicities earlier reported in the low latitude regions [Klostermeyer, 1973]. The important observation on 8th night was the sudden pulse like increase in temperature i.e. a change by $\sim 800\text{K}$ in just one hour. This pulse like perturbation seemed to be superimposed upon the smaller wavelike perturbations observed later in the night after 0100hrs. The temperatures as observed on 9th night were devoid of any such sudden increase but the wavelike perturbation was very clearly discernible. The model temperatures generated taking into consideration the average solar decimetric flux ($F_{10.7}$) and the level of geomagnetic activity on that particular day are also depicted. The average temperatures on 9th Dec. seemed to be lying close to the MSIS model predictions. The temperature on 10th night remained low (i.e. $\sim 800\text{K}$) for more than 1 hour during 2000-2100hrs premidnight hours and also at $\sim 0200\text{hrs}$, late in the night. Because of the lack of sufficient points, between 2200hrs to 0100hrs, it was difficult to associate any particular feature or variation to the temperature. The MSIS model predicted temperatures agreed well with the measurements during the early evening hours and later beyond midnight.

The observations during the third storm, on 5th, 6th and 7th Feb'94, displayed very high temporal variabilities. The 5th night, which corresponded to the main phase of the storm, seemed to be responding well to the variations in the storm energy inputs. The energy deposition, during this storm, took place in the form of recurring depressions in the D_{st} indices. On Feb 5th, the temperatures $\sim 700\text{K}$ at 2200hrs seemed to have risen to $\sim 1500\text{K}$ at 0100hrs and $\sim 1200\text{K}$ at 0400hrs. However, such enhancements in the main phase of the storm, can be explained on the basis of the meridional circulation pattern. As

explained earlier, such circulation cells get generated and the effects percolate to low latitudes within 8-10hrs of initial energy deposition over higher latitudes. Similar kind of trend was observed on 6th Feb also. However, the extent of variabilities in temperature seem to have reduced on Feb 7th. The reason for for this was that the intensity of the magnetospheric ring current as obtained from the D_{st} , had started decreasing implying that most

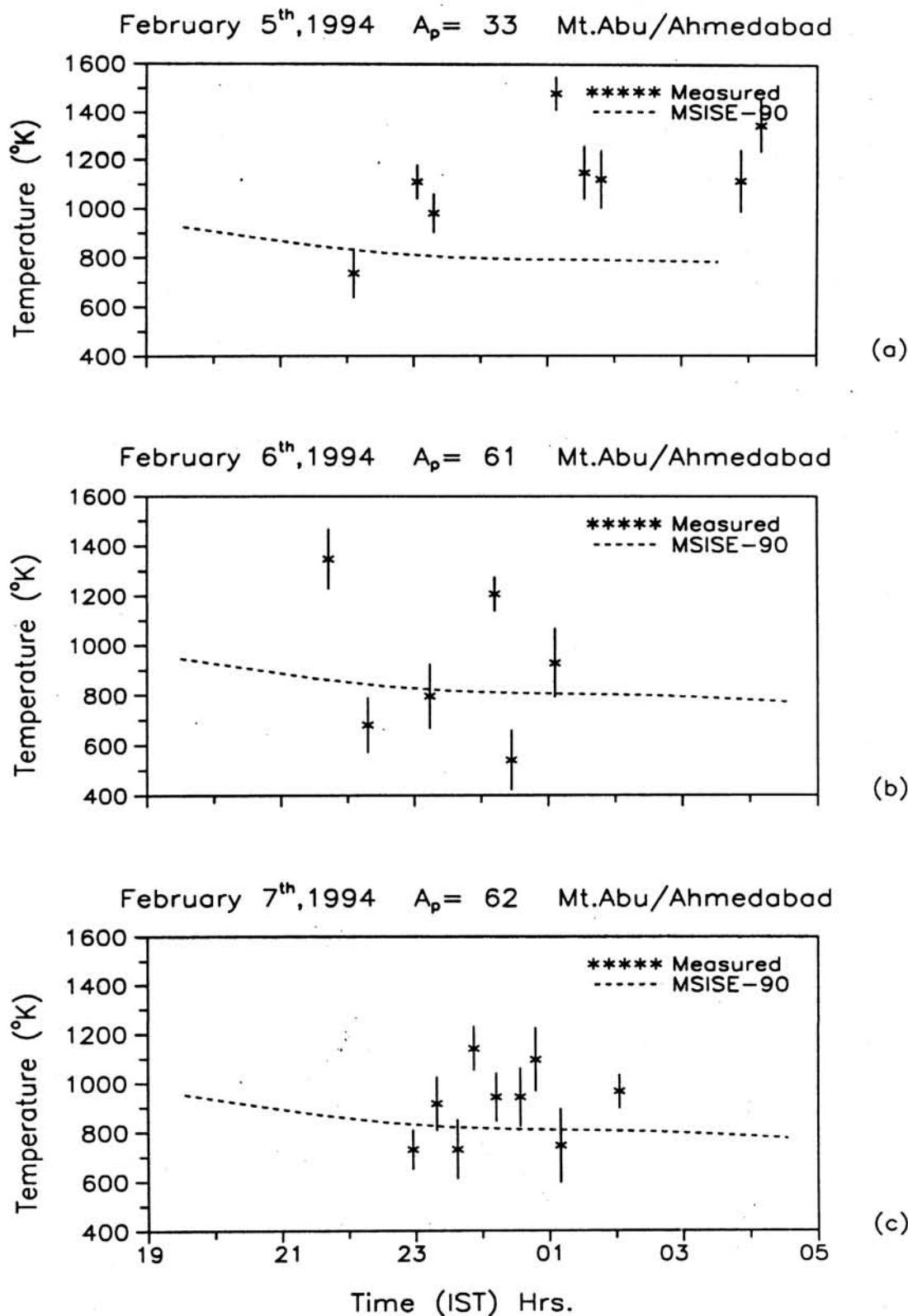


Figure 4.13: The thermospheric temperature variation over Mt.Abu on February 5th, 6th and 7th, 1994.

of the primary storm energy input into the atmosphere had already taken place. However, the recurring nature of this storm can recharge the atmosphere with energy making it difficult to interpret the observed temperature variations on different nights. The Feb 6th and 7th were geomagnetically the most active nights, as the average planetary indices A_p on these days were 61 and 62 respectively.

Since Mt. Abu is situated at a low geographic latitude, the neutral dynamics or wind pattern under quiet geophysical conditions is dominated by the EUV forcing. The winds would tend to blow away from the equator, poleward during the day and evening hours, and equatorward later in the night as the polar regions remain relatively hotter at that time. During storms however, this wind circulation gets modified and results in a predominantly equatorward flow carrying and redistributing the storm energy to the lower and equatorial latitudes. The effects of these perturbations are not uniform in thermosphere and the ionosphere.

In the following section, an attempt is made to study the prevailing coupling between the low latitude thermosphere and the ionosphere during geomagnetically active periods in similar lines to that discussed in chapter 3 with regard to magnetically quiet periods.

4.13 The Low Latitude Thermosphere-Ionosphere Coupling During Geomagnetic storms

The observed thermospheric temperatures, meridional winds and the ionospheric variations on each night are discussed in conjunction with Rishbeth's servo model. Figures(4.14 to 4.20) display four panels, of which the top two panels show the thermospheric temperature and wind variation with time,

and the lower two display the ionospheric parameters. In panel(c) the observed airglow intensity is also compared along with the measured electron density at 250 km. And in the panel(d) the measured F-layer heights are compared with the servo model estimated heights. These panels are generated for each individual nights. The discussion corresponding to the panel (c) are done in the next section where some important aspects of the atmospheric chemistry during the geomagnetic storms are discussed.

The measured meridional wind on Nov. 8th [Figure(4.14b)] showed change from initial poleward wind at 2045hrs to weak equatorward wind at 2150hrs. The wind, later became poleward again after 2300hrs. The overall equatorward flow of the wind was relatively weaker ($\sim 70\text{m/s}$) in magnitude than the poleward flow ($\geq 150\text{m/s}$ at 2045hrs). The predominantly poleward wind on this night indicated towards a hotter lower latitude thermosphere. This was further indicated by the large thermospheric temperatures measured simultaneously on this night. The observed F-layer equilibrium height was at around 250km in the initial hours around $\sim 2030\text{hrs}$. Afterwards, the gradual equatorward flow of meridional wind forced the F-layer plasma up along the magnetic field lines. After 0030hrs, when the wind became poleward, a simultaneous downward movement was registered in F-layer altitude.

In order to establish the variabilities involved in the coupling between the thermosphere and the ionosphere, the ionospheric heights h_{max} were estimated using observed temperatures and winds in conjunction with the Rishbeth's servo model. The estimated h_{max} altitudes were compared with the observed F-layer heights [figure(4.14d)]. The agreement between the the two was remarkably good during 2100-2200hrs. However, at other times the estimated heights were found to be lower than the observed one. The differences between the two indicate towards the variabilities due to electric field induced movement to the

layer, which has not been taken into account. However, the absence of the simultaneous measurements on electric field makes it difficult to substantiate the contribution of these fields. But, the very fact that differences exist between the two need a more detailed examination of the electrodynamical processes governing the low latitude F-region, especially during storms.

However, a different situation was seen on Nov. 9th [Figure(4.15)]. On this night, during 2100 to 2230hrs when the temperatures were low the meridional wind flow strong poleward ($\sim 200\text{m/s}$). In the next hour, the poleward flow gradually weakened in magnitude becoming almost zero at 2330hrs. A rise in thermospheric temperatures was observed during this period. A similar exercise, comparing the theoretical and measured F-region equilibrium heights, was carried out for Nov.

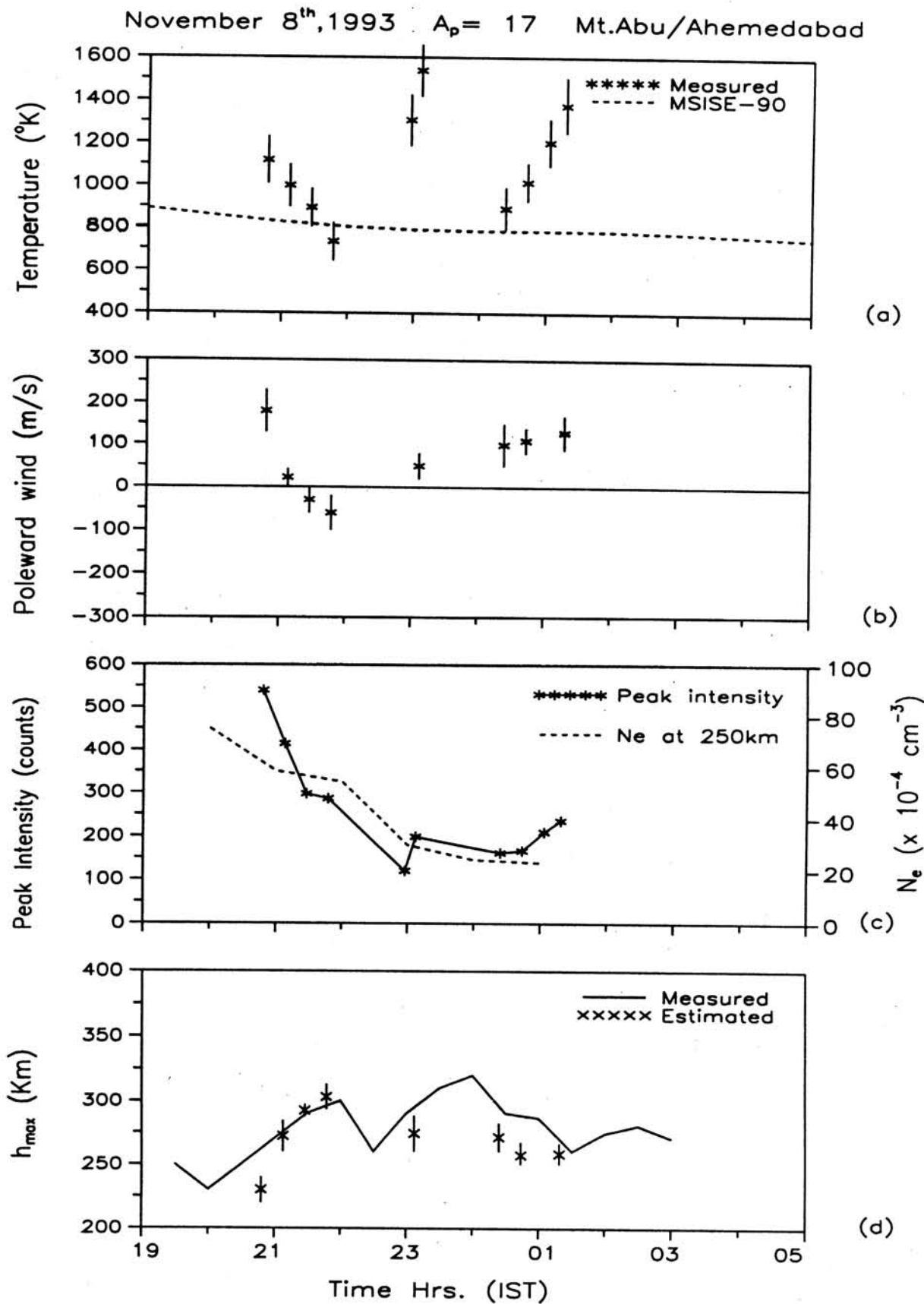


Figure 4.14: The thermosphere ionosphere system (TIS) behaviour on 8th November 1993

9th also. The poleward phases of the wind between 2100-2200hrs were associated with downward movement of the F-layer. The gradual change of the poleward wind to equatorward between 2200-2300hrs was seen to coincide with the upward excursion of the F-layer. The servo model estimated h_{max} altitudes when compared with the observed heights, were found to be agreeing well during 2100-2330hrs. This substantiates the observation that the neutral temperature and the winds are the main drivers of the low latitude ionospheric dynamics. This also means that the electrodynamical effects must be minimal at the time of the observations. However, the same cannot be said for the measurement at 0230hrs.

The measured meridional thermospheric wind for December 8th [Fig(4.16b)] showed a large equatorward trend ~2200-0200hrs. During the initial hours i.e. upto 2100hrs the wind was poleward and small in magnitude (~50 m/s). The small poleward wind on this occasion indicates towards the competing roles played by the storm induced equatorward wind and the poleward wind caused by the daytime equatorial heating by EUV radiation and the transequatorial winds from summer hemisphere to winter hemisphere since Mt.Abu is in the winter hemisphere during this period. Another important observation was, that, the sudden increase of temperature during 2100-2200hrs was concurrent with the strong equatorward surge in the meridional wind. This could be an indication for the meridional winds playing a crucial role in carrying the energy from poles to the lower latitudes. The F-layer height exhibited a steady upward movement rising upto a max height of 400 km [fig(4.16d)]. This excursion of F-layer was associated with the strong equatorward movement of meridional wind occurring at the same time. However, the excursion rate of the F-layer was slower than the changes in the meridional wind velocity. To estimate the extent upto which the neutral wind and the temperatures would

affect the F-layer movement, the F-layer balance heights h_{max} were theoretically estimated using the observed neutral parameters in the Rishbeth's servo model.

Comparison between the measured and the servo model estimated h_{max} revealed that the agreement between the two is not good, except during 0100-0300hrs. Significant differences were observed between the two for the remaining times. This

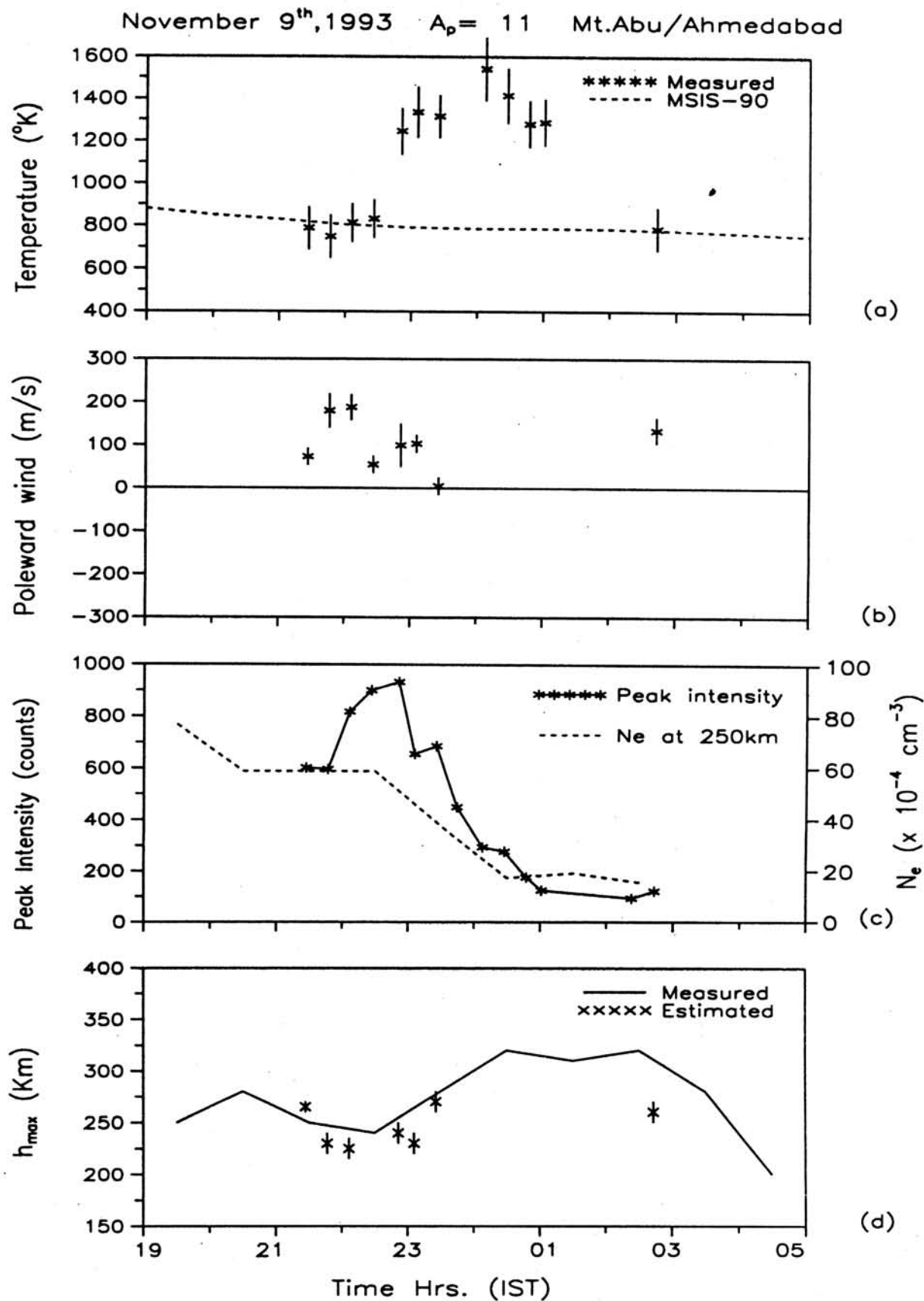


Figure 4.15: The thermosphere ionosphere system (TIS) behaviour on 9th November 1993

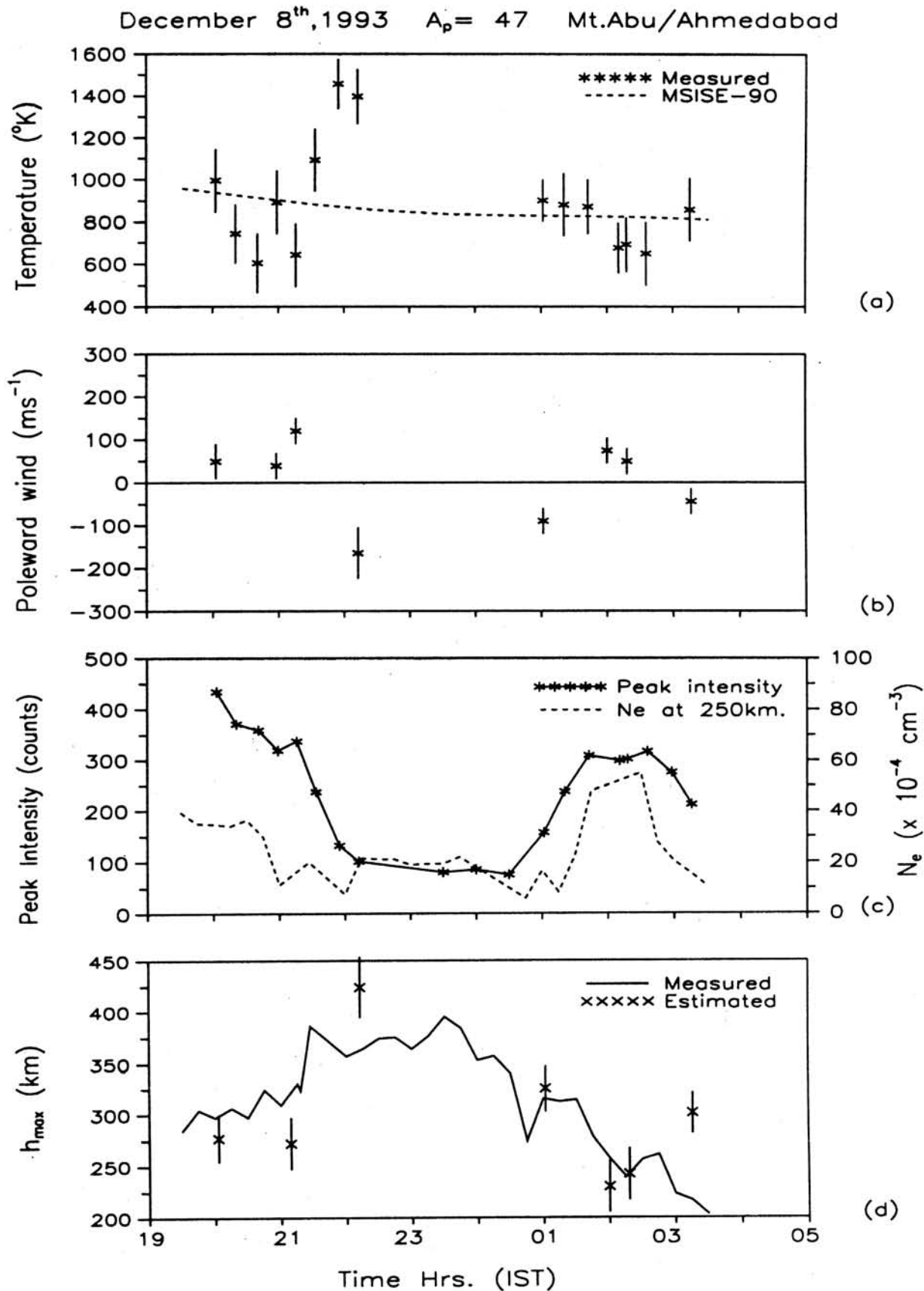


Figure 4.16: The thermosphere ionosphere system (TIS) behaviour on 8th December 1993

indicated towards the fact that the movement of the F-layer is no longer governed solely by the neutral parameters. The electrodynamic forcings seem to be having pronounced effects on the plasma motions. It has been reported in the literature that strong electric fields of magnetospheric and polar origins, can be mapped down to low latitude ionosphere during geomagnetically active periods [Fejer 1997 and references therein]. These electric fields and their associated variabilities can cause additional movement in the F-region plasma. The observed differences indicated towards the presence of such fields. However, no direct electric field measurements could be made during the course of this study.

The meridional wind on Dec. 9th before 2130hrs, as seen in figure(4.17b), was poleward with small magnitudes which gradually became equatorward (~ 100 m/s) at ~ 2200 hrs. The altitude of the F-layer peak electron density (h_{max}) observed on this night seemed to follow the variabilities in the wind. The h_{max} altitude remained more or less at the same altitude whenever the wind magnitudes were small. The large upward excursion of the h_{max} corroborated well with the equatorward phases of the meridional wind. The servo model estimated h_{max} altitudes using observed thermospheric temperatures and the winds, were found to be agreeing well with measured h_{max} heights. The differences observed between the two were within the errors ($\pm 30-50$ km) [fig(4.17d)]. Unlike the previous night, the movement of the F-layer of ionisation on this night seemed to be dominated more by the variations in neutral parameters than the electrodynamic parameters like electric fields. The variabilities as seen in temperature, were also discernible in the observed h_{max} altitudes, though the effect was not very pronounced. These variabilities can be attributed to the presence of the traveling atmospheric disturbances (TADs) in the low latitude thermosphere.

On Dec. 10th, the F-layer remained more or less at the same altitude i.e. ~ 270 km [fig(4.18d)]. The observed meridional wind on this night was equatorward before 2200hrs. The comparison of the servo model estimated h_{max} with the measured ones, also revealed a close agreement between the two. However, at 1930 and 2230hrs, the estimations were more than the measured heights which call for further investigation. On February 5th [fig(4.19)], the observed F-region behaviour

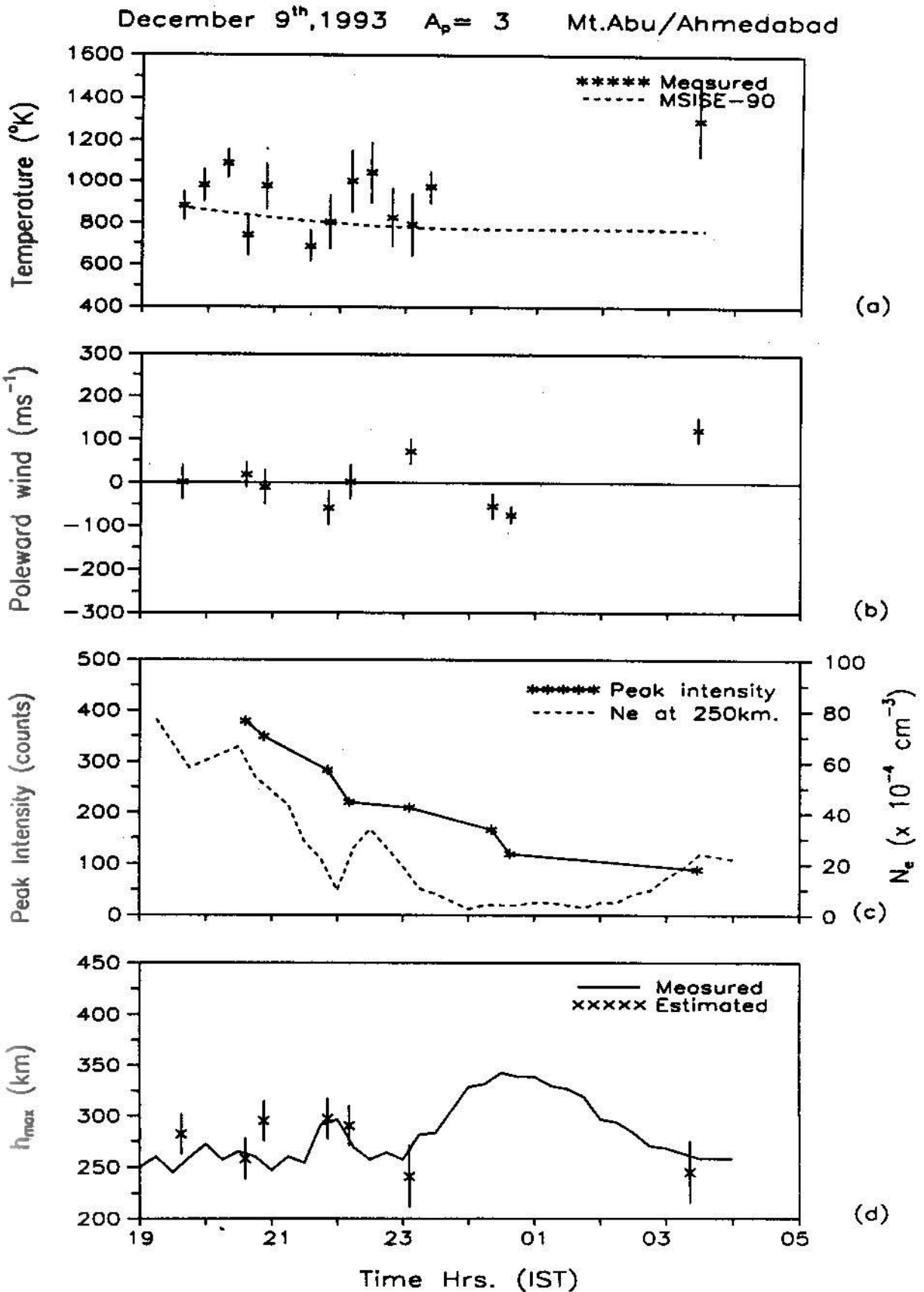


Figure 4.17: The thermosphere ionosphere system (TIS) behaviour on 9th December 1993

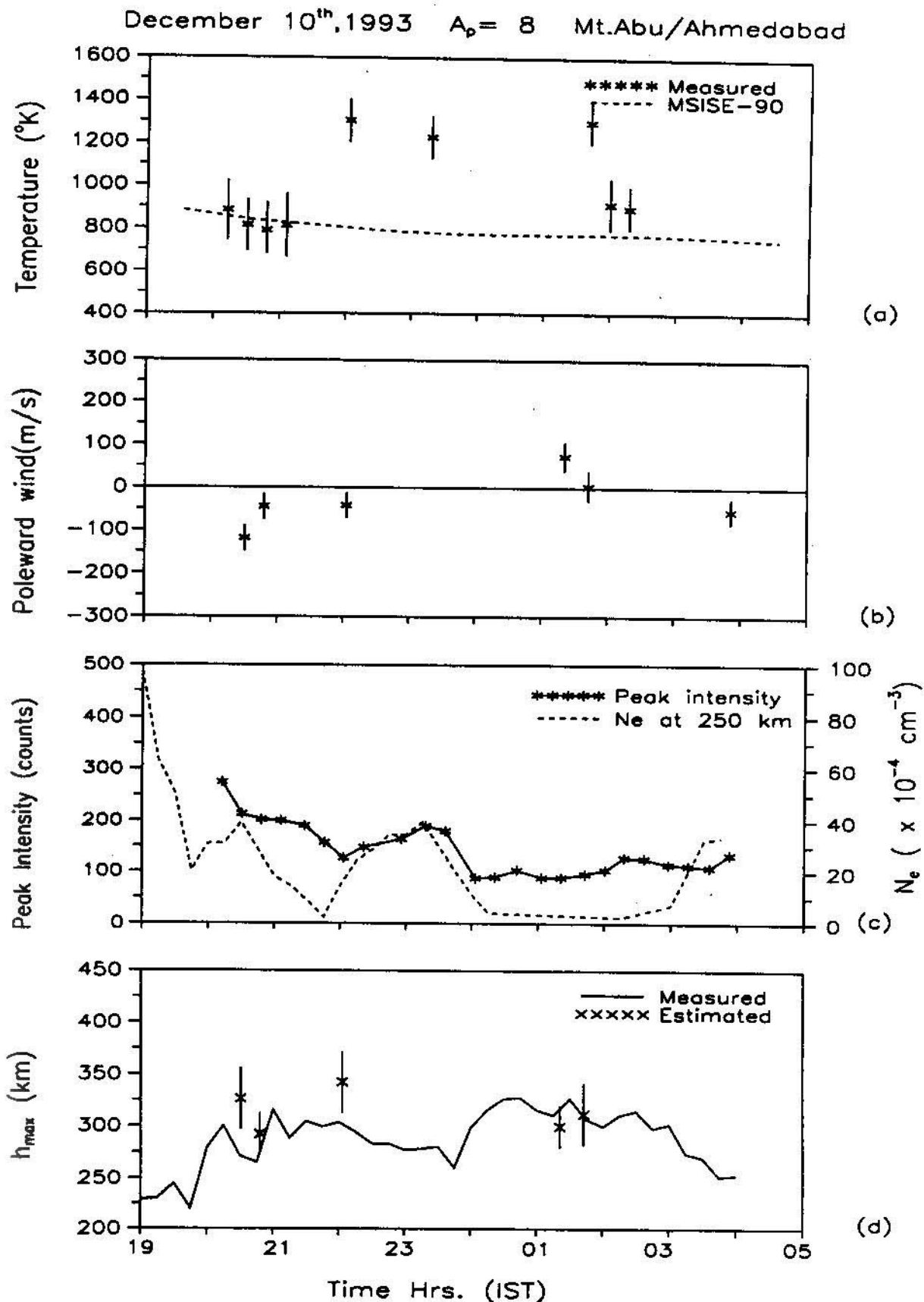


Figure 4.18: The thermosphere ionosphere system (TIS) behaviour on 10th December 1993.

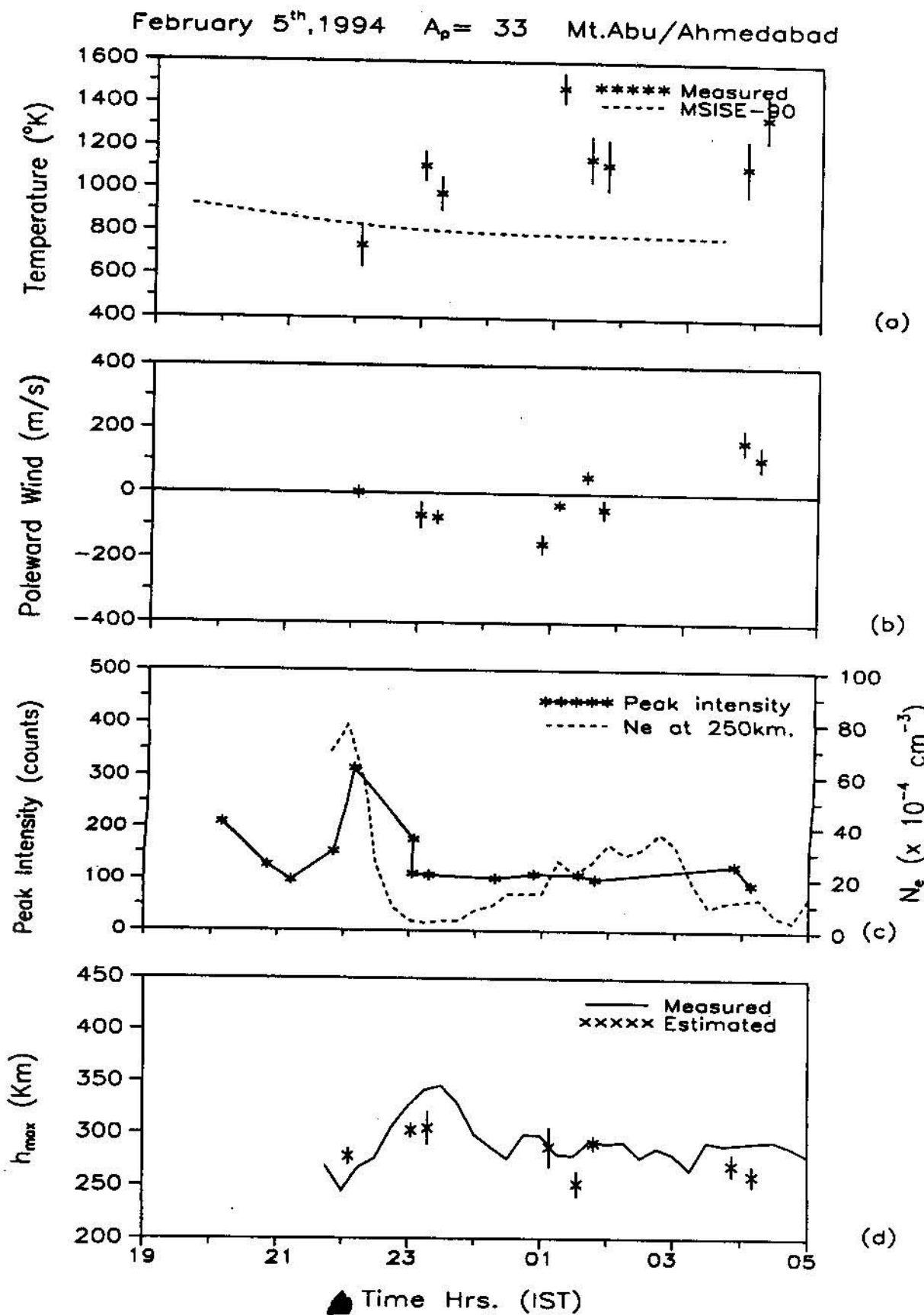


Figure 4.19: The thermosphere ionosphere system (TIS) behaviour on 5th February 1994.

was much similar to that on Dec. 9th. The F-region remained at the same altitude for an extended period of time on this night after 0030hrs till morning 0500hrs. However, before midnight, there was a brief upward excursion in F-layer height from 2200 to 2330hrs. The layer came down from 350km at 2330hrs to 270Km at 0030hrs and maintained the altitude throughout the night. While the meridional wind underwent significant changes from equatorward (200m/s) at ~0100hrs to poleward (150k/m) at 0400hrs. The reason for the equilibrium height to remain constant for such a long time despite the ongoing changes in the polarity of the meridional wind could be the compensating role played by the temperatures. The presence of electric fields get reflected in terms of differences between the observed and estimated h_{max} altitude as discussed earlier. Deviations were observed between the two on this night except at 0100 and 0140hrs which could be due to this.

In a similar exercise for Feb. 7th [figure(4.20)], a remarkable agreement between the theoretical and measured F-layer equilibrium heights was observed for most of the times. The observed meridional winds were predominantly poleward on this night. The observed temperatures seemed to have come down in magnitude in comparison to earlier days. This indicated towards the diminishing storm effects over low latitude thermosphere ionosphere system. However, the magnetic indices ap (~ 62) showed this day to be a geomagnetically active day, though the observed temperatures reveal the contrary.

4.14 Airglow Intensity Variations during Storms

An important insight into the F-region airglow chemistry is obtained by comparing the observed OI6300Å red line intensity with F-region electron density. At any given instant of time in the night, the airglow intensity is proportional to the electron density at the emission region (250km) [Barbier and Glaume,

1962]. Therefore, during nighttime, the electron density at 250km would undergo an exponential decrease with time unless supplied with additional ionisation from indirect sources such as energetic electrons from high latitudes. As a result, similar decrease in airglow intensity would also be expected. However, Figure(4.16c)

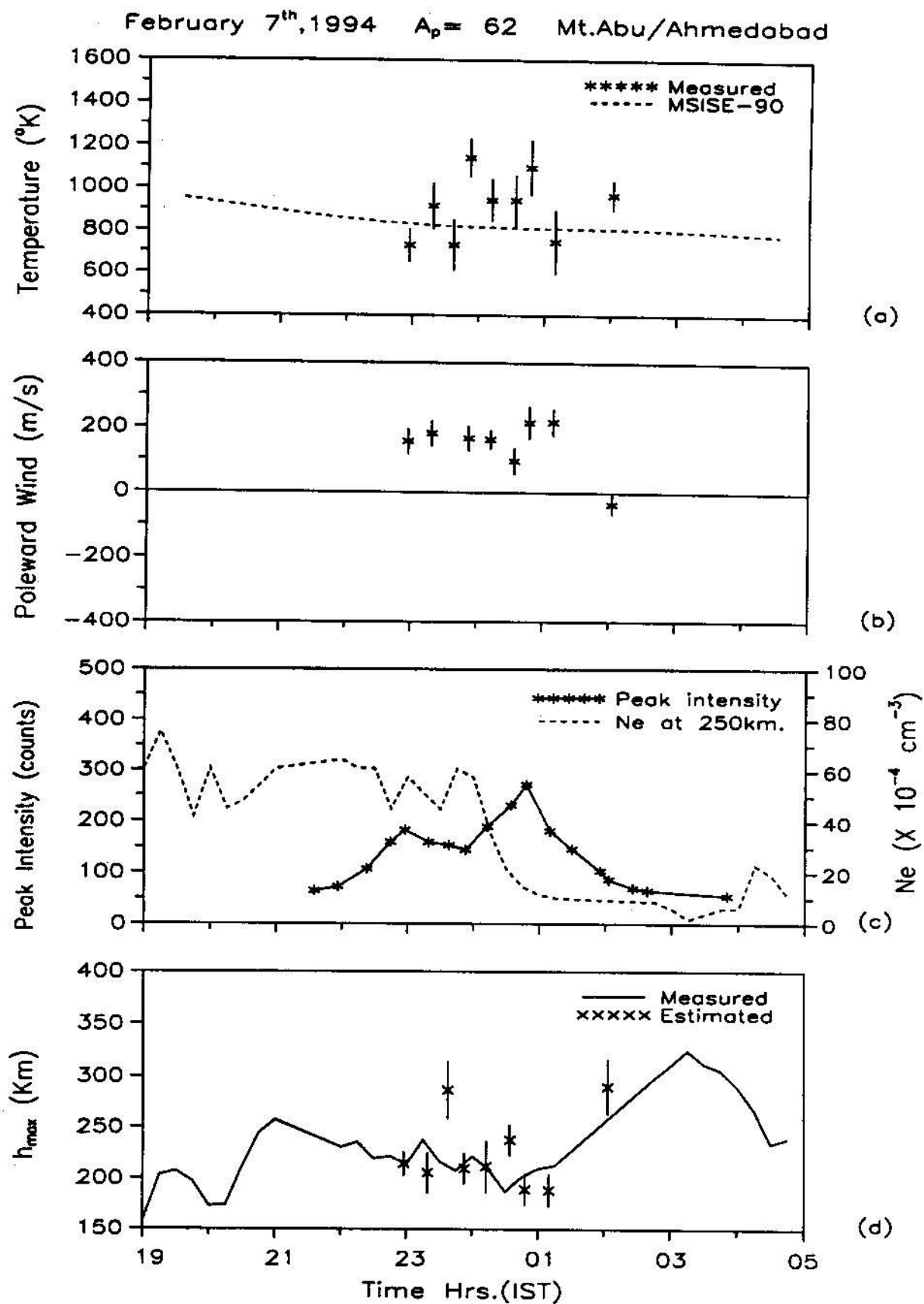


Figure 4.20: The thermosphere ionosphere system (TIS) behaviour on 7th February 1994.

(pp 143) of Dec. 8th, shows a very striking feature between 21:00 hrs to 22:00 hrs. The observed airglow intensity in that time span experienced a change by a factor of 3, while corresponding change in electron density is only about 3-4%. In other words, electron density remained almost constant, while airglow intensity underwent a dramatic change. Rest of the times, however, the variations of airglow and electron density were proportional and go hand in hand. This was the first time that such an anomalous behaviour in airglow intensity was seen over low latitude station like Mt.Abu.

There can be two reasons for this anomalous decrease in airglow intensity, (i) if the formation of O_2^+ ions is dramatically reduced, (ii) the excited metastable oxygen atoms ($O(^1D)$) which emit the airglow, are quenched even before they could radiate. The possibility of first reason being true is ruled out as, in the nocturnal ionosphere, the main cause of O_2^+ formation is the charge exchange between O^+ and O_2 . During geomagnetic storms, an increase in molecular density over F-region heights has been reported by many earlier researchers [Pross 1981]. However, such an increase in molecular density would be expected to have resulted in an increase in airglow emissions. Therefore, the main source of excited $O(^1D)$ atoms i.e. the dissociative recombination of O_2^+ ions, remains totally unaffected as the electron density remains the same. But because of the fact that molecular concentrations are increased during storms, the quenching of excited $O(^1D)$ also becomes more efficient. This deactivation by quenching would be caused by collisions with molecular species. The additional energy lost in the quenching would be utilised in the excitation of the quenching molecule. The dominant quenching species for the $O(^1D)$ atoms is molecular N_2 .

The increased thermospheric energy input in the lower thermosphere during

geomagnetic storms might cause the upwelling of N_2 rich air in the airglow region. The high N_2 quenching rate coefficients of $7.9 \times 10^{-11} \text{ cm}^3/\text{s}$ would lead to drastic reduction of airglow intensity as seen from a ground based station. [N_2 quenching rate coefficient is much faster than any other quenching agent eg. molecular O_2]. Therefore it is suggested that any thermospheric temperature rise of ~ 800 K during a geomagnetic storm can at times lead to a simultaneous decrease in observed airglow intensity by more than 30% because of the enhanced quenching by molecular N_2 .

There are other instances too when a sudden rise in thermospheric temperature was seen but with no corresponding airglow quenching effects. For instance, on Nov. 8th and 9th. temperature enhancements were seen around midnight. The airglow intensity on Nov. 8th, however, was seen to be following the decay of the electron density at 250km, as can be seen in the figure(4.14c). On Nov 9th, a sudden rise in intensity was observed at 2200hrs. This can be understood by seeing the position of the altitude of the F-layer peak at that time. The F-layer, which can bring additional ionisation for such an increase in airglow, was also found to be at 250km. This is supported by further observations when the F-layer height moved upwards from the airglow emission region at ~ 2300 hrs and both the electron density and the airglow intensity immediately showed a decay. The airglow intensity pattern on Feb. 5th, 7th could also be explained in similar lines.

4.15 Conclusions

Based on the results presented in this chapter, it could be concluded that the low latitude TIS continue to behave as a closely coupled system even during geomagnetically disturbed periods inspite of large variabilities inflicted on the thermospheric parameters namely temperatures and winds. The large

scale neutral dynamical effects like meridional winds, Traveling Atmospheric Disturbances are also getting reflected in the behaviour of the TIS, and one is able to explain these variabilities using the servo model. On most of the occasions, similar to the quiet time behaviour, the electrodynamical effects are only marginal. The significant variations in thermospheric composition is offered as a viable explanation for the large changes in the airglow intensities observed on occasions.

Chapter 5

Variabilities in the Thermospheric Temperatures and their Representation by the Model

5.1 Introduction

In the last two decades, the increase in the number of coordinated programs involving both ground based radio and optical techniques, along with the spaceborne instruments have provided high quality measurements on various thermospheric, ionospheric and magnetospheric parameters. Based on the important and diverse results obtained by means of these coordinated measurements, it is now becoming possible to successfully initiate the development of global models of thermosphere and ionosphere. These theoretical models generate a number of thermospheric- ionospheric parameters for all locations and times as a function of season for a wide range of geomagnetic activity levels. They predict only the average climatic conditions of the upper atmosphere at any given time. In spite of the limitation in representing the instantaneous conditions, the models do provide us a means of theoretically studying the fundamental processes that affect the upper atmosphere vis-a-vis the experimental results on individual atmospheric parameters obtained during isolated event based studies.

In the present study an attempt has been made to compare the neutral temperature measurements with the model predictions , and the differences are

analysed in detail. The purpose of such a study is to account for these temperature differences, keeping in view the atmospheric processes which are not already included in the model. This analysis has been carried out for various geophysical conditions in order to understand the response characteristics of the low latitude thermosphere ionosphere system.

In the following sections, a brief background to the thermospheric model namely MSIS (mass spectrometer incoherent scatter) used extensively in the present investigation, is given in a historical perspective. Following this, a discussion on the comparison of measured thermospheric (F-region) temperatures over the low latitude station Mt.Abu (24.6° N, 72.7° E geographic; 20° N dip lat.), with the corresponding 'MSIS' (thermospheric) model predictions are given. Finally, the limitations of MSIS utility over low latitudes as on today are discussed keeping in view the experimental results obtained by various studies from locations like Mt.Abu and elsewhere in the globe.

5.2 Development of MSIS model - A Perspective

It is well appreciated that the thermosphere is a nonlinear medium [Rees *et al.* 1988] which is constantly under the influence of solar radiation energy. The energetics of the thermosphere is modified to a great extent by the continuously fluctuating transfer of energy and momentum from the magnetosphere higher above, and also from the lower and middle atmosphere. The processes and mechanisms redistributing the energy and momentum between the neutral and ionised species i.e. thermosphere and ionosphere system (TIS) are known and understood to a good extent. However, only few individual processes could be modeled so far and a true, self consistent, coupled thermosphere - ionosphere model formulation is still in its infancy. Though, during geomagnetically quiet times, the solar wind energy input to the TIS via the

magnetosphere is significantly reduced in comparison to the solar radiation energy, even then, a quantitative description of quiet-time thermospheric effects is incomplete due to the lack of understanding of a reliable definition of the quiet-time base line as would become clearer later in this chapter. On the other hand, the periods of low geomagnetic activity could serve as a reference or base line for the storm phases.

At present the stress is on the development of empirical and theoretical models to (i) integrate the data obtained from numerous satellite based missions and ground based observations, and (ii) provide a self-consistent physical description of these observations and understand the phenomenology of underlying processes. The era of modern global empirical/semi-empirical thermospheric models commenced with the publication of the *Jacchia's* 1965 (J65) model [Jacchia, 1965] for which the data base was the total densities as determined from the measurements of air drag on satellites. This model calculated densities, having a fixed lower boundary at 120 km and considering a diffusive distribution of each species above. It also calculated the thermospheric temperature profiles by an exponential equation extending asymptotically to exospheric heights. Some additional provisions were made for estimating the diurnal, seasonal, semiannual, annual variations along with the variabilities introduced by the solar and geomagnetic activity levels. Subsequent revisions extending the predictions down to 90 km culminated in Jacchia 1977 version (J77) [Jacchia, 1977]. After the commencement of OGO-6 satellite mission with mass spectrometer on board, the observations indicated significant differences in the behaviour of individual thermospheric species from those predicted by earlier models such as J71 and J77. The lower boundary was still kept at 120 km similar to the Jacchia models, but the exospheric temperatures were inferred from the N_2 densities. The densities of O and He at 120 km were allowed to vary

with geographical and geophysical parameters as necessary, to fit the satellite measurements at higher altitudes [*Hedin, 1974*].

The importance of 'global circulation system' was realised for the first time then, and as a consequence an understanding of the variations at 120 km were thought necessary in order to correctly model the departures from diffusive equilibrium in lower half of the upper atmosphere. The temperature variations predicted by the OGO-6 model were similar to the temperature variations found by incoherent scatter technique [*Carru et al. 1967; Nisbet et al. 1967*]. However, the OGO-6 model, also had significant limitations in terms of a limited altitude coverage (data base roughly from 400 - 600 km) and apparent scale height errors leading to an average temperature higher by 56K. Also, the data used in this model covered, only a portion of a sunspot cycle ($F_{10.7} \simeq 150$) and the extrapolation to mean $F_{10.7}$ indices, very different from 150, was later found to be inaccurate. In spite of all these limitations, the OGO-6 model temperatures agreed well with incoherent scatter data and this led the subsequent modeling efforts in the same direction. OGO-6 was the first model, based on in-situ composition measurements. The continuous comparisons of measured thermospheric temperatures with existing models then, resulted in an improved and revised model called the MSIS (Mass Spectrometer Incoherent Scatter) model which incorporated temperature data from incoherent scatter radars and mass spectrometer data from five satellites [*Hedin et al. 1977a,b*]. The incoherent radar data were obtained from Jicamarca (12°S), Arecibo (18°N), Millstone Hill (43°N), St. Santin de. Maurs (45°N) and the data on neutral density were obtained from mass spectrometers onboard AE-B, OGO-6, San Marco-3, Aeros A and AE-C satellites. The coverage of the data available was over a wide range of altitudes ($\sim 140\text{-}500$ km). Also, somewhat wider range of magnetically disturbed conditions were included in the model

formulation, but in spite of it, the model did not represent the longitude variations properly.

The time span and altitude coverage of the data sets used in MSIS formulation are illustrated in figure(5.1) [*Hedin et al. 1977a,b*]. Similar to OGO VI, temperatures were inferred from N_2 , as changes in N_2 density are expected to reflect temperature variations more closely than the density variations of any other species or the total density [*Roble and Hays, 1973; Mayr et al. 1974*]. As a result, in the MSIS model, the global average exospheric temperature for an average $F_{10.7}$ solar flux of 150 and an A_P (magnetic activity index) of 4 came out to be 1040K. This estimate of temperature was 56K lower than that of OGO-6 model and 35K above that of Jacchia model. While using only N_2 density, the data gave an average temperature of 1030K. The measurements [*Offermann 1974*], Jacchia model 71 and the MSIS at 150 km agreed well within 2%; however, an error of 5% in thermospheric temperature at 120 km ultimately led to an error by about 10% in density for the MSIS model. Earlier estimations and incoherent scatter observations inferring the temperature gradient at 120 km [*Donahue and Carignan, 1975; Alcadyde et al. 1972; Salah and Wand, 1974*] came very well in consonance with the MSIS prediction i.e. 16.7K/km at 120 km. It is

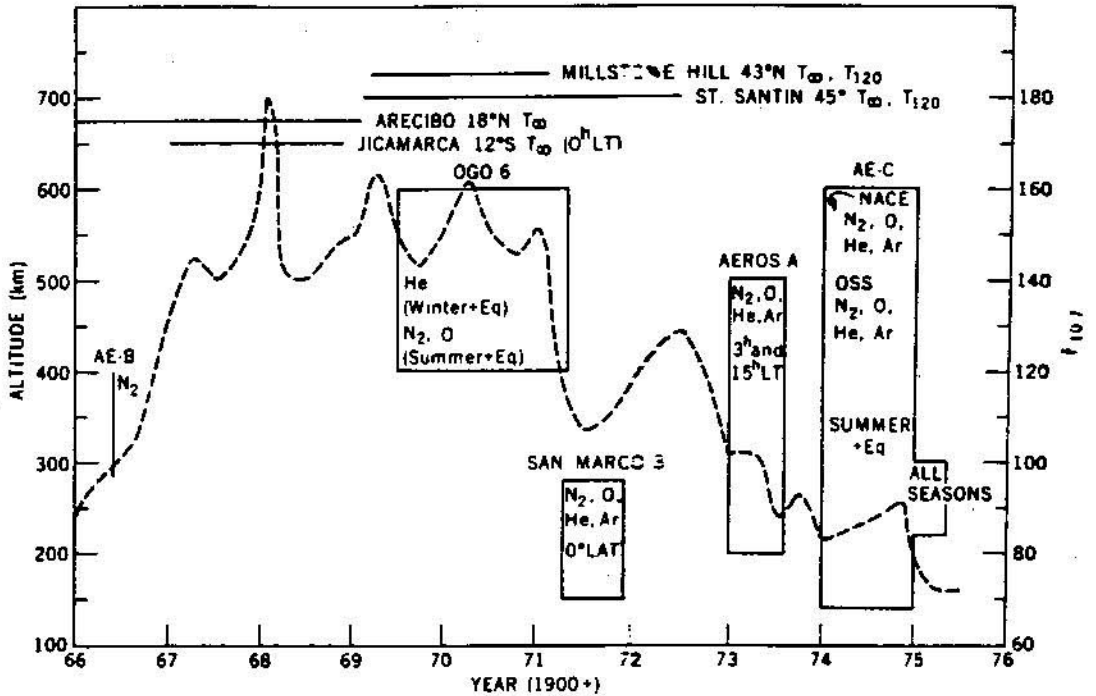


Figure 5.1: MSIS model data coverage in altitude and year-day of the year coordinates. The dashed line shows the trend in the $F_{10.7}$ index during this period. (Hedin et al. 1977)

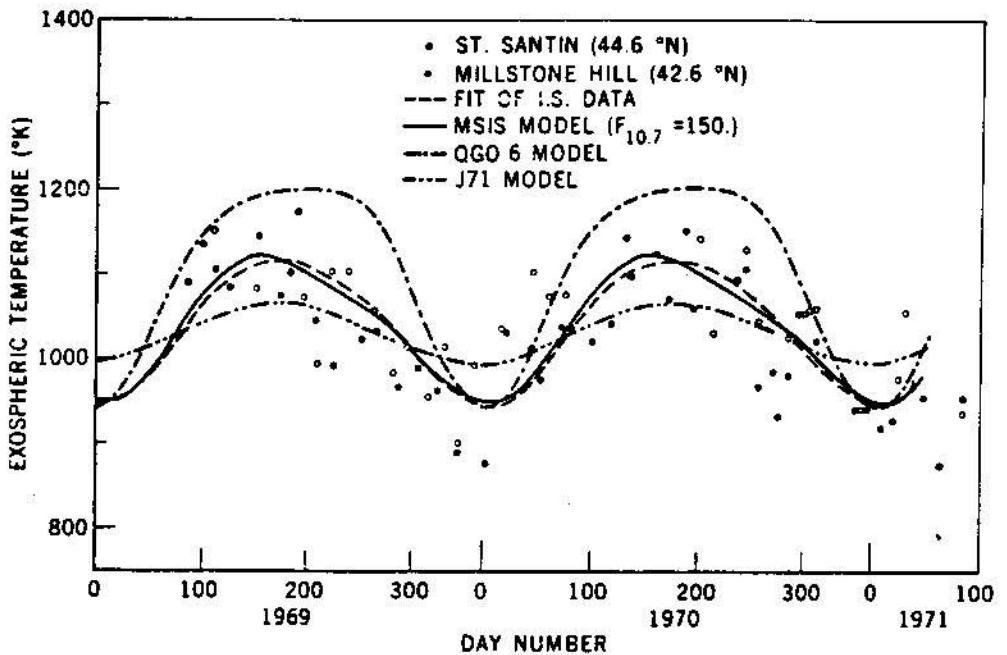


Figure 5.2: The daily exospheric temperature measurements at 45° latitude, a direct fit of these data (Salah et al. 1976), and comparison with the OGO 6, MSIS and J71 models for $F_{10.7} = 150$ and $A_p = 7$. (Hedin et al. 1977)

clear from figure(5.2), the estimation of auroral thermospheric temperature variation by MSIS model was in excellent agreement with incoherent scatter measurements. However, a better understanding of low latitude diurnal and semi-diurnal variations, longitude variations, and year to year changes in various thermospheric parameters were still to be incorporated in the MSIS model. Continued efforts in this direction, following MSIS in 1977, resulted in a revised version of MSIS to appear as MSIS-83 [Hedin 1983]. The enlarged data base of the MSIS-83 model was based on temperature, composition and density measurements from several rocket flights, seven satellites and five incoherent scatter radars. Similar to the earlier version, this revised thermospheric model was an empirical model of thermospheric temperature, density and composition. Also included were the longitude and local time effects, in the improved version. Keeping the same basic structure in the upper thermosphere as in the previous MSIS model, the MSIS-83 presented a more comprehensive and unified description. The most important revision was in the representation of geomagnetic activity effects by using summed 3-hours A_p magnetic indices, combined with a 8-10 hour exponential decay in thermospheric temperature and density after the disturbances/storm events. Figure(5.3) clearly illustrates this aspect [Hedin et. al. 1981]. It is understood that the effects of the magnetic storms could only be modeled in an average way, as the energy sources causing geomagnetic perturbations are highly variable both spatially and temporally. As another major improvement in MSIS-83, the lower boundary condition was reduced even lower i.e. to 85 km from 120 km, to represent more or less the whole thermosphere.

The severe limitation of the earlier MSIS model, namely the dependence of O_2 variations on ion measurements and chemistry, was also overcome by incorporating EUV absorption and mass spectrometer measurements into the model

formulation [*Offermann 1974; Ackermann et al. 1974; Cooley and Reber, 1969 and Trinks et al. 1978*] encompassing a wide range of solar activity i.e. $F_{10.7}$ ranging from 70 to over 200. The MSIS-83 model had been used very widely and proved to be of great utility for a number of upper atmospheric studies. A further revision of the MSIS model was undertaken to incorporate the observations as obtained by

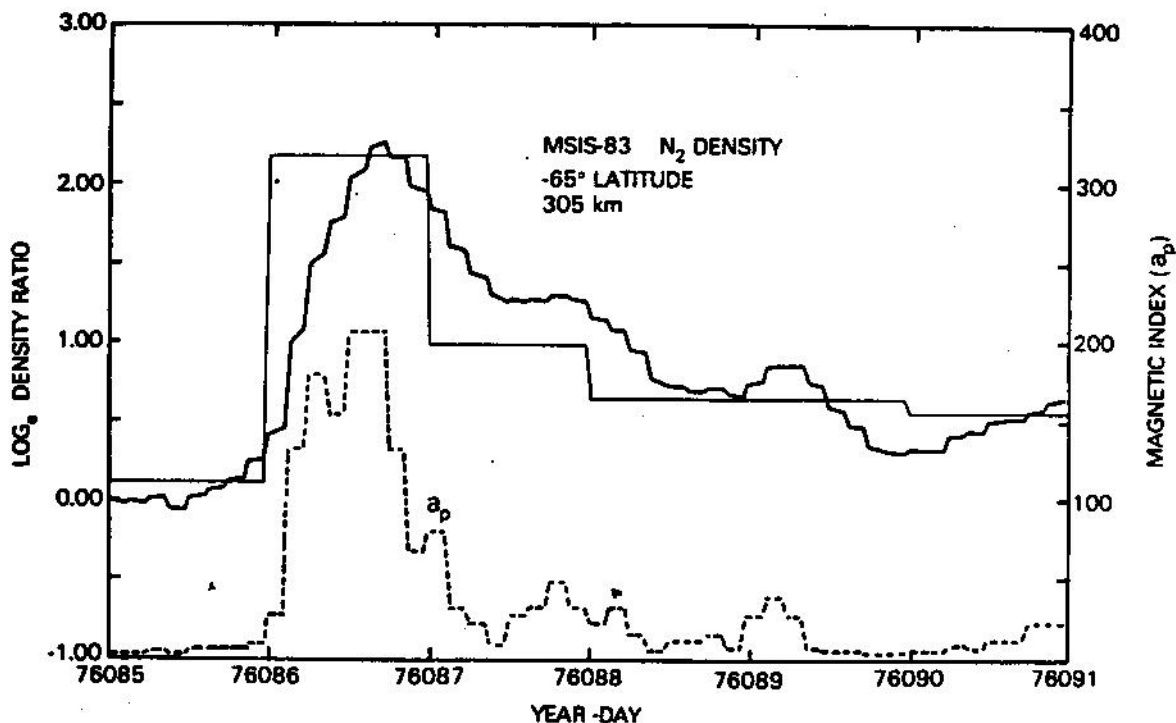


Figure 5.3: N_2 density Vs. day at latitude -65° and an altitude of 305km for an actual storm in 1976 with $F_{10.7}$ near 72, comparing results using daily a_p index with that using the sum of a_p indices (heavy line). (Hedin 1983)

various instruments onboard the Dynamics Explorer (DE-2) satellites. The data base was expanded to include both composition and temperature data from DE-2. The description of atomic nitrogen was added to the species incorporated in the earlier version. Similar to MSIS-83, it had the additional ability to describe the seasonal differences in the morphology of composition under both geomagnetically quiet and disturbed conditions, in the high latitude regions. This new version was termed as MSIS-86. Nearly, at the same time the need to assimilate various thermospheric models, which were based on direct observational data and developed independently, and to arrive at a standard Reference Atmospheric Model was realised. The result was the CIRA-86 model. It included all the new sources of observational data available after 1972 and the theoretical models that had been developed since then. The MSIS-86 thermospheric model was accepted as the standard reference atmosphere model - CIRA-86 (Committee for International

MSIS-86 thermospheric model was accepted as the standard reference atmosphere model - CIRA-86 (Committee for International reference atmosphere). Good consistency between the data sets and the model predictions for varying geophysical conditions, in general, proved MSIS-86 to be a stable user-friendly thermospheric model describing the average conditions very well. However, as it is realised that the global experimental coverage for density and temperature is very less between 90-150km, the model predictions in this altitude range tend to be less reliable than that at higher altitudes. The mesopause had remained an important region for the models as it serves as the base and controls the processes in the thermosphere and the lower atmosphere. With the growing understanding of different regions of atmosphere with the help of programs like CEDAR (Coupled Energetics and Dynamics of Atmospheric Regions), and LTCS (Lower Thermosphere Coupling Study) and MISETA programme (Multi instrumented study of equatorial atmosphere), the need for reducing the lower limit of MSIS-86 model down to lower and middle atmospheric altitudes was realised. As a result, the MSIS-86 empirical model was revised and extended to represent lower atmosphere and mesosphere in order to provide a single analytical model for estimating composition and temperature profiles representative of the climatological average for various geophysical conditions [Hedin 1987, 1991]. This revised and extended model was to be known as MSISE-90. Supplemented by Rockets and incoherent scatter data over upper mesosphere and lower thermosphere, the MSISE-90 predicted temperatures fit to the observed temperature data to an overall standard deviation of 3K and pressure data to 2%. This model represents current knowledge of the 'climatological' averages, reasonably well. However, there is still a scope for modification in MSISE-90 model near mesopause boundary. MSISE-90 utilises considerably fewer parameters than other models and perhaps as mentioned

earlier, is the most user friendly and readily accessible of all the thermospheric models. Therefore in the present comparative study with measurements, only the MSIS model is made use of.

5.3 Low Latitude Thermospheric Temperature During Storms and 'MSIS' Model

Rishbeth in 1975, reviewed the ideas about thermospheric/ionospheric (F-region) storms and conclusively showed that the changes in global thermospheric circulation, affected and modified by the storm time energy inputs over high latitudes, have significant effects on low latitude thermosphere and F-region of ionosphere as well. Though several studies had been conducted on the behaviour of the thermosphere at high and mid latitudes during geomagnetic storms [*Hernandez and Roble, 1976, 1978; Jacka et al. 1979; Rees et al. 1984a, 1984b; Yagi and Dyson, 1985; Fagundes et al. 1995a*], the behaviour of the thermosphere at low and equatorial latitudes is studied the least. Very few measurements exist in this region during geomagnetic disturbances [*Biondi and Meriwether, 1985; Ranjan Gupta et al. 1986; Tinsley et al. 1988; Burnside et al. 1991, Burns and Killeen, 1992; Wu et al. 1994; Fagundes et al. 1996*]. It is now accepted that the low latitude thermospheric temperatures during storms, at times exhibit fluctuations and enhancements relative to those during quiet conditions. *Burnside et al. [1991]* in a study of the neutral thermosphere at Arecibo (a low/mid latitude station) during two severely disturbed nights (14-15 Jan. 1986 and 13-14 July 1985) clearly showed an increase in neutral temperature around noon i.e. on 14th July 1985 by about 200K when compared with the MSIS-86 model predicted temperatures. Also, *Burrage et al. [1992]*, compared the thermospheric temperatures, inferred from the density measurements obtained by mass spectrometer onboard AE-E satellite, with the MSIS-86 predictions and found that

there was only a qualitative agreement between the two.

Number of studies similar to the ones described above, brought out the important fact that 'MSIS' is limited by the low resolution of the magnetic activity parameterisation that has gone into its formation of the model. MSIS-86 storm response, is a limited function of local time, hence could not represent all the observations in case of *Burrage et al.* [1992]. In a similar study, focusing on low latitude thermospheric and mesospheric temperatures. *Fagundes et al.* [1996] showed that during the sudden storm commencement (SSC) phase, the observed nocturnal thermospheric temperatures are generally higher than those predicted by MSIS-86 model. However, the measured temperatures were found to be lower than MSIS-86 predicted temperatures during the recovery phase of the storm. For majority of moderate storms, the above results were found to be true [*Fagundes et al.*, 1996).

5.4 Deviation of Thermospheric Temperatures from the MSIS Model

Perhaps, one of the important aspects of a geomagnetic storm related studies would be to investigate the atmospheric response for a sudden surge of storm energy input as compared to the gradually changing solar cycle and seasonal effects. Results show that most of the changes in low latitude thermosphere during a geomagnetic storm are caused by the processes whose sources lie in the high latitudes. But, there are instances, when direct deposition of energy over these latitudes has also been reported [*Ranjan Gupta et al.* 1986; *Prolss* 1981]. The energetic particles originating from the 'Ring current' are believed to play a crucial role in this regard [*Tinsley* 1979, 1981]. Though, the magnitudes of storm effects in the thermosphere are smaller at low latitudes, still they do persist for significantly longer periods even after the storm subsides

[Fuller-Rowell and Rees, 1997; Fuller-Rowell et al. 1997; Abdu 1997]. Gurubaran et al. [1995] while compiling the thermospheric data from Mt. Abu noted that for high solar activity conditions and for geomagnetically quiet periods, significant deviations existed between the measured and model temperatures on several occasions. In most of those occasions, the model was found to be underestimating the observed temperatures.

In the light of the above discussion, we set out a case study on four geomagnetic storm days i.e. December 8th, 9th, 1993 and February 5th, 6th, 1994 making use of the spectroscopically obtained thermospheric temperatures from Mt. Abu alongwith those estimated from MSISE-90 model. The description of the data, has already been presented in Chapter 2 and here we concentrate only on the differences between the measurements and the model. The following, [figure(5.4)] panels depict the measured neutral temperatures (T_n), for all the four days, with error bar alongwith the MSISE-90 model values predicted for the occasion. The A_p value is given for each individual day at the top of the respective panels. The observed deviations of measured thermospheric temperatures from the model predictions are clearly seen. The important thing to be noted here is that these deviations, especially on 8th December, were both positive and negative with respect to the

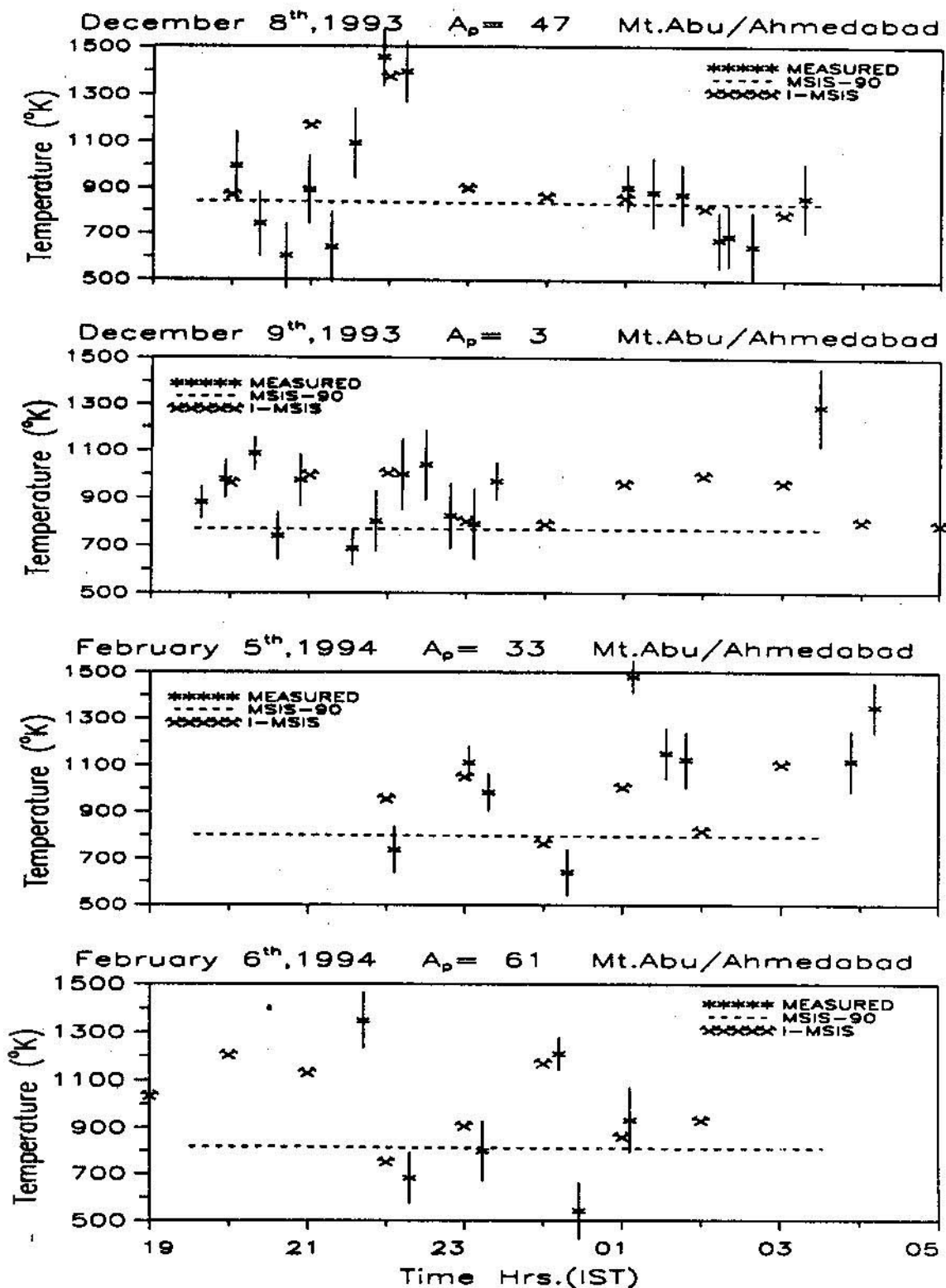


Figure 5.4: Improved model (I-MSIS) representation of the thermospheric temperatures as observed from Mt. Abu. Also shown are the actual measurements with MSISE-90 predictions.

MSISE-90 predictions and were to the extent of $\sim 500\text{K}$ on December 8th and on February 5th; large scale wave structures were seen on December 8th and 9th, which are suggestive of large scale processes like TADs being active in the upper atmosphere. The above comparison indicates that the model does not probably take into account all the essential energy inputs over low latitudes, which incidentally become significant with the increase of geomagnetic activity. These observations prompt questions like- what causes the enhancement and variations in temperature over low latitudes during geomagnetic storms, and, how the model can be augmented to predict these temperatures realistically.

Therefore, two important aspects of low latitude thermospheric behaviour emerge for the present study i.e. (i) Study of the time response of low latitude thermosphere to geomagnetic forcings at the time of storms; (ii) Increasing the utility of 'MSIS' model by appropriately incorporating certain unaccounted factors after suitably parameterising them, based on the four storm days and eventually generalising the same.

5.5 Time Response of Low Latitude Thermosphere to Geomagnetic Forcings

The temporal development of thermospheric effects during storms is essentially determined by the changing intensity of the solar wind energy source. The additional temporal variations are introduced 'globally' by large-scale dynamics of the thermosphere; and 'locally' by changes in the spatial distribution of the energy injection. Apart from this, the presence of local dynamical processes also affect time variations mentioned above.

Results show that at high latitudes the time delay between the magnetic and thermospheric disturbances is rather short and of the order of an hour (even

less); however larger time lags are observed at low latitudes as expected [Berger and Barlier, 1981; Prolss, 1982]. Though, all the observed changes in the thermosphere at any latitude cannot be associated and adequately described by a single local or global time constant, but at times during storms, the observed thermospheric/ionospheric changes can be related, temporally to storm time global dynamics. For instance the observed temperature and density changes as a result of large scale meridional circulation have typical time constant of 2-8 hrs globally [Mayr and Hedin 1977, Rishbeth 1985, Prolss et al. 1988].

According to the present understanding, over low and equatorial latitudes the 'storm' is understood on the basis of phenomenology of middle and low latitude geomagnetic variations identified by the 'Ring current' as a source of magnetic field intensity variation and, is represented by the D_{st} index. Hernandez and Roble (1978) showed a linear relation between the $\frac{d(D_{st})}{dt}$ i.e. the rate at which energy gets transferred into and from the earth's ring current and the fluctuations of the meridional velocities observed over Fritz peak ($39^{\circ}N;105.5^{\circ}W$) a mid-latitude station. Quite a few similarities were shown to be prevalent in meridional wind patterns and corresponding $\frac{d(D_{st})}{dt}$ parameter and there had been a time delay of 3-4 hours between the two on different occasions. This suggests a time delayed response of midlatitude thermosphere to an imposed geomagnetic disturbance. This study provides the first positive indication for a 'possible means' of relating the thermospheric effects to ring current in terms of $\frac{d(D_{st})}{dt}$ parameter (time delayed), and a possible use of $\frac{d(D_{st})}{dt}$ as an input parameter for global dynamic models of the thermosphere. Since, the model predicted temperatures, for given parameters/conditions represent only the average thermospheric state, deviations of the observed temperatures ΔT_n from this average were estimated for each temperature point and for each night, i.e. on December 8th, 9th, 1993; Feb. 5th, 6th, 1994. Also, for each night, the $\frac{d(D_{st})}{dt}$

i.e. rate of change of D_{st} was estimated. The ' D_{st} ' indices are hourly indices supplied by the Kyoto University, Japan.

A cross correlation analysis was performed, and no agreement was found between ΔT_n and the instantaneous values of $\frac{d(D_{st})}{dt}$. This, in a way was quite expected because the geomagnetic perturbations and various energy inputs to the thermosphere during storms would take sometime before appearing as low-latitude thermospheric temperature variations. So, a time delay was invoked between the $\frac{d(D_{st})}{dt}$ and ΔT_n and a cross-correlation exercise was performed. The time delay was varied from 0 to 24 hrs, and a strong positive correlation was found between the two

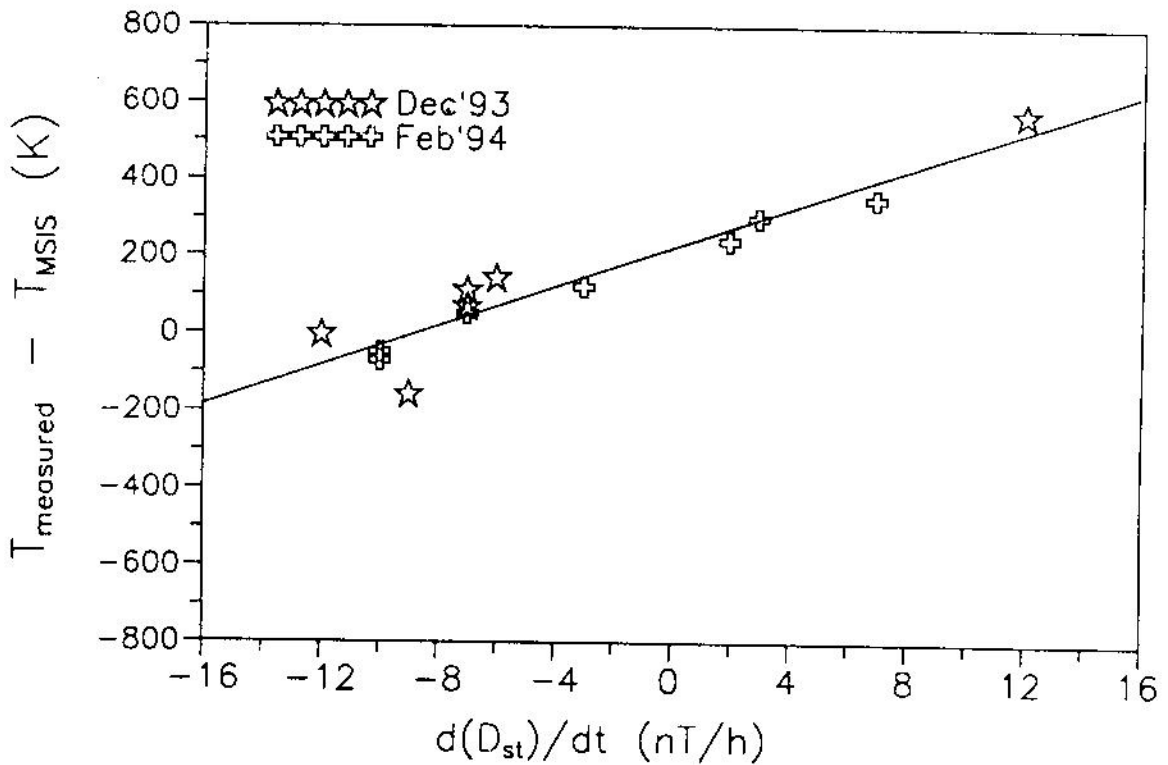


Figure 5.5: Scatter plot for deviation of measured thermospheric temperatures from the MSIS model as a function of time rate of change of D_{st} , for December 8th and February 5th.

in all the four days for a time delay varying between of 16-18 hrs. The observed correlations were ≥ 0.8 for all the four nights [figure(5.5)]. The important outcome of the correlation study is that, the T_n with all its temporal variabilities and a corresponding variation in $\frac{d(D_{st})}{dt}$ 16-18 hrs before, indicate towards a time delayed response of the thermosphere or in other words an 'inertia-effect' of the thermosphere. So, the 16-18 hrs time delay in the choice of $\frac{d(D_{st})}{dt}$ through correlation exercise, stands for the response time for the latitude region of Mt. Abu ($24.6^\circ \text{N}; 73.2^\circ \text{E}; 19.2^\circ \text{diplatt.}$), during periods of moderate geomagnetic storms. However it should be borne in mind that the response time would be dependent on the atmospheric conditions at that instant.

Earlier studies on the response of the equatorial thermosphere - ionosphere system using DE-2 data revealed that in the morning sector during summer months, it takes about 12 hours for the storm effects to be registered in the neutral temperatures [Burns and Killeen, 1992]. It was ascribed to gravity waves triggered

triggered by the storm. *Richmond* [1979] suggested that meridional circulation is also important and it could take ~ 10 -12 hrs to produce similar effects. In the present investigation, the time-delay is significantly longer (16-18 hrs). Since the observations were made during winter months, the longer time delays could very well be due to the transequatorial winds from the summer hemisphere opposing the equatorward distribution of storm energy. However, a reliable determination of the 'response-time' is not an easy task, especially using data from only one site. Therefore, it is extremely important to complement the satellite observations with continuous ground based measurements. Owing to these limitations, very few studies had been performed in the low latitudes to investigate this aspect. In this regard, the result of the present investigation that it takes ~ 16 -18 hrs for the high latitude effects to percolate down to $\sim 20^\circ$ dip lat. is important. However, it is understood very well that all the variations in D_{st} are not solely due to the ring current as the low latitude perturbation in magnetic field is also influenced by contributions from substorm related current systems eg. the asymmetric ring current involving field aligned currents [*Fukushima and Kamide, 1973; Clauer and McPherron, 1978*], the ionospheric currents [*Takahashi et al. 1991; Fejer, 1997*] and also the occasional collapse of the cross tail current near the edge of the plasma sheet [*Liu et al, 1991*].

Taking the lead from the above finding of the 'response-time' of low latitude thermosphere, we set out a first order exercise to augment the existing 'MSIS' model for the same period. A detail of this exercise is discussed in the following section.

5.6 Parameterisation of D_{st} and Augmentation of the MSIS Model

Till now the prediction of thermospheric variations and perturbations in empirical models are keyed to the geophysical indices like K_p and A_p which are taken to represent the geophysical processes to a good measure. However, these indices might not be representing the actual conditions especially over low latitudes [I. Almar *et al.* 1992, 1996] and indeed it has been found that they tend to smoothen out the variations. Therefore, making the model solely depend on the K_p and A_p indices would have limitations as revealed by the earlier studies. On the basis of results on the thermospheric response time, an attempt has been made to parameterize the D_{st} index in order to be able to explain the observed thermospheric temperatures. The logic that has been adopted is as follows: During the main phase of any geomagnetic storm, energy is pumped into the 'ring current' and it builds up. Later, in the recovery phase, the stored energy gets released into the system, more favourably at high latitudes i.e. along the geomagnetic field lines. As mentioned in the previous chapters, advection, diffusion and traveling atmospheric disturbances, redistribute the energy, and, there would definitely be a time delay before the low latitude region would start experiencing the impact of the geomagnetic storm. Our results in the previous section also confirms this particular aspect.

The rate at which the the D_{st} index changes with time i.e. $\frac{d(D_{st})}{dt}$ is taken as a measure of the energy exchange into the atmospheric system. The rationale for treating it so is discussed later. These time delays, obtained after the cross correlations for individual events are considered to be reasonable in complying with the available information on meridional winds and gravity wave propagation characteristics and it turned out to be ~ 18 h for the month of December. An empirical linear model is fitted to the data, following this delayed

correlations for the December data and a relation was established between the deviations in the measured and model predicted temperatures (ΔT_n) and the rate at which the D_{st} variations occurred before 18 h.

$$\Delta T_n = 19.124 \times \frac{d(D_{st})}{dt} + 171.464 \quad (5.1)$$

A similar relation was arrived at, for the month of February 1994 data, also independently. This sort of a relation could therefore be considered as representative of this particular solar epoch and the constant term would then be the background thermospheric condition not getting represented by the MSIS model. In addition there are quite a few other processes that contribute to the low latitude energetics which are not quantified as yet. The lack of understanding of these processes limits our efforts. However during geomagnetic storms, the storm energy input is expected to dominate and therefore no attempt is made in this part of the study to consider and account for some of the prominent local processes. This aspect has also been attempted in the present study and would be discussed in the later chapters.

Using the above relation to represent the periods under consideration, the ΔT_n values were estimated for the remaining three nights. Thus obtained ΔT_n is treated as an additive term to the standard MSIS model temperature. The estimated temperatures using this empirical relationship (after applying the correction to the MSIS model) are depicted in figure(5.4)(pp 162) by crossed swords, while the actual measurements are represented by crosses with error bars. One can notice that the observed features are now reproduced remarkably by the improved model, termed as I-MSIS model. The large shooting up of temperature at ~ 2200 IST on 8th December 1993, the oscillatory features of 5th and 6th February, 1994, do get reproduced fairly well. The 9th December temperature data revealed much faster fluctuations with periodicities of < 1 h. Since the D_{st} data used in the present analysis is from the hourly D_{st} values,

smaller periods could not be extracted. At least ten minute D_{st} values would be needed for a further detailed study. In spite of this limitation the I-MSIS model values are seen to pass through the actual data points.

In this exercise, a relationship between the rate at which the energy of the ring current gets dissipated in the TIS and the difference between observed and model predicted temperatures has been established and has been successfully used to improve the model on a case study basis. This study brings out the important point that the temporal evolution and development of geomagnetic activity effects has to be taken into account while modeling the same. Some earlier studies have also indicated towards this aspect [*Hedin et al.* 1981; *Nisbet et al.* 1983; *Prolss and Roemer*, 1987; *Slowey* 1987; *Fuller-Rowell et al.* 1997 and references therein]. Apart from this, the crucial point for the augmentation of MSIS model for low latitudes, is the proper identification and analysis, of the form in which the magnetic indices are to be used in modeling the various effects for both geomagnetically quiet and disturbed conditions.

Therefore, we set out a detailed study for further validation of $\frac{d(D_{st})}{dt}$ as a potential index to be used in the MSIS model extending the study to various states of the thermosphere during different geophysical conditions. The following sections deal with this aspect in detail.

5.7 Thermospheric Temperatures During Geomagnetically Quiet Conditions and the Model (MSIS) Predictions

It is clear now that the D_{st} variations represent the variabilities in the neutral temperatures during disturbed conditions. It is extremely difficult to define a baseline for geomagnetically quiet conditions because of the continuous inflow of solar wind energy, however small it may be, even during these so called quiet times. So the question which comes naturally to our mind is - whether

the imprint of the ' D_{st} ' variabilities on thermospheric temperature holds true even during geomagnetically quiet periods. To find an answer, we extended our correlation analysis of measured thermospheric temperature data from Mt. Abu without making any distinction for the data in terms of geomagnetic activity. These measurements span the period of October 1986 to March 1987 and November 1990 to April 1991. Data samples range between the minimum of solar cycle 21 and the maximum of solar cycle 22. All the data correspond to geomagnetically quiet periods i.e. (max. $A_p = 17$). The temperature data have already been reported by *Gurubaran et al.* [1995] indicating the limitations of neutral atmospheric model MSIS-86. Figure (5.6) depicts the thermospheric temperatures for four nights during February 1991 as a sample for the variabilities and deviations from the model typically encountered. Dashed lines represent the MSISE-90 model values for each day under consideration. The deviation at times is as large as ~ 300 K. Though the mean temperature during high solar activity period i.e. 1991 has risen here (800 to 1200K), still the deviations of the measurements from the model predictions on most of the nights is quiet notable. Not only temperature enhancements were seen, but some kind of wavelike fluctuations were also discernible during many nights. Data corresponding to October, November 1986, January 1987, and February and April 1991

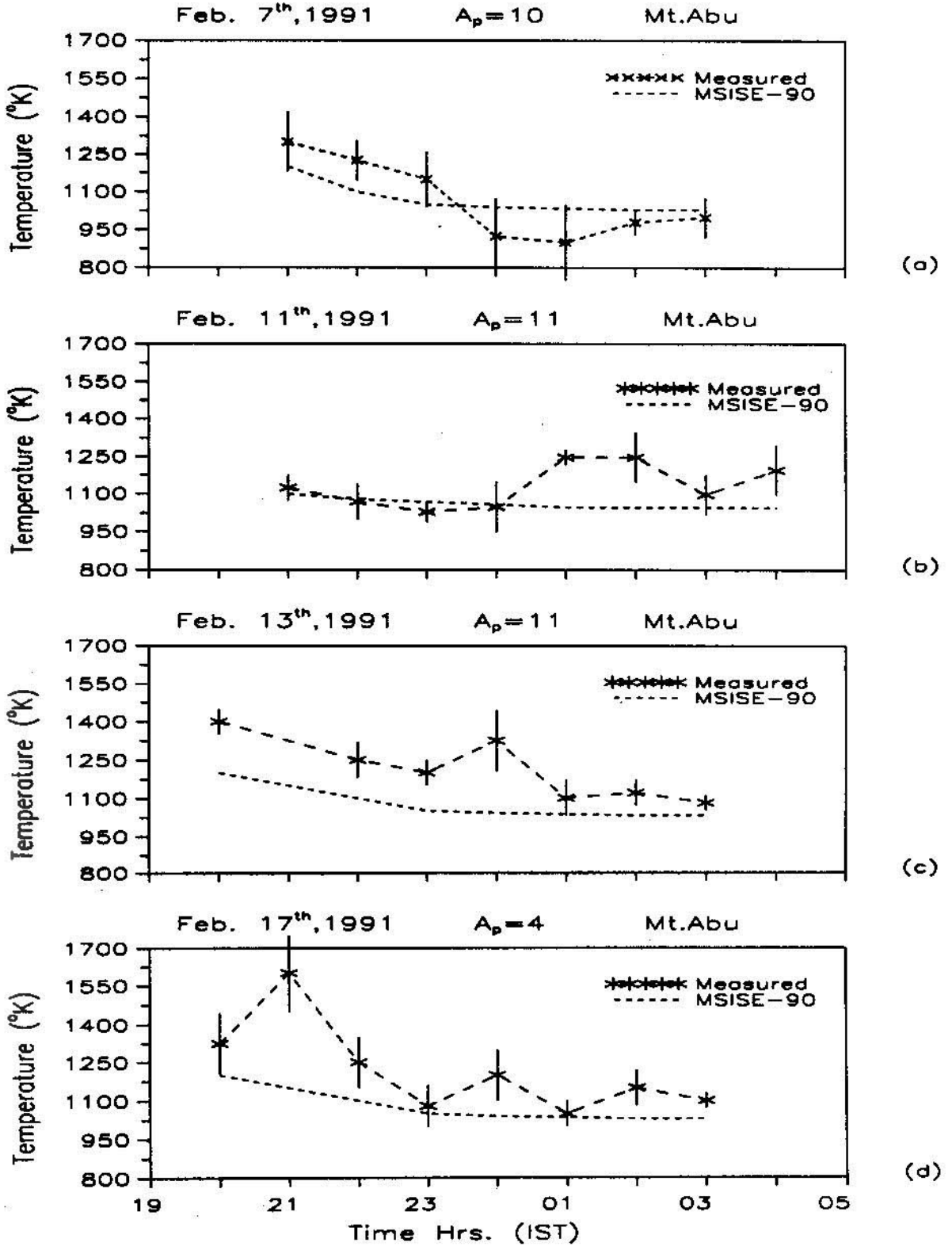


Figure 5.6: Comparison of observed thermospheric temperatures from Mt. Abu with MSIS model for the month of February 1991.

were subjected to detailed time delayed correlation analysis. The data being presented in this section, not only was distributed over high and low solar activity epochs but covered different seasons, though in different years. Due to the bad viewing conditions during the Indian monsoon (July-Sept) each year, there is no data available during these months. The correlation analysis here aims at bringing out the response time of low latitude thermosphere, and a seasonal dependence of the 'response-time', if there is any.

Though the time resolution of the D_{st} is coarse, i.e. 1 hour, still the obtained correlation coefficients were high, of the order of ~ 0.8 and more; for individual nights. In fact it was found that the estimated time-delays corresponding to the nights belonging to a particular month were found to be lying in the same range, and these time delays were different for different months. In other words, it turns out that the thermosphere has, seasonally, a characteristic time delay or response time.

Figure(5.7) shows these estimated response-times as a function of the month. The seasonal changes are superimposed over the changes dependent on the solar activity. These two superimposed contributions in total 'response time' can be filtered out only, if we have continuous observations of thermospheric temperatures over a year during a particular solar epoch. Ideally one should have a chain of observatories along a particular meridian in order to arrive and validate these results. The possible coupling mechanism between the high and low latitude regions during quiet times are briefly discussed below.

5.8 Neutral Dynamical Effects

In a recent study of quiet time upper thermospheric winds over millstone Hill (a mid latitude station 43°N , 72°W) between 1984 and 1990 *Hagan* [1993], brought forth a re-confirmation of the earlier results that the meridional winds

over MHO (Millstone hill observatory) were southward for prolonged periods diurnally for most of the days of the year. Weak northward winds were observed only briefly during the morning hours. These winds, apart from the regular zonal flow, are the ones which redistribute the polar energies to lower latitudes and vice-versa,

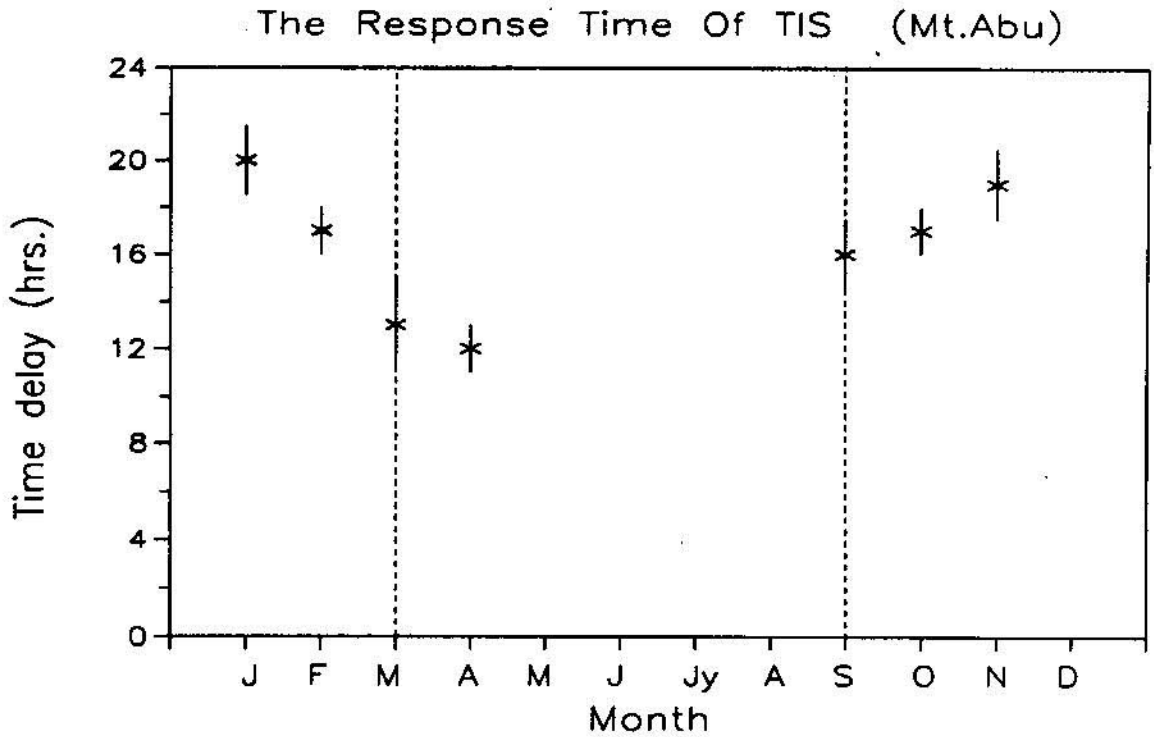


Figure 5.7: The TIS response in terms of time delays estimated for different months using the ground based spectroscopic data from Mt.Abu.

though their contribution to overall energetics is small. This result provides an evidence, that the aurorally driven circulation cell is important even during geomagnetically undisturbed periods, and the average auroral activity is strong enough to drive thermospheric circulation equatorward for most of the days, throughout the year, even during low solar activity epoch. Significant local time effects also modulate this prevailing circulation pattern to a great deal. The contribution of these thermospheric circulations in producing the low latitude thermospheric temperature variations are extremely important in defining the thermospheric energy budget during geomagnetically quiet periods. At the same time, results from theoretical studies also support the above argument. In fact, *Roble and Dickinson* [1973], *Roble and Emery* [1983], *Roble et al.* [1987] while discussing their results on NCAR-TGCM/TIGCM model simulations, have shown that the high-latitude heat source is present all the times. However, the meridional winds alone, in a way, cannot explain the observed seasonal dependence of response-time.

Short term changes in tidal forcing of global winds, atmospheric gravity waves

seasonal dependence of response-time.

Short term changes in tidal forcing of global winds, atmospheric gravity waves and planetary waves also give rise to these observed perturbations in electric field over low latitudes during geomagnetically quiet times [*Balachandran et al. 1992; Sastri et al. 1995; Richmond, 1994; Forbes et al. 1992; Parish et al. 1994; Chen, 1992*]. One very important result about the gravity waves is that their propagation speed is much faster during summer (hotter thermosphere) than during winters [*Fuller-Rowell et al. 1997*]. As, the gravity waves also facilitate the redistribution of energy, the above fact indicate towards smaller response-time during summer.

5.9 Electrodynamical Effects

The contributions from electrodynamic effects which may be both local and nonlocal in origin also may have to be taken into account. One thing which can be said about some of the local electrodynamic effects is that they produce almost instantaneous effects in the ionosphere. The low latitude thermosphere, apart from being constantly under the influence of meridional thermospheric circulation even during quiet times, experiences the indirect neutral heating caused by the ionospheric currents, quiet-time ring currents and associated magnetospheric current systems. It has been known that even during quiet-time, equatorial electric fields and currents often exhibit fluctuations with quasi-periodicities ranging from few minutes to few tens of minutes. These short term variations can be associated with ionospheric wind dynamo system [*Richmond 1994*].

Further, it is known that a steady magnetospheric electric field creates a charge separation in the plasmasphere in such a way that the electric fields are shielded out from low latitudes during quiet periods. This charge separation region is

known as Alfvén-layer. Now, with any perturbation in magnetospheric field from steady state value temporarily disrupts the charges from shielding configuration and the field penetrates down to low latitudes. In other words, the low latitude electric field fluctuations may occur due to Alfvén layer charges which exist even when no other external source is found to be present [Kelley 1989]. Ring currents at an L value of $4R_E$, over the equatorial region plays important role in creating the Alfvén Layer i.e., charge separation layer. Earle and Kelley [1987] reported experimental evidence that the shielding process acts like a high pass filter, allowing electric fields with periods shorter than about 8h to penetrate to the equatorial ionosphere. The process of neutral heating by electric field fluctuations is a complex phenomenon based on the coupling and feedback mechanisms between the ionosphere and the thermosphere. These fluctuating electric fields in the ionosphere, can be responsible for the dynamic input of energy and momentum to the neutral atmosphere through processes of joule heating and ion-drag. Since, the correlation study was done using D_{st} (a magnetic field component) as an index representing ring current energy fluctuations, contributions to observed low latitude fields from higher above i.e., magnetospheric ring current and its associated current systems over high latitudes, cannot be ruled out. Though, the energy deposition to low latitudes in the form of energetic neutral atom precipitation as a result of resonant charge exchange processes of the ring current ions is not very significant during quiet conditions, the linkage of ring current to the inner magnetospheric auroral current system is important. The low latitude electrodynamics is influenced by these currents which give rise to electric field perturbations over these latitudes, as explained above. Therefore, it is obvious that a combination of all these various processes must be responsible for causing both instantaneous and delayed perturbations over low and equatorial thermosphere - ionosphere

system [Fejer 1997]. Gonzalez *et al.* [1979] clearly showed examples of both type of effects in a study of measured electric field change over Jicamarca (Peru) and Chatanika (Alaska).

However, it is important to mention here that the response-time of the thermosphere is not just the time taken in transporting the energy from high latitude to the latitude of our interest, instead, it is the time taken by thermosphere after absorbing any additional energy pulse at any place and manifest it in terms of temperature fluctuations. Also the nature of the energy pulse can be both local and nonlocal for the place where we want to study the thermosphere. Therefore, the 'response-time' in this context is a more fundamental and complex property of thermosphere than just the traveling time of disturbance in thermosphere from high to low latitudes. Unfortunately we are still very far from a complete understanding of these various dynamical processes and involved time-delays. We lack in understanding of the relative effects of these processes on the lower latitudes diurnally, monthly (seasons), yearly and on longer time scales. On the basis of the understanding and explanations provided above, we reiterate that the observed time delays or response-times obtained as a result of the present investigation are an outcome of the manifestations of various processes within a larger magnetosphere - ionosphere - thermosphere system in terms of the involved coupling and feedback mechanisms. In simple terms its taken that the observed differences of the neutral temperatures from model predictions are due to the redistribution of high latitude energy over the latitude of our interest, mainly through quiet time thermospheric circulation. However, the seasonal dependence needs further investigation both experimentally, and theoretically.

In the following section, we have discussed the results of the ongoing augmentation of the 'MSIS' on the basis of the 'response-times' for Mt. Abu latitudes

during quiet times. A comparison of the augmented 'MSIS' model (I-MSIS) prediction with the observed thermospheric temperature is also presented.

5.10 Augmentation of the MSIS Model for Quiet Conditions

Similar to the Dec. 1993 data, a relation between the $\frac{d(D_{st})}{dt}$ and ΔT_n , was established for each individual day, already described in section(5.6). A linear model was fitted to the difference of observed neutral temperatures from the model predictions and the properly time-delayed $\frac{d(D_{st})}{dt}$ defined according to the response time, characteristic of the day/month of the year. There are two important aspects of the observed low latitude F-region thermospheric temperatures, (i) the observed absolute temperature difference from the model predictions; (ii) the observed temporal variabilities on individual nights.

In the linear model fitted to the ΔT_n and $\frac{d(D_{st})}{dt}$ data on individual nights, no clear trend emerged in the estimated slopes and gradients. Since, the data used in this analysis belonged to different months in different years, seasonal variations of gradients and intercepts exhibited a scatter. These estimated gradients and intercepts were used to estimate the I-MSIS predictions using the Mt.Abu spectroscopic data. However, to investigate the seasonal variations in gradients and intercepts, one should have a continuous data base at least for one year. This limitation has successfully been overcome by using DE-2 satellite data, to be presented and discussed in the next chapter. Using the linear relations, found on the basis of gradients and intercepts for each month, we estimated the additive terms to be used for the augmentation of MSIS, for each individual day characterised by the D_{st} and the response-time of the month. These additional terms when added temporally to MSIS predicted temperatures gives us the new improved 'MSIS' (I-MSIS) model predicted temperatures.

The figure(5.8) depicts the two nights of temperature observations for the month of October 1986. Also shown are the corresponding MSIS predicted temperatures, represented by the dashed line. The I-MSIS model predictions are depicted for comparison with the observed temperatures. Oct. 26th was a geomagnetically quiet day ($A_p \sim 3$). The observed temperatures, restricted only to premidnight hours, showed a gradual rise in temperature from $\sim 650\text{K}$ at 1900hrs to $\sim 900\text{K}$ at 2200hrs. The MSIS predictions were overestimating the observations before 2000hrs and underestimating after that. While the improved MSIS (I-MSIS) predictions were able to reproduce the observations remarkably well. The observed temperature pattern on Oct. 28th was very similar to the one seen on Oct. 26th. The temperatures, on this night also, increased from a low value of 750K at 2000hrs to $\sim 850\text{K}$ at 2200hrs. The deviations in observed temperatures from the MSIS model predictions are relatively smaller on this night. The I-MSIS predictions were lower by $\sim 100\text{K}$ than the observed temperatures before 2100hrs. However, the I-MSIS predictions were able to reproduce the variability, and also the absolute magnitude of temperatures after 2100hrs.

The days considered for the month of Nov. 1986 are geomagnetically, relatively more active, as can be seen in terms of the magnetic indices A_p . Figure(5.9) depicts the observed thermospheric temperatures from Mt.Abu on Nov. 23rd and 26th.

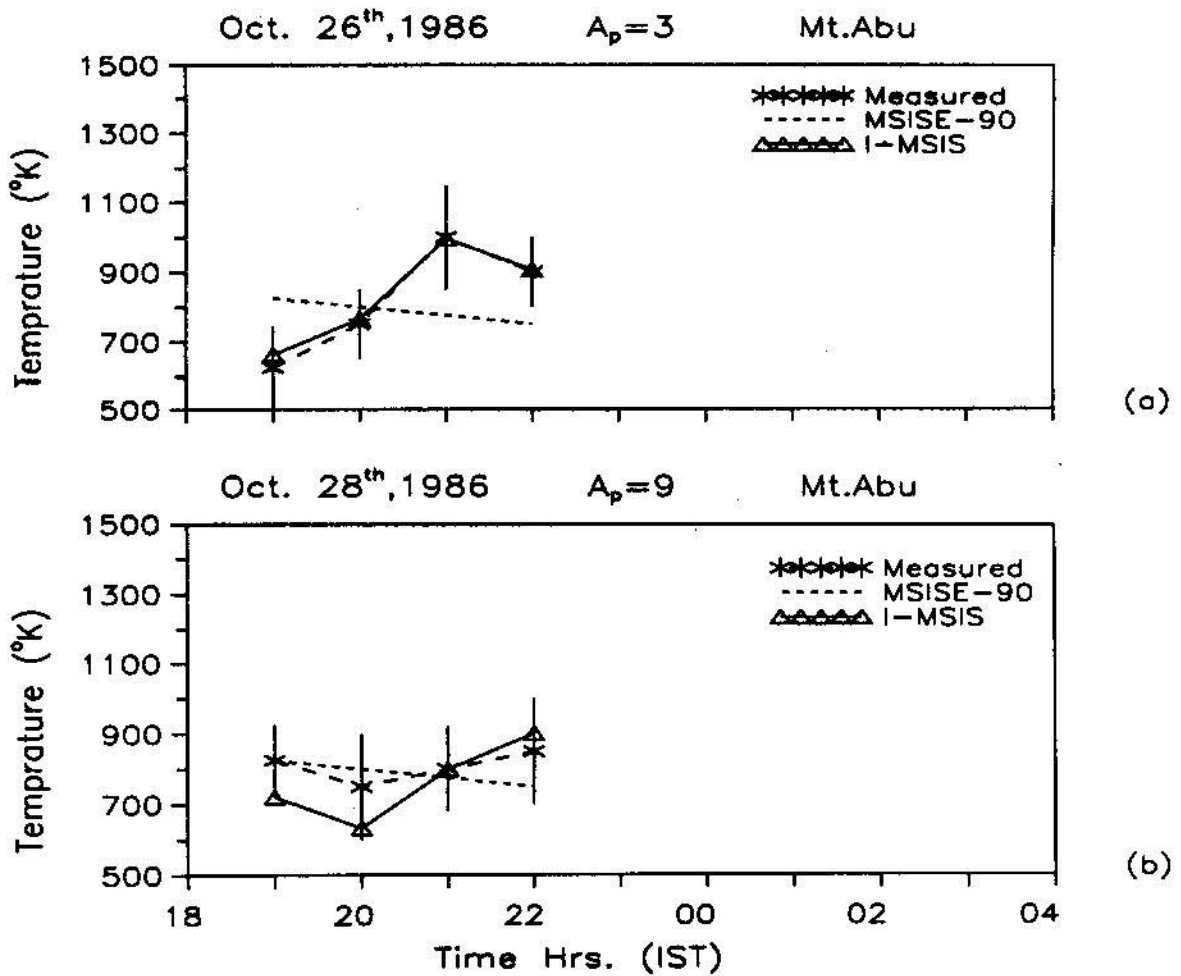


Figure 5.8: Comparison of observed thermospheric temperatures from Mt. Abu with MSIS model for the month of October 1986. Also shown are the I-MSIS model predictions.

The observed temperatures on the night of Nov. 23rd were higher than the corresponding MSIS predictions. The deviation of the observed temperature from the model at 2100hrs was more than $> 300\text{K}$ while at 2200hrs the prediction of the model was perfect. Rest of the times, the temperatures remain grossly underestimated by the model. The I-MSIS predictions also could not explain all the observations except at 2200hrs. Even the variabilities shown by the observed temperatures are not being reproduced on this night. At the same time, the I-MSIS model was able to reproduce all the observed temperature variabilities on Nov 26th. The day being geomagnetically more active, the temperature on this night were significantly higher eg. $\sim 1200\text{K}$ at 1900hrs. The deviations from the MSIS predictions were quite large, for instance deviation at 1900K was $\sim 400\text{K}$. The I-MSIS model

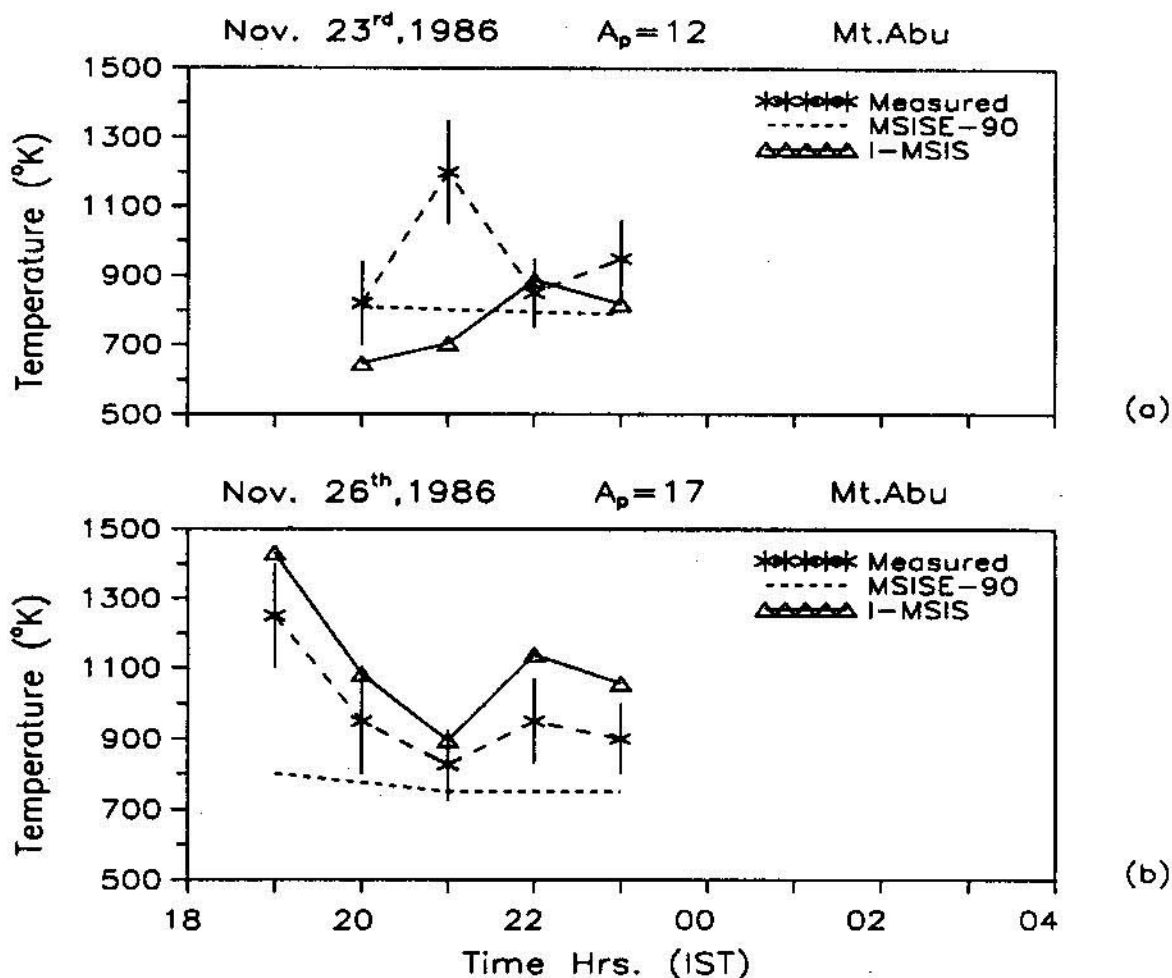


Figure 5.9: Comparison of observed thermospheric temperatures from Mt. Abu with MSIS model for the month of November 1986. Also shown are the I-MSIS model predictions.

though reproduced the temporal variability in observed temperatures, its predictions seemed to overestimate the observations at all the times. It is important to note that the extent of overestimation seem to be constant corresponding to each observation.

Figure(5.10) depicts the temperature observations corresponding to Jan. 24th and 25th 1987. The geomagnetic conditions on both the days seemed to be nearly the same, as is evident from the corresponding A_p values. The average temperature levels were also the same ($\sim 900\text{K}$). The MSIS prediction remained less than the observations on both the occasions. The I-MSIS, like on other occasions, was able to reproduce the temperature variabilities quite well. The I-MSIS prediction after 2200hrs on 24th and before 2000hrs on 25th were remarkably good. However, at

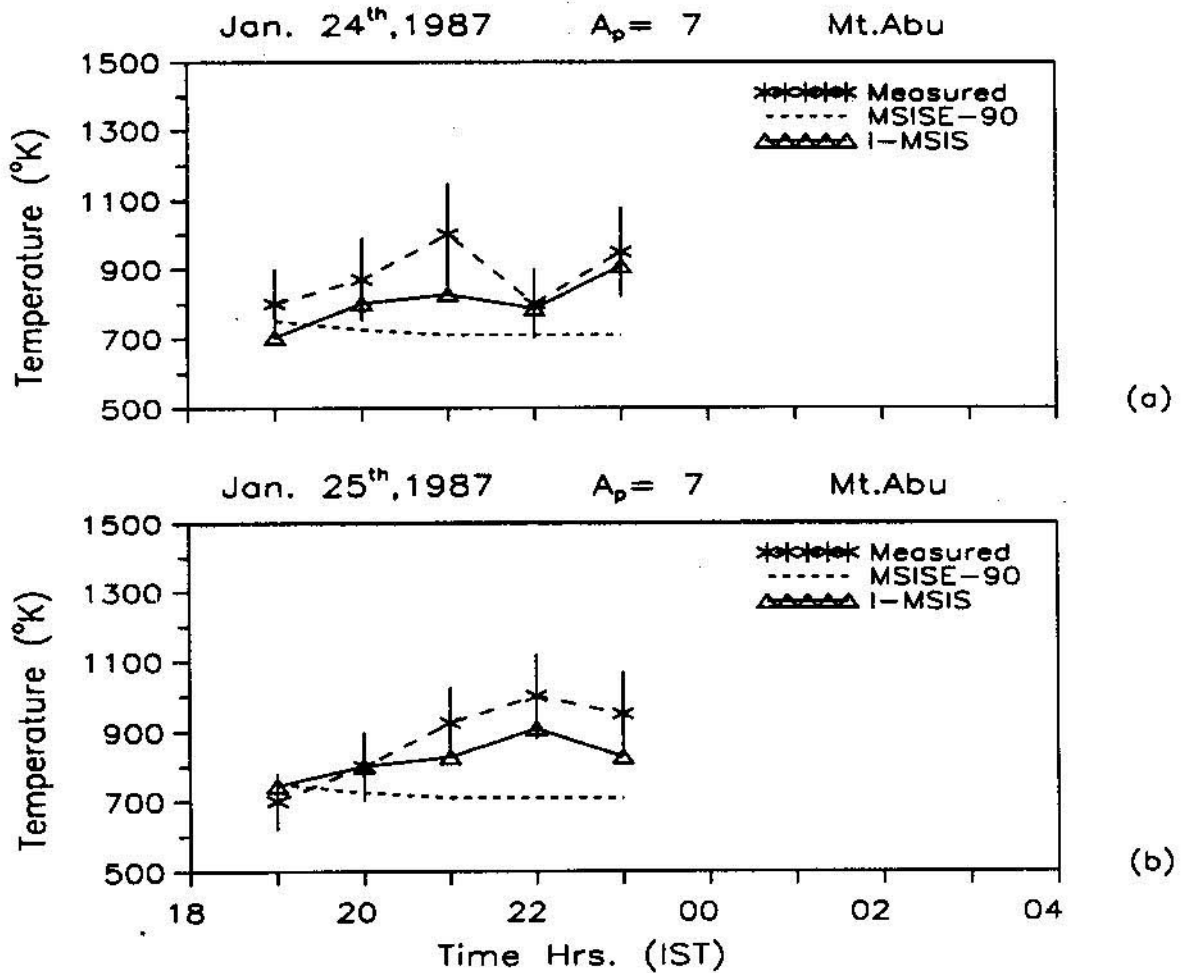


Figure 5.10: Comparison of observed thermospheric temperatures from Mt. Abu with MSIS model for the month of January 1987. Also shown are the I-MSIS model predictions.

other times on both the nights the I-MSIS fell short ($\leq 100\text{K}$) of the observations in terms of absolute magnitude.

The four days in the month of Feb. 1991 represent the solar maximum conditions. Figure(5.11) depicts measurements alongwith the model predictions for all the four days. The temperature showed lot of temporal variabilities on all the nights. The observed temperatures on Feb. 7th, decreased from an initial high of $\sim 1300\text{K}$ at 2100hrs to $\sim 900\text{K}$ at 0100hrs, which showed a slight recovery in the later hours. The MSIS model predicted average temperature trend. The deviations of observed temperatures from the model were by $\sim 150\text{K}$. The I-MSIS model seemed to be well capable of reproducing the observed temperature trends, though, before

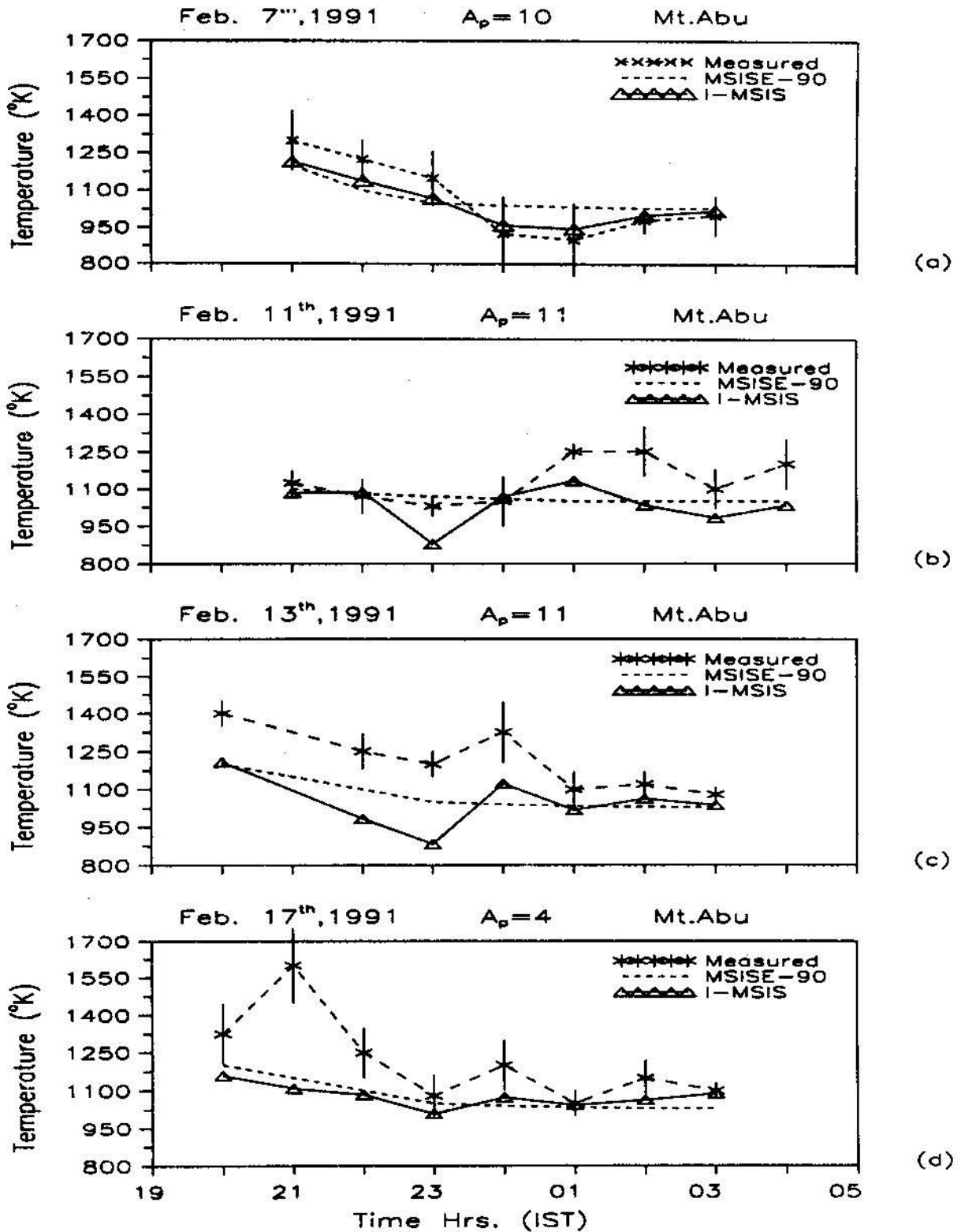


Figure 5.11: Comparison of observed thermospheric temperatures from Mt. Abu with MSIS model for the month of February 1991. Also shown are the I-MSIS model predictions.

2300hrs the I-MSIS predictions fell close to MSIS predictions. The temperatures on Feb. 11th, before 0000hrs, seemed to be well predicted by the MSIS model. But, the MSIS fell short to explain the enhanced observed temperatures after 0000hrs. The observed deviations were to the tune of $\geq 200\text{K}$). The reproduction of observed temperatures by the I-MSIS model seemed to be remarkable in terms of the temporal variability. However, the I-MSIS predictions were less than the measurements after 0100hrs. The observed temperatures on Feb. 13th were all the times higher than the MSIS model predictions. The average deviation observed was $\sim 150\text{K}$ on this night. The I-MSIS model seemed to be able to reproduce the variability but underestimated the temperatures before 0100hrs. The deviation between the observed and I-MSIS produced temperatures was also quite large i.e $\sim 300\text{K}$ at 2300hrs. These deviations, however got reduced after 0100hrs. The observed temperature on Feb 17th exhibited wavelike perturbation, its magnitude decreasing with time. The temperature at 2100hrs was quite large i.e $\sim 1625\text{K}$, deviating from the corresponding MSIS predictions significantly. The deviations got reduced after 2100hrs except at 0000hrs and 0200hrs. The I-MSIS model predictions, noticeably, were very similar to that of the MSIS model. The variability observed in temperature also did not reflect prominently in its predictions.

The variation of the measured thermospheric temperatures with time for the days during April 1991 is depicted in figure(5.12). Five days are considered for the month of April. The observed temperature on all the five nights showed a tendency of decreasing from a high premidnight value to a low postmidnight value. As was evident in the figure, the observed temperature on 10th April decreased from 1400K at 2000hrs to $\sim 800\text{K}$ at 0200hrs, increasing afterwards

steadily to $\sim 1200\text{K}$ at 0400hrs. The MSIS is incapable of predicting the variabilities observed in temperatures. On the other hand, the I-MSIS model remarkably reproduced all the temperatures till 0100 hrs. After 0100hrs, I-MSIS could not predict the sudden rise observed in the measurements, instead it remained constant after 0200hrs. The observed temperature on 11th, showed a nearly constant deviation ($\sim 100\text{K}$) from the corresponding MSIS predictions except during 0100-0200hrs. The model

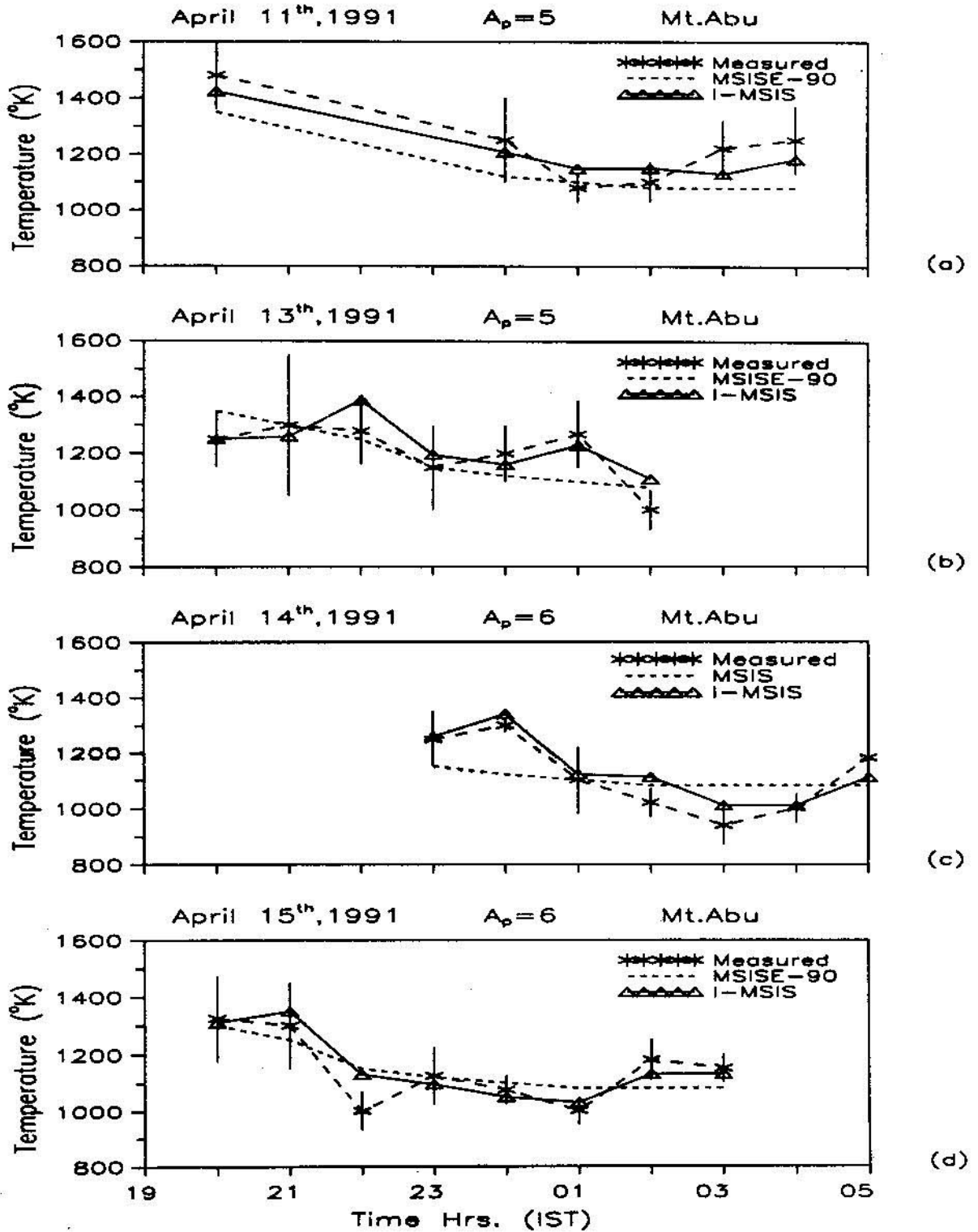


Figure 5.12: Comparison of observed thermospheric temperatures from Mt. Abu with MSIS model for the month of April 1991. Also shown are the I-MSIS model predictions.

predictions were almost exact during this time. The I-MSIS predictions significantly reduced the deviations to $\leq 50\text{K}$ at all the times, but the predictions slightly overestimated the temperatures in the interval 0100-0200hrs. The prediction of observed temperatures was fairly good on 13th April. It is clearly seen in the figure, that the I-MSIS model reproduced nearly all the measurements, including the fast temporal changes.

The observed temperatures on 14th April exhibited a gradual change from 1300K at 0000hrs to 900K at 0300hrs. The temperature increased steadily afterwards. The temperatures deviated from the MSIS model predictions. The deviations are both positive and negative w.r.t. the model predictions. The deviation was to the extent of $\sim 200\text{K}$ at 0000hrs and 0300hrs. The prediction of I-MSIS was remarkably good for this day. A slight difference ($\leq 30\text{K}$) was observed between the two in the post midnight period. However, the reproduction, by the I-MSIS, of the overall temperature variability with time can be considered to be very good. Similar, situation was observed on 15th April also. The observed temperatures were found to be deviating on both sides with respect to the MSIS model predictions. The deviations, however, were low on this night except at 2200hrs. The I-MSIS, like all the previous occasions, reproduced all the measurements within $\sim 40\text{K}$ including the temporal variability. The deviation of the I-MSIS predictions from the measurement is comparatively larger at 2200hrs.

On the basis of the above discussion, two things can be noted, when the observed temperatures are compared with the 'I-MSIS' predictions. (a) all the temporal variabilities exhibited by the measured temperatures are fairly well reproduced by the I-MSIS model. (b) Though, On many occasions even the 'dc' difference between the observed and I-MSIS predictions were explained ,

there were occasions at times, when it seems to be underestimating the temperatures.

Detailed analysis of the deviations of temperature measurements even after taking into account the sudden changes of solar flux ($F_{10.7}$) and the magnetic activity indices (A_p), revealed that there is an inherent 'limitation' embedded in the spectroscopically observed data which might lead to the discrepancies between the observed and model predicted temperature substantiating earlier suggestions [Hernandez and Roble, 1995]. The temporal variations does not, however, seem to get affected by the above stated limitation. The cause of this limitation in view of the current understanding is discussed in the following text.

5.11 Limitations of Ground Based (Optical) Spectroscopic Techniques in Estimating the Thermospheric Temperatures

Biondi and Meriwether [1985], while discussing the measured response of the equatorial thermospheric temperature from Arequipa Peru (16.4°S , 71.5°W ; 4.4°S magnetic) to geomagnetic activity and solar flux changes, using Fabry-Perot interferometric technique showed that the nightly variation of T_n measured on 62 nights, agreed well with MSIS model predictions only occasionally but, on an average, exceeded the model predictions by $\sim 180\text{K}$. In an even earlier study of winds and temperature over Kwajalein Atoll, Marshall islands (94°N , 167.5°E ; 8.6° diplat.), it was observed that the thermospheric temperatures, on an average were higher by 330 K than the MSIS model predictions. In a similar study, the measurements of temperature from Natal (5.9°S , 35.2°W , geographic; 6.4°S diplat.) for 15 nights during August and September 1982 as a part of the Brazil Ionospheric Modification Experiment (BIME) showed that the measured neutral temperatures exhibited good agreement with the

MSIS model values only during early part of the night but a significant post-midnight increase of 250K existed on some nights. Contrary to these observations, *Sahai et al.* [1992] have reported results from Brazil (23°S geographic) which are in good agreement with MSIS-86 predictions. Simultaneous FPI and incoherent scatter measurements of temperatures reported in two papers [*Cogger et al.* 1970; *Hernandez et al.* 1975] revealed only small differences of ~ 30 K. But in more recent results from the Indian zone, *Sastri et al.* [1994] and *Gurubaran et al.* [1995] showed the optically measured temperatures from Kavalur (12.5°N, 78.5°E) and Mt. Abu (24.6°N, 72.7°E) respectively to be significantly deviating from the MSIS predicted temperatures; the difference ranging from ~ 100 to 500 K. Since all the versions of the MSIS models involved empirical fitting of temperature data base (derived mainly from incoherent scatter radar and in situ mass spectrometer measurements) to solar and geomagnetic indices, intercomparison of the T_n values determined by FP and MSIS techniques, might suggest that the source of discrepancy between the observed thermospheric temperatures and predictions of MSIS model could be due to the different methods of temperature determination. The nonthermal broadening of the 6300Å nightglow emission line by remnants of dissociative kinetic energy from the recombination reaction which produced O(¹D) atom, [*Torr and Torr*, 1984] cannot account for these elevated temperatures. So the FP measurements should be in agreement with at least one element of MSIS data base.

These different observations indicate towards something which is intrinsic to the ground based optical interferometric techniques which might reflect in terms of comparatively broader Doppler profiles i.e. larger thermospheric temperatures. The effects of wind shear and temperature gradients within the instrumental field of view are usually neglected on the basis of an assumption that the observations are so heavily weighted to the emission peak (i.e. ~ 250

km), so that the FPI wind and temperatures can be assigned uniquely to that altitude. From the earlier results one could appreciate the reigning controversy. *Sica et al.* [1986] presented temperature measurements in the auroral regions, which were significantly lower than the expected exospheric temperatures. This was ascribed to the fact that the centroid of the $O(^1D)$ auroral emission extends predominantly to lower altitudes than the $O(^1D)$ nightglow emission peak. This is a clear example for the discrepancies that can be induced to inferred temperatures because of the uncertainties associated with location of the peak emission height with respect to the exobase.

In fact, the peak altitude of the $O(^1D)$ emission layer can vary on occasions by tens of kilometers [*Hays et al.* 1978] and the interpretation of the FPI observations, therefore, is subject to this ambiguity. Significant temperature changes may be observed as the rise/fall of the emission layer can move it to the regions of strong temperature gradients below the exosphere. As discussed by *McCormac et al.* [1987], as an example, for solar maximum conditions, the exospheric temperature is not reached below 400 km, and therefore the $O(^1D)$ emission peak (~ 250 km) would lie in a region where strong altitude gradients of thermospheric temperatures exist. This, consequently would lead to erroneous interpretation of observed FPI Doppler profiles from the region. Similarly for solar minimum conditions, when the atmosphere is thought to be nearly isothermal above ~ 250 km, the altitude gradients are very small. Therefore, the recovered FPI temperatures and winds would nearly be representing the exospheric values. As is clear from the above discussion, the altitude region covered by the interferometer depending on its viewing geometry, the actual location of the peak of emission profile, and the shears if any present in the airglow emission etc., would play a very crucial role in deciding the nature of the Doppler profile as observed from the ground. To understand the relationship

between FPI measurements and corresponding exospheric values, we carried out a simulation exercise taking into account the measurement processes and conditions of our observing station Mt.Abu (24.6° N, 72.7° E geographic; 20° N dip lat.), and developed a theoretical 'station processor'. The analogy is drawn from earlier works of [McCormac *et al.* 1987; Hernandez *et al.* 1995]. This station processor calculates the emission weighted, height-integrated Doppler line profiles as would be observed from a ground station. The discussion of this station processor is given in the following section.

5.12 Station Processor

Every volume element falling in the altitude range covered by the field of view of the interferometer at the thermospheric heights, is a source of emission characterised by the emission rate and the temperature at that altitude. In other words, every single volume element is represented by a unique Doppler profile depending upon the instantaneous thermodynamic state. A ground based instrument, located at any particular location and gazing the sky at an arbitrary azimuthal and zenithal direction would observe an integrated sum of all the Doppler profiles, specified above, emanating from individual volume elements falling in the line of sight of the instrument. Also associated with it would be the Van-Rhijn effect. We have assumed the atmosphere to be in the form of isothermal layers like 'onion-peels' as proposed by Hernandez *et al.* [1995]. Therefore, an emission line profile that would be observed by a ground based spectrometer is, the emission-rate weighted sum of all the line profiles from layers (onion-peels) in its line of sight at a slant angle related to the zenith angle of observation. If the altitude region covered by the instrument is infested with altitudinal or horizontal temperature gradients and wind shears, thus observed Doppler profile as per the above description, would lead to an over estimate of the temperatures and also the winds.

The response of the FPI to the emission originating from a thermospheric volume element along the line of sight can be given by following expression.

$$N(Z) = cS(\lambda, U(Z), T(Z), \eta(Z)) \star \psi(\lambda)$$

where $S(U, T, \lambda, \eta)$ represents the source function which is a function of (i) neutral wind U ; (ii) neutral temperature T ; (iii) real volume emission rate ; (iv) the wavelength and ψ is the instrumental function, all at the altitude of ' Z '. The final sum or the integrated profile as observed at the ground is given by:

$$N_{\text{line of sight}} = c \int S(\lambda, U, T, \eta) \star \psi(\lambda) dl$$

here ' l ' is the path length along the line of sight and the summation is carried out for all volume elements (Layers) separated by a given altitude increment. In our case, we have taken this increment to be discrete and of 5 km step. The volume emission rates at 20° lat. i.e., the latitude of our interest, were obtained from the earlier works of *Abreu et al.* [1982] during solar minimum, and *Fesen and Abreu* [1987] observations from the VAE (Visible Airglow Instrument) on AE-E satellite during solar maximum, spring equinox conditions. Altitude profiles of temperature for both solar maximum and minimum conditions were generated using MSISE-90 model for geomagnetically quiet conditions. Taking into account the volume elements covered by the layers each of width 5 km (vertical), inside the instrument

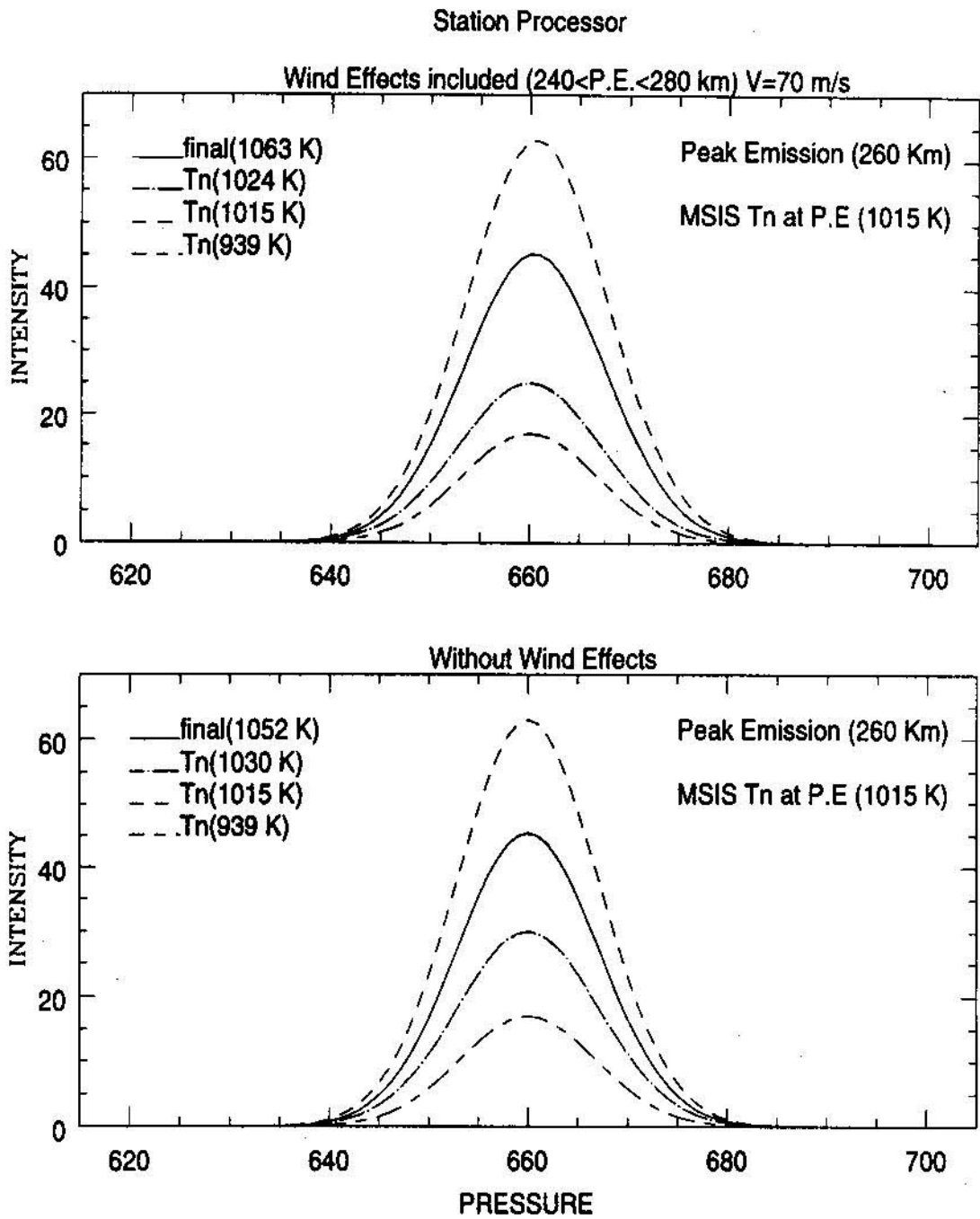


Figure 5.13: top: The station processor estimation of the resultant profile (solid line) in the region between 240-280km with a uniform wind of 70m/s. bottom: The similar simulation done without the wind effects. The profiles denoted by the dashed lines in both the panels represents the sample profiles at three different altitudes.

field of view at thermospheric heights, and integrating it along with volume emission rates for corresponding temperature at that representative altitude, the resultant profiles were obtained. Figure (5.13) (bottom) shows three representative profiles from three different altitudes and also shown is the resultant profile estimated for the given conditions. Further analysis of the resultant profile and its comparison with model estimated exospheric temperatures, revealed that the spectroscopically measured temperatures are 5-7% higher. Similar result was obtained when we induced a shear of ~ 70 m/s for the emission layer peak in the volume element having altitudinal width of 50 km and the results are depicted in Figure(5.12).

For comparison, only four nights of data during Oct. and Nov. 1986, corrected using the station correction term i.e 5-7% for Mt.Abu are presented here [figure(5.13)]. The corresponding IMSIS predictions were not shown in this figure. In fact, new equations would have to be worked out after proper station correction to the spectroscopically measured temperatures. Therefore comparisons were made only with respect to the MSIS model temperatures. It is clear from the figure that the station corrected temperatures still exhibited large deviations from the MSIS predictions. On 28th. Oct, the temperatures after station correction deviated more from MSIS before 2000hrs and after 2000hrs, the agreement with MSIS predictions got improved. For the Nov 23rd night, more number of corrected measurements seemed to be close to the MSIS predictions. The same holds true for the observations on 26th Nov'1986 too.

Therefore, while measuring the thermospheric temperatures, it is important to know the atmospheric processes which are responsible for the steep temperature and wind gradients under quiet conditions. A correct identification

and quantification of those processes can only explain all the discrepancies between measured neutral temperatures and the model predictions, more significantly so over low latitudes. In addition, the presence of large scale processes always increases the uncertainties on account of the steep spatial gradients, and dynamical changes produced by them. Therefore it becomes extremely important to delineate the effect

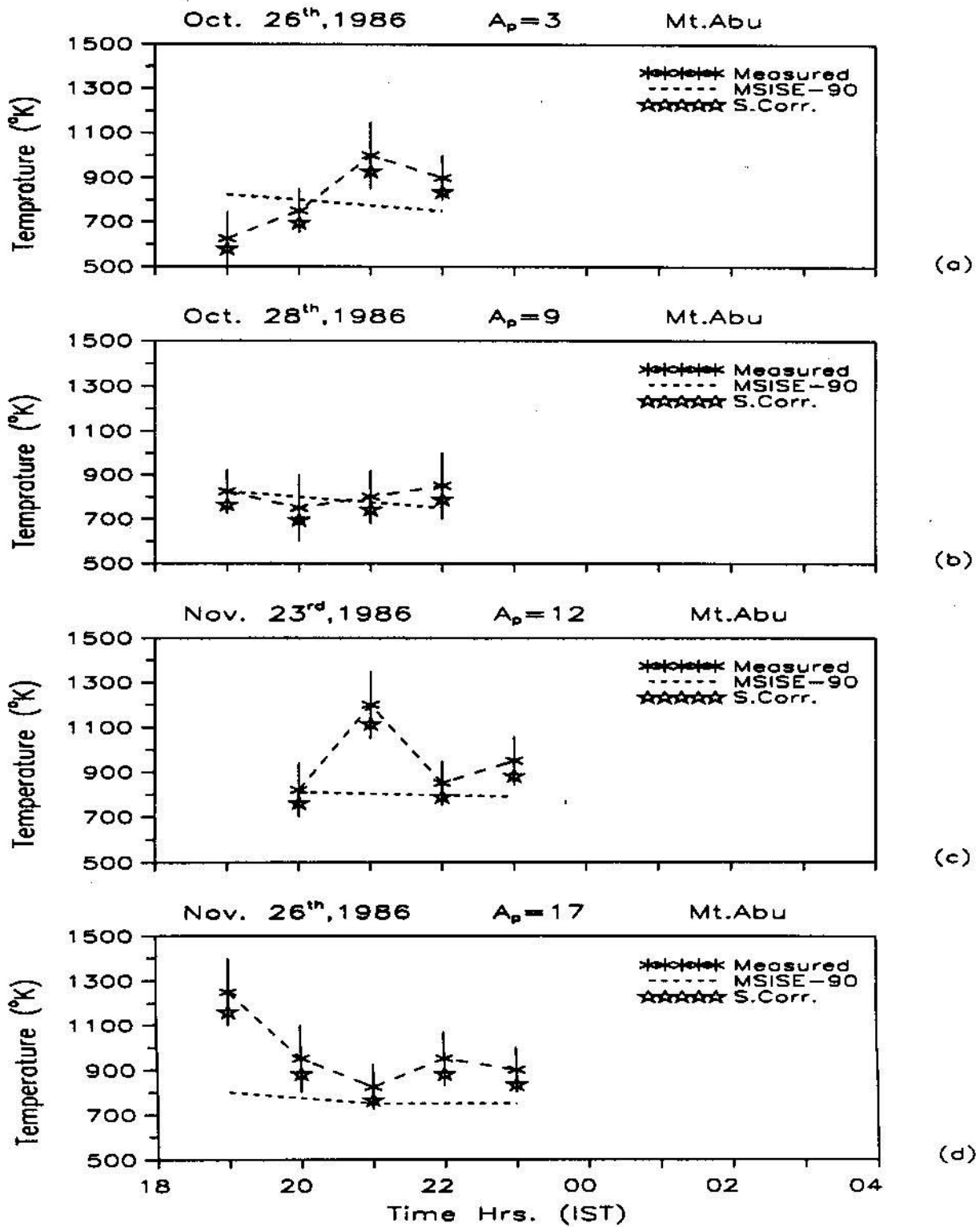


Figure 5.14: Comparison of observed thermospheric temperatures from Mt. Abu with MSIS model for the month of Oct. and Nov. 1986. Also shown are the station corrected measurements, for comparison.

of these local processes to parameterise and model their behaviour. Thus these spectroscopically measured temperatures put a constraint, if used directly i.e., without a station correction, for the comparison with existing thermospheric model predictions.

In the following Chapter, a detailed discussion follows on the importance of in situ temperature measurements and their representation by the model. The role of large scale processes over low latitudes especially around the latitude of Mt. Abu ($\sim 24.6^\circ$) in the context of augmentation of the existing thermospheric model (MSIS-90) for more realistic representation of neutral temperatures is discussed comprehensively. Results on the quantification of one of these most prominent large scale processes will also be presented.

Chapter 6

Parameterisation of Local and Nonlocal Processes and their Incorporation into the MSIS Model

6.1 Introduction

It has been shown in the earlier chapters, that the spectroscopically observed thermospheric temperatures very often exhibit significant deviations from the MSIS model predictions. The existence of such large temperatures and the associated variabilities had also been reported by other direct measurements as well. In case of the, ground based estimation by optical interferometry, the deviations from the model could arise mainly due to two factors. One is the inherent limitation of the ground based optical techniques leading to an over-estimation of the thermospheric temperatures to an extent of 5-7% and the other factor is that all the processes and energy inputs for quiet and disturbed geophysical conditions are not adequately accounted for by the model especially when it comes to low latitudes. The parameterization of these processes, in terms of $\frac{d(Dst)}{dt}$ based on the low latitude thermospheric 'response time' during different seasons as developed in the present investigation, is an important step towards indirectly incorporating these unaccounted nonlocal energy sources into the MSIS model which significantly improved the MSIS model predictions for variabilities in thermospheric temperatures. However, a capability for the prediction of overall temperature levels is still to be achieved.

It is known that the low latitude TIS is continuously under the influence of many large scale local processes which also contribute significantly to its thermal balance and are not accounted for by the MSIS model. Some of them are the Equatorial Temperature and Wind Anomaly (ETWA) associated with the Equatorial Ionisation Anomaly (EIA) [Raghavarao *et al.* 1991]; Equatorial spread-F (ESF) [Cole, 1974]; Midnight temperature maximum (MTM) [Spencer *et al.* 1979]; and the ring current associated neutral particle precipitation [Tinsley *et al.* 1981]. ETWA/EIA, being the most dominant process of the equatorial regions, is expected to affect the low latitude temperatures the most. Therefore, an exercise was carried out in order to quantify the contribution of ETWA to low latitude energetics.

In the following section, we discuss the salient features of EIA followed by a comprehensive discussion on the role played by the ETWA in the energetics of low latitude TIS. Towards the end of the chapter, results are provided on the comparison of in situ measured temperatures with the ones predicted by the MSIS model after taking into account the contributions due to processes such as ETWA and magnetospheric current systems and incorporating them in the MSIS model.

6.2 Manifestations of Equatorial Ionisation Anomaly over Equatorial and Low Latitudes

In the low and equatorial thermosphere, the process of Equatorial Ionisation Anomaly (EIA) [Appleton 1946] is a result of the complex neutral gas-plasma interactions. The discovery of EIA was based on the equinoctial data of a low sunspot year viz. March 1944, when two peaks in electron density were found at $\pm 18^\circ$ magnetic lat. When one would expect the electron density to be maximum over equator monotonically decreasing on both sides. This deviation in

the observed ionisation density from the expected distribution prompted the name Equatorial Ionisation Anomaly (EIA). The EIA was further confirmed for both high and low sunspot years [*H. Maeda* 1955, *K. Maeda*, 1955]. It has been probed by various techniques like the ground based ionosondes, satellite borne topside sounders and by the satellite beacon monitoring of total electron content (TEC) of the ionosphere [*Rastogi*, 1959; *Croom et al.* 1960; *Duncan*, 1960; *Lyon and Thomas*, 1963; *Rao and Malhotra*, 1964; *Walker and Ma*, 1972; *Anderson and Klobuchar*, 1983]. The equatorial anomaly was first explained by *Mitra* [1946], who suggested that the ionisation produced by the solar UV radiation in the upper atmosphere above the magnetic equator, was capable of being guided towards north and south along the magnetic lines of force. Later, *Martyn* [1947] proposed the drift theory and showed that, it is actually the vertical drift of plasma over dip equator followed by diffusion along magnetic field lines, which is responsible for this double humped anomalous distribution of electron density. Later it was suggested by *Goldberg* [1965] that the EIA is simply the natural, steady state electron density distribution under the combined influence of gravity, electric and magnetic fields, and the process of chemical production and loss. The ionospheric interactions with neutral medium were proposed to be negligible. *Moffet* [1979] reviewed the gross features of EIA taking into consideration the physical and electrodynamic processes that control this phenomena. *Anderson* [1981] combined the production, recombination and the vertical drifts of ionospheric species and brought forth a reasonable realistic model describing the diurnal and latitudinal variation of the ionospheric plasma density which also provided a visual representation of the EIA development [figure(6.1)]. This study also highlighted the importance of vertical plasma drifts caused by electric fields in the presence of the earth's magnetic field. The zonal electric field (\vec{E}) which is eastward during the day, causes a

steady upward plasma drift i.e., $\vec{E} \times \vec{B}$ where \vec{B} is the earth's magnetic field at lower thermospheric heights. This vertical drift is independent of charge and mass, hence both the electrons and the ions get affected alike. The net result is a fountain of dense equatorial plasma rising under the action of $\vec{E} \times \vec{B}$ drift, until the resulting meridional pressure gradient become strong enough, so that the plasma start diffusing down the magnetic field lines assisted by gravity, and the poleward winds towards the low latitude ionosphere. This leads to the redistribution of plasma density [figure(6.1)].

Large day to day variability is observed in the development of EIA. One of the remarkable variability shown by EIA is its latitudinal extent with varying geomagnetic conditions, season and solar epochs. Topside sounding and the Total Electron Content (TEC) revealed large longitudinal differences and a high degree of variability in the meridional direction [Garg *et al.* 1983; Raghavarao *et al.* 1988a, Sharma and Raghavarao, 1989; Rastogi and Klobuchar, 1990; Sastri, 1990, Abdu

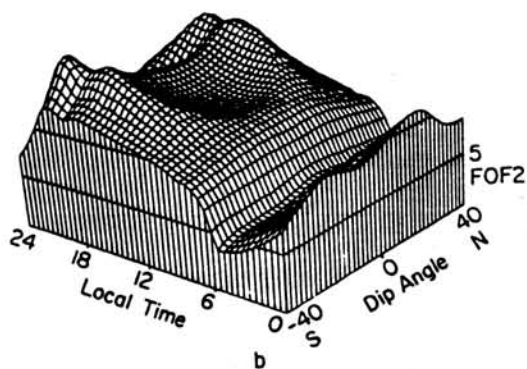
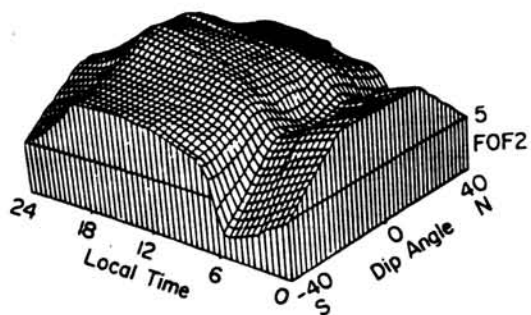
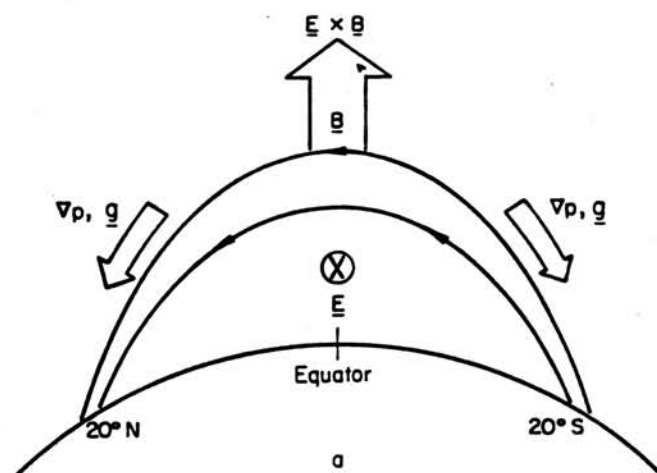


Figure 6.1: Schematic diagram of the process of the generation of the EIA. (Anderson 1981)

et al. 1991; *Walker et al.* 1991, 1994]. Following this development, a need was felt to define a general parameter in order to characterize the process of EIA and to find any correlation this process could have with other low latitude processes. *Rush and Richmond* [1973] devised a parameter called the 'strength of anomaly' which was defined as the product of the ratio of electron densities at the crest to that at the trough of EIA and the dip latitude of the crest. *Raghavarao et al.* [1978] used this parameter and showed that the development of EIA was indeed related to the equatorial phenomena called the Equatorial Electrojet (EEJ) and the strength of the EIA had a high degree of positive correlation with electrojet strength integrated between morning to the time of observation. This result was quite significant as it indicated towards the control of the zonal electric fields on the EIA which, in other words, meant that the development of the anomaly could be studied on the basis of intensification of the equatorial electrojet.

During daytime, the equatorial anomaly is produced by tide induced E-region dynamo electric field which is, mapped along the field lines on to the F-layer heights. Though predominantly a daytime phenomenon, EIA can extend well beyond the post-sunset and predawn hours depending on the season and solar activity phases. The significant post-sunset EIA are caused by the complex coupled ion-neutral dynamics near sunset hours, when the F-region dynamo takes control from the daytime E-region dynamo. During quiet times, in fully developed form, the ratio, the EIA crests bear with the trough is typically of two orders of magnitude [*Abdu et al.* 1990]. The extent of the crests tend to stretch farther in latitude during high solar activity phase and tend to shrink during geomagnetically disturbed conditions. However, the transequatorial meridional winds as a part of global circulation system can cause deviations in the form of north-south asymmetry in the crests.

The magnetospheric disturbance fields as a part of global electrodynamic system during geomagnetic storms most often cause inhibition of EIA development, and occasionally result in an enhancement too. Examples of both types of events have been reported in literature [*Rajaram, 1977; Raghavarao and Sivaraman, 1973; Abdu et al. 1991*]. During the presence of EIA, a steep density gradient exists from crest to trough. Because of the coupled nature the redistribution of ionisation during the formation of EIA, affects the distribution of neutrals too.

Hedin and Mayr [1973] while studying the latitudinal distribution of molecular species i.e., N_2 obtained from OGO-6 data, showed an enhancement (20%) in (N_2) density at $\pm 17^\circ$ dip latitude and a decrease over the dip latitude at 1700 LT. While N_2 density was found to be maximising over the dip equator in the morning hour i.e., ~ 0600 LT. This aspect of neutral density distribution with respect to the magnetic equator was quiet intriguing as the magnetic and electric fields are not expected to have a direct control on the movement and distribution of neutral species. Therefore, this behaviour of molecules in their latitudinal distribution, where the crests and trough were found to be colocated with EIA crests and trough, was considered quite anomalous [Figure(6.2)]. This anomaly came to be known as the Neutral Anomaly (NA). *Hedin and Mayr [1973]* tried to explain the NA on the basis of enhanced ion drag/friction offered to the zonal flow of neutrals from the hot dayside to the cold nightside, by the enhanced densities over the EIA crest regions.

Raghavarao et al. [1991] using DE-2 satellite data, discovered an another important effect where they found that the latitudinal distribution of thermospheric temperatures and zonal winds also showed a close linkage with the EIA. This new effect was referred to as the Equatorial Temperature and Wind Anomaly (ETWA). The phenomenon of ETWA has very important implications in the

thermal budget of low latitude TIS, and it also has a significant bearing in the present investigation in the context of improvement of the model (MSIS) for realistic representation of low latitude neutral temperatures. In the following section all the salient features of ETWA are discussed, following which the details of the quantification of the same based on ionospheric and neutral atmospheric parameters alongwith the final results are presented.

6.3 The Equatorial Temperature and Wind Anomaly

The Wind And Temperature Spectrometer (WATS) and Langmuir probe (LP) experiments onboard DE-2 (Dynamics Explorer-2) satellite during high solar activity epoch (1981- 1982) provided evidences of anomalous variations of zonal winds and

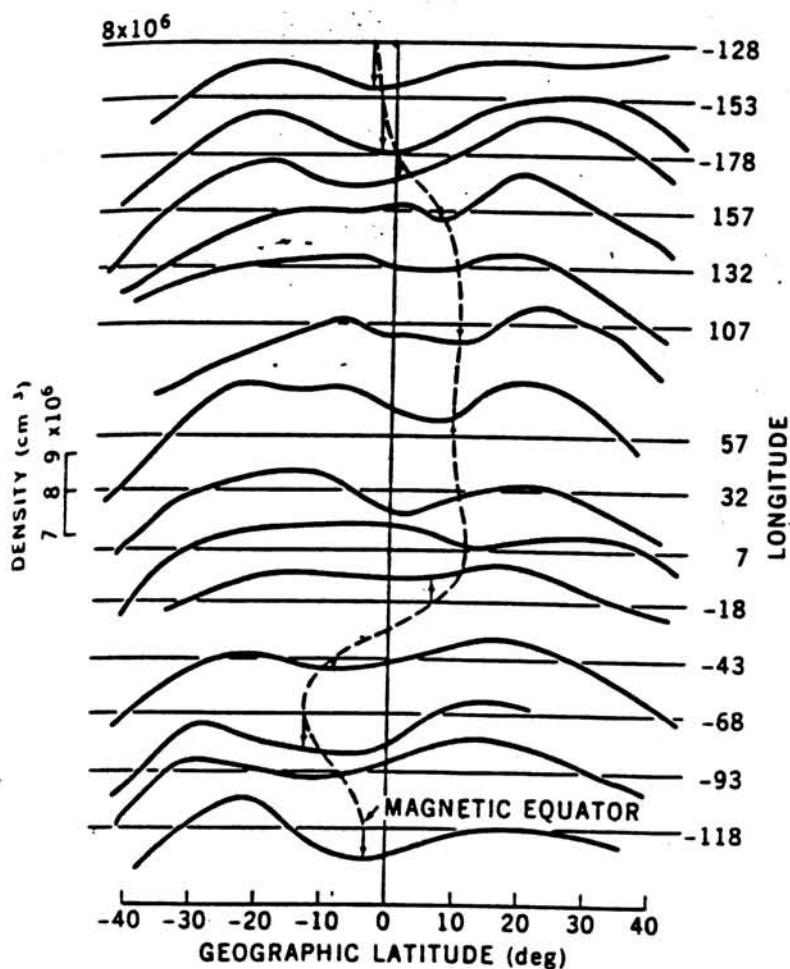


Figure 6.2: The neutral anomaly seen in N_2 densities extrapolated to 450 km as a function of geographic latitude for various longitudes on March 16, 1970. The reference line for each orbit is $1 \times 10^6 \text{ cm}^{-3}$. The local time is approximately 0600 hrs. (Hedin and Mayr 1973)

temperatures over low latitudes [Raghavarao et al. 1991, 1993]. The Zonal winds were found to exhibit a broad maximum around the dip equator, associated with minimas on both sides at $\pm 25^\circ$ diplatitude, while the temperature, on the contrary, showed a minimum around the dip equator flanked by maxima on both sides. In addition to this, the two minima of zonal winds and the maximas in the neutral temperature were found to be nearly colocated with the crests of the EIA, while the maximum in the zonal winds and the minimum in temperature were found to be colocated with the trough of the EIA. This was the first experimental evidence where the neutral wind dynamics also was shown to be controlled by the geomagnetic field configuration similar to EIA. Raghavarao et al. [1991] presented DE-2 measurements for the electron density, as well as the temperature and zonal winds,

density, as well as the temperature and zonal winds, plotted as a function of universal time, altitude, geographic and geomagnetic latitude and longitude. One of the example shown by *Raghavarao et al.* is depicted in the figures(6.3), with orbit and day number at the top of the respective panels. In the top panel, the observed electron density (P) distribution in the form of a well developed equatorial ionisation anomaly is shown; the crests and trough are clearly discernible. The density at the crests is typically two orders of magnitude higher than at the trough. The observed asymmetries, such as the sharp density peak in northern winter hemisphere in contrast to broad maxima in summer hemisphere, are due to the altitude variation in the satellite trajectory in the region of measurements.

The zonal wind (Z), as shown in figure, which is eastward in the late afternoon and westward in the morning, revealed a clear maxima/enhancement over the dip equator. A clear anti correlation exists between the electron density and zonal wind variation. The horizontal wind model (HWM87) [*Hedin et al.* 1988], as expected, did not reveal any latitudinal modulations in the predicted zonal winds (also shown in the figure). The zonal winds seemed to be significantly impeded (by $\sim 50\text{-}60$ m/s) at the locations of the ionisation crests that make up the EIA. The observed variations in neutral temperature 'T', shown in lower panels of figure(6.3) displayed a clear maximum in the temperature in the winter hemisphere at latitudes colocated with, the peaks in electron density and minima in zonal velocity. At the same time, the model (MSIS) predicted only the average summer to winter hemisphere temperature changes. It is quite apparent from the simultaneous behaviour of the temperature, zonal wind and electron density that the phenomenon of ETWA is dynamically connected to EIA. In the following section, a detailed description of the plausible causative mechanisms of ETWA is given.

6.4 Plausible Causative Mechanisms of ETWA

As has been shown the figure(6.3), the relative variations characterizing the temperature anomaly in ETWA, are between 4-10%. This is deemed to be very significant, as the extent of diurnal temperature variations over low latitude itself

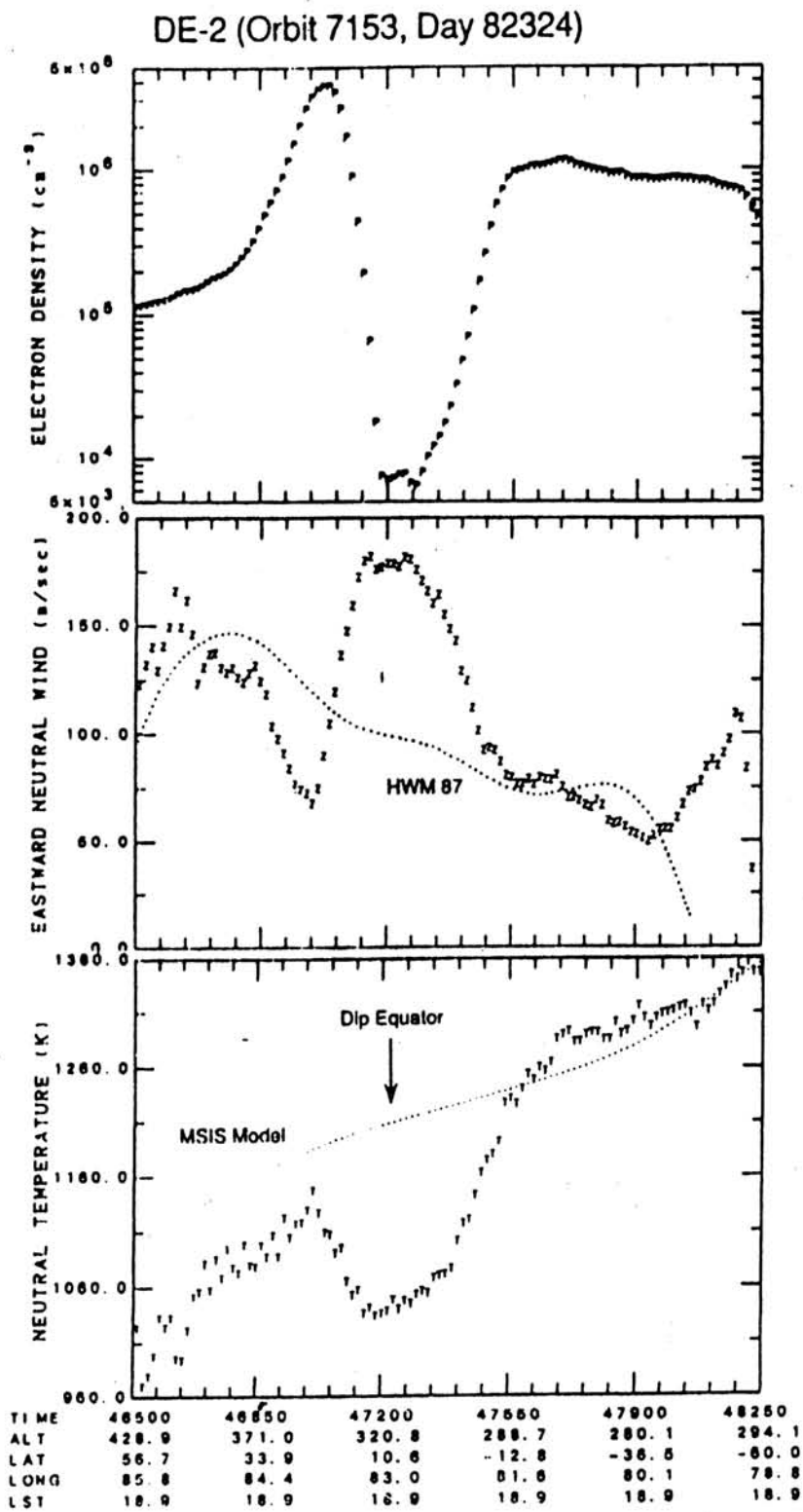


Figure 6.3: The Equatorial Temperature and Wind Anomaly (ETWA) as seen in the DE-2 (WATS) data. (Raghavarao et al. 1993).

amount to only about 13%. The decrease in zonal wind velocities from equatorial maximum to minima on either side had been as large as 100m/s, and temperature increase amounts to an extent of 50-100 K. These results amply demonstrate that the observed latitudinal variation of zonal winds and temperatures are different manifestations of the same process i.e. EIA and its interactions with neutral atmosphere.

After the discovery of EIA, many studies by considering ion-neutral interactions, proposed similar effects in temperature and wind as that of EIA. In fact, *Chandra and Goldberg* [1964] proposed that the ion neutral collisions can actually lead to geomagnetic control of neutral species, by disturbing the hydrostatic equilibrium in the thermosphere. But, in reality the ion-drag affects the neutral species through dynamics in the thermosphere in all circumstances, including the above proposed condition of hydrostatic equilibrium [*Dickinson et al.* 1971]. *Jacchia and Slowey* [1967], discussed even the possibility of the shape of the diurnal temperature bulge over low latitudes being closely related to the ion density distribution, as a consequence of the control of ion-drag on the redistribution of solar energy through neutral motion. *Hedin and Mayr* [1973] through a simple two dimensional theoretical model dealing with both the viscosity and the ion-drag, tried to estimate the diurnal component of temperature and density variations over low latitudes. It was shown that, at the crest regions i.e., $\sim 20^\circ$ latitude, the energy transport from the hot dayside to cold nightside by means of zonal thermospheric flow, is damped by the increased ion-neutral drag due to enhancements of electron density at the crests of EIA. They proposed that it is the gradual variation of the ion-drag from dayside to the nightside which might be the cause for the ETWA.

The mechanism of horizontal transport of energy from the hot dayside to the nightside as proposed by *Hedin and Mayr* [1973] fails to explain the observed

temperature feature in ETWA. As per their mechanism the zonal wind carrying energy from dayside should create a local warming in evening sector, as the efficiency of transporting the energy would gradually be reduced while going from dayside to nightside. The zonal wind over the dip equator, because of their enhanced magnitude should be carrying the energy more efficiently, so more heating would be expected at the evening sector. But such a localized warming is contrary to the observations. The second mechanism of adiabatic cooling and heating proposed by *Anderson and Roble* [1974] is in contradiction with the observed effects.

Following this, *Anderson and Roble* [1974] attempted to explain the variability of zonal wind field near the equator at sunset hours on the basis of, changing ion drag and, by using the OGO-6 empirical model [*Hedin et al.* 1974] of neutral atmosphere. They considered movement of neutral species in connection with the ionospheric F-layer movement, which meant that large upward drifts of F layer to higher altitudes would significantly deplete the ionisation in lower altitudes resulting in a decrease in ion-drag there, which in turn would lead to enhancements of zonal wind. The thermodynamic coupling between the temperature and wind variations were not considered by them. A continuity in air circulation was invoked to suggest an upwelling of air to feed the zonal acceleration, and a subsequent downwelling in response to deceleration. They tried to explain the twilight temperature decrease and the nighttime temperature perturbations over low latitudes on the basis of F-layer movement up and down producing adiabatic cooling and heating effects respectively. For instance, the adiabatic cooling leading to temperature reduction should occur in a region which is undergoing expansion (upwelling) i.e., over the trough, but vertical wind observations reveal a clear downwelling [*Raghavarao et al.* 1993] at those locations. Therefore, these theories have serious drawbacks in

explaining the ETWA.

Recently, in order to find an appropriate mechanism for the generation of the ETWA; the equatorial thermosphere ionosphere system was theoretically simulated, by combining neutral thermospheric model [Fuller-Rowell and Rees, 1980; Fuller-Rowell et al. 1994] with a parameterised ionospheric model (PIM) [Daniell and Anderson, 1995; Daniell et al. 1995, Fuller-Rowell et al. 1997]. Combination of these two models mentioned above, produced the zonal wind and corresponding EIA density distribution features which were remarkably similar to the Dynamics Explorer observations. Figure(6.4) shows the result of this simulation of ETWA with the above stated hybrid thermosphere ionosphere model. It is to be noted that the temperature anomaly feature of ETWA could not be simulated properly, though EIA and the wind fields were generated quite satisfactorily. This indicates towards our lack of understanding of the appropriate mechanism responsible for the generation of ETWA. All the causative mechanisms thought of earlier to explain ETWA, could only qualitatively and partially explain the observed temperature structure. Therefore, in the absence of any concrete understanding of the causative mechanisms especially of the temperature anomaly, it is really difficult to theoretically generate the temperature structure associated with ETWA. However, in recent times, two schools of thought regarding the causative mechanisms of ETWA have emerged. One, favoured by Raghavarao et al. [1993] where they propose that the latitude variation of ion-drag associated with EIA, can explain all the observed features of ETWA, which includes the observed vertical wind structure. The other is initiated by Fuller-Rowell et al. [1997], where they invoke chemical heating to explain the observed temperature and vertical wind field variations. In the following section a brief account of both these theories is given.

6.5 Temperature Anomaly in ETWA: Ion-drag and/or Chemical Heating

From the above discussion, the mechanisms which appear to hold the key for a viable explanation of ETWA temperature feature seems to be based on (i) ion drag, (ii) chemical heating. The zonal wind as generated by the diurnal tide experiences a severe resistance in the presence of EIA, thus inhibiting the movement of hot neutral species across the crests. The resistance offered to the flow of neutral species is more on EIA crest because of the enhanced ionisation density. As a result, the loss of momentum of zonal winds appear as an energy deposit at the crests causing a net enhancement of temperature. Due to the abatement of zonal winds, pressure crests also get formed which are colocated with the temperature crests. This

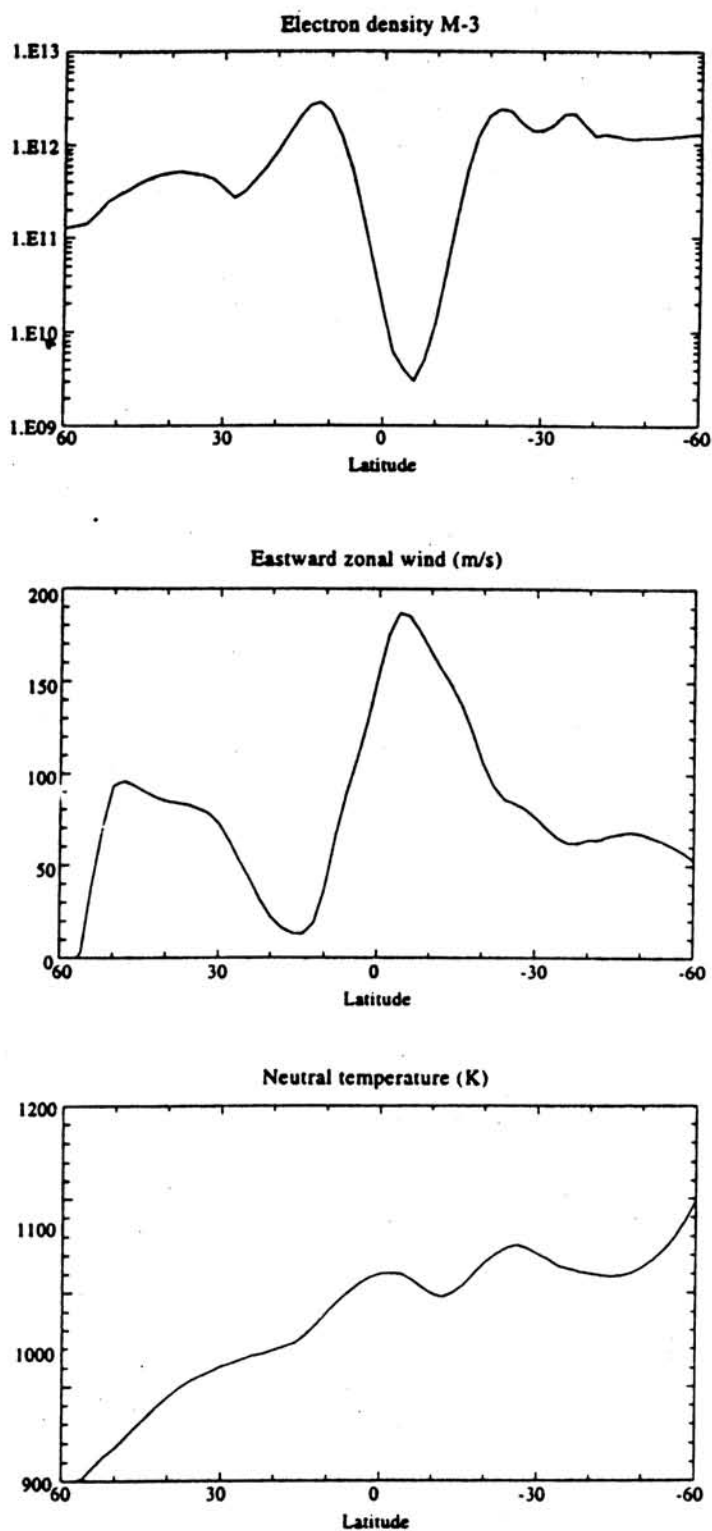


Figure 6.4: Simulation of ETWA with a hybrid thermosphere/ionosphere model. The figure shows ion density from PIM, zonal neutral winds, neutral temperature from -60° to 60° latitude, at 1.2 UT, local time 22.8 h, at an altitude of about 400km in the upper thermosphere. (Fuller-Rowell et al. 1997).

heating due to winds, as mentioned above, is an adiabatic process [*Dickinson et al.* 1971; *Hedin and Mayr*, 1973]. In the evening sector, the enhancement of ionisation density at the EIA crests due to the prereversal enhancement of the equatorial zonal electric field would further abate the zonal wind flow through ion-drag and would sustain the temperature crests even in the late evening hours. It was proposed by *Raghavarao et al.* [1993] that the pressure ridges, formed along the meridian, might give rise to a new wind system, depicted in figure(6.5). The new wind velocity vector would be upward near the pressure crests, equatorward between the crests and downward at the trough. The ground based measurements of vertical, meridional and zonal winds also seem to be agreeing with the above described mechanism and the observations by *Biondi and Sipler*, (1985). The agreement between the observed vertical winds and proposed wind field as a result of neutral temperature anomaly lend credence of the theory of ion-drag heating for the generation of ETWA. The proposed pressure ridges and vertical velocity structure is known to be extended over a wide range of longitudes whenever EIA and ETWA are strong.

However, results based on numerical simulations, indicate the possibility that the exothermic chemical reactions could also contribute to ETWA [*Fuller-Rowell et al.* 1997]. As a matter of fact, the chemical heating is always active as it depends only on the constituents of the region. At the crests of EIA, where the ionisation density is high and could continue to be so, well beyond the day into the night, the exothermic two stage recombination of O^+ is proposed to be the main chemical heating source [*Fuller-Rowell et al.* 1997]. It is known that the same two stage recombination reaction is responsible for thermospheric nightglow at 6300\AA .

As estimated by *Fuller-Rowell et al.* [1997], the net heating rate at 360 km at an exospheric temperature of 1000K was over 200K/h. Figure(6.6) shows the

longitudinal variation of the estimated chemical heating rate. The important thing to be noted is that the vertical wind system driven by the chemical heat source at EIA crests agrees with the observed wind field by DE-2 [*Raghavarao et al.* 1993]. However, the chemical heating effects over low latitude can be modulated by tidal interactions and such interactions would either reinforce the temperature feature

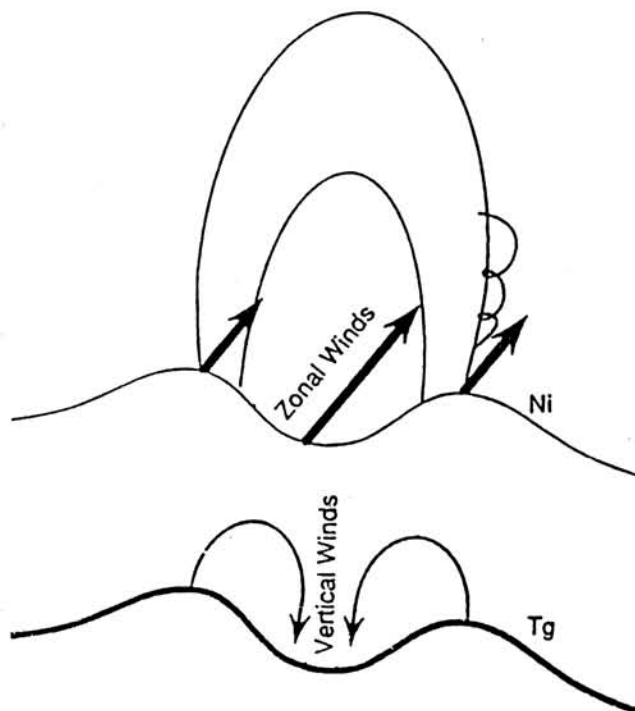
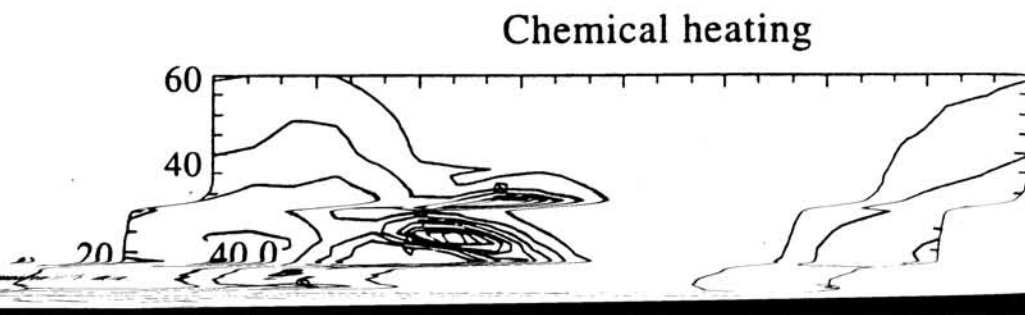


Figure 6.5: Schematic showing the vertical wind associated with the ETWA. (Raghavarao et al. 1993)



of ETWA or mitigate it. Therefore it is suggested that both ion-drag and chemical heating are critical for the observed temperature enhancements in ETWA. During daytime, both these processes of heating would be operative while during nighttime only chemical heating is of consequence as the ion drag effects would be insignificant due to the F-region dynamo which ensures very little differential velocities between the F-region plasma and the neutrals.

Apart from these two mechanisms, namely the ion drag and the exothermic reactions an increase in Joule heating at the anomaly crests has also been suggested as a possible cause for the enhancement of temperatures [Fuller-Rowell *et al.* 1997]. Since the electric fields are found to be usually small in the region under consideration, the Joule heating would only result in very small temperature rise at the anomaly crests. This can at the most be ~ 15 K, while the anomaly in temperature usually is of the order of ~ 50 to 100K.

After seeing its implications it is clear that any general thermospheric model should necessarily account for these local processes quantitatively. Therefore, it is not surprising that the MSIS model shows significant deviations from observed thermospheric temperatures, more so, in lower latitudes, as it does not account for these dominant local process like ETWA. To quantify both the chemical and ion-drag associated heating in ETWA, we used simultaneously observed composition, temperature and wind data from DE-2 satellite during high solar activity epoch (1981-1983) since, by far the most comprehensive set of data on various thermospheric and ionospheric parameters are available only from it. In the following section, a brief description of the DE-2 data is given, followed by details of the procedure adopted for the quantification of ETWA.

6.6 Dynamics Explorer Satellite (DE-2) Data: An Overview

The Dynamics Explorer mission, consisting of two satellites launched by NASA, was aimed to study the strong and complex interactive processes within thermosphere-ionosphere-magnetosphere system. The instruments onboard were capable of measuring as many as eighteen parameters of upper atmosphere. The parameters are density, temperature composition and bulk motion for thermal ions and neutral particles, while for electrons only temperature and density were measured. For suprathermal particles, electron and ion distribution functions along with composition were measured. Vector magnetic field, vector electric field, plasma waves and auroral optical images were the other parameters monitored and measured.

The DE-2 satellite had its perigee at 300 km. The wind and temperature spectrometer (WATS) instrument [Spencer *et al.* 1981] with modified baffle technique onboard DE-2 provided the insitu measurements of neutral gas temperature and zonal as well as vertical wind components. In situ measurements of electron density were provided by the Langmuir Probe [Krehbiel *et al.* 1981]. A neutral atmospheric composition spectrometer described by Carignan *et al.* [1981] provided measures of the abundances of neutral species in the region 300- 500 km. The error in WATS measured temperatures was about 5K at 150km, while the monitoring rate of temperatures was one per second, while the sampling rate for winds was one per two seconds. The error in measurement of winds was estimated to be nearly 10 - 20 m/s at 650km for a solar flux (F10.7) of 175 during noon [Spencer *et al.* 1981]. These errors were shown to be even less in lower altitudes [Raghavarao *et al.* 1993]. The high accuracies, with which the gas temperature and winds were measured by WATS, so far, have remained unparalleled. The absolute error in the electron density measurements were reported to be $\sim 10\%$ in the region around the F2 maximum.

Neutral composition was obtained with a temporal resolution of one second, and the measurement accuracies of $\sim 15\%$ over the specified altitude range.

6.6.1 Choice of the DE-2 Data for the Present Study

The DE-2 data, spanning the period of November 1981 to January 1983, provided measurements corresponding to different local solar time sectors, over a full 24 hours period of local time in about a year, due to the precision of its orbit around the earth. Hence, it is possible to investigate the average behaviour of the local time variations of the different atmospheric parameters. In our case these parameters are the thermospheric temperatures and winds. Since the DE-2 measurements were carried out in the solar maximum epoch, the EIA was found to be present for most of the days, and at times for extended periods during nights making it an ideal choice to investigate EIA/ETWA related processes.

During the low latitude passes of the satellite, the presence of ETWA was clearly detected on several occasions. Under these conditions, the latitudinal distribution of temperature (T_n) and wind (Z) at the EIA crests and trough could be studied at different local solar times. We took all the temperature and wind data corresponding to the low latitude regions of EIA during varying geomagnetic conditions. In the present study, more emphasis is given only to those DE-2 passes which were close to the perigee altitude (300km). However, passes at other altitudes were also considered, to make this analysis more general. To have a better comparison between Mt.Abu results and results based on DE-2 data, emphasis was given to low latitude passes and the choice of 20° latitude for the present investigation was considered appropriate. The WATS/DE-2 measurements of zonal winds and temperature at any given local solar time represent essentially the latitudinal variations. For, the present study, the measurements were averaged over a period of 16 seconds providing the latitudinal resolution of around one degree. During solar maximum,

the latitudinal movement of the ionisation crests of the EIA is more important than the longitudinal variation [Raghavarao *et al.* 1988 and references therein]. Taking longitudinal variabilities as minimal though not always true, we had taken the longitudinal average to bring out the local solar time effects. The neutral temperature (T_n) and zonal winds (Z) were averaged for all the longitudes falling in one local time zone i.e. 1 hour interval each as this is the time resolution of the data sampled at different longitudes. Since the number of passes falling in each time zone to be averaged were not the same, a weighted average was taken for equal time intervals of 1 hour. The same averages were also taken for the model (MSISE-90) predicted temperatures in order to maintain uniformity.

The satellite based measurements overcome all the limitations of the ground based optical methods, especially the ones described in the Chapter 4. The results obtained so far, in the present analysis reveal that the low latitude thermal budget has a significant contribution from two sources. One is rather remote i.e. the contribution from magnetospheric and ionospheric current systems partially represented by magnetic indices like D_{st} . The other contribution comes from local processes like EIA/ETWA. It is understood now, why our earlier efforts to augment the models using just the $\frac{d(D_{st})}{dt}$ could account for only for the variabilities observed in temperatures and not the magnitude. The unaccounted temperature difference indicate the presence of an extra energy source which at low latitudes could very well be the ETWA. Moreover, our optical observations too correspond to latitudes (Mt.Abu 24.6° N) close to EIA/ETWA crests. Therefore, it is important to delineate the heating contribution of ETWA from the observed thermospheric temperatures before performing time delayed correlation analysis on WATS data in terms of $\frac{d(D_{st})}{dt}$, similar to the analysis carried out on Mt.Abu temperature data.

6.7 Local Time Variation of ETWA

Figure(6.7) depicts the average local time behaviour of neutral temperatures at crests in the presence of ETWA, and the dashed line represents the MSIS predicted temperatures [Raghavarao *et al.* 1997]. The average temperature reached its minimum at ~ 0300 LST increasing to a maximum at around 1130 LST. A secondary minimum in the temperature occurred at ~ 1530 LST which is followed by a rise in temperature. Figure(6.7) depicts the average local time behaviour of zonal winds at the crests [Raghavarao *et al.* 1997]. The average wind pattern confirmed the one shown earlier by Wharton *et al.* [1984] and Wu *et al.* [1994]. The zonal winds were westward between 0500 to 1600 LST and eastward during the remaining hours. The eastward wind maximised around 2000 LST, while the westward maximum corresponded to local noon. It is important to note here that the data corresponding to different LST actually belongs to different seasons. For instance, the data in the 0800-1400LST and in 2000-0200LST periods were acquired by the DE-2 during the equinoxes, while those in 0200-0800 and 1400-2000LST correspond to the solstice periods. Therefore, the local solar time variation of winds and temperatures at the crests as shown here have a seasonal variation embodied in it.

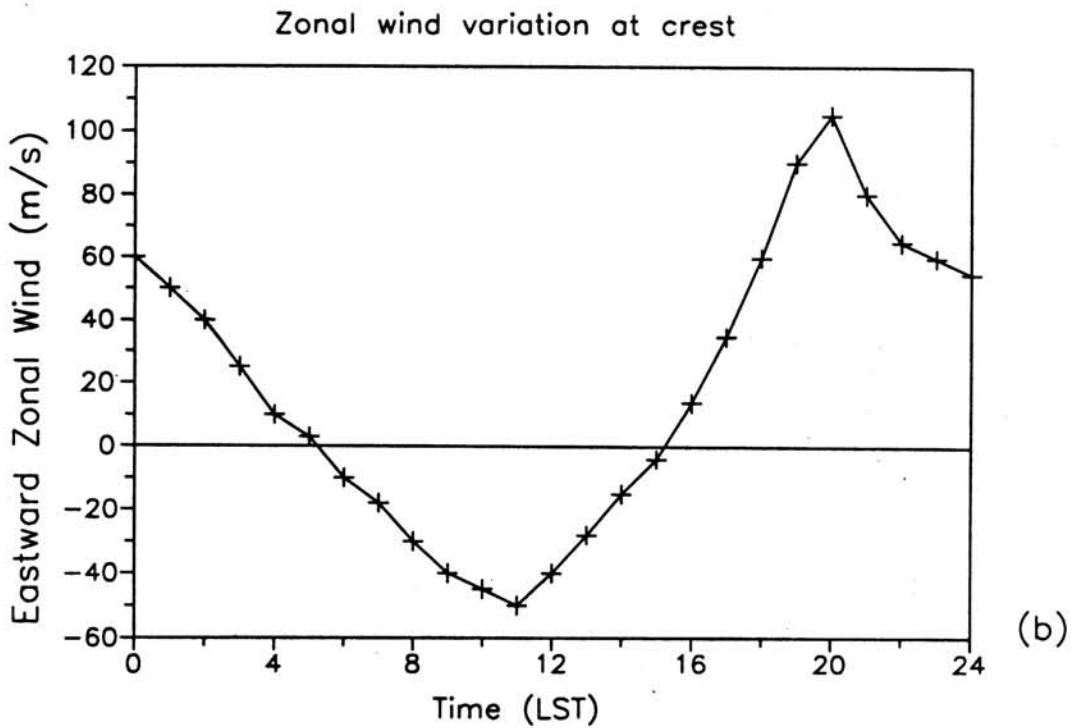
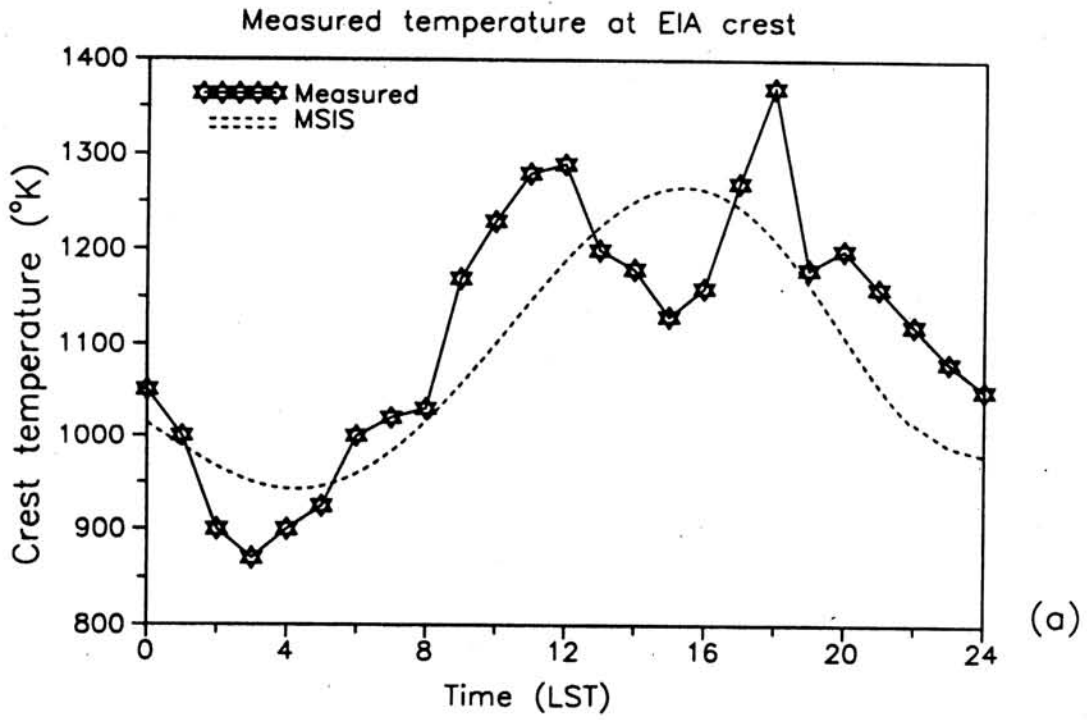


Figure 6.7: top: Local time variation of thermospheric temperature at crest (20° lat. The dashed line represents the MSIS model prediction. bottom: Local time variation of thermospheric temperature at crest (20° lat.

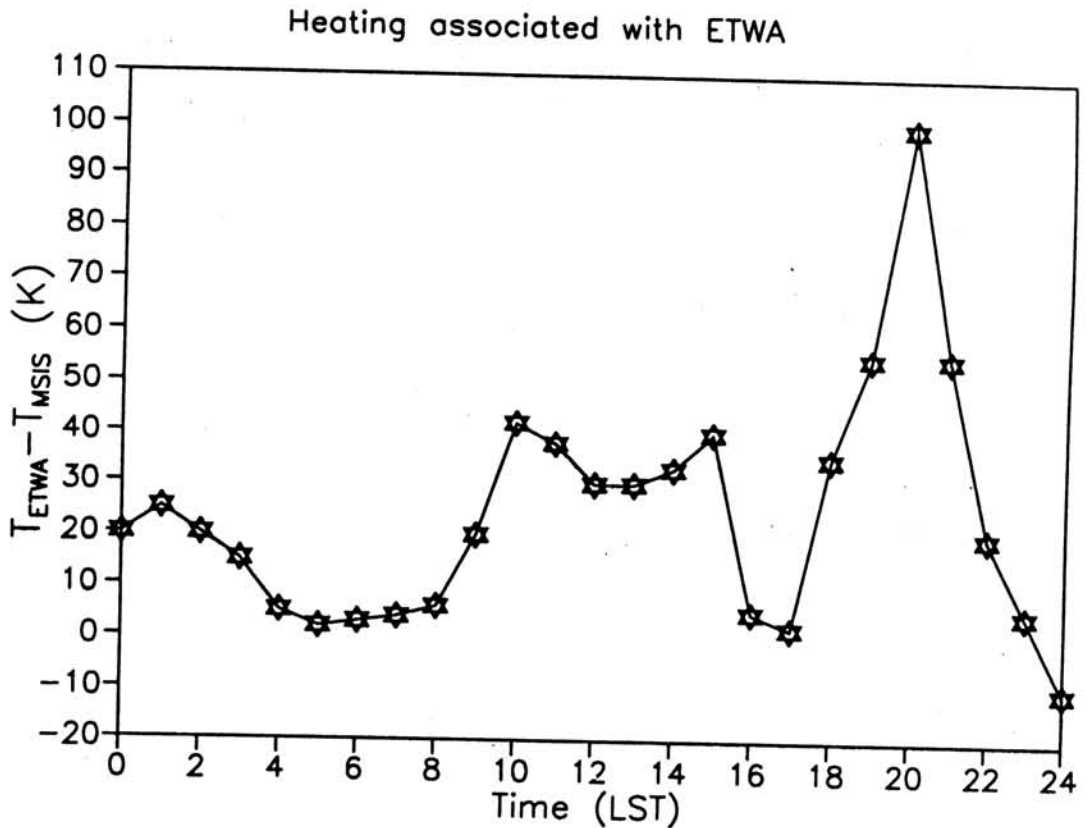


Figure 6.8: Local time variation of the deviations of thermospheric temperatures at crest from the MSIS model prediction.

For comparison with the satellite measurements, model values of T_n were generated using MSIS model [Hedin et al. 1991]. These model values were estimated for the period of the observation, longitude, latitude and height, and for the specific geophysical conditions as represented by the solar flux ($F_{10.7}$) and magnetic activity index A_p . The smoothed deviations of the crest temperature from model predictions are plotted in Figure(6.8). It is seen that the difference between the measurements and the model predictions is very less in the time interval 0000-0800LST, and at 1600LST. Most prominent deviations exist between the two during 1000-1500LST and at around 2000 LST. Except at 1600 LST, the low differences in the post midnight hours correspond to the time when ETWA is ineffective. The large differences during daytime clearly highlight the possible role of ETWA in giving rise to these deviations. The presence of two maxima at 1130hrs LST and 1800hrs LST with

of two maxima at 1130hrs LST and 1800hrs LST with a minima in between at 1600hrs LST has been reported also by *Wu et al.* [1994]. These deviations indirectly correspond to the variation of the relative contribution of chemical and ion-drag associated heating with local solar time. This means, that the above described average curve represents purely the ETWA associated heating. The variabilities due to D_{st} term is expected to get smoothed out because of the weighted averaging along the longitudes, as already described.

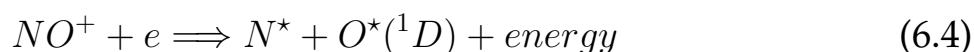
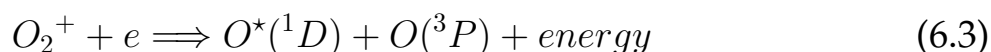
6.8 Quantification of ETWA

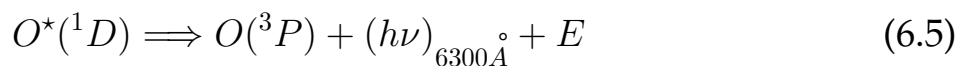
6.8.1 Contribution Due to Chemical Heating

It is the two stage recombination reaction of O^+ during nighttime and is exothermic in nature. This provides the source of chemical heating in the region of the ionisation crests, contributing to ETWA. The important reactions to be considered, can be classified into two categories, one where the reactant species are in ground state, and the other where metastable species get formed. The kinetic heating rates for the reactions involving the ground state species are the highest for molecular dissociative recombination reactions involving O_2^+ and N_2^+ at F-region altitudes. Since the rate of reaction for radiative recombination is slow, the atomic ions are lost through a much faster ion-atom/molecular charge exchange reaction followed by molecular dissociative recombination. The dominant charge exchange reactions are:



Followed by the molecular dissociative recombination reactions





O^* is the metastable species, undergoing the forbidden transition resulting in the emission of 6300\AA wavelength in the upper thermosphere at $\geq 250\text{km}$ region. Torr *et al.* [1980] presented graphically, the various kinetic heating rates involving the ground state species and showed that these processes could result in a transfer of $0.205 \text{ erg cm}^{-2}\text{sec}^{-1}$ to the rest of the neutrals, which is equivalent to about $\sim 14\%$ of the incoming solar UV energy [Figure(6.9)]. The excited species can decay to the ground state spontaneously emitting radiation as airglow if the transition is permitted. And only a very small fraction of this energy will be reabsorbed in the medium. But, if the species reach ground state via forbidden transitions as is the case with atomic oxygen and the resulting 6300\AA emission, their life time in the excited states can be long enough for radiationless deactivation through collisions with surrounding neutral species. These collisions can result in significant amount of energy transfer to the neutral surroundings. The major quenching reaction at F-region altitudes is that by molecular nitrogen (N_2). Approximately 30% of the energy could be channeled to N_2 molecule by quenching. These metastable species deposit around $0.433 \text{ erg cm}^{-2}\text{sec}^{-1}$ into the neutral atmosphere, which amounts to $\sim 30\%$ of total incoming solar UV radiation. The earlier estimates of the total columnar heating due to exothermic reaction is about $0.630 \text{ erg cm}^{-2}\text{sec}^{-1}$ or $\sim 44\%$ of the solar UV energy above 125 km [Figure(6.10)]. For the estimation of chemical heating in the present study, we concentrated on the reactions described above. Reaction(6.1) is slow as it's reaction cross section varies by 2 orders of magnitude, between thermal to higher energies ($\sim 3\text{eV}$). The magnitude of this reaction depends upon the vibrational distribution of ground state N_2 . O_2 is

the important source of O_2^+ in the F-region during normal conditions. Reaction(6.4), which is exothermic, represents the dissociative recombination process for NO^+ ion, which can give the total excess energy of the reaction to be 0.38 eV or 2.75 eV, depending on whether the N atom is produced in the excited 2D state or in ground 4S state. Reaction(6.5) is the main source of metastable $O(^1D)$ atoms in the F-region, more so during nighttimes, and is capable of giving out 7 eV excess energy which is eventually shared by the product of the reaction. Considering the reaction sequence for the production of $O(^1D)$, the rate at which these states are created indicates towards the rate of chemical energy released into the system.

Under equilibrium conditions, the rate of production of $O(^1D)$ would be equal to the rate of the chemical energy (P_{ch}) released in the system. ' P_{ch} ' is proportional to

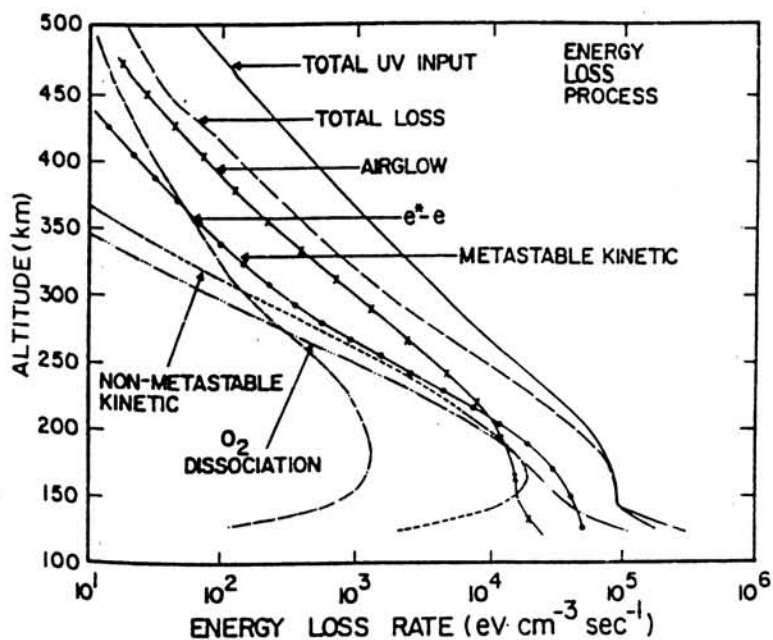


Figure 6.9: Comparison of solar UV energy deposition rate and major energy partition. (Torr et al. 1980)

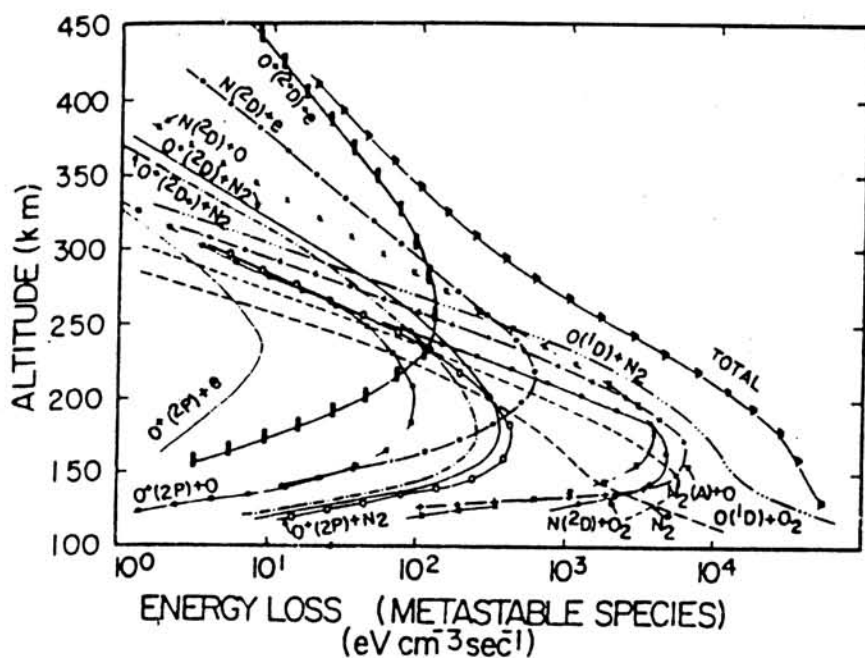


Figure 6.10: kinematic heating rates from exothermic reactions involving metastable species. (Torr et al. 1980)

the electron density N_e and the available O_2^+ ions

$$P_{ch} \propto [O_2^+][N_e] \quad (6.6)$$

Since the dissociative recombination reaction is faster than the charge exchange reaction, the overall reaction rate is governed by the slower. It means, for a given F-region densities the availability of $[O_2^+]$ states will depend upon the efficiency of charge exchange reaction or the density of $[O_2]$ in the first reaction(6.2).

$$[O_2^+] \propto [O_2] \quad (6.7)$$

or combining (6.6) and (6.7) we have

$$P_{ch} \propto [O_2][N_e] \quad (6.8)$$

Therefore, the chemical heating in upper thermosphere at any time, at any place, is expected to be proportional to the product of O_2 and the electron density N_e .

For the estimation and quantification of chemical heating in the ETWA, only those satellite passes over low latitudes were considered which were in the nighttime when the F-region dynamo renders the 'ion-drag' to be negligible. It was made sure that the chosen passes belong to periods of relatively steady D_{st} so that the ring current effects are not significant. The temperature differences (ΔT_n) between the measurements as obtained during the above stated satellite passes at the EIA crests and the model, then could represent the chemical heating. The deviations (ΔT_n) of the observed temperature from the model were calculated and plotted with the corresponding product of O_2 and electron density [Figure(6.11)]. A linear relation was obtained from a fit to these data points, which can be used for calculating ΔT_n for a given product of O_2 and electron density at any given time. The reason for very few data points being used in the above curve is because of the limited number of low latitude passes

during nighttime and steady D_{st} index phases. Though the data points are less, the linear trend as seen in the figure is quite apparent. The curve clearly shows that for effective chemical heating not only the EIA crests should be well developed, the ambient molecular density should also be large. Using the linear relation, the temperature rise due to chemical heating (ΔT_{ch}) was

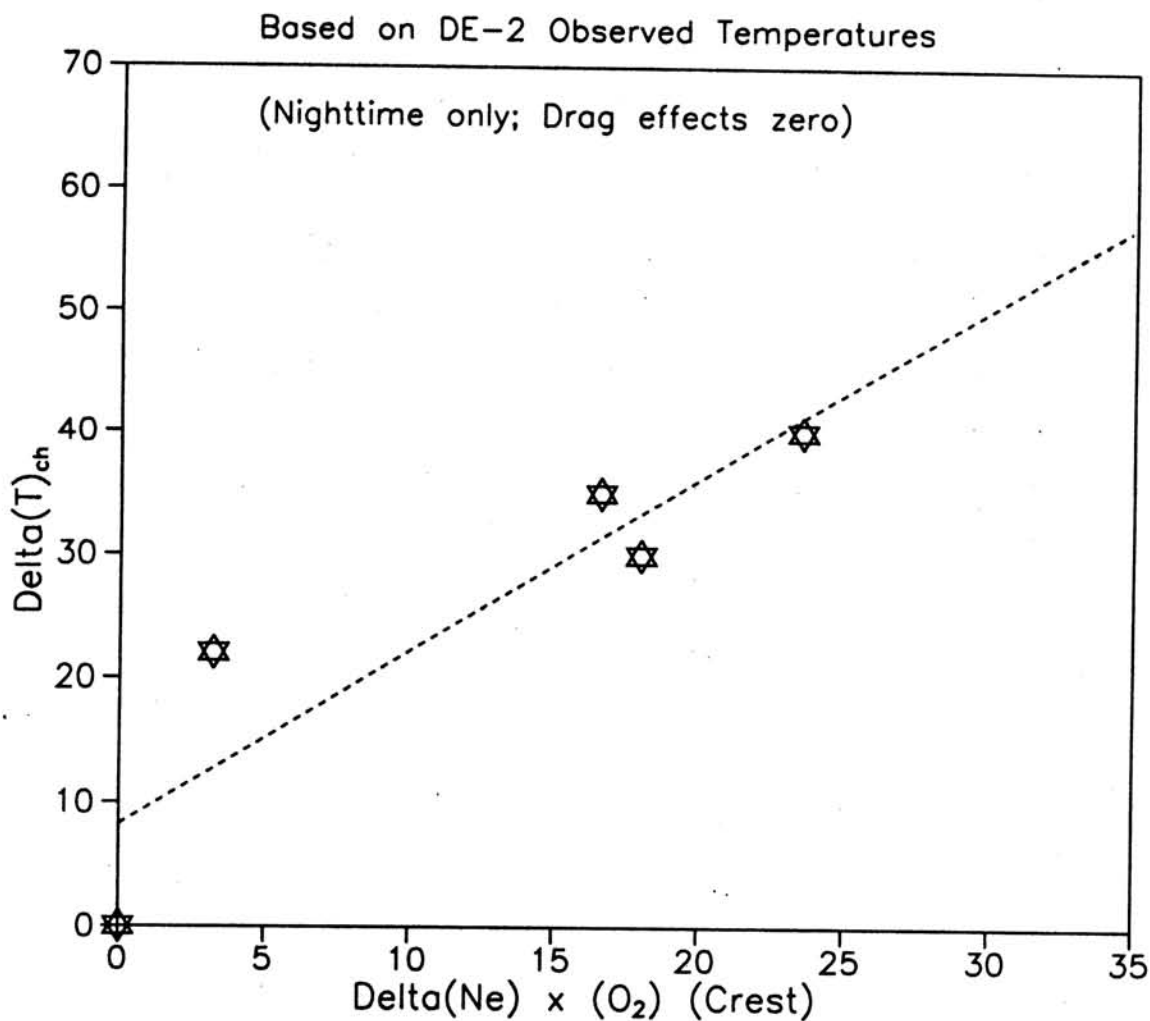


Figure 6.11: The dependence of the chemical heating on the electron and the molecular Oxygen density for nighttime when the ion-drag effects are negligible.

estimated for all the DE-2 passes used in the present study. Figure(6.12a) (pp 220) depicts the chemical heating ΔT_{ch} estimated for the days at different local solar time zones and it represents the typical local solar time dependence of chemical heating. Due to enhanced ionisation during the day, the chemical heating reaches a maximum during the local noon, and is least during post midnight hours. As seen from the figure, the maximum difference the chemical heating can create is of the order of 20-25K.

6.8.2 Contribution of Ion-drag

The ion-drag couples the momentum of neutral and ionised species through ion-neutral collisions. Depending on the relative magnitudes of ion drift velocity and the neutral wind, each can drive or drag the other. This drag is primarily the resistance offered by the magnetically confined ions, to the bulk flow of neutral species. The diurnal variation of ion-drag effects in the upper atmosphere depends upon the coupling of the E and F-regions via the highly conducting geomagnetic field lines. During daytime any polarization field or wind driven current in the F-region gets short circuited by the currents flowing along the field lines to the electrically conducting E-layer. Therefore, no polarization field would be developed in the F-region. In other words, the F region dynamo is rendered inactive and the electric fields are determined eventually by the E-region tidal winds and the global scale dynamo action. Due to the absence of the F-region dynamo, there is a significant amount of relative motion between the ions and the neutral species during daytime. As a result the ion-drag, is also significant.

However, after sunset when the solar radiation, the main source of ionisation is absent, the E-layer electron density gets reduced due to recombinations, by a factor of ~ 50 from its daytime value, while the F-region plasma density is retained due to its long lifetime at this altitude. This would result in a dramatic drop in E-region conductivity during nighttime. Consequently, the F-region dynamo would take over the overall electrodynamical effects and the electric field produced in the F-region during nighttime, which could no longer be shorted out by the E region would, build up to a level where the zonal plasma drift speed ($\vec{V}_d = \vec{E} \times \vec{B}$) would approach the neutral wind speed. As a result, the movement of plasma and neutral species in the same direction with nearly same velocity would reduce the ion-drag effects to nearly zero.

In addition to this, the large eastward electric field due to prereversal enhancement can lift the F-region plasma to a very high altitudes where recombinations and collisions are rare. This enhancement of vertical drift of plasma has many interesting consequences in the lower F-region too. Due to the significant decrease in ionisation at ~ 250 km, the ion-drag would considerably get reduced and as a result, one would expect strong zonal thermospheric winds at these altitudes. In fact, high eastward thermospheric wind velocity is most commonly observed during postsunset to premidnight period [Anderson and Roble, 1974; Richmond 1975, 1987; Fejer, 1985]. However, it is to be noted here, that, the post sunset upliftment of ionisation is in addition to the normal F-region dynamo effect which reduces the ion-drag throughout thermosphere during nighttime. Hence, only during the daytime, ion drag would play a significant role by abating the zonal flow. The loss of momentum in this process would then appear as enhanced Temperature at the crests. At the same time, in the (EIA) trough region, the ion-drag is very little because of very low ionisation density there. Therefore, the zonal wind would flow with maximum velocity at the trough.

Taking a clue from the above, the product of the change of zonal wind velocity (ΔZ) and ionisation density (ΔN_e) at the crests with respect to the dip equator (trough) at anytime is taken to be the measure of 'ion-drag'. In figure(6.12b), the above product is estimated for all available low latitude DE-2 passes and plotted as a function of local solar time. Only those satellite passes were chosen which covered the latitude region of more than -40° to 40° lat. It is clearly seen from the figure that the product is most significant only during daytime. And, its variation is similar as that of the zonal wind, as seen earlier. However, in an alternative approach, the difference between the net DE-2 based averaged (ΔT_n) and the ΔT_{ch} (chemical heating) over the crests would also be expected

to yield the heating due to ion drag (ΔT_{drag}) at any time. Therefore such a difference ΔT_{drag} curve was also generated using ΔT_n and ΔT_{ch} from fig(6.12a) for all local solar times. The ion-drag heating (ΔT_{drag}) estimated using both approaches are compared and shown in figure(6.12b). The similarity between the two clearly indicates that the proposed product of ΔZ and ΔN_e indeed could represent the contribution due the ion-drag.

The final exercise, dealing with all the three, namely D_{st} , ion-drag and chemical heating which contribute towards the low latitude thermospheric temperature and its variabilities, was carried out using only DE-2 satellite data covering all the months of the year (1981-1982). A detailed discussion is given in the following section.

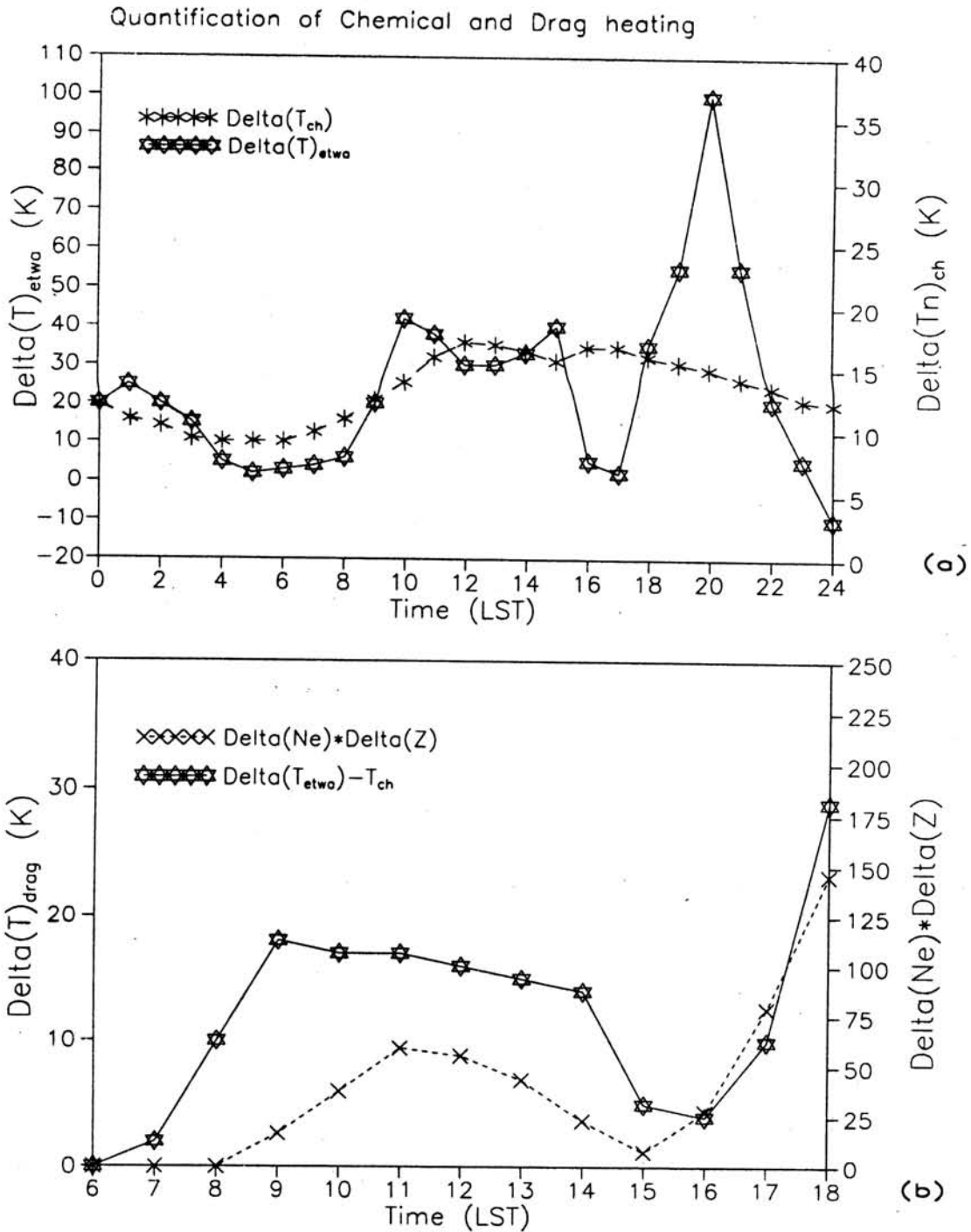


Figure 6.12: top: The local solar time variation of the net heating associated with the ETWA at the ELA crest and the estimated chemical heating bottom: The representation of Ion-drag associated heating in terms of the change in zonal wind and the electron density at the crest and its Local time variation. Also shown is the indirectly estimated ion-drag heating for the comparison.

6.9 Seasonal Dependence of the Thermospheric Response to the External Forcings

Following the approach adopted in the case of Mt.Abu time delay analysis using the D_{st} magnetic index, a detailed time delayed correlation analysis was performed independently on WATS (DE-2) temperature data corresponding to each month of the year (1981-82). One of the important outcomes of this study being that, the time delay is less for summer months (6-8 hrs) and more for winter months (18-20 hrs), [figure(6.13)] confirming the earlier result for Mt.Abu. However, the time delay for individual months turned out to be less than those obtained for Mt.Abu. The response time corresponding to Mt.Abu spectroscopic data characterize the thermospheric behaviour during solar minimum, while the DE-2 corresponds to a solar maximum epoch. A decrease of 2 hrs could be seen from the figure with solar cycle for solstice periods. Response-time for the November - December 1982 turns out to be much more than that for January - February, One also notices slight skewness in the variability. The only cause for this asymmetry in the observed times of thermospheric response could be due to the decreasing solar activity from Jan'82 to Dec'82 during which the sunspot number decreased from ~ 150 to ~ 75 . More detailed investigations are called for in this direction.

Corresponding to the response times for each month, an attempt to linearly model the $\frac{d(D_{st})}{dt}$ and ΔT_n was made for representative different days in each month, after properly accounting for the heating in terms of the local phenomena i.e. ETWA. Following the quantification processes described in the earlier section, the contributions from chemical and ion-drag heating to the observed low latitude (20° lat.) temperatures by DE-2, were removed, which ensured

that the remaining differences would represent only the ring current associated energetics. The gradients and the intercepts, obtained through the linear fitting described above for each month, were plotted separately as a function of the month of the year Figure(6.14). The value of the gradients and the intercepts for any particular month were estimated by averaging and calculating the deviation from the mean as the error

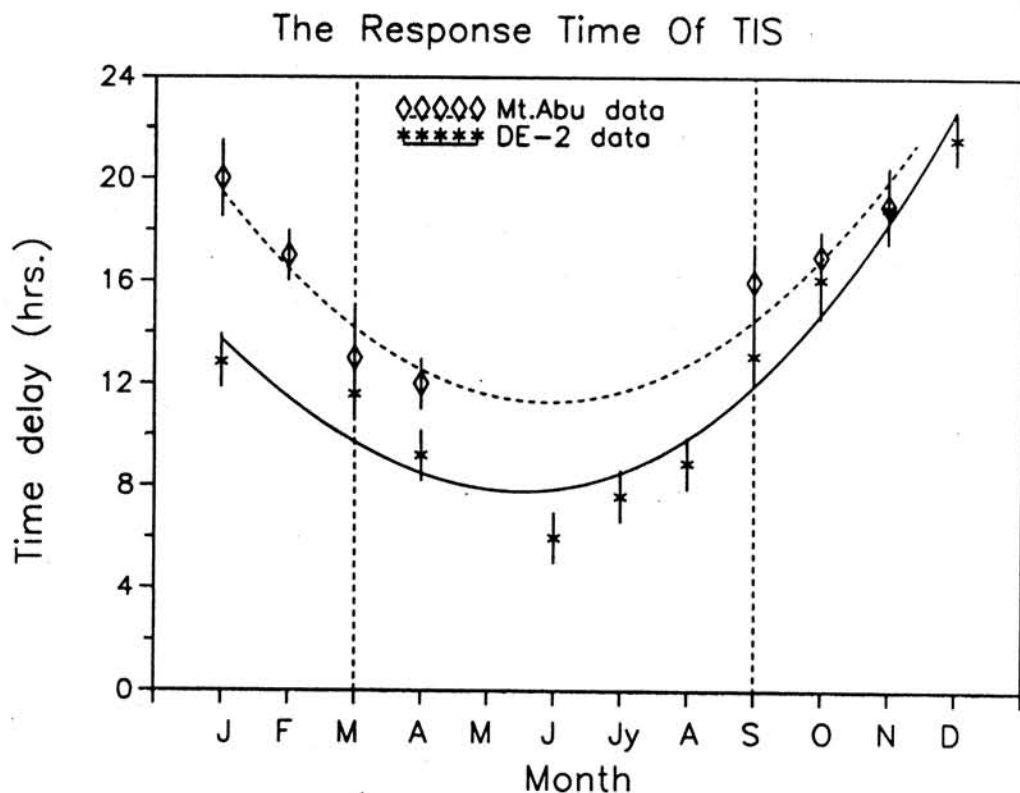


Figure 6.13: A comparison of the TIS response times estimated using the ground based spectroscopic measurements and the in situ satellite measurements.

in their estimation for individual days in a particular month. The physical significance of these intercepts and gradients is understood by the following.

Its clear from figure that the gradient remains more or less steady throughout the year and no apparent variation with season is exhibited. Since, the gradient is the D_{st} dependent term in each linear equation, it indicates that the effects of the currents contributing to the low latitude thermal budget manifesting themselves through variations of D_{st} , remain unaffected by the seasonal variations in the state of the TIS. On the other hand, the plot shows a clear annual pattern in the variation of intercept showing a minimum during summer (May) and maximum in winter months. The curve is produced using only one year data which is swapped over three times in order to achieve a better fitting for the seasonal trend. The intercept can be considered to represent the variations in the background thermospheric conditions. As explained in the earlier chapter also, an attempt has

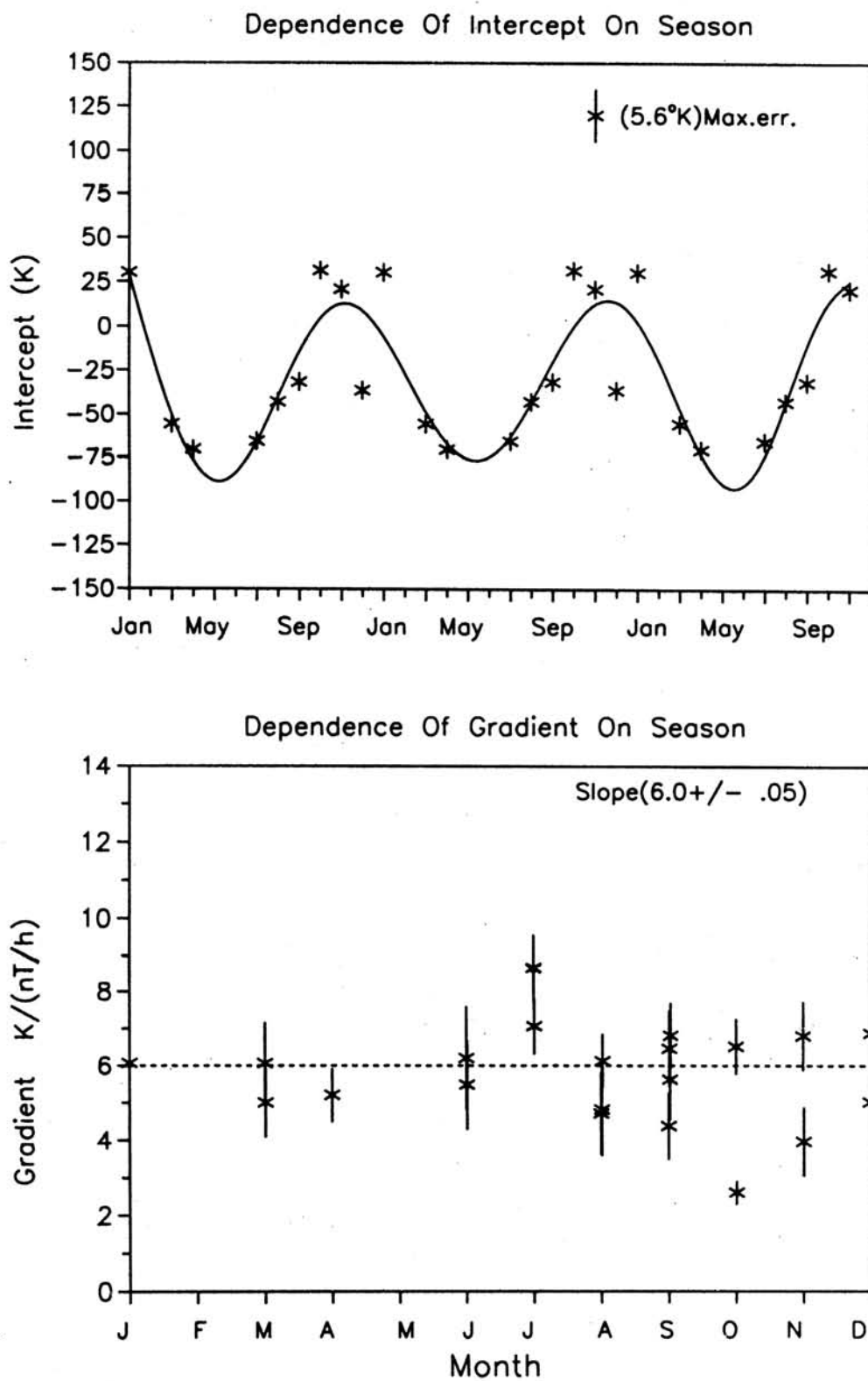


Figure 6.14: Seasonal dependence of the gradients and the intercepts obtained for different months.

been made to establish the concept of response-time as an important, necessary, physical parameter for the TIS. However, it is realised that, to understand all the implications of this parameter, still larger and continuous low latitude database is required. Notwithstanding this limitation, we have used this parameter in the augmentation of the existing thermospheric model i.e. MSIS.

6.10 Results on Thermospheric Temperatures and I-MSIS Prediction

It has been amply demonstrated that the in situ measured thermospheric temperatures also differ significantly from the model predicted temperatures. There are examples of both types when observed temperatures are found either significantly higher or lower than the model predictions. As seen for 12th November 1982 (pp. 236), all the measured temperatures fell below the model predicted temperatures, while they are much higher than model for 8th Nov'82 (pp. 236). In both the cases the deviation from the model is more than 100K. Interestingly they were found to be least for the month of March. However we did not have the temperature measurements for September month to compare with the results for March. These cases presented in detail below, reveal a whole range of deviations observed for different months.

Now that the methodology has been worked out for making an estimate of contributions due to ETWA in terms of chemical heating and ion drag and also the nonlocal sources by parameterising the D_{st} index, one could estimate the contributions from all the three main sources for a geophysical location of 20°N. The addition of these estimated temperature differences ΔT_n due to these three sources to the MSIS predictions would yield an improved model (I-MSIS). It is seen that the I-MSIS model predicts the neutral temperatures both

in terms of magnitude and temporal variability to a reasonable accuracy better than 20-30K, in almost all the occasions described below, barring a very few exceptions.

Twenty five days of data were selected representing all the seasons and geophysical conditions for the final temperature analysis during the year 1981-83. All the three, namely the in situ measured temperatures, standard MSIS predictions and the improved MSIS (I-MSIS) predictions are depicted together for better comparison of the results [figures(6.15-6.26)]. Also provided are the values of solar flux on the previous day $F_{10.7p}$ and on the same day $F_{10.7s}$; along with the altitude, daily average magnetic index A_p and local solar time. Each figure has three panels a,b,c corresponding to three different days. All the temperature variations are plotted as a function of universal time (UT).

Corresponding to three days in the month of Jan'82, the DE-2 (WATS) measured temperature variations with time are shown in figure(6.15a,b,c). These three days are 3rd, 5th and 12th January. As is clear from the figure, the extent of deviations shown by the temperatures from the model (MSIS) predictions are different on each day. It is to be noted that the average model prediction on each day lied at a different level eg. $\sim 970\text{K}$ on 3rd, $\sim 930\text{K}$ on 5th and $\sim 830\text{K}$ on 12th, and similar kind of dc variations were seen in the average measured temperature levels. The largest deviation ($\sim 100\text{K}$) was seen on 3rd Jan'82 with the estimates turning out to be lower, and so is the case on 5th January. The measured temperatures on 12th Jan. revealed an oscillating feature about the model predicted temperatures with relatively less deviations. 12th Jan. happened to be a very quiet day with the average D_{st} index around $\sim -5\text{nT}$.

The average D_{st} for Jan 3rd, 5th were around $\sim -25\text{nT}$ and $\sim -12\text{nT}$ respectively. At the same time, the solar flux($F_{10.7}$) value for 12th was also the least among the three. It is obvious from the figure that, while MSIS could not reproduce the

measurements with their variabilities, the I-MSIS predictions, after additive terms, were able to bring out all the variabilities similar to those as measured on these three days. The agreement between the measured and the I-MSIS predicted temperatures is best seen on Jan 12th, while on 5th it is only partial. On Jan. 3rd, there remains a significant dc difference between the two which seems to be nearly constant all through the night. It is possible that there were certain additional sources like energetic neutral atom precipitation etc. [Tinsley 1981, Lui *et al.* 1991] as the geomagnetic activity level was moderate. During the month of Feb.'82 there were not enough low latitude DE-2 passes on a

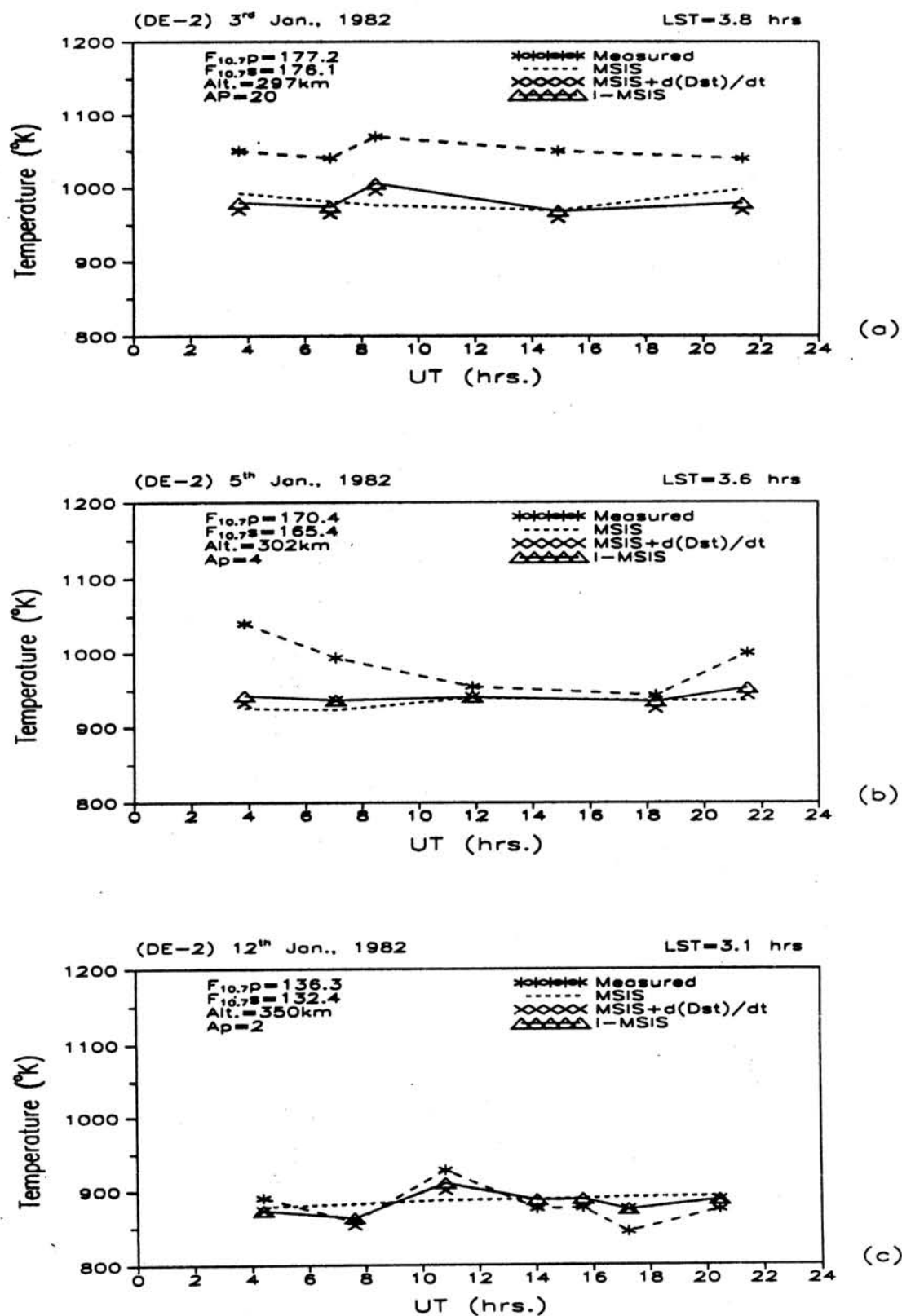


Figure 6.15: A final estimation of temperatures by I-MSIS model and its comparison with the in situ measured satellite (DE-2) measurements for January 1982.

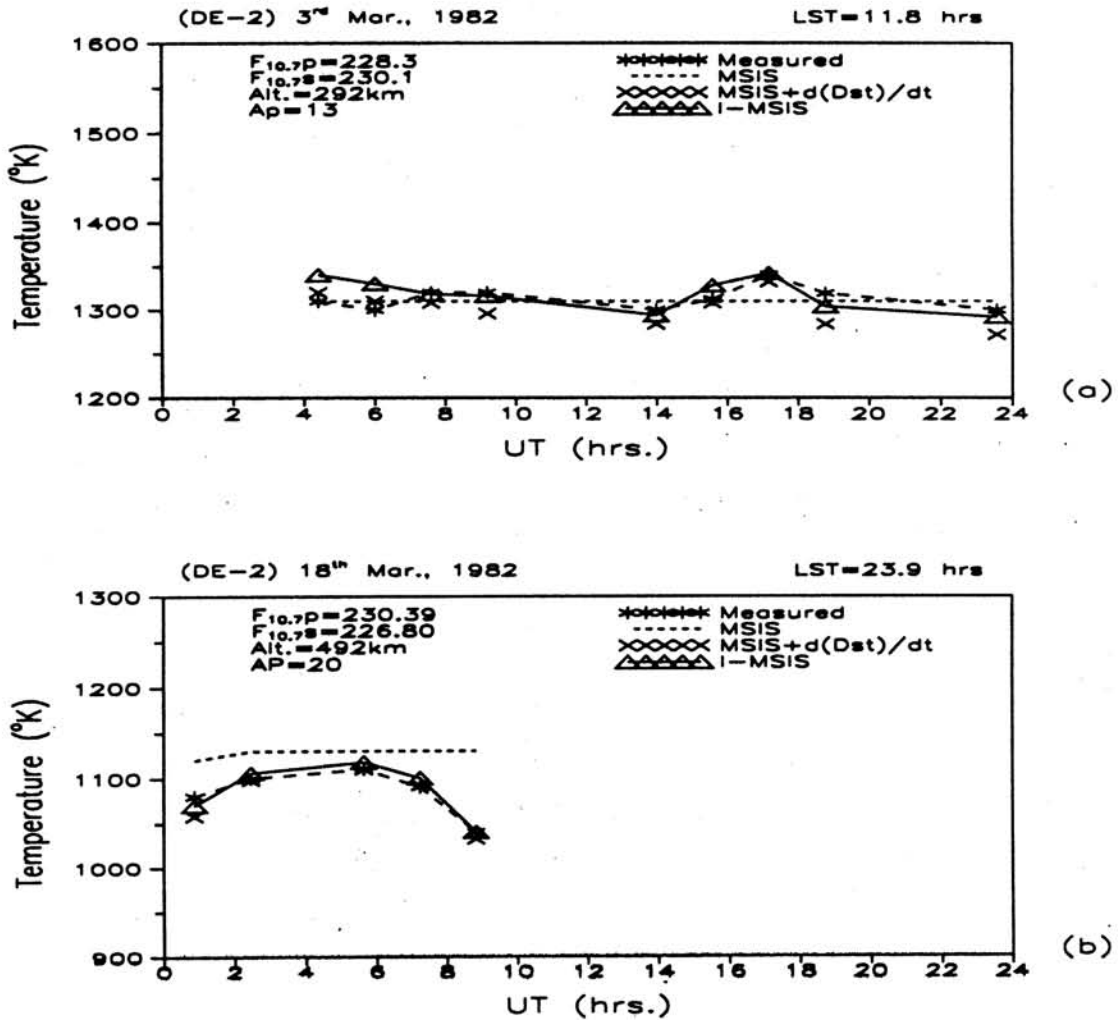


Figure 6.16: A final estimation of temperatures by I-MSIS model and its comparison with the in situ measured satellite (DE-2) measurements for March 1982.

single day to carry out a similar investigation. However, it is to be noted, that this month was geomagnetically very active. The activity slowly decreased towards the end of February.

The panels(6.16a) and (6.16b) correspond to the days of 3rd and 18th of March. As said earlier, 3rd March happened to be on the early recovery phase of a moderate geomagnetic storm which commenced on 1st March. The effects of the additional storm energy inputs appear in the form of higher average temperatures on this day which is $\sim 1300\text{K}$ while it is $\sim 1070\text{K}$ on 18th March which is a relatively quiet day with the average D_{st} being $\sim -6\text{nT}$. Both the days i.e. 3rd and 18th March were

single day to carry out a similar investigation. However, it is to be noted, that this month was geomagnetically very active. The activity slowly decreased towards the end of February.

The panels(6.16a) and (6.16b) correspond to the days of 3rd and 18th of March. As said earlier, 3rd March happened to be on the early recovery phase of a moderate geomagnetic storm which commenced on 1st March. The effects of the additional storm energy inputs appear in the form of higher average temperatures on this day which is $\sim 1300\text{K}$ while it is $\sim 1070\text{K}$ on 18th March which is a relatively quiet day with the average D_{st} being $\sim -6\text{nT}$. Both the days i.e. 3rd and 18th March were in different local time sector of the satellite passes. 18th March temperatures belonged to the midnight sector i.e. 23.9 hrs LST, while 3rd March corresponded to 11.8hrs LST. The $F_{10.7}$ solar flux on these

two days were nearly the same. Contrary to 3rd Jan [figure(6.15)], as shown in the figure(6.15b) the measured temperatures were nearly following the MSIS predictions. Though MSIS could not reproduce the variabilities, the I-MSIS predictions was able to explain all the temperature measurements including the variabilities. The MSIS predictions were grossly inadequate to explain DE-2 temperature on 18th [figure(6.16b)]. The deviation between the two at 9 hrs UT is as large as $\sim 100\text{K}$. The I-MSIS, is shown to be capable of explaining all the measurements nearly 100%.

Figures(6.17a,b) correspond to the days in the month of April 1982. Both the days belong to the same local time sector and represent nearly the same altitude range $\sim 330\text{km}$. $F_{10.7}$ Solar flux on both the days didn't undergo any major change. On 17th April, the D_{st} had undergone a very fast decrease from 4nT to -71nT in just 5 hours. The D_{st} eventually increased after 10hrs UT on 17th. Whereas on April 18th the D_{st} remained more or less in the same level ($\sim -29\text{nT}$). On both the days, the MSIS model grossly overestimated the in situ measured temperatures. The deviations from the model were to the extent of $\sim 100\text{K}$. The I-MSIS, on the other hand remarkably reproduced all the measured features. Reproduction of observed variabilities between 16-20hrs on both these days by I-MSIS highlights the significance of the suggested improvements in the model.

Though, the I-MSIS predictions were in remarkable agreement with the measurements on most of the occasions, it is limited in representing the measured temperatures for the days considered in the month of June. It is important to notice that no unusual fluctuation in D_{st} values was observed on or previous to the days under consideration here. The measured temperatures exhibited a lot of variability on June 1st and 17th. The measurements on these two days correspond to the same altitude (304Km) and same local time sector (6.1hrs).

But, as shown in figure(6.18a) for June 1st and figure (6.18b) for June 17th, the solar flux value increased significantly from 134.2 to 206.0. The I-MSIS prediction on both the days is not able to represent the measurements, though it reproduced nearly all the

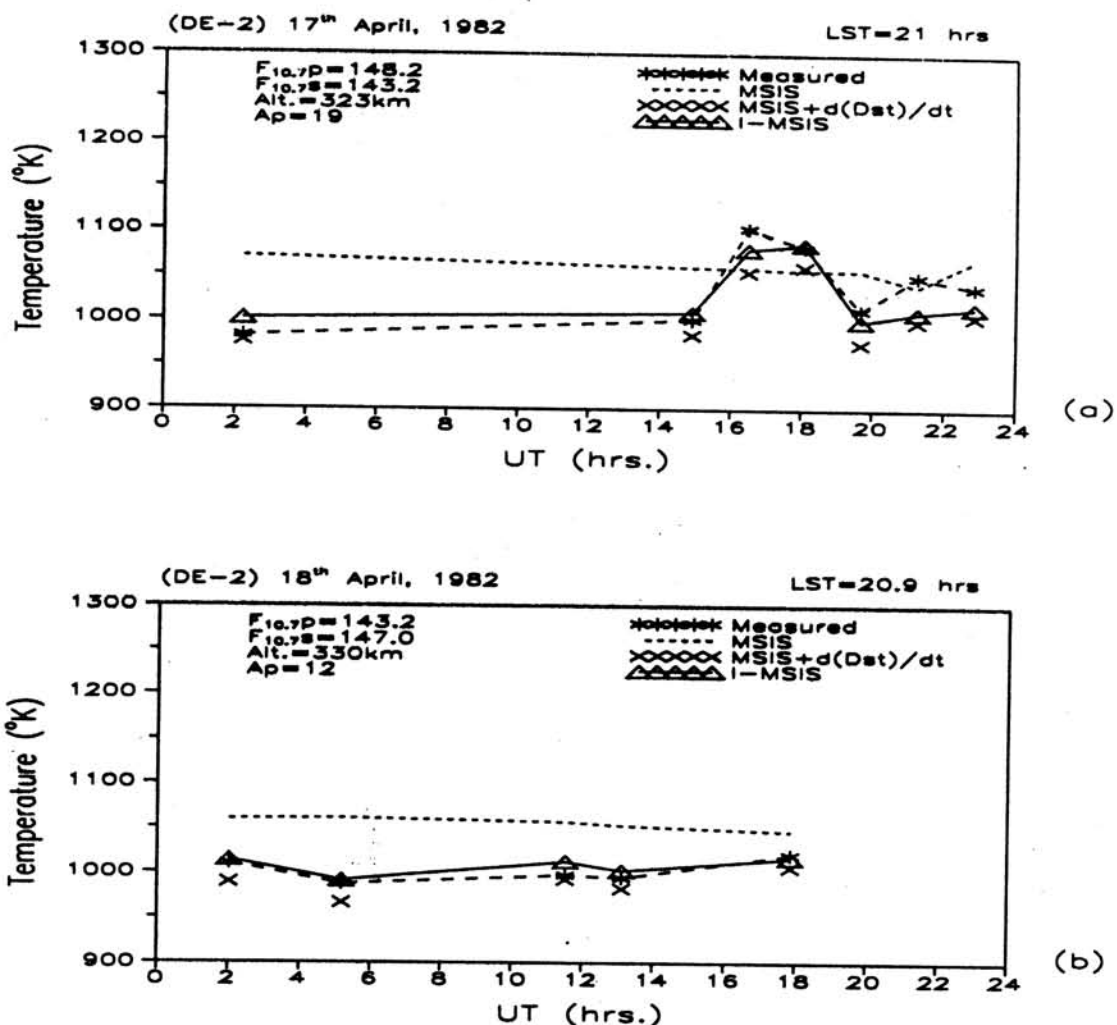


Figure 6.17: A final estimation of temperatures by I-MSIS model and its comparison with the in situ measured satellite (DE-2) measurements for April 1982.

variabilities observed in the measurements. However, the cause of the large deviations on both these days remain unexplained.

In the month of July, five days i.e. 4th, 11th, 19th, 21st and 26th are included in the present investigation. All the five days happened to be in the same local time zone, but significant changes are seen in solar flux for each of these days. Incidentally, July 19th, 21st and 26th happened to be at different stages of the recovery phases of an intense geomagnetic storm ($D_{st} \sim -338\text{nT}$), which got triggered on July 11th. 4th July, however, corresponded to a quiet day. As seen in figure(6.19a,b) for 4th and 11th July respectively, solar flux value was nearly doubled on 11th July. The storm effects can clearly be seen in the temperatures on these days. For instance,

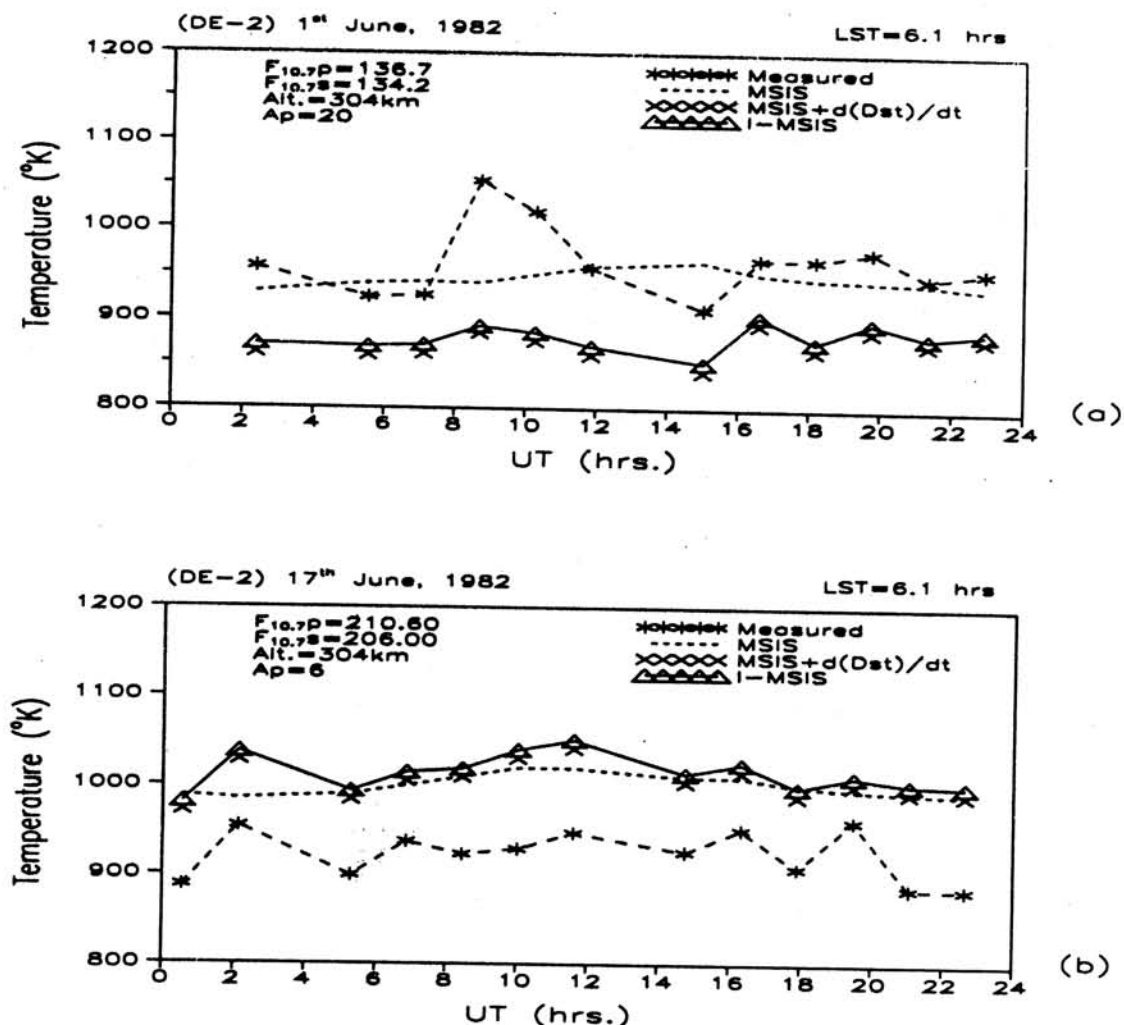


Figure 6.18: A final estimation of temperatures by I-MSIS model and its comparison with the in situ measured satellite (DE-2) measurements for June 1982.

4th July being a quiet day showed an average thermospheric temperature of $\sim 1070\text{K}$. This remained the same for July 11th too. But on 19th July, the average temperature shot up to 1350K . Later days i.e. on 21st and 26th the temperature showed a tendency to decrease down to the prestorm value. On 21st the average temperature lied at around 1250K recovering down to 1050K on 26th July. The standard MSIS model overestimated the measurements for these days. The magnetic activity levels too showed significant variabilities on these occasions. In spite of these, it is interesting to note that the I-MSIS prediction explained almost all the measurements on 4th July except at 1400 UT while the predictions fell short by $\sim 50\text{K}$ on 11th July with the variabilities getting accounted for remarkably. The value of the

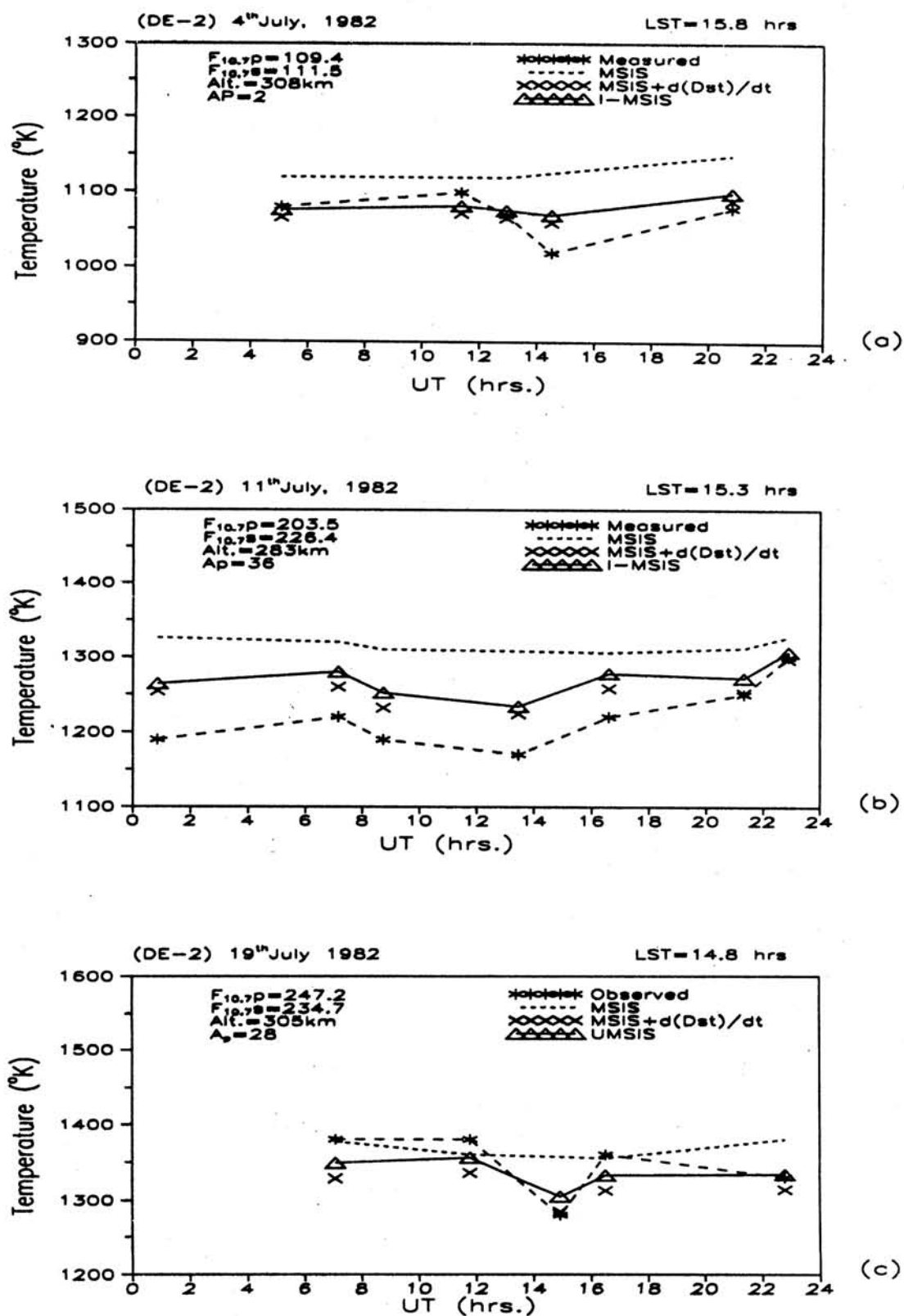


Figure 6.19: A final estimation of temperatures by I-MSIS model and its comparison with the in situ measured satellite (DE-2) measurements for July 1982.

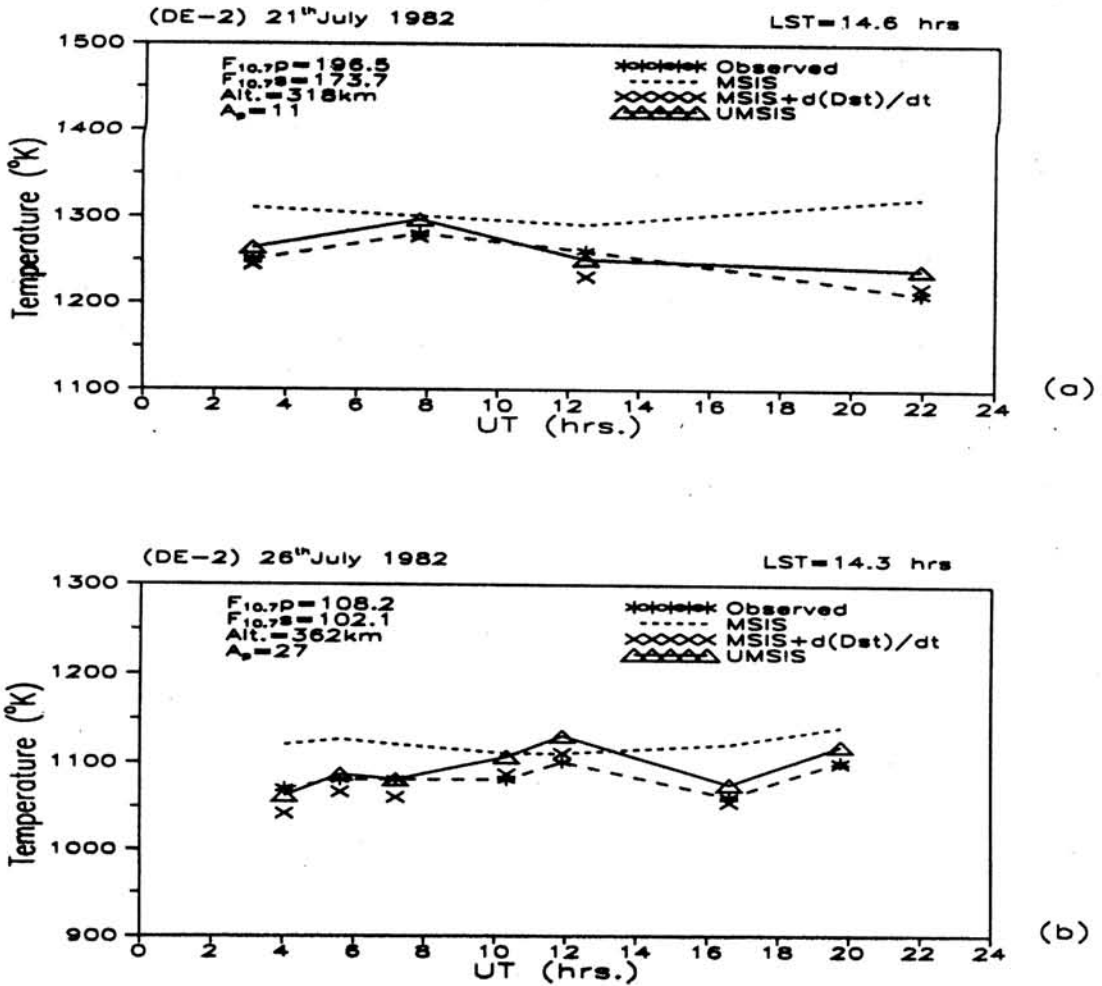


Figure 6.20: A final estimation of temperatures by I-MSIS model and its comparison with the in situ measured satellite (DE-2) measurements for July 1982.

$F_{10.7}$ solar flux which was 234.7 on 19th July gradually reduced to 173.7 on 21st and to 102.1 on 26th. This change is reflected clearly in the MSIS temperature predictions too. The average MSIS temperature on 19th July lied at $\sim 1400\text{K}$ figure(6.19c); at $\sim 1300\text{K}$ on 21st July figure(6.20a) and $\sim 1200\text{K}$ on 26th figure(6.20b). Deviations of the measurements from the MSIS model are the largest on 21st July. However, irrespective of the magnetic activity and flux changes, I-MSIS predictions agreed very well with the measurements, except on 11th July which would call for further investigations.

In the month of August, only on 27th Aug'82 large number of low latitude satellite passes were available which could be included in the present analysis. The passes

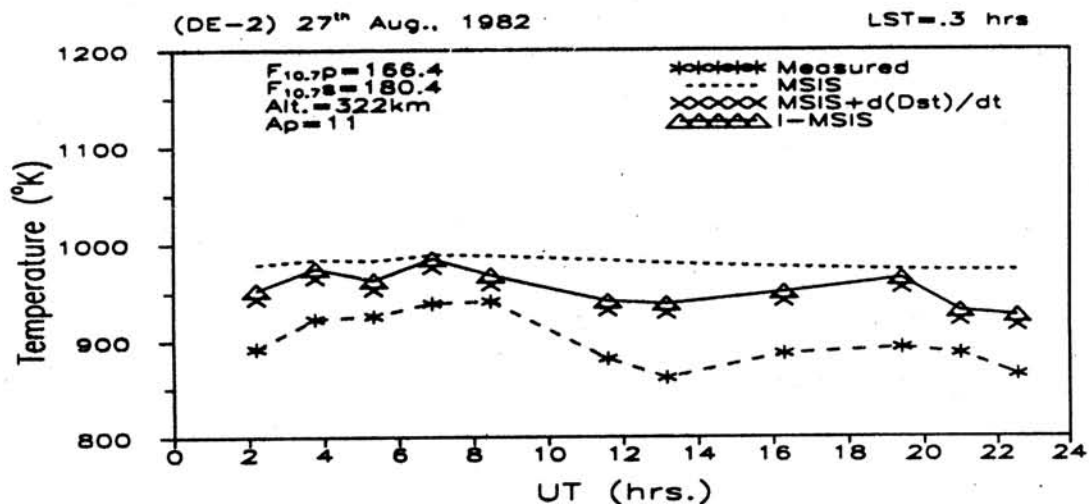


Figure 6.21: A final estimation of temperatures by I-MSIS model and its comparison with the in situ measured satellite (DE-2) measurements for August 1982.

corresponded to 0.3hrs LST at an altitude of ~ 322 Km. The measurements on this day showed very large deviations from the corresponding MSIS prediction [figure(6.21)]. For instance, the deviation at around 13hrs UT is of the order of ~ 120 K. From the point of view of geomagnetic activity, it seemed to be preceded by a phase where the D_{st} had remained at nearly the same level for several days. In this context, the observed temperature deviations are rather unusual. The I-MSIS predictions also could not appropriately reproduce the absolute measurements. However, the variabilities in the temperatures are satisfactorily reproduced.

The $F_{10.7}$ solar flux value for 4th, 17th and 18th Sept'82 underwent only marginal change. However, the magnetic activity level on 17th Sept'82 dropped down to $A_p \sim 11$ from $A_p \sim 32$ on 4th. The average D_{st} level was nearly the same for all the three days. The activity level again increased to ~ 30 on 18th. The average MSIS prediction lied at ~ 1000 K on all the three days. As seen in the figure(6.22a,b,c); the measured temperatures exhibited large temporal variability. The I-MSIS prediction explained almost all the measurements on 4th Sept. before 10hrs UT. However, a difference appeared as if an additional modulation was present between the two after 10hrs UT. Similarly, on 17th Sept. I-MSIS reproduced all measurements after 15hrs. However, before 15 hrs on this day, a small difference (~ 20 K) between them is observed. On Sept 18th too, most of the in situ measured temperatures got

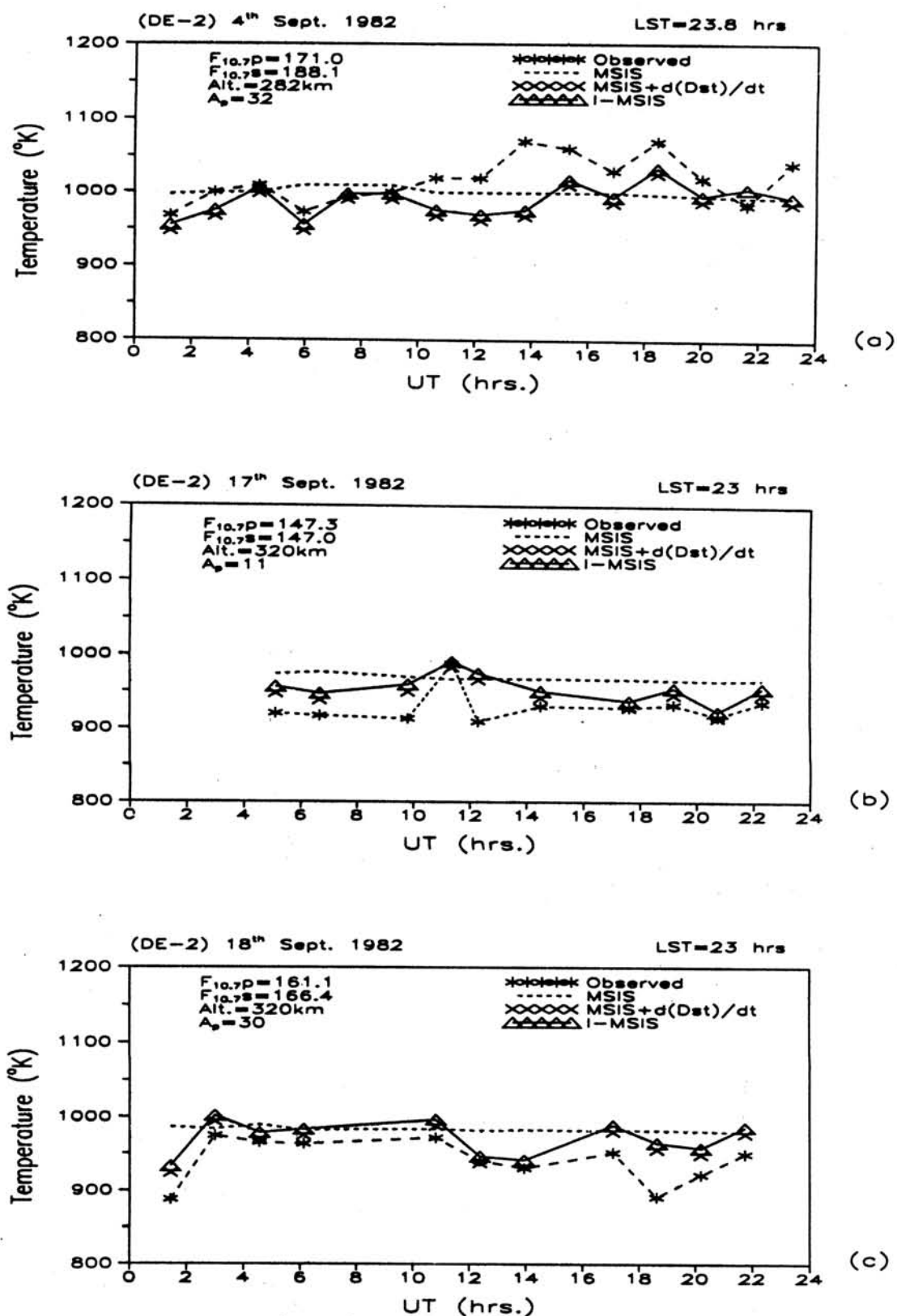


Figure 6.22: A final estimation of temperatures by I-MSIS model and its comparison with the in situ measured satellite (DE-2) measurements for September 1982.

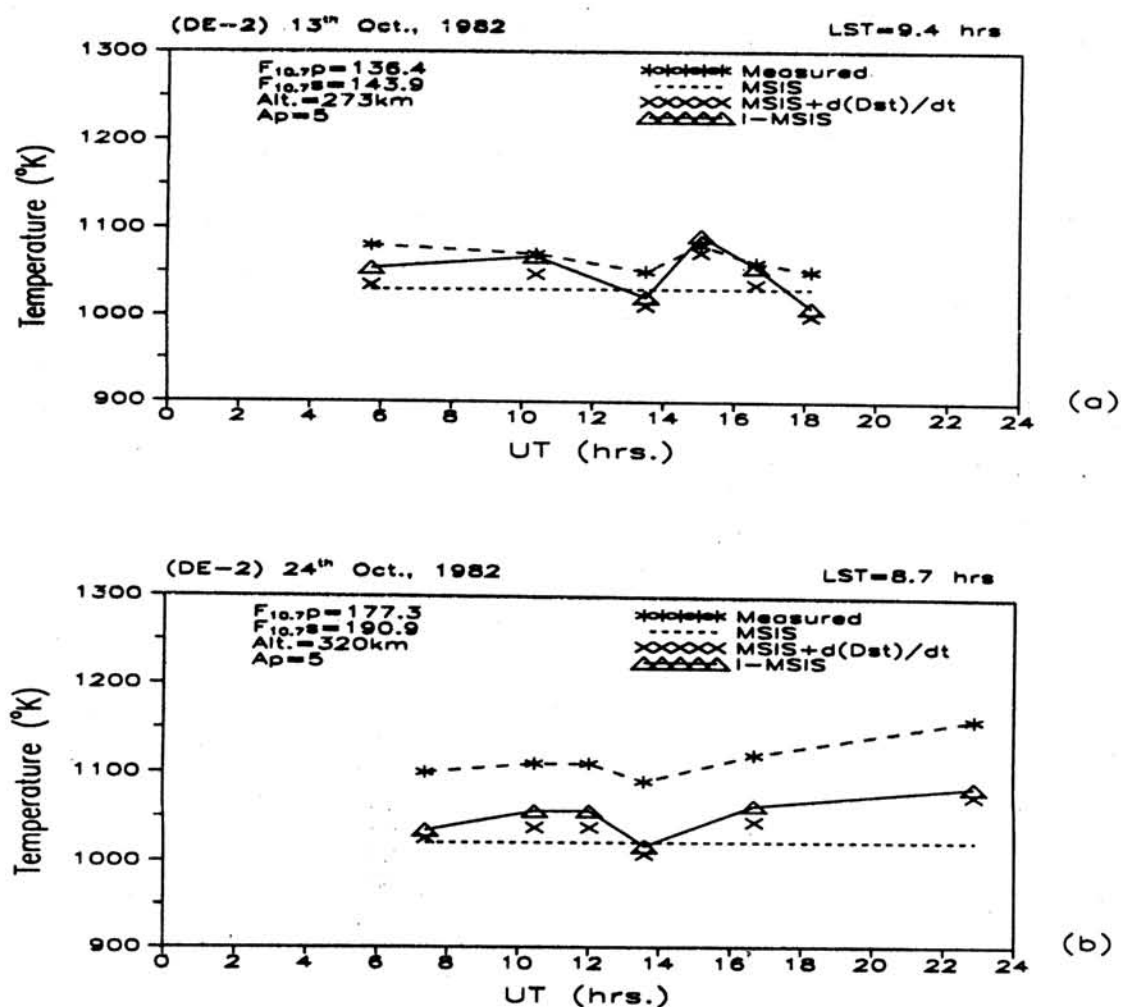


Figure 6.23: A final estimation of temperatures by I-MSIS model and its comparison with the in situ measured satellite (DE-2) measurements for October 1982.

explained with a difference of $\sim 20\text{K}$. In the month of Oct. and Nov., for all the days included in the present study, large deviations are observed between the in situ temperature measurements and the MSIS predictions for similar geophysical conditions. As shown in the figure(6.23a), the satellite passes on 13th Oct'82 belonged to a thermospheric altitude of about $\sim 273\text{km}$ while on 24th [fig(6.23b)] it is for higher altitudes of 320km . Though, the average magnetic activity level didn't change on these two days, the solar flux had undergone a change of nearly 40 units. Also the average D_{st} levels were different for both the days i.e. -23nT on 13th and -15nT on 24th. The average measured temperatures on 24th Oct. were slightly higher than on 13th Oct. However the average MSIS model prediction remained

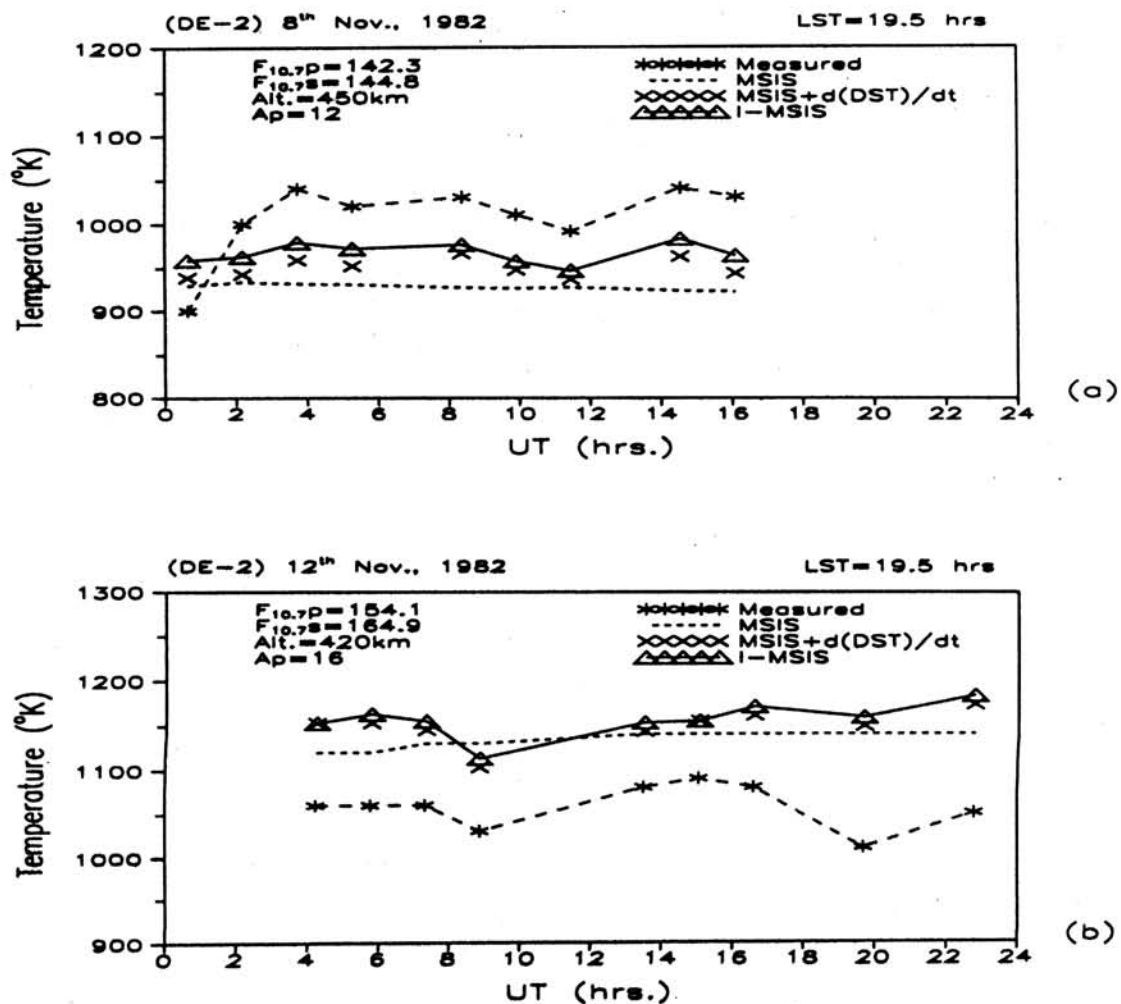


Figure 6.24: A final estimation of temperatures by I-MSIS model and its comparison with the in situ measured satellite (DE-2) measurements for November 1982.

nearly the same. The I-MSIS explained nearly all the measurements on 13th, but on 24th only the variabilities got explained.

As mentioned earlier, figure(6.24a,b) illustrate the large difference shown by the measurements from the MSIS model. The average flux value on 8th Nov. and 12th Nov. is nearly the same within 10% and so also the average D_{st} index levels. All the satellite passes on these two days correspond to the same altitude zone and the local time sector. It can be seen in the figure, though the average measured temperatures were the same ($\sim 1050K$) on both the days, the average MSIS prediction significantly differed. On 8th it was around $\sim 930K$ while its about $\sim 1120K$ on 12th Nov. On 8th Nov., the I-MSIS predictions underestimated the measurements

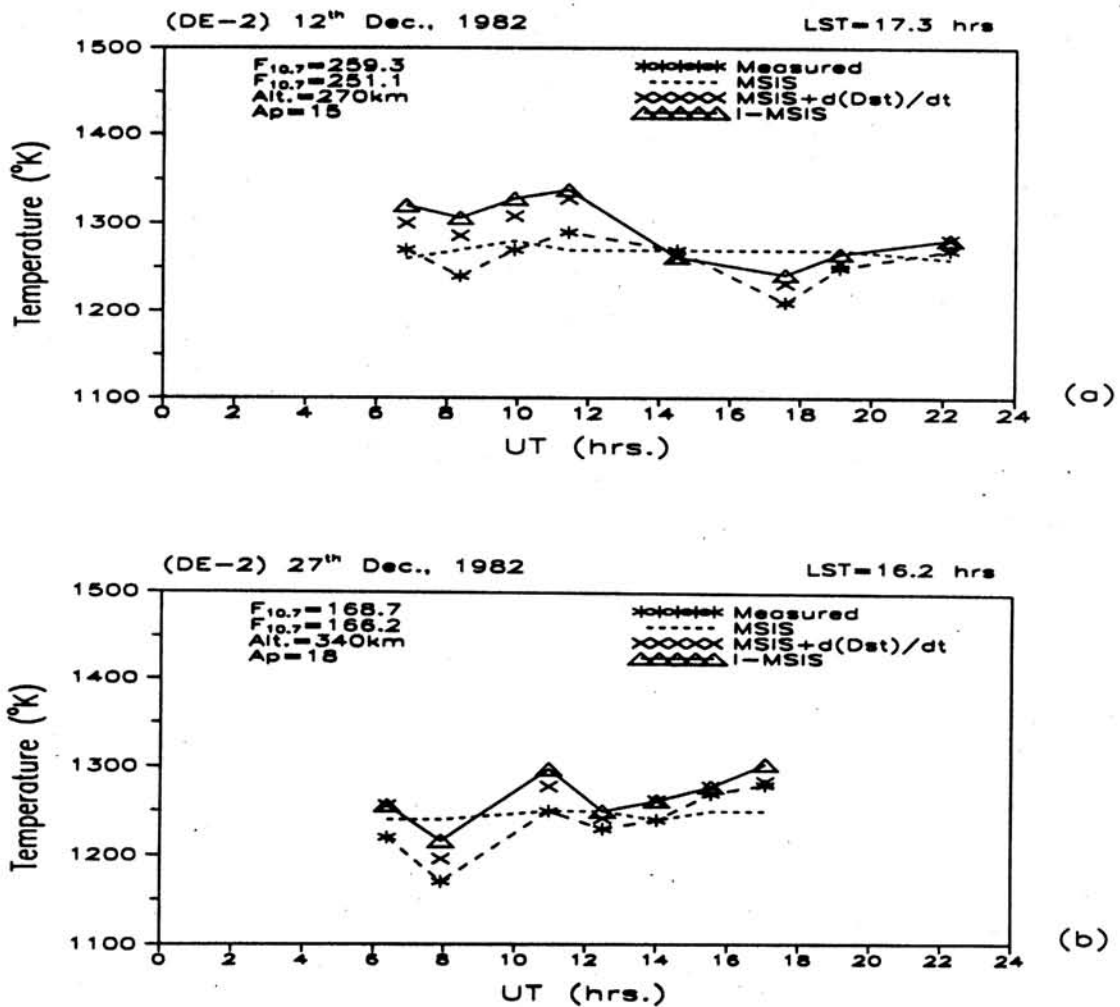


Figure 6.25: A final estimation of temperatures by I-MSIS model and its comparison with the in situ measured satellite (DE-2) measurements for December 1982.

while it overestimated them on 24th Nov. On both the occasions, I-MSIS differ significantly from measurements in absolute magnitude but once again successfully reproduced the periodicities/variabilities.

As shown in figure(6.25a,b) for Dec 12th and 27th Dec. 1992 respectively; the $F_{10.7}$ solar flux underwent a significant decrease from 251.1 on 12th to 166.2 on 27th Dec. In terms of D_{st} , 12th Dec. was more active than 27th. The altitude range for the passes changed from 270km to 340km on 27th. However, the global magnetic activity levels were nearly the same on these two days. The average MSIS prediction levels were the same ($\sim 1250\text{K}$). The measured temperatures exhibited significant temporal variabilities. The I-MSIS temperature predictions explained

predictions explained almost all the measurements especially after 13hrs UT on both the days. However before 13hrs the I-MSIS seems to be overestimating the measurements by about $\sim 20\text{-}25\text{K}$. Like in all the previous occasions, the temporal variabilities seen in the measurements were reproduced one to one by the I-MSIS.

6.11 Conclusions

In conclusion it could be seen that the above study clearly brings out the consistency in I-MSIS predictions especially with regard to the variabilities thus highlighting the importance of the improvement done in the model using the standard MSIS model as the basis. However, there are cases when the I-MSIS prediction fell a bit short in terms of absolute magnitudes but even then, the variabilities still do get explained satisfactorily. This indicates towards the presence of some extra energy sources which at times become active over low latitudes and are yet to be understood and quantified. We have attempted to quantify only one and the most important low latitude process i.e. ETWA, but the contribution of processes other than ETWA to low latitude energetics is still to be understood and a proper quantification is called for, before incorporating them in the existing model.

Chapter 7

Summary

Regular studies on the behaviour of low latitude Thermosphere - Ionosphere System (TIS) have been carried out from the low latitude Aeronomy Laboratory, Mt. Abu (24.6°N , 72.7°E), India. The emphasis has been on the investigation of the basic interactive nature of neutrals (thermosphere) and the ions (ionosphere) in the upper atmosphere. In this context, coordinated measurements of the neutral temperature and wind are regularly carried out using a high resolution central aperture scanning Fabry-Perot interferometer on the OI 6300\AA airglow emission originating at 250 km. The relevant ionic parameters such as the layer height are obtained from ground based ionosonde at Ahmedabad (23°N , 72.1°E geographic, 18.4° diplat.), India. The low latitude thermosphere- ionosphere system was studied under the purview of Rishbeth's servo model which is based on the physics governing the closed cycle of interactions between the plasma and the neutral species. It was observed on many occasions that there existed a difference between the measured thermospheric temperatures and the thermospheric model (MSIS) predictions. Further, the exact dynamical nature of the low latitude thermosphere - ionosphere system during varying geophysical condition was explained. It has been demonstrated that, during geomagnetic storms, the processes which were earlier thought to be effective only over polar latitudes can also have significant effects in low latitude energetics and dynamics. A major part of the

energy associated with some of these processes eg. the ring current and its associated magnetospheric current systems could indirectly affect the low and equatorial latitudes. The nature of low latitude TIS gets further complicated by the presence of many local large scale dynamical processes. The Equatorial Ionisation Anomaly (EIA) and the Equatorial Temperature and Wind Anomaly (ETWA), being the most prominent of them are shown to be modifying significantly the energetics and dynamics.

The present investigation was carried out in order to understand and model the behaviour of the low latitude TIS during varying geophysical conditions and in the presence of local processes like the ETWA. The questions which made the theme of the present study are the following:

(A) How does the low latitude TIS behave during different geophysical conditions especially during geomagnetically disturbed times in both the low and high solar epoch?

(B) Can the existing thermospheric model (MSIS) be appropriately augmented for more realistic representation of thermospheric temperatures of low latitudes?

(C) Can the effects of low latitude processes like Equatorial Temperature and Wind Anomaly (ETWA) be quantified, which is essential to be answered before addressing the questions above mentioned?

Since, the present study belonged to the low solar activity epoch, the airglow (OI 6300Å) intensity most of the time has been too low to derive meaningful temperatures. Therefore, the data used in the present study are limited, but sufficient enough to provide answers to some of the question mentioned above. The Dynamics Explorer Satellite (DE-2) data on composition, wind and temperature was also made use of, to overcome the limitations of the ground based spectroscopic measurements. The important results as presented in this

thesis are summarized in the following text:

Using special techniques to analyse the observed airglow profiles, a geomagnetically quiet thermosphere was studied from Mt. Abu, to start with. In spite of the day-to-day solar flux variation being minimal for the days considered in the investigation, the observed thermospheric temperatures revealed significant temporal variabilities. Prominent short term variabilities, were observed along with day to day variations too. These observed temperatures when compared with thermospheric model (MSIS) which represents only an average thermospheric behaviour, failed to agree with each other. The deviations between the measurements and the model indicate towards a possible role of local and nonlocal processes which are not accounted for in the model. The TIS was also studied by means of Rishbeth's servo model using the observed temperatures and winds. The role of thermospheric parameters over ionosphere during geomagnetically quiet and the low solar activity phases, and the existence of enhanced observed temperatures was indeed confirmed by the close agreement between the servo model estimated F-layer equilibrium heights and the measured heights. This study also brought out the dominant role of thermospheric temperature and winds over the ionospheric electric fields in driving the low latitude dynamics during quiet time low solar activity epoch.

Having studied the low latitude TIS during geomagnetically quiet times, the next step has been to investigate the same during geomagnetically perturbed periods when the solar wind energy enhances manifold and can even temporarily exceed the solar radiation energy with lot of spatial and temporal variability. The low latitude TIS is known to respond to these transient events in terms of thermospheric/ionospheric energetics and dynamics. It is known that during strong auroral heating, large scale pressure gradients get set up

and a net outward flow from the heated regions results by meridional circulation and through traveling atmospheric disturbances. The temperatures at low latitudes show severe modulations under the influence of these TADs. The terrestrial ring current and the other storm time current systems also play important roles in the processes of energy transfer between the magnetosphere and the ionosphere.

In terms of energetics, this study revealed that the low latitude TIS undergoes significant changes in terms of thermospheric energy during geomagnetic storms. However, it had been demonstrated that the servo model is equally applicable for the magnetically disturbed periods as well. More detailed investigation has been done to account for the differences observed between the measured and MSIS model predicted thermospheric temperatures for both geomagnetically quiet and disturbed times. In an empirical model like MSIS, the predictions of thermospheric temperature variations are keyed to the geophysical indices like A_p which are average planetary indices of magnetic activity. Index A_p , being more of a global nature, describes the high latitude storm-response more accurately. Therefore, based on more recent studies, the stormtime ring current index D_{st} has been taken as an appropriate index to represent the low and equatorial latitudes better. Ring current being the main store house of storm time energy, the time rate of D_{st} variation represents the changes in the corresponding energy flux associated with ring current. It is this energy which could get released into the earth's atmosphere and affect the energy budget in the upper atmosphere. To analyse any relation between the D_{st} and the observed low latitude temperatures, a systematic correlative analysis was performed for the D_{st} variations and the observed thermospheric temperatures which brought forth the time delay associated with the response of low latitude TIS to the geomagnetic forcing during storms. A relationship

between the rate at which the energy of ring current system gets dissipated in TIS and the difference between observed and model predicted temperatures has been derived and has been successfully used to improve the model.

Since, there is no clear baseline for defining a geomagnetically quiet period, we extended the above mentioned correlative analysis for relatively quiet periods. The D_{st} variations were observed to have a control on the variabilities in the neutral temperatures even during geomagnetically quiet periods and showed a clear seasonal and solar activity dependence. Understandably, these effects on TIS depends on the ambient condition of the atmosphere at anytime as observed in the time delays shown by the TIS during different months. It has been shown that the temperature difference estimated by the use of these relations when added to the MSIS model predictions sufficiently improved the model predictions. All the variabilities in spectroscopically observed temperature got explained by the I-MSIS predictions but the magnitude remained largely underestimated. Further work in this direction has shown that the spectroscopically observed temperatures would always overestimate the actual thermospheric temperatures. This is due to the inherent limitation of the spectroscopic techniques. For Mt.Abu, this extent has been estimated to be 5-7%.

In order to improve the models further, estimation of contribution from processes like Equatorial Temperature and Wind Anomaly (ETWA) were made. It has been concluded that a quantitative estimation of ETWA contribution to low latitude thermosphere is essential before making comparisons of measured temperatures with the ones predicted by the model. To estimate the extent of heating due to ETWA, we made use of the Dynamics Explorer-2 (DE-2) satellite data on composition and temperature, as measured by the 'Wind And Temperature spectrometer (WATS)' on board, as they are free from the

limitations usually a ground based instrument encounters. We estimated the contribution from both the processes chemical heating and ion drag which are supposed to be responsible for the generation of ETWA. The final exercise, dealing with all the three, namely, ring current, ion drag and chemical heating which contribute towards low latitude thermospheric temperatures and its variabilities, was done for more than 30 nights covering all the months of the year(1981-82). Some of the important results are as follows:

The processes of EIA/ETWA greatly modify the temperature structure over the low latitude, more so during solar maximum. The product of ΔZ and ΔN_e is also a measure of the ion-drag. The heating due to ion-drag (ΔT_{drag}) during day time can be as large as 30K which is not effective during nighttime. Chemical heating (ΔT_{ch}) which is operative irrespective of the time of the day, could account for a maximum of 15K in the observed differences between the measurements and the model. After the inclusion of all the three terms, additively in the MSIS model, all the observed temperatures are reproduced fairly well on most of the occasions.

7.1 Scope of Future Work

The work done in this thesis has opened up several new areas which need further investigation and detailed exploration. A brief outline of these possible areas and useful scientific problems, as perceived at present, is given below:

Systematic simultaneous measurements of both thermospheric and ionospheric parameters from a chain of stations over different latitudes would definitely provide useful insight into the competing roles played by various known and unknown physical processes in thermosphere - ionosphere system. For instance, simultaneous information about the thermospheric temperature, wind and electric field strength would help in understanding the coupling aspect

of thermosphere - ionosphere system. At the time of geomagnetic storms, the simultaneous measurements mentioned above, would prove extremely relevant in bringing out the temporal response of TIS systematically over different latitudes. Important energetic and dynamic changes in TIS over low and equatorial latitudes, as caused by the neutral and electrodynamic forcing at different stages of the evolution of a geomagnetic storm, can be studied in detail.

The possible use of the parameter $\frac{d(D_{st})}{dt}$ can be studied at different latitudes which would improve our understanding of the latitudinal extent of the possible effects of magnetospheric current systems over the thermosphere and ionosphere in general.

Simultaneous faster measurements of earth's magnetic field strength variations would prove extremely useful for modeling the effects of the overhead currents, and for investigating the various aspects of the thermosphere - ionosphere system globally.

The existing thermospheric model, is to be augmented to represent the low latitude temperature and composition better which is one of the primary goals of Aeronomers and space scientists. The first step in this direction would be to identify and parameterize various geophysical processes active over low latitudes, e.g. Midnight Temperature Maximum (MTM) and Equatorial Spread-F (ESF). The former being an outcome of ion-neutral coupling or lower atmosphere-upper atmosphere coupling while the latter is due to plasma instabilities. The faster multi-directional scanning now possible with the present spectrometer can be used to study the zonal and meridional flow of thermospheric winds in the wake of ESF, which would provide important clues about the generation mechanism of irregularities.

By means of coordinated measurements with Multiwavelength Dayglow Photometer and the present Nighttime Spectrometer; the evolution of EIA and its effects over low latitude thermosphere can be studied. The variations in airglow intensity and thermospheric temperatures would give important information about anomaly movement and generation of ETWA respectively. The possibilities explored during the course of the present investigation and the achieved instrumental capabilities would prove to be extremely useful for generating a wide data base which would complement the future satellite missions. Such a database would also help in understanding the complex Thermosphere - Ionosphere - Magnetosphere System, as a whole. The present thesis is considered as a beginning in this direction.

References

1. Abdu, M. A., G. O. Walker, B. M. Reddy, J. H. A. Sobral, B. G. Fejer, T. Kikuchi, N. B. Trivedi and E. P. Szuszczewicz, Electric field versus neutral wind control of the equatorial anomaly under quiet and disturbed conditions: A global perspective from SUNDIAL 86, *Ann. Geophys.*, 8, 419, 1990.
2. Abdu, M. A., J. H. A. Sobral, E. R. de-Paula and I. S. Batista, Magnetospheric disturbance effects on the equatorial ionisation anomaly, *J. Atmos. Terr. Phys.*, 53, 757, 1991.
3. Abdu, M. A., Major phenomena of the equatorial ionosphere - thermosphere system under disturbed conditions, *J. Atmos. Terr. Phys.*, 59, 1505, 1997.
4. Abreu, V. J., G. A. Schmitt, P. B. Hays and T. P. Dacher, Volume emission rate profiles of 6300Å - a tropical nightglow obtained from the AE-E satellite: Latitudinal and seasonal variations, *J. Geophys. Res.*, 87, 6346, 1982.
5. Ackermann, M., P. Simon, U. Von Zahn, and U. Laux, Simultaneous upper air composition measurements by means of UV monochromators and mass spectrometers, *J. Geophys. Res.*, 79, 4757, 1974.
6. Akasofu, S.-I., and S. Chapman, The ring current, geomagnetic disturbance and the Van Allen radiation belts, *J. Geophys. Res.*, 66, 1321, 1961.
7. Akasofu, S.-I., B. Fogle and B. Haurwitz, Sydney Chapman, Eighty from his friends, Univ. of Colorado Press (1968).
8. Alcayde, D., P. Bauer, C. Jacck and J. L. Falin, Latitudinal diurnal variation of some atmospheric parameters determined by a simultaneous analysis of incoherent scatter and satellite drag data, *J. Geophys. Res.*, 77, 2368, 1972.
9. Anandarao, B. G., and R. Suhasini, A deconvolution method for astronomical photometric and spectrometric observations, *Bull. Astr. Soc. India*, 14, 34, 1986.
10. Anderson, D. N., and R. G. Roble, The effect of vertical $\vec{E} \times \vec{B}$ ionospheric drifts on F-region neutral winds in the low-latitude thermosphere, *J. Geophys. Res.*, 34, 5231, 1974.
11. Anderson, D. N., Modeling the ambient, ion latitude F-region ionosphere - a review, *J. Atmos. Terr. Phys.*, 43, 753, 1981.
12. Anderson, D. N., and J. A. Klobuchar, Modeling the total electron content observations above Ascension Island, *J. Geophys. Res.*, 88, 8020, 1983.
13. Appleton, E. V., *Nature*, 157, 691, 1946.

14. Armstrong, E. B., A note on the use of the Fabry-Perot etalon for upper atmospheric temperature measurements, *J. Atmos. Terr. Phys.*, 3, 274, 1953.
15. Armstrong, E. B., *Planet. Space Sci.*, 17, 957, 1969.
16. Atherton P. D., N. K. Reay, J. Ring and T. R. Hicks, Tunable Fabry-Perot filters, *Optical Engineering*, 20(6),806, 1981.
17. Axford, W. I., and C. O. Hines, A unifying theory of high latitude geophysical phenomena and geomagnetic storms, *Can. J. Phys.*, 39, 1433, 1961.
18. Babcock, H. D., A case study of the green auroral line by interference method, *Astrophys. J.*, 57, 209, 1923.
19. Baker, W. G., and D. F. Martyn, Electric Currents in the ionosphere. I. Conductivity., *Phil. Trans. Roy. Soc. London*, A246, 281, 1953.
20. Balachandran, R. N., N. Balan, G. J. Bailey, and P. B. Rao, Spectra of the ac electric fields in the post sunset F-region at the magnetic equator, *Planet. Space Sci.*, 40, 655, 1992.
21. Balan, N., and G. J. Bailey, Equatorial plasma formation and its effects: Possibility of an additional layer, *J. Geophys. Res.*, 100, 21421, 1995.
22. Balan, N., K. I. Oyama, G. J. Bailey, S. Fukao, S. Watanabe, and M. A. Abdu, A plasma temperature anomaly in the equatorial topside ionosphere, *J. Geophys. Res.*, 102, 7485, 1997.
23. Banks, P. M., and G. Kockarts, *Aeronomy*, Academic Press, New York, 1973.
24. Banks, P. M., Observations of joule and particle heating in the auroral zone, *J. Atmos. Terr. Phys.*, 39, 197, 1977.
25. Barbier, D., and J. Galume, La couche ionospherique nocturne F dans la zone intertropicale et ses relations avec l'emission de la raie 6300Å du ciel nocturne, *Planet. Space Sci.*, 9, 133, 1962.
26. Bartels, J., Report on the numerical characterization of days, *IATME Bull.*, 11, 27, IUGG Publ. Office, Paris, 1940c.
27. Barth, C. A., Three body reaction, *Ann. Geophys.*, 20, 182, 1964.
28. Batista I. S., J. H. Sastri, R. T. de Medeiros and M. A. Abdu, Nighttime thermospheric meridional winds at Cacheoira Paulista (23°S, 45°W): Evidence for effects of the equatorial midnight pressure bulge, *J. Geophys. Res.*, 102, 20059, 1997.
29. Baumjohanan, W. and Y. Kamide, Hemispherical Joule heating and AE indices, *J. Geophys. Res.*, 89, 383, 1984.

30. Behnke R. A. and Harper R. M., Vector measurements of F region ion transport at Arecibo, *J. Geophys. Res.*, 78, 8222, 1973.
31. Berger, C., and F. Barlier, Response of the equatorial thermosphere to magnetic activity analyzed with accelerometer total density data, Asymmetrical structure, *J. Atmos. Terr. Phys.*, 43, 121, 1981.
32. Bevington, P. R., Data Reduction and Error Analysis for the physical sciences, McGraw-Hill Book Co., New York, 1969.
33. Biondi, M. A., and W. A. Feibelman, Twilight and nightglow spectral line shapes of oxygen 16300 and 15577 radiation, *Planet. Space. Sci.*, 16, 431, 1968.
34. Biondi, M. A., and J. W. Meriwether, Jr., Measured response of the equatorial thermospheric temperature to geomagnetic activity and solar flux changes, *Geophys. Res. Lett.*, 12, 267, 1985.
35. Biondi, M. A., and D. P. Sipler, Horizontal and vertical winds and temperatures in the equatorial thermosphere: Measurements from Natal, Brazil during August - September, *Planet. Space. Sci.*, 33, 817, 1985.
36. Bittencourt, J. A., Tinsley, B. A., Hicks, G. T., and Reed, E. I., 1976 Tropical F-region winds from 1356Å and 6300Å emission II - analysis of OGO-4 data, *J. Geophys. Res.*, 81, 3786, 1976.
37. Brekke, A., C. L. Rino, High Resolution Altitude profiles of the auroral zone energy dissipation due to ionospheric currents, *J. Geophys. Res.*, 83, 2517, 1978.
38. Bruce, C. F., Aperture corrections in Fabry-Perot interferometer measurements, *Rev. Sci. Inst.*, 37, 349, 1966.
39. Buonsanto, M. J., Observations of neutral circulation at mid latitudes during the equinox transition study, *J. Geophys. Res.*, 94, 16987, 1989.
40. Buonsanto, M. J., Observed and calculated F2 peak heights and derived meridional winds at mid-latitudes over a full solar cycle, *J. Atmos. Terr. Phys.*, 52, 223, 1990.
41. Burns, A. G., and T. L. Killeen, The equatorial neutral thermosphere response to geomagnetic forcing, *Geophys. Res. Lett.*, 10, 977, 1992.
42. Burnside et. al., The neutral thermosphere at Arecibo during geomagnetic storms, *J. Geophys. Res.*, 96, 1289, 1991.
43. Burrage, M. D., V. J. Abreau, and N. Orsini, C. G. Fesen and R. G. Roble, Geomagnetic activity effects on the equatorial neutral thermosphere, *J. Geophys. Res.*, 97, 4177, 1992.
44. Burrage, M. D., W. R. Skinner, A. R. Marshall, P. B. Hays, R. S. Lieberman, S. J. Franke, D. A. Gell, D. A. Ortland, Y. T. Morton, F. T. Schmidlin, R. A. Vincent, and D. L. Wu, Comparison of HRDI measurements with radar and rocket observations, *Geophys. Res. Lett.*, 20, 1259, 1993.

45. Burrage, M. D., Arvin N., Skinner W. R., and Hays P. B., Observations of the O_2 atmospheric band nightglow by the high resolution Doppler imager, *J. Geophys. Res.*, 99, 15017, 1994.
46. Carignan, G. R., B. P. Block, J. C. Maurer, A. E. Hedin, C. A. Reber, and N. W. Spencer, The neutral mass spectrometer on Dynamic Explorer B, *Space Sci. Inst.*, 5, 429, 1981.
47. Carru, H., M. Petit, and P. Waldteufel, On the diurnal variation of the thermopause temperature, *Planet. Space Sci.*, 15, 944, 1967.
48. Chabbal, R., Recherche des mellenres conditions d'vtilisation d'un spectrometer photoelec-trique Fabry-Perot, *J. Rech (CRNS)*, 24, 138, 1953.
49. Chamberlain, J. W., Physics of the Aurora and Airglow, Academic Press, New York, 1961.
50. Chapman, S., Some phenomena of the upper atmosphere, *Proc. R. Soc. London*, Ser, A, 132, 353, 1931.
51. Chapman, S., The electrical conductivity of the ionosphere : A review, *Nuovo Cimento*, 4(10), 1385, 1956.
52. Chandra, S., and R. A. Goldberg, Geomagnetic control of diffusion in the upper atmosphere, *J. Geophys. Res.*, 69, 3187, 1964.
53. Chandra, S., and R. G. Rastogi, Spread-F at magnetic equatorial station, Thumba, *Ann. Geo-phys.*, 709, 1972.
54. Chen, P. R., Two-day oscillation of the equatorial ionisation anomaly, *J. Geophys. Res.*, 97, 6343, 1992.
55. Chiu, Y. T., An improved phenomenological model of ionospheric density, *J. Atmos. Terr. Phys.*, 37, 1563, 1975.
56. Clauer C. R. and R. L. McPherron, On the relationship of the partial ring current to substorms and interplanetary magnetic field, *J. Geomagn. Geoelectr.*, 30, 195, 1978.
57. Cole, K. D., and M. P. Hickey, Energy transfer by gravity wave dissipation, *Adv. Space. Res.*, 1, No. 12, 65, 1981.
58. Cogger, L. L., G. J. Nelson, M. A. Biondi, R. D. Hake, Jr., and D. P. Sipler, Coincident F-region temperature determinations from incoherent backscatter and Doppler broadening of $OI\ 6300\text{\AA}$, *J. Geophys. Res.*, 75, 4887, 1970.
59. Cogger, L. L., J. C. G. Walker, J. W. Meriwether, Jr., and R. G. Burnside, F-region airglow: Are the ground-based observations consistent with recent satellite results?, *J. Geophys. Res.*, 85, 3013, 1980.

60. Colerico M., M. Mendillo, D. Nottingham, J. Baumgardner, J. Merowether, J. Mirick, B. W. Reinisch, J. L. Scali, C. G. Fesen and M. A. Biondi, Coordinated measurements of F-region dynamics related to thermospheric midnight temperature maximum, *J. Geophys. Res.*, 101, 26783, 1996.
61. Cooley, J. E., and C. A. Reber, Neutral atmosphere composition measurement between 135 and 533 kilometers from the Geoprobe rocket mass spectrometer, *Rep. NASA/GSFC*, X-621-69-260, 1969.
62. Cole, K. D., Energetics and a source of energy for equatorial spread-F events, *J. Atmos. Terr. Phys.*, 36, 1099, 1974.
63. Coley, W. R., R. A. Heelis, and N. W. Spencer, Comparison of low latitude ion and neutral zonal drifts using DE-2 data, *J. Geophys. Res.*, 99, 341, 1994.
64. Cooper, M. J., Deconvolution: If in doubt, do it, *Physics Bulletin*, Oct. Issue, 463, 1977.
65. Cowling, T. G., The electrical conductivity of an ionised gas in a magnetic field, with applications to the solar atmosphere and the ionosphere, *Proc. Roy. Soc. London*, A183, 453, 1945.
66. Crain, D. J., R. A. Heelis, G. J. Bailey and A. D. Richmond, Effects of electrical coupling on equatorial ionospheric plasma motions: When is the F-region a dominant driver in the low latitude dynamo? *J. Geophys. Res.*, 98, 6033, 1993.
67. Craven, J. D., L. A. Frank, and K. L. Ackerson, Global observations of a SAR Arc, *Geophys. Res. Lett.*, 9, 961, 1982.
68. Craven, J. D., and L. A. Frank, Latitudinal motions of the aurora during substorms, *J. Geophys. Res.*, 92, 4565, 1987.
69. Croom, S., A. Robbins and J. O. Thomas, Variations of electron density in the ionosphere with magnetic dip, *Nature*, 185, 902, 1960.
70. Crowley, G., B. A. Emery, R. G. Roble, H. C. Carlson, Jr., J. E. Sahah, V. B. Wickwar, K. L. Miller, W. L. Oliver, R. G. Burnside and E. A. Marcos, Thermospheric dynamics during September 18 - 19, 1984, 2, Validation of NCAR thermospheric general circulation model, *J. Geophys. Res.*, 94, 16945, 1989b.
71. Dalgarno, A., Ambipolar diffusion in the F-region, *J. Atmos. Terr. Phys.*, 26, 939, 1964.
72. Daniel, R. E., L. D. Brown, D. N. Anderson, M. W. Fox, P. H. Doherty, D. T. Decker, J. J. Sojka and R. W. Schunk, PIM: A global ionospheric parameterisation based on first principle models, *Radio Sci.*, 30, 1499, 1995.
73. Daniel, R. E. and D. N. Anderson, Realtime operational ionospheric specification and forecast models, AIAA, 95-0549, 33rd Aerospace Science Meeting., 1995.

74. Dickinson, R E., R. G. Roble and E. C. Ridley, Response of the neutral thermosphere at F-layer heights to interaction of a global wind with anomalies of ionisation, *J. Atmos. Sci.*, 28, 1280, 1971.
75. Donahue, T. M. and G. R. Carignan, The temperature gradients between 100-120 km, *J. Geophys. Res.*, 80, 4565, 1975.
76. Draper, N. R., and H. Smith, Applied Regression Analysis, John Wiley and Sons, Inc., New York, 1966.
77. Duncan, R. A., the equatorial F-region of the ionosphere, *J. Atmos. Terr. Phys.*, 18, 80, 1960.
78. Dungey, J. W., Interplanetary magnetic field and the auroral zones, *Phys. Rev. Lett.*, 6, 47, 1961.
79. Earle, G. D., and M. C. Kelley, Spectral studies of the sources of ionospheric electric fields, *J. Geophys. Res.*, 92, 213, 1987.
80. Elphic R. C., and C. T. Russle, ISEE 1 and 2 magnetometer observations of the magnetopause, In *Magnetospheric boundary layers*, ESA publication'1979.
81. Evans, D. S., N. C. Maynard, J. Troim, T. Jacobson and A. Egeland, Auroral vector electric field and particle comparison 2. electrodynamics of an arc, *J. Geophys. Res.*, 82, 2235, 1977.
82. Fagundes, P. R., Sahai, Y., Bittencourt, J. A., and H. Takahashi, Observation of thermospheric neutral winds and temperatures at Cacheocira Paulista (23°S, 45°W) during a geomagnetic storm, *Adv. Space. Res.*, 16(5), 27, 1995a.
83. Fagundes, P. R., Y. Sahai, J. A. Bittencourt and H. Takahashi, Plasma drifts inferred from thermospheric neutral winds and temperature gradients observed at low latitudes, *J. Atmos. Terr. Phys.*, 58, 1219, 1996.
84. Farely, D. T., E. Bonelli, B. G. Fejer, and M. F. Larsen, The prereversal enhancement of the zonal electric field in the equatorial ionosphere, *J. Geophys. Res.*, 91, 13723, 1986.
85. Farrugia, C. J., M. P. Freeman, L. F. Burlaga, R. P. Lepping and K. Takahashi, The earth's magnetosphere under continued forcing, substorm activity during the passage of an interplanetary magnetic cloud, *J. Geophys. Res.*, 98, 7657, 1993.
86. Fejer, B. G., and M. C. Kelley, Ionospheric irregularities, *Rev. Geophys. Space. Phys.*, 18, 401, 1980.
87. Fejer, B. G., E. Kudeki and D. T. Farley, Equatorial F-region zonal plasma drifts, *J. Geophys. Res.*, 90, 12249, 1985.

88. Fejer, B. G., R. W. Spiro, R. A. Wolf, and J. C. Foster, Latitudinal variation of perturbation electric fields during magnetically disturbed periods: 1986 SUNDIAL observations and model results, *Ann. Geophys.*, 8, 441, 1990.
89. Fejer, B. G., E. R. de Paula, S. A. Gonzales, and R. F. Woodman, Average vertical and zonal F-region plasma drifts over Jicamarca, *J. Geophys. Res.*, 96, 13901, 1991.
90. Fejer, B. G., The electrodynamics of the low-latitude ionosphere: recent results and future challenges, *J. Atmos. Terr. Phys.*, 59, 1465, 1997.
91. Fesen, C. G., R. E. Dickinson and R. G. Roble, Simulation of the thermospheric tides at equinox with the National Center for Atmospheric Research Thermospheric General Circulation Model, *J. Geophys. Res.*, 91, 4471, 1986.
92. Fesen, C. G., and V. J. Abreu, Modeling of 6300Å low latitude nightglow, *J. Geophys. Res.*, 92, 1231, 1987.
93. Fesen, C. G., Simulations of the low-latitude midnight temperature maximum, *J. Geophys. Res.*, 101, 26063, 1996.
94. Fieldstein, Y. I., Some problems concerning the morphology of auroras and magnetic disturbances at high latitudes, *Geomag. Aeron.*, 3(2), 183, 1963.
95. Fieldstein, Y. I., and G. V. Starkov, Dynamics of auroral belt and polar geomagnetic disturbances, *Planet. Space. Sci.*, 15, 209, 1967.
96. Forbes, J. M., Atmospheric tides, 1, Model description and Results for the solar diurnal components, *J. Geophys. Res.*, 87, 5222, 1982.
97. Forbes, J. M., R. G. Roble, and F. A. Marcos, Thermospheric dynamics during the March 22, 1979, magnetic storm, 2, comparisons of model predictions with observations, *J. Geophys. Res.*, 92, 6069, 1987.
98. Forbes, J. M., and R. G. Roble, Thermosphere-ionosphere coupling: An experiment in interactive modeling, *J. Geophys. Res.*, 95, 201, 1990.
99. Forbes, J. M., and S. Leveroni, Quasi 16-day oscillation in the ionosphere, *Geophys. Res. Lett.*, 19, 981, 1992.
100. Foster, J. C., J. M. Holt, R. G. Musgrove and D. S. Evans, Ionospheric connection associated with discrete levels of particle precipitation, *Geophys. Res. Lett.*, 13, 656, 1986.
101. Foukal, P and J. Lean, A model of total solar irradiance variation between 1874-1900, *Science*, 247, 556, 1990.
102. Fujii, R., T. Iijima, T. A. Potemra, and M. Sugiura, Seasonal dependence of large-scale Birkland currents, *Geophys. Res. Lett.*, 8, 1103, 1981.

103. Fuller-Rowell, T. J., and D. Rees, A Three dimensional, time-dependent global model of thermosphere, *J. Atmos. Sci.*, 37, 2545, 1980.
104. Fuller-Rowell, T. J., and D. Rees, Derivation of a conservation equation for mean molecular weight for a two constituent gas within a three dimensional time dependent model of the thermosphere, *Planet. Space. Sci.*, 31, 1209, 1983.
105. Fuller-Rowell, T. J., and D. S. Evans, Height-integrated Pederson and Hall conductivity patterns inferred from the TIROS-NOAA satellite data, *J. Geophys. Res.*, 92, 7606, 1987.
106. Fuller-Rowell, T. J., D. Rees, S. Quegan, R. J. Moffet and G. J. Bailey, Interactions between neutral thermospheric composition and polar ionosphere using a coupled ionosphere-thermosphere model, *J. Geophys. Res.*, 92, 7744, 1987.
107. Fuller-Rowell, T. J., D. Rees, S. Quegan, R. J. Moffet and G. J. Bailey, Interactions between neutral thermospheric composition and the polar ionosphere using a coupled ionosphere - thermosphere model, *J. Geophys. Res.*, 92, 7744, 1987b.
108. Fuller-Rowell, T. J., D. Rees, S. Quegan, R. J. Moffet, and G. J. Bailey, Simulations of the seasonal and universal time variations of the thermosphere and ionosphere using a coupled, three-dimensional, global model, *PAGEOPHYSY*, 127, 189, 1988.
109. Fuller-Rowell, T. J., D. Rees, B. A. Tinsley, H. Rishbeth, A. S. Rodger and S. Quegan, MOdeling the response of the thermosphere to geomagnetic storms: Effects of midlatitude heat source, *Adv. Space Res.*, 10(6), 215, 1990.
110. Fuller-Rowell, T. J., Codrescu M. J., Moffett R. J. and Quegan S., Response of the thermosphere and ionosphere to geomagnetic storms, *J. Geophys. Res.*, 99, 3893, 1994
111. Fuller-Rowell, T. J., M. V. Codrescu, B. G. Fejer, W. Barer, F. Marcos and D. N. Anderson, Dynamics of the low-latitude thermosphere: quiet and disturbed conditions, *J. Atmos. Terr. Phys.*, 59, 1533, 1997.
112. Fukushima, N., and Y. Kamide, Partial ring current models for worldwide geomagnetic disturbances, *Rev. Geophys.*, 11, 795, 1973.
113. Garcia, R. R. and S. Solomon, The effect of breaking gravity waves on the dynamics and chemical composition of the mesosphere and lower thermosphere, *J. Geophys. Res.*, 90, 3850, 1985.
114. Goembel L., and F. A. Herraro, Anomalous meridional thermospheric neutral winds in the AE-E NATE data: Effects of the equatorial nighttime pressure bulge, *Geophys. Res. Lett.*, 22, 271, 1995.

115. Groves, G. V. and J. M. Forbes, Equinox tidal heating of the upper atmosphere, *Planet. Space Sci.*, 32, 447, 1984.
116. Garg, S. C., Y. V. Somayajulu, Lakha Singh, T. R. Tyagi, Evidence for the development and decay of a post sunset equatorial anomaly at low latitude, *Proc. Ind. Symp. Beacon. Sat. studies of earth environment*, held at New Delhi, 359, Feb. 7-11, 1983.
117. Geisler, J. E., Atmospheric winds in the middle latitude F-region, *J. Atmos. Terr. Phys.*, 28, 703, 1966.
118. Gloecker, G., F. Iparich, D. Hamilton, S. Wilken, W. Studemann, G. Kremser, Solar wind carbons, nitrogen and oxygen abundances measured in the earth's magnetosheath with AMPTE/CCE, *Geophys. Res. Lett.*, 13, 793, 1986.
119. Goldberg, R. A., *Proc. Second International Symposium on Equatorial Aeronomy* at Sao Jose dos Campos, Brazil, Sept. 1965, Ed. F. de Mendonca, 204, 1965
120. Gonzales, C. A., M. C. Kelley, B. G. Fejer, J. F. Vickrey, and R. F. Woodman, Equatorial electric fields during magnetically disturbed conditions, 2, Implications of simultaneous auroral and equatorial measurements, *J. Geophys. Res.*, 84, 5803, 1979.
121. Gonzales, W. D., B. T. Tsurutani, A. L. C. Gonzalez, E. J. Smith, F. Tang and S. I. Akasofu, Solar wind magnetospheric coupling during intense magnetic storms (1978-1979), *J. Geophys. Res.*, 94, 8835, 1989.
122. Gosling, J. T., D. J. McComas, J. L. Phillips and S. J. Bame, Geomagnetic activity associated with earth passage of interplanetary shock disturbances and coronal mass ejections, *J. Geophys. Res.*, 96, 731, 1991.
123. Gosling, J. T., The solar flare myth, *J. Geophys. Res.*, 98, 18937, 1993.
124. Grechko, G. M., L. S. Yevlashin, H. W. Ivanchenkov, V. V. Kovalenok, A. I. Lazarev, and V. Romanenko Yu., *Aurorae Airglow Acad. Sci. U.S.S.R.*, 31, 5, 1982.
125. Gurubaran, S., Investigation of low latitude thermosphere-ionosphere system, Ph.D. thesis, Gujrat Univ., 1993.
126. Gurubaran, S., and R. Sridharan, Effect of neutral temperatures and meridional winds on F-layer height, *J. Geophys. Res.*, 98, 11629, 1993.
127. Gurubaran, S., R. Sridharan, R. Suhasini and K. G. Jani, Variabilities in the thermospheric temperatures in the regions of the crest of the equatorial ionisation anomaly - a case study, *J. Atmos. Terr. Phys.*, 57, 695, 1995.
128. Hagan, M. E., Quiet-time upper thermospheric winds over Millstone Hill between 1984 and 1990, *J. Geophys. Res.*, 98, 3731, 1993.

129. Hagan, M. E., Thermospheric Connections, *Rev. Geophys. Suppl.*, 33, 729, 1995.
130. Hanson, W. B., and J. N. Patterson, The maintenance in the nighttime F-layer, *Planet. Space Sci.*, 12, 979, 1964.
131. Hardy, D. A., M. S. Gussenhoven and E. Holeman, A statistical model of auroral precipitation, *J. Geophys. Res.*, 90, 4229, 1985.
132. Haerendel, G., Report-Theory of equatorial spread-F, *Max-Planck Inst. fur Phys. und Astrophys.*, Garching, Germany, 1974.
133. Haerendel, G., G. Paschmann, N. Sckopke, H. Rosenbauer and P. C. Hedgecock, The frontside boundary layer on the magnetosphere and the problem of reconnection, *J. Geophys. Res.*, 83, 3195, 1978.
134. Haerendel, G., and J. V. Eccles, The role of the equatorial electrojet in the evening ionosphere, *J. Geophys. Res.*, 97, 1181, 1992.
135. Hays, P. B. and R. G. Roble, Direct observations of thermospheric winds during geomagnetic storms, *J. Geophys. Res.*, 76, 5316, 1971a.
136. Hays, P. B., and R. G. Roble, A technique for recovering Doppler line profiles from Fabry-Perot interferometer fringes of very low intensity, *Appl. Optics*, 10, 193, 1971b.
137. Hays, P. B., D. W. Rush, R. G. Roble, and J. C. G. Walker, The OI(6300Å) airglow, *Rev. Geophys. Space Phys.*, 16, 225, 1978.
138. Hays, P. B., High resolution optical measurements of atmospheric winds from space. 1.: lower atmosphere molecular absorption, *Appl. Opt.*, 21, 1136, 1982.
139. Hays, P. B., T. L. Killeen, N. W. Spencer, L. E. Wharton, R. G. Roble, B. A. Emery, T. J. Fuller-Rowell, D. Rees, L. A. Frank and J. D. Graven, Observations of the dynamics of the polar thermosphere, *J. Geophys. Res.*, 89, 5547, 1984.
140. Hedin, A. E., and H. G. Mayr, Magnetic control of the near equatorial neutral atmosphere, equilibrium electron distributions in the ionospheric F2 layer, *J. Atmos. Terr. Phys.*, 18, 234, 1960.
141. Hedin, A. E., and H. G. Mayr, Magnetic control of the near equatorial neutral thermosphere, *J. Geophys. Res.*, 78, 1688, 1973.
142. Hedin, A. E., H. G. Mayr, C. A. Reber, N. W. Spencer and G. R. Carrigan, Empirical model of global thermospheric temperature and composition based on data from OGO 6 quadrupole mass spectrometer, *J. Geophys. Res.*, 79, 215, 1974.
143. Hedin, A. E. *et al.*, A global thermosphere model based on mass spectrometer and incoherent scatter data, MSIS 1, N_2 density and temperature, *J. Geophys. Res.*, 82, 2139, 1977a.

144. Hedin, A. E. *et al.*, A global thermosphere model based on mass spectrometer and incoherent scatter data, MSIS 2, Composition, *J. Geophys. Res.*, 82, 2148, 1977b.
145. Hedin, A. E., N. W. Spencer, H. G. Mayr, and H. S. Porter, Semiempirical modeling of thermospheric magnetic storms, *J. Geophys. Res.*, 86, 3515, 1981.
146. Hedin, A. E., A revised thermospheric model based on mass spectrometer and incoherent scatter data: MSIS-83, *J. Geophys. Res.*, 88, 10170, 1983.
147. Hedin, A. E., MSIS-86 thermospheric model, *J. Geophys. Res.*, 4649, 1987.
148. Hedin, A. E., N. W. Spencer and T. L. Killeen, Empirical global model of upper thermosphere winds based on Atmosphere and Dynamics Explorer satellite data, *J. Geophys. Res.*, 93, 9959, 1988.
149. Hedin, A. E., Extension of the MSIS thermosphere model into the middle and lower atmosphere, *J. Geophys. Res.*, 96, 1159, 1991.
150. Heelis, R. A., P. C. Kendall, R. J. Moffett, D. W. Windle, and H. Rishbeth, Electrical coupling of the E and F regions and its effects on F-region drifts and winds, *Planet. Space. Sci.*, 22, 743, 1974.
151. Heelis, R. A., W. B. Hanson, C. R. Lippincott, D. R. Zuccaro, L. H. Harmon, B. J. Holt, J. E. Doherty and R. A. Power, The ion-drift meter for Dynamics explorer-B, *Space Sci. Instrum.*, 5, 511, 1981.
152. Heppner, H. P. and N. C. Maynard, Empirical high latitude electric field models, *J. Geophys. Res.*, 92, 4467, 1987.
153. Hernandez, G., Analytical description of a Fabry-Perot photoelectric spectrometer, *Appl. Opt.*, 5, 1745, 1966.
154. Hernandez, G., Contamination of the OI ($^3P_2 - ^1D_2$) emission line by the (9-3) band of OH X²Π in high resolution measurements of the nightsky, *J. Geophys. Res.*, 79, 1119, 1974.
155. Hernandez, G., T. I. Van Zandt, V. L. Paterson and J. P. Turtle, Comparison of optical and incoherent scatter measurements of nighttime exospheric temperature at the magnetic equator, *J. Geophys. Res.*, 80, 3271, 1975.
156. Hernandez, G., and R. G. Roble, Director measurements of thermospheric winds and temperatures, 1. Seasonal variations during geomagnetically quiet periods, *J. Geophys. Res.*, 81, 2065, 1976.
157. Hernandez, G., and R. G. Roble, Relationship between midlatitude thermospheric winds and the time rate of change of D_{st} , *Geophys. Res. Lett.*, 5, 835, 1978.

158. Hernandez, G., and R. G. Roble, Thermospheric dynamics investigations with very high resolution spectrometers, *Appl. Opt.*, 18, 3376, 1979.
159. Hernandez, G., R. G. Roble, and J. H. Allen, Midlatitude thermospheric winds and temperatures and their relation to the auroral electrojet activity index, *Geophys. Res. Lett.*, 7, 677, 1980.
160. Hernandez, G., Analytical description of a Fabry Perot Spectrometer, 6, Minimum number of samples required for the determination of Doppler widths and shifts, *Appl. Opt.*, 21, 1695, 1982a.
161. Hernandez, G., Analytical description of a Fabry Perot Spectrometer, 8, optimum operation with equidistant equal noise sampling, *Appl. Opt.*, 24, 2442, 1985.
162. Hernandez, G., Fabry Perot interferometers, *Cambridge Univ. Press*, Cambridge, 1986.
163. Hernandez, G., and T. L. Killeen, Optical measurements of winds and kinetic temperatures in the upper atmosphere, *Adv. Space Res.*, 8, (5)149, 1988.
164. Hernandez, G., and R. G. Roble, Thermospheric nighttime neutral temperature and winds over Fritz peak observatory: Observed and calculated solar cycle variation, *J. Geophys. Res.*, 100, 14647, 1995.
165. Herraro, F. A., H. G. Mayr and N. W. Spencer, Latitudinal (seasonal) variations in the thermospheric midnight temperature maximum: A tidal analysis, *J. Geophys. Res.*, 88, 7225, 1983.
166. Herraro, F. A., and J. W. Meriwether, The 630nm MIG and the vertical neutral wind in the nighttime thermosphere at low latitude, *Geophys. Res. Lett.*, 21, 97, 1994.
167. Hines, C. O., Internal gravity waves at ionospheric heights, *Can. J. Phys.*, 38, 1441, 1960.
168. Hoffman, R. A. and E. R. Schmerling, Dynamics Explorer Program: An Overview, *Space Science Instrumentation*, 5, 345, 1981.
169. Holzworth, R. H., and C. I. Meng, Mathematical representation of the auroral oval, *Geophys. Res. Lett.*, 2(9), 377, 1975.
170. Howard, R. A., Scheeley, N. R. Jr., Kooman, M. J., and Micheles, D. J, Coronal mass ejections, 1979-1981, *J. Geophys. Res.*, 90, 8173, 1995.
171. Hoyt, D. V., and K. H. Schatten, A discussion of plausible solar irradiance variations, 1700-1992, *J. Geophys. Res.*, 98, 18895, 1993.
172. Hunsucker, R. D., Atmospheric gravity waves generated in the high latitude ionosphere - A review, *Rev. Geophys. Space Phys.*, 20, 293, 1982.

173. Iijima, T., and T. A. Potemra, Large-scale characteristics of field aligned currents associated with substorms, *J. Geophys. Res.*, 81, 3999, 1976a.
174. Iijima, T., and T. A. Potemra, The amplitude distribution of Field-aligned currents at Northern high latitudes observed by trial, *J. Geophys. Res.*, 81, 2165, 1976b.
175. Ishimoto, M., M. R. Torr, P. G. Richards and D. G. Torr, The role of energetic O^+ precipitation in mid-latitude aurora, *J. Geophys. Res.*, 91, 5793, 1986.
176. I. Almar, E. Illes-Almar, A. Horvath, Z. Kollath, D. V. Bisikalo and T. V. Kasimenko, Improvement of the MSIS 86 and DTM thermospheric models by investigating the geomagnetic effect, *Adv. Space Res.*, 12, (6)313, 1992.
177. I. Almar, E. Illes-Almar, A. Horvath, J. Kelemen, D. V. Bisikalo, T. V. Kasimenko, Investigation and modelling of an improved geomagnetic term for the CIRA'86 model at low latitudes, *Adv. Space Res.*, 18, (9/10)375, 1996
178. Jacquinet, P., The luminosity of spectrometers with prisms gratings or Fabry-Perot etalons, *J. Opt. Soc.*, 44, 761, 1954.
179. Jacquinet, P., New developments in interference spectroscopy, *Repts. Prog. Phys.*, 23, 267, 1960.
180. Johnson, R. M., and V. B. Wickwar, Incoherent scatter measurements of high-latitude lower-thermospheric density and dynamics, *Proc. Atmospheric Density and Aerodynamic Drag Workshop*, AFGL, Oct 10, 1987.
181. Jones W. B. and Gallet R. M., The representation of diurnal and geographic variations of ionospheric data by numerical means, *Tele. Comm. J.*, 29, 129, 1962.
182. Kamide, Y., and G. Rostoker, The spatial relationships of field-aligned currents and auroral electrojets to the distribution of nightside auroras, *J. Geophys. Res.*, 82, 5589, 1977.
183. Kelley. M. C., La Belle, E. Kudeki, B. G. Fejer, Sa. Basu, Su. Basu, K. D. Baker, C. Hanuise, P. Arog, R. F. Woodman, W. E. Swartz, D. T. Farley, J. W. Meriwether Jr., The condor equatorial spread-F campaign: Overview and results of the large scale measurements, *J. Geophys. Res.*, 91, 5487, 1986.
184. Kelley. M. C., The earth's ionosphere, Plasma physics and Electrodynamics, Academic, New York, 1989.
185. Khorosheva, O. V., The diurnal drift of the closed Auroral ring, *Geomag. Aeron.*, 2(5), 696, 1962.

186. Killeen, T. L., and R. G. Roble, An analysis of the high latitude thermospheric wind pattern calculated by a thermospheric general circulation model 2. Neutral parcel transport, *J. Geophys. Res.*, 91, 11291, 1986.
187. King, J. W., and H. Kohl, *Nature*, 206, 699, 1965.
188. Klostermeyer, J., Numerical calculation of gravity wave propagation in a realistic thermosphere, *J. Atmos. Terr. Phys.*, 34, 765, 1973.
189. Knight, S., Parallel electric fields, *Planet. Space Sci.*, 21, 741, 1973.
190. Koomen, M. J., R. Scolnik, and R. Tousey, Direct measurements of the night airglow, in *The Threshold of Space*, edited by M. Zelikoff, p.217, Pergamon New York, 1957.
191. Kozyra, J. W., T. E. Cravens and A. F. Nagy, Energetic O^+ precipitation, *J. Geophys. Res.*, 84, 2481, 1982.
192. Krehbiel, J. P., L. H. Brace, R. F. Theis, W. H. Pinkns and R. B. Koplan, The Dynamic Explorer Langmuir Probe instrument, *Space Sci. Instrum.*, 5, 493, 1981.
193. Krishnamurthy, B. V., S. S. Hari, and V. V. Somayajulu, Nighttime equatorial thermospheric meridional winds from hF data, *J. Geophys. Res.*, 95, 4307, 1990.
194. Lee, J. S., J. P. Doering, T. A. Potemra, and L. H. Brace, Measurements of the ambient photoelectron spectrum from Atmosphere Explorer: II AE-E measurements from 300-100km during solar minimum conditions, *Planet. Space Sci.*, 28, 973, 1980.
195. Lindzen, R. S., Turbulence and stress owing to gravity wave and tidal breakdown, *J. Geophys. Res.*, 86, 9707, 1981.
196. Lockwood, M., and M. N. Wild, On the quasi-periodic nature of magnetopause flux transfer events, *J. Geophys. Res.*, 98, 5935, 1993.
197. Lui, A. T. Y., Current disruption in the earth's magnetosphere: Observations and models, *J. Geophys. Res.*, 101, 13067, 1996.
198. Lyons, A. J. and L. Thomas, The F2 region equatorial anomaly in the African, American and East Asian sectors during sunspot maximum, *J. Atmos. Terr. Phys.*, 25, 373, 1963.
199. Maeda, H., *Rept. Ionos. Spce. Res.*, Japan, 9, 59, 1955.
200. Maeda, K., *Physics of the ionosphere, Physical Society, London*, 245, 1955
201. Manson, A. H., C. E. Meek, S. K. Avery, G. J. Fraser, R. A. Vincent, A. Phillip, R. R. Clark, R. Schminder, D. Kurschner, and E. S. Kasimirovsky, Tidal winds from the mesosphere, lower thermosphere global radar network during the second LTCS campaign: December 1988, , *J. Geophys. Res.*, 96, 1117, 1991.

202. Martyn, D. F., Atmospheric tides in the ionosphere, I, Solar tides in the F_2 region, *Proc. R. Soc. London*, A189, 241, 1947.
203. Martyn, D. F., Processes controlling ionisation distribution in F2 region of the ionosphere, *Aust. J. Phys.*, 9, 161, 1956.
204. Matsushita, S., Dynamo currents, winds, and electric fields. *Radio Sci.*, 4, 771, 1969.
205. Matsushita, S., J. D. Tarpley, and W. H. Campbell, IMF sector structure effects on the quiet geomagnetic field, *Radio Sci.*, 8, 963, 1977.
206. Matuura N., Theoretical models of ionospheric storms, *Space Sci. Rev.*, 13, 124, 1972.
207. Mayaud, P. N., Morphology of the transient irregular variations of the terrestrial magnetic field, and their main statistical laws, *Ann. Geophys.*, 34, 243, 1978a.
208. Mayaud, P. N., and M. Menvielle, A report on *Km* observatory visits, *IAGA BULL.*, 32i, IUGG Publ. Office, Paris, 1980.
209. Mayaud, P. N., Derivation, Meaning, and Use of geomagnetic indices, *Geophysical monograph* 22, AGU, 1980.
210. Mayr, H. G., and H. Volland, Magnetic storm characteristics of the thermosphere, *J. Geophys. Res.*, 78, 2251, 1973.
211. Mayr, H. G., I. Harris and N. W. Spencer, Thermosphere 'temperatures', *J. Geophys. Res.*, 79, 2921, 1974.
212. Mayr, H. G., and H. Volland, Composition waves in the thermosphere, *J. Geophys. Res.*, 81, 671, 1976.
213. Mayr, H. G., and A. C. Hedin, Significance of large-scale circulation in magnetic characteristics with application to AE-C neutral composition data, *J. Geophys. Res.*, 82, 1227, 1977.
214. Mayr, H. G., I. Harris, and N. W. Spencer, Some properties of upper atmosphere dynamics, *Rev. Geophys. Space Phys.*, 16, 539, 1978.
215. Mayr, H. G., I. Harris, N. W. Spencer, A. E. Hedin, L. E. Wharton, H. S. Porter, J. C. G. Walker, and H. C. Carlson, Atmospheric tides and midnight temperature anomaly in the thermosphere, *Geophys. Res. Lett.*, 6, 447, 1979.
216. McComas, D. J, Tongues, bottles, and disconnected loops, The opening and closing of the interplanetary magnetic field, *Reviews of Geophysics*, Supple. 603, 1995.
217. McCormac F. G., T. L. Killeen and B. Nardi, How close are ground based Fabry-Perot thermospheric wind and temperature measurements to exospheric values?, A simulation study, *Planet. Space Sci.*, 35, 1255, 1987.

218. Mendillo, M., Baumgardner J., Pi, X., Sultan P. J., and Tsunoda R. T., Onset conditions for equatorial spread-F, *J. Geophys. Res.*, 97, 13865, 1992.
219. Meriwether, J. W., J. W. Moody, M. A. Biondi and R. G. Roble, Optical interferometric measurements of nighttime equatorial thermospheric winds at Arequipa, Peru, *J. Geophys. Res.*, 91, 5547, 1986.
220. Miller, N. J., H. G. Mayr, N. W. Spencer, and L. H. Brace, Observations relating changes in thermospheric composition to depletions in topside ionisation during the geomagnetic storm of September 1982, *J. Geophys. Res.*, 89, 2389, 1984.
221. Miller, K. L., D. G. Torr, and P. G. Richards, Meridional winds in the thermosphere derived from measurements of F2 layer heights, *J. Geophys. Res.*, 91, 4531, 1986.
222. Miller, K. L., J. E. Sahah, and D. G. Torr, The effect of electric fields on measurements of meridional winds in the thermosphere, *Ann. Geophys.*, 5A, 337, 1987.
223. Mitra, S. K., *Nature*, 158, 668, 1946.
224. Moffett, R. J., The equatorial anomaly in the electron distribution of the terrestrial F-region, *Fund. Cosmic Phys.*, 4, 313, 1979.
225. Namboothiri, S. P., N. B. Balan and P. B. Rao, Vertical plasma drifts in the F-region at the magnetic equator, *J. Geophys. Res.*, 94, 12055, 1989.
226. Narayanan, R. , J. N. Desai, N. K. Modi, R. Raghavarao and R. Sridharan, Dayglow Photometry: A new approach, *Appl. Opt.*, 28, 2138, 1989.
227. Narcisi, R. S., and E. P. Szuszczewicz, Direct measurements of electron density temperature and ion composition in an equatorial spread-F ionosphere, *J. Atmos. Terr. Phys.*, 43, 463, 1981.
228. Nelson, G. J., and L. L. Cogger, Dynamical behaviour of the nighttime ionosphere at Arecibo, *J. Atmos. Terr. Phys.*, 33, 1711, 1971.
229. Nisbet, J. S., Neutral atmospheric temperature from incoherent scatter observations, *J. Atmos. Terr. Phys.*, 24, 586, 1967.
230. Nisbet, J. S., C. Stehle, and E. Bleuler, Initial tests of an index based on AL values for modeling magnetic storm related perturbations of the thermosphere, *J. Geophys. Res.*, 88, 2175, 1983.
231. Noxon J. F. and R. M. Goody, Observations of day airglow emission, *J. Atmos. Sci.*, 19, 342, 1962.
232. Offermann, D., Composition variations in the lower thermosphere, *J. Geophys. Res.*, 79, 4201, 1974.

233. Ogilvie, K. W., and M. A. Coplan, Solar wind composition, *Reviews of Geophysics, Supple.*, 615, 1995.
234. Ossakow, S. L., S. T. Zalesak, B. E. McDonald, and P. K. Chaturvedi, Nonlinear equatorial spread-F: Dependence on altitude of the F-peak and bottomside background electron density gradient scale length, *J. Geophys. Res.*, 84, 17, 1979.
235. Ossakow, S. L., Spread-F theories - A review, *J. Atmos. Terr. Phys.*, 43, 437, 1981.
236. Otto, A., Magnetic reconnection at the magnetopause: A fundamental process and manifold properties, *Reviews of Geophysics, Supple.*, 657, 1995.
237. Pallam Raju D., R. Sridharan, S. Gurubaran, and R. Raghavarao, First results from ground based daytime optical investigations of the development of equatorial ionisation anomaly, *Ann. Geophys.*, 14, 238, 1996.
238. Pant, T. K. and R. Sridharan, A case study of the low latitude thermosphere during geomagnetic storms and its new representation by improved MSIS model, *to Appear in Ann. Geophys.*, 1998.
239. Parish, H. F., T. J. Fuller-Rowell, D. Rees, T. S. Viridi, and P. J. S. Williams, Numerical simulations of the seasonal response on the thermosphere to propagating tides, *Adv. Space Sci.*, 10, 287, 1990.
240. Parish, H. F., G. R. Gladstone, and S. Chakrabarti, Interpretation of satellite airglow observations during the March 22, 1979, magnetic storm, using the coupled ionosphere-thermosphere model developed at University College London, *J. Geophys. Res.*, 99, 6155, 1994.
241. Patra P. K., Anandan V. K., Rao P. B., and Jain A. R., First observations of equatorial spread-F from Indian MST radar., *Radio Science*, 30, 1159, 1995.
242. Prolss, G. W., K. Najita, and P. C. Yuen, Heating of the low latitude upper atmosphere caused by the decaying magnetic storm ring current, *J. Atmos. Terr. Phys.*, 35, 1889, 1973.
243. Prolss, G. W., and M. J. Jung, Traveling atmospheric disturbances as a possible explanation for daytime positive storm effects of moderate duration at middle latitudes, *J. Atmos. Terr. Phys.*, 40, 1351, 1978.
244. Prolss, G. W., Magnetic storm associated perturbations of the upper atmosphere: Recent results obtained by satellite-borne gas analysers, *Rev. Geophys. Space Phys.*, 18, 183, 1980.
245. Prolss, G. W., Latitudinal structure and extension of the polar atmospheric disturbances, *J. Geophys. Res.*, 86, 2385, 1981.
246. Prolss, G. W., Perturbation of the low-latitude upper atmosphere during magnetic substorm activity, *J. Geophys. Res.*, 87, 5260, 1982.

247. Prolss, G. W., Correlation between upper atmospheric temperature and solar wind conditions, *J. Geophys. Res.*, 90, 11096, 1985.
248. Prolss, G. W., and M. Roemer, Thermospheric storms, *Adv. Space. Res.*, Vol. 7, 10, (10)223, 1987.
249. Prolss, G. W., M. Roemer and J. W. Slowey, Dissipation of solar wind energy in the earth's upper atmosphere: The geomagnetic effects, *Adv. Space. Res.*, 8, (5)215, 1988.
250. Prolss, G. W., L. H. Brace, H. G. Mayr, G. R. Carignan, T. L. Killeen and J. A. Klobuchar, Ionospheric storm effects at subauroral latitudes: A case study, *J. Geophys. Res.*, 16, 1275, 1991.
251. Prolss, G. W., Common origin of positive ionospheric storms at midlatitudes and the geomagnetic activity effect at low latitudes, 98, 5981, 1993.
252. Raghavarao, R., P. Sharma and M. R. Sivaraman, Correlation of the ionisation anomaly with the intensity of the electrojet, *Adv. Space Res.*, XVII, 277, 1970.
253. Raghavarao, R., and M. R. Sivaraman, Enhancement of the equatorial anomaly in the topside ionosphere during magnetic storms, *J. Atmos. Terr. Phys.*, 35, 2091, 1973.
254. Raghavarao, R., P. Sharma and M. R. Sivaraman, Correlation of Ionisation anomaly with the intensity of the electrojet, *Space Res.*, XVIII, 277, 1978.
255. Raghavarao, R., Desai J. N., Anandrao B. G., Narayanan R., Sekar R., Ranjan Gupta, Babu V. V. and Sudhakar V., Evidence for a large scale electric field gradient at the onset of equatorial spread-F, *J. Atmos. Terr. Phys.*, 46, 355, 1984a.
256. Raghavarao, R., J. N. Desai, B. G. Anandrao, R. Narayanan, R. Sekar, Ranjan Gupta, V. V. Babu, and V. Sudhakar, Evidence for a large scale electric field gradient at the onset of equatorial spread-F, *J. Atmos. Terr. Phys.*, 46, 355, 1984.
257. Raghavarao, R., S. P. Gupta, R. Sekar, R. Narayanan, J. N. Desai, R. Sridharan, V. V. Babu, and R. Sudhakar, *In situ* measurements of winds, electric fields and electron densities at the onset of equatorial spread-F, *J. Atmos. Terr. Phys.*, 49, 485, 1987.
258. Raghavarao, R., R. Sridharan, J. H. Sastri, V. V. Agashe, B. C. N. Rao, P. B. Rao and V. V. Somayajulu, The equatorial ionosphere, World Ionospheric/Thermospheric Study, WITS Handbook, 1, 48, 1988a.
259. Raghavarao, R., L. E. Wharton, N. W. Spencer, H. G. Mayr and L. H. Brace, An equatorial temperature and wind anomaly (ETWA), *Geophys. Res. Lett.*, 18, 1193, 1991.
260. Raghavarao, R., L. E. Wharton, N. W. Spencer and Hoegy W. R., Neutral temperature anomaly in the equatorial thermosphere-A source of vertical winds, *Geophys. Res. Lett.*, 20, 1023, 1993.

261. Raghavarao, R., R. Suhasini, W. R. Hoegy, H. G. Mayr and L. Wharton, Local time variation of Equatorial Temperature and Zonal Wind Anomaly (ETWA), *J. Atmos. Space Terr. Phys.*, to appear, 1997
262. Rajaram, G., Structure of the equatorial F-region, topside and bottomside - a review, *J. Atmos. Terr. Phys.*, 39, 1125, 1977.
263. Ranjan Gupta, J. N. Desai, R. Raghavarao, R. Sekar, R. Sridharan and R. Narayanan, Excess heating over the equatorial latitudes during storm sudden commencement, *Geophys. Res. Lett.*, 13, 1055, 1986.
264. Rao, C. S. R., and P. L. Malhotra, A study of geomagnetic anomaly during I.G.Y., *J. Atmos. Terr. Phys.*, 26, 1075, 1964.
265. Rao, H. N. R., and J. H. Sastri, Characteristics of the equatorial midnight temperature maximum in the Indian sector, *Ann. Geophys.*, 12, 276, 1994.
266. Rastogi, R. G., The diurnal development of the Anomalous equatorial belt in the F2 region of the ionosphere, *J. Geophys. Res.*, 64, 727, 1959.
267. Rastogi, R. G., and J. A. Klobuchar, Ionospheric electron content within the equatorial F_2 layer anomaly belt, *J. Geophys. Res.*, 95, 19045, 1990.
268. Ratcliffe, J. A., The formation of the ionospheric layers F-1 and F-2, *J. Atmos. Terr. Phys.*, 8, 260, 1956.
269. Rees, D., T. J. Fuller-Rowell, R. Gordon, T. L. Killeen, P. B. Hays, L. E. Wharton and N. W. Spencer, A comparison of wind observations of the upper thermosphere from the dynamics explorer satellite with the predictions of global time dependent model, *J. Geophys. Res.*, 88, 6289, 1983.
270. Rees, D., T. J. Fuller-Rowell, R. Gordon, T. L. Killeen, P. B. Hays, L. Wharton and N. W. Spencer, *Planet Space Sci.*, 31, 1299, 1983a.
271. Rees, D., R. W. Smith, P. J. Charletron, F. G. McCormac, N. Lloyd and A. Steev, The generation of vertical thermospheric winds and gravity waves at auroral latitudes, 1, Observations of vertical winds, *Planet. Space. Sci.*, 32, 667, 1984a.
272. Rees, D., M. F. Smith and R. Gordon, The generation of vertical thermospheric winds and gravity waves at auroral latitudes, 2, Theory and numerical modeling of vertical winds, *Planet. Space. Sci.*, 32, 685, 1984b.
273. Rees, D., R. Gordon, T. J. Fuller-Rowell, M. F. Smith, G. R. Carignan, T. L. Killeen, P. B. Hays and N. W. Spencer, The composition, structure, temperature and dynamics of the upper thermosphere in the polar regions during October to December 1981, *Planet. Space Sci.*, 33, 617, 1985.

274. Rees, D., T. J. Fuller-Rowell, R. Gordon, M. F. Smith, N. C. Maynard, J. P. Heppner, N. W. Spencer, L. Harton, P. B. Hays and T. L. Killeen, A theoretical and empirical study of the Response of the high latitude thermosphere to the sense of the "Y" component of the interplanetary magnetic field, *Planet. Space. Sci.*, 34, 1, 1986.
275. Rees, D., and T. J. Fuller-Rowell, Seasonal and Universal time variations of the geomagnetic response of the thermosphere and ionosphere, *Proc. AGARD/NATO Symp.*, Munich (May) 1988.
276. Rees, D., An introduction to CIRA model, *Adv. Space. Res.*, 8(5), 5, 1988.
277. Richardson, I. G., C. F. Farrugia, D. Winterhalter, 'Solar activity and coronal mass ejections on the western hemisphere of the sun in Mid-August 1989, association with interplanetary observations at ICE and IMPS Spacecraft, *J. Geophys. Res.*, 99, 2573, 1994.
278. Richmond, A. D. and S. Matsushita, Thermospheric response to a magnetic substorm, *J. Geophys. Res.*, 80, 2839, 1975.
279. Richmond, A. D., S. Matsushita, and J. D. Tarpley, On the production mechanism of electric currents and fields in the ionosphere, *J. Geophys. Res.*, 81, 547, 1976.
280. Richmond, A. D., Nature of gravity wave ducting in the thermosphere, *J. Geophys. Res.*, 83, 1385, 1978.
281. Richmond, A. D., Large-amplitude gravity wave energy production and dissipation in the thermosphere, *J. Geophys. Res.*, 84, 1880, 1979.
282. Richmond, A. D., and R. G. Roble, Electrodynamical effects of thermospheric winds from the NCAR thermospheric general circulation model, *J. Geophys. Res.*, 92, 12365, 1987.
283. Richmond, A. D., E. C. Ridley, and R. G. Roble, A thermosphere/ionosphere general circulation model with coupled electrodynamics, *Geophys. Res. Lett.*, 19, 601, 1992.
284. Richmond, A. D., The Upper Mesosphere and Lower Thermosphere, Johnson, R. M. and Killeen, T. L. (Eds.), *Ann. Geophys. Union*, Washington, DC., 1994.
285. Richmond, A. D., The ionospheric wind dynamo: effects of its coupling with different atmospheric regions, *Geophysical monograph*, 87, 49, 1995.
286. Rino, C. L., R. T. Tsunoda, J. Petriceks, R. C. Livingston, M. C. Kelley, and K. D. Baker, Simultaneous rocket-borne beacon and *in situ* measurements of equatorial spread F - Intermediate wavelength results, *J. Geophys. Res.*, 86, 2411, 1981.
287. Rishbeth, H., and D. W. Barron, Equilibrium electron distributions in the ionospheric F_2 layer, *J. Atmos. Terr. Phys.*, 18, 234, 1960.

288. Rishbeth, H., F_2 layer rates at sunspot minimum, *J. Atmos. Terr. Phys.*, 28, 94, 1966.
289. Rishbeth, H., The effect of winds on the ionospheric F_2 peak, *J. Atmos. Terr. Phys.*, 29, 225, 1967.
290. Rishbeth, H., and O. K. Garriott, Introduction to Ionospheric Physics, Academic Press, New York, 1969.
291. Rishbeth, H., Polarisation fields produced by winds in the equatorial F-region, *Planet. Space Sci.*, 19, 357, 1971.
292. Rishbeth, H., F region storms and thermospheric circulation, *J. Atmos. Terr. Phys.*, 37, 1055, 1975.
293. Rishbeth, H., S. Ganguly and J. C. G. Walker, Field-aligned and field-perpendicular velocities in the ionospheric F_2 layer, *J. Atmos. Terr. Phys.*, 40, 767, 1978.
294. Rishbeth, H., Ion-drag effects in the thermosphere, *J. Atmos. Terr. Phys.*, 41, 885, 1979.
295. Rishbeth, H., The F-region dynamo, *J. Atmos. Terr. Phys.*, 43, 387, 1981.
296. Rishbeth, H., The quadrupole ionosphere, *Ann. Geophys.*, 3, 293, 1985.
297. Rishbeth, H., On the F_2 layer continuity equation, *J. Atmos. Terr. Phys.*, 48, 511, 1986.
298. Rishbeth, H., The ionospheric E-layer and F-layer dynamos- a tutorial review, *J. Atmos. Terr. Phys.*, 59, 1873, 1997.
299. Roble, R. G., P. B. Hays, and A. F. Nagy, Calculated $[OI]6300\text{\AA}$ nightglow Doppler temperatures for solar cycle minimum, *Planet. Space Sci.*, 16, 1109, 1968.
300. Roble, R. G., and R. E. Dickinson, Atmospheric response to heating within a stable auroral red arc, *Planet. Space Sci.*, 18, 1489, 1970.
301. Roble, R. G. and R. E. Dickinson, Is there enough solar EUV radiation to maintain the global mean thermospheric temperatures?, *J. Geophys. Res.*, 78, 249, 1973.
302. Roble, R. G., A. D. Richmond, W. L. Oliver and R. M. Harper, *J. Geophys. Res.*, 83, 999, 1978.
303. Roble, R. G., and B. A. Emery, On the global mean temperature of the thermosphere, *Planet. Space Sci.*, 31, 597, 1983.
304. Roble, R. G., B. A. Emery, R. E. Dickinson, E. C. Ridley, T. L. Killeen, R. B. Harp, G. R. Carignan and N. W. Spencer, *J. Geophys. Res.*, 88, 1711, 1984.
305. Roble, R. G., J. M. Forbes, and F. A. Marcos, Thermospheric dynamics during the March 22, 1979, magnetic storm, 1. Model simulations, *J. Geophys. Res.*, 92, 6045, 1987.

306. Roble, R. G., E. C. Ridley, A. D. Richmond and R. E. Dickinson, A coupled thermosphere/ionosphere general circulation model, *Geophys. Res. Lett.*, 15, 1325, 1988.
307. Roelof, E. C., Energetic neutral atom image of a storm time ring current, *Geophys. Res. Lett.*, 14, 652, 1987.
308. Rush, C. M., and A. D. Richmond, The relationship between the structure of the equatorial anomaly and the strength of the equatorial electrojet, *J. Atmos. Terr. Phys.*, 35, 1171, 1973.
309. Russle, C. T., and R. L. Mcpherson, Semiannual variation of geomagnetic activity, *J. Geophys. Res.*, 78(1), 92, 1973.
310. Sahai et al., Observations of thermospheric neutral winds at 23°S, *Planet. Space. Sci.*, 40, 767, 1992a.
311. Sahai et al., Observations of thermospheric temperatures at 23°S, *Planet. Space. Sci.*, 40, 1545, 1992b.
312. Salah, J. E., and R. H. Wand, Tides in the temperature of the lower thermosphere at mid-latitudes, *J. Geophys. Res.*, 79, 4295, 1974.
313. Sastri, J. H., Equatorial Anomaly in F-region - A review, *Ind. J. Radio and Space Res.*, 119, 225, 1990.
314. Sastri, J. H., H. N. Ranganatha Rao. V. V. Somayajulu and H. Chandra, Thermospheric meridional neutral winds associated with equatorial mid-night temperature maximum (MTM), *Geophys. Res. Lett.*, 1994.
315. Sastri, J. H., Huang Y. N., Shibata T., Okuzawa T., *Geophys. Res. Lett.*, 22, 2645, 1995.
316. Schaefer, E. J. and Brown, J., Additional rocket-borne mass spectrometer measurements of the dissociation of oxygen, *J. Geophys. Res.*, 69, 1455, 1964.
317. Schroder S., and G. W. Prolss, Heating of the upper atmosphere by oxygen ions precipitated from the ring current, *Ann. Geophys.*, 9, 267, 1991.
318. Sharma, P. and R. Raghavarao, Simultaneous occurrence of ionisation ledge and counter-electrojet in the equatorial ionosphere: observational evidence and its implications, *Can. J. Phys.*, 67, 166, 1989.
319. Sipler, D. P., M. A. Biondi and R. G. Roble, F-region neutral winds and temperatures at equatorial latitudes: Measured and predicted behaviour during geomagnetically quiet conditions, *Planet. Space Sci.*, 31, 53, 1983.
320. Sekar, R. and Raghavarao R., Role of vertical winds on the Rayleigh-Taylor mode instabilities of the nighttime equatorial ionosphere, *J. Atmos. Terr. Phys.*, 49, 981, 1987.

321. Sekar, R., Suhasini R. and Raghavarao R., Effects of vertical winds and electric fields in the non-linear evolution of equatorial spread-F, *J. Geophys. Res.*, 99, 2205, 1994.
322. Sekar, R. and Raghavarao R., A case study of on the evolution of equatorial spread-F by a non-linear numerical model using the results from a set of coordinated measurements, *J. Atmos. Solar Terr. Phys.*, 59, 343, 1997.
323. Senior, C., and M. Blanc, On the control of magnetospheric convection by the spatial distribution of ionospheric conductivities, *J. Geophys. Res.*, 89, 261, 1984.
324. Shepherd, G. G., R. G. Roble, C. Mclandress and W. E. Wand, WINDII observations of the 558nm emission in the lower thermosphere: the influence of dynamics on composition, *J. Atmos. Solar Terr. Phys.*, 59, 655, 1997.
325. Shimazaki T., Dynamical structure of the ionospheric F2 layer, *J. Radio Res. Labs.*, Japan 4, 309, 1957.
326. Sica, R. J., M. H. Rees, R. G. Roble, G. Hernandez, and G. J. Romick, The altitude region sampled by ground based Doppler temperature measurements of the [OI] 15867 K emission line Aurora, *Planet. Space. Sci.*, 34, 483, 1986.
327. Sinha, H. S. S., Misra, R. N., Chandra H., Raizada S., Dutt, N., and G. D. Vyas, Multiwavelength optical imaging of ionospheric plasma depletions, Ind. *J. Radio Space Phys.*, 25, 44, 1996.
328. Sipler, D. P. and M. A. Biondi, Equatorial F-region neutral winds from nightglow OI 630 nm Doppler shifts, *Geophys. Res. Lett.*, 5, 373, 1978.
329. Sivjee, G. G., Airglow Hydroxyl Emissions, *Adv. Space Res.*, 40, 235, 1992.
330. Slavin, J. A., E. J. Smith and D. S. Intriligator, A comparative study of distant magnetotail structure at venus and earth, *Geophys. Res. Lett.*, 11, 1074, 1984.
331. Slavin, J. A., and Y. Kamide, Solar wind-magnetosphere coupling: Introduction. In solar wind-magnetosphere coupling (ed. Y. Kamide and J. Slavin), pp. ix - xii, Terra Scientific, Tokyo and Reidel, Dardrecht., 1986.
332. Slipher, V. M., Spectrographic studies of the planets, *Mon. Not. Rev. Astron. Soc.*, 93, 657, 1933.
333. Slowey, J. W., Thermospheric storm effects, *Adv. Space Res.*, 7(10), 237, 1987.
334. Sommer, L. A., Uber den Lengwelligen teil des sichtbaren spektrums des NOchthimmelichetes, *Z. Phys.*, 80, 273, 1933.

335. Sonnerup, B. U. O., Magnetic field reconnection at the magnetopause: An overview. In *Magnetic Reconnection in Space and Laboratory plasma* (ed. EW. Hones Jr.), pp. 92-103, *Geophysical Monograph*, 30, AGU. Washington, D.C., 1984.
336. Spencer, N. W., G. R. Carignan, H. G. Mayr, H. B. Niemann, R. F. Theis and L. E. Wharton, The midnight temperature maximum in the earth's equatorial thermosphere, *Geophys. Res. Lett.*, 6, 444, 1979.
337. Spencer, N. W., L. E. Wharton, H. B. Niemann, A. E. Hedin, G. R. Carignan and J. C. Maurer, The Dynamic Explorer wind and Temperature Spectrometer, *Space Sci. Instrum.*, 5, 417, 1981.
338. Spencer, N. W, L. E. Wharton, G. R. Carignan, and J. C. Maurer, Thermosphere zonal winds, vertical motions and temperatures as measured from Dynamics Explorer, *Geophys. Res. Lett.*, 9, 953, 1982.
339. Spiro, R. W., P. H. Reiff and L. J. Maher, Precipitating electron energy flux and auroral zone conductances: An empirical model, *J. Geophys. Res.*, 87, 82115, 1982.
340. Sridharan et al., Winds, wind-shears and plasma densities during the initial phase of a magnetic storm from equatorial latitudes, *J. Atmos. Terr. Phys.*, 51, 169, 1989.
341. Sridharan, R., S. Gurubaran, R. Raghavarao and R. Suhasini, Coordinated thermospheric and F-region measurements from low latitudes, *J. Atmos. Terr. Phys.*, 33, 575, 1991.
342. Sridharan, R., Optical investigation of upper atmosphere: some of the recent development, *Vikram Sarabhai Award Lectures*, August, 1992.
343. Sridharan, R., R. Narayanan, N. K. Modi and D. Pallam Raju, Novel Mask design for multi-wavelength dayglow photometry, *Appl. Opt.*, 32, 4178, 1993.
344. Sridharan, R., Pallam Raju D., Raghavarao R. and Ramarao P. V. S., Precursor to equatorial spread-F in OI630.0nm dayglow, *Geophys. Res. Lett.*, 21, 2797, 1994.
345. Sridharan, R. et al., Ionisation hole campaign - a coordinated rocket and ground-based study at the onset of equatorial spread-F: first results, *J. Atmos. Solar Terr. Phys.*, 59, 2051, 1997.
346. Sridharan, R. et al., Multiwavelength Daytime photometer-A new tool for the investigation of atmospheric processes, *Measurement Sci. Tech.*, 1998.
347. Steele, D. P., and L. L. Cogger, Polar patches and the 'tongue of ionisation', *Radio Sci.*, 31, 667, 1996.
348. Stolarski, R. S., P. B. Hays, and R. G. Roble, Atmospheric heating by solar EUV radiation, *J. Geophys. Res.*, 80, 2266, 1975.

349. Stolarski, R. S., Energetics of the midlatitude thermosphere, *J. Atmos. Terr. Phys.*, 38, 863, 1976.
350. Stubbe, P., and S. Chandra, The effect of electric fields on the F-region behaviour as compared with neutral winds, 32, 1909, 1970.
351. Stubbe, P. and S. Chandra, Ionospheric heating by neutral winds, *Planet. Space Sci.*, 19, 731, 1971.
352. Sugiura M. and S. Chapman, The average morphology of geomagnetic storms with sudden commencement, *Abandl. Akad. Wiss. Gottingen Math. Phys.*, K1(4), 1960.
353. Tausch, D. R., G. R. Carignan, and C. A. Reber, Neutral composition variation above 400 kilometers during a magnetic storms, *J. Geophys. Res.*, 76, 8318, 1971.
354. Takahashi, S., M. Takeda, and Y. Yamade, Simulation of storm-time ring current system and the dawn dusk asymmetry of geomagnetic variations, *Planet. Space. Sci.*, 39, 821, 1991.
355. Taylor G. N., Meridional F_2 -region plasma drifts at Malvern, *J. Atmos. Terr. Phys.*, 36, 267-286, 1974.
356. Testud, J., P. Amayeng and M. Blank, Middle and low latitude effects of auroral disturbances from incoherent scatter, *J. Atmos. Terr. Phys.*, 37, 989, 1975.
357. Thomas L., and R. B. Norton, Possible importance of internal excitation in ion molecule reactions in the F-region, *J. Geophys. Res.*, 71, 227, 1966.
358. Tinsley, B. A., Energetic neutral atom precipitation as a possible source of midlatitude F-region winds, *Geophys. Res. Lett.*, 6, 291, 1979.
359. Tinsley, B. A., Neutral atom precipitation - A review, *J. Atmos. Terr. Phys.*, 43, 617, 1981.
360. Tinsley, B. A., Y. Sahai, M. A. Biondi, and J. W. Meriwether, Equatorial particle precipitation during geomagnetic storms and relationship to equatorial thermospheric heating, *J. Geophys. Res.*, 93, 270, 1988.
361. Torr, M. R., J. G. G. Walker and D. G. Torr, Escape of the fast oxygen from the atmosphere during geomagnetic storms, *J. Geophys. Res.*, 79, 5267, 1974.
362. Torr, M. R. , P. G. Richards and D. G. Torr, A new determination of the ultraviolet heating efficiency of the thermosphere, *J. Geophys. Res.*, 85, 6819, 1980.
363. Torr M. R. and D. G. Torr, The role of metastable species in the thermosphere, *Rev. Geophys. Space Phys.*, 20, 91, 1982.
364. Torr M. R. and D. G. Torr, Atmospheric spectral imaging, *Science*, 225, 169, 1984.

365. Trinks, H., K. H. Fricke, U. Laux, G. W. Prolss, and U. Von Zahn, Esro-4 gas analyzer result 3. Spatial and temporal structure of the mid latitude atmosphere during a geomagnetic storm, *J. Geophys. Res.*, 80, 4571, 1975.
366. Trinks, H., D. Offermann, U. Von Zahn, and C. Steinhauer, Neutral composition measurements between 90 and 220 km altitude by Rocket-borne mass spectrometer, *J. Geophys. Res.*, 83, 2169, 1978.
367. Tsurutani, B. T., W. D. Gonzales, F. Tang and Y. T. Lee, Great magnetic storms, *Geophys. Res. Lett.*, 19, 73, 1992.
368. Turgeon E. C. and G. G. Shepherd, Upper atmospheric temperatures from Doppler line widths -II, *Planet. Space Sci.*, 32, 1737, 1962.
369. Vickrey, J. F., R. R. Vovdrak and S. J. Mathew, Energy deposition by precipitating particles and Joule dissipation in the auroral ionosphere, *J. Geophys. Res.*, 87, 5184, 1982.
370. Vorob'yev, V. G, Sc-Associated effects in Auroras, *Geomag. Aeron.*, 14, 72, 1974.
371. Walker, G. O., and J. H. K. Ma, Influence of solar flux and the equatorial electrojet on the diurnal development of the latitude distribution of total electron content in the equatorial anomaly, *J. Atmos. Terr. Phys.*, 34, 1419, 1972.
372. Walker, G. O., J. H. K. Ma, R. G. Rastogi, M. R. Deshpande and H. Chandra, Dissimilar forms of the ionospheric equatorial anomaly observed in East Asia and India, *J. Atmos. Terr. Phys.*, 42, 629, 1980.
373. Walker, G. O., Longitudinal structure of the F-region equatorial anomaly - a review, *J. Atmos. Terr. Phys.*, 43, 763, 1981.
374. Walker, G. O., T. Y. Y. Li, J. Soegijo, T. Kikuchi, T. N. Hnang, V. Badillo and E. P. Szuszczewicz, North-south asymmetry of the equatorial ionospheric anomaly observed in East Asia during the SUNDIAL-87 campaign, *Ann. Geophys.*, 9, 393, 1991.
375. Walker, G. O., J. H. K. Ma and E. Gotton, The equatorial ionosphere anomaly in electron content for solar minimum to solar maximum South-East Asia, *Ann. Geophysicae*, 12, 195, 1994.
376. Walker, J. C. G., Correlation of wind and electric field in the nocturnal F-region, *Geophys. J. R. Astron. Soc.*, 60, 85, 1980.
377. Wallace , L. and M. B. McElroy, The visual dayglow, *Planet. Space Sci.*, 14, 677, 1966.
378. Weber, E. J., Buchau J., Eather H. and Mende S. B., North-South aligned equatorial airglow depletions, *J. Geophys. Res.*, 83, 712, 1978.

379. Wharton, L. E., N. W. Spencer and H. G. Mayr, The earth's thermospheric super rotation from Dynamics Explorer 2, *Geophys. Res. Lett.*, 11, 531, 1984.
380. Wilson, R. M., On the distribution of sunspot cycle periods, *J. Geophys. Res.*, 92, 10101, 1987.
381. Willson, R. C. and H. S. Hudson, The sun's luminosity over a complete solar cycle, *Nature*, 381, 42, 1991.
382. Woodman R. F., Vertical drift velocities and east-west electric fields at the magnetic equator, *J. Geophys. Res.*, 75, 6249, 1970.
383. Woodman R. F., and La Hoz C., Radar observations of F-region equatorial irregularities., *J. Geophys. Res.*, 41, 5447, 1976.
384. Wright, J. W., Horizontal drifts accompanying large vertical motions of the nocturnal F-regions, *Planet. Space Sci.*, 19, 1327, 1971.
385. Wu Q., T. L. Killeen, and N. W. Spencer, Dynamics Explorer 2, Observations of equatorial thermospheric winds and temperatures: Local time and longitudinal dependences, *J. Geophys. Res.*, 99, 6277, 1994.
386. Yagi, T., and P. L. Dyson, The influence of neutral temperatures and winds on the F-layer heights, *J. Atmos. Terr. Phys.*, 47, 575, 1985.
387. Zalesak, S. T., and Ossakow S. L., Nonlinear equatorial spread F: Specially large bubbles resulting from large horizontal scale initial perturbations, *J. Geophys. Res.*, 85, 2131, 1980.
388. Zalesak, S. T., Ossakow S. L. and Chaturvedi, P. K., Nonlinear equatorial spread F: The effect of neutral winds and background Pedersen conductivity, *J. Geophys. Res.*, 87, 151, 1982.